Carbon-isotope stratigraphy, geochemistry and geochronology of the Lower Jurassic of the Cardigan Bay Basin (Llanbedr (Mochras Farm) borehole), UK, and the Neuquén Basin, Argentina

Marisa Storm

St. Peter's College

University of Oxford

Thesis submitted for the degree of

Doctor of Philosophy

Supervised by Professor Hugh Jenkyns, Professor Stephen Hesselbo and Doctor Micha Ruhl

Declaration

I declare that the work presented in this thesis is wholly my own, except where otherwise stated. The views and interpretations expressed herein are mine, and do not represent those of any other person or group except where this is cited to be the case.

Abstract

The lack of a continuous high-resolution carbon-isotope ($\delta^{13}C$) record based on a single material, and thus a single carbon reservoir, has so far inhibited investigation on the secular evolution of the Early Jurassic (~201–175 Myr) carbon cycle. The existing $\delta^{13}C$ records for the Lower Jurassic Series tend to cover short stratigraphic intervals, originate from a variety of different sedimentary basins and different carbon reservoirs, or are of relatively low stratigraphic resolution. New $\delta^{13}C_{TOC}$ data from the continuous strata of the stratigraphically expanded Llanbedr (Mochras Farm) drill-core provides the most expanded Lower Jurassic $\delta^{13}C_{TOC}$ record to date. The record aggregates several $\delta^{13}C_{TOC}$ excursions of different stratigraphical extent and magnitude. Based on stratigraphic correlations, several of these excursions appear approximately coeval in several NW European sedimentary basins, in multiple carbon reservoirs. Geochemical characterization reveals an organic-lean character of the Lower Jurassic sediments, dominated by terrestrial organic matter. Changes in the relative admixture of marine vs terrestrial organic matter appear as a likely subordinate mechanism driving changes in $\delta^{13}C$. Consecutively appearing small-amplitude fluctuations (~0.5–2 ‰) of comparable magnitude and stratigraphic thickness, including those recorded elsewhere, and hitherto unrevealed excursions, appear to be largely orbitally paced, corresponding to long (405-kyr) eccentricity cycles. Orbital tuning of the continuous Hettangian to Pliensbachian record allows an astronomical timescale to be established, which closely agrees with previous timescales for the Hettangian and Pliensbachian stages, and provides the basis for a Sinemurian chronology.

Furthermore, a stratigraphical framework is developed on Lower Jurassic sections in the Neuquén Basin, Argentina, providing the grounds for future work on the radioisotopic dating of the onset of the Toarcian oceanic anoxic event (T-OAE). A chemostratigraphic dataset allows the correlation to same-age records. Coeval appearance of siderite in the lower Toarcian of the Mochras core and the Neuquén Basin suggests a disturbance of the global sulphur cycle (possible low sulphate ocean) during the T-OAE.

Extended Abstract

The Early Jurassic (~201–175 Myr) was a time of global environmental changes. Most significant was the Toarcian oceanic anoxic event (T-OAE, ~183 Myr) marked by widespread transient low-oxygen environments and organic-carbon burial, and disturbance of the global carbon-cycle, witnessed by changes in the $\delta^{13}C$ signature of sedimentary materials from both the marine and terrestrial realm. Other $\delta^{13}C$ excursions, although smaller in magnitude, have been recognized prior to the T-OAE in Hettangian to Pliensbachian strata. However, there is no comprehensive understanding of the timing of these events, trigger mechanisms or possible causal links. The lack of a continuous high-resolution $\delta^{13}C$ record has so far inhibited investigation of the secular evolution of the Early Jurassic carbon-isotope signature and its relevance in relation to the global carbon cycle.

The first part of this thesis aims to improve the overall understanding of the evolution of the Early Jurassic $\delta^{13}C$ record based on a single material, and thus a single carbon reservoir. Therefore, a bulk-organic carbon ($\delta^{13}C_{TOC}$) record is generated for the continuous Hettangian, Sinemurian and Pliensbachian stages of the stratigraphically expanded Mochras core, in order to investigate the timing, pacing, and geochemical nature of excursion intervals. The record aggregates several carbon-isotope excursions (CIEs) of different stratigraphical extent and magnitude. Based on stratigraphic correlations, several of these excursions appear approximately coeval in the Hettangian to Pliensbachian record of several NW European sedimentary basins, in multiple carbon reservoirs.

Individual small-amplitude (~0.5–2‰) CIEs identified and characterized in previous datasets appear less singular in the collective context of the continuous and stratigraphically expanded Mochras record, where CIEs of similar magnitude and stratigraphical thickness appear consecutively, also including $\delta^{13}C_{TOC}$ excursions not previously identified elsewhere. Spectral and time-series analysis of the Mochras $\delta^{13}C_{TOC}$ record indicates the small-amplitude variations to be largely paced by orbital forcing and corresponding to long (405 kyr) eccentricity cycles. Changes in the relative amount of marine/terrestrial organic matter do appear with some, but not all eccentricity-paced $\delta^{13}C_{TOC}$ excursions. The organic-matter composition does therefore not appear to be the main driving mechanism changing the isotopic composition of the

bulk organic matter. Although several eccentricity-paced isotope excursions occur in multiple carbon-isotope reservoirs, and some with a regional spatial extent, it is also not conclusive whether eccentricity-paced fluctuations in $\delta^{13}C_{TOC}$ record of the Mochras core indicate changes in the global carbon cycle.

Orbital tuning of dominant spectral peaks provides a floating timescale which agrees largely with previous timescales on the Hettangian and Pliensbachian, and provides the first astronomical time scale for the Sinemurian Stage and constituent biostratigraphical zones, suggesting a stage duration of 7.4 Myr. In total, the orbitally tuned $\delta^{13}C_{TOC}$ record of the Hettangian to Pliensbachian of the Mochras core comprises ~18.28 Myrs, and provides the most expanded Early Jurassic astronomical timescale to date. The time scale, anchored to a numerical age corresponding to the Triassic–Jurassic boundary, agrees (within uncertainties) with biostratigraphically calibrated radioisotopic ages for the Hettangian-Sinemurian boundary, the late Pliensbachian (mid-*margaritatus* Zone) and the Pliensbachian–Toarcian boundary. According to the time scale developed herein, the large-scale (~4‰) negative Sinemurian–Pliensbachian boundary excursion appears to coincide with increased volcanic activity linked to a late phase of the central Atlantic Magmatic Province. The temporal correlation supports previous work suggesting volcanogenic subaerial release of CO_2 as the causal mechanism behind the negative excursion.

The geochemical characterization of the sediments, based on Rock-Eval analysis and organic petrography, reveals an immature to early mature, organic-lean nature throughout the study interval. The organic-matter assemblage is dominated by allochthonous terrestrial material, however, a slight increase in the relative abundance of marine organic compounds appears in the upper Sinemurian and Pliensbachian strata, which onsets concomitantly with the Sinemurian–Pliensbachian boundary negative excursion. This episode of relatively higher organic-matter preservation and productivity is likely linked to changes in the environment, possibly induced by the opening of the Hispanic corridor inducing changes in water circulation, climate and/or nutrient supply. The increase in isotopically light marine organic-matter appears, however, to be subordinate in driving the $\delta^{13}C_{TOC}$ signature. The Upper Pliensbachian *margaritatus* and *spinatum* Zone negative excursion recorded in the Mochras core appears larger in magnitude (~4.5‰) compared to other locations that recorded the

event. The local expression of the $\delta^{13}C_{TOC}$ excursions in the Mochras core appears, however, not to be amplified by changes in the bulk organic-matter assemblage.

The second part of this thesis provides work towards the accurate numerical dating of the onset of the Toarcian oceanic anoxic event (~183 Myr, T-OAE) in order to elucidate a causal relationship between the event and the emplacement of the Karroo-Ferrar large igneous province. Therefore, a well-defined biostratigraphical and geochemical framework is presented, generated from stratigraphically expanded Lower Jurassic sections in the northern part of the Neuquén Basin.

Four sections (Arroyo Serrucho E–E', F–F', Las Overas and Las Overas-C), located in the Mondoza Province of the northern Neuquén Basin, were studied. The stratigraphic intervals correspond to the Upper Puesto Arraya and Lower Tres Esquinas Formation and record Late Pliensbachian to Late Toarcian early marine sedimentation during gradual deepening of the basin. The two stratigraphically higher sections, Las Overas and Las Overas-C were biostratigraphically calibrated. Correlation to the previously studied nearby Arroyo Serrucho sections validates the biostratigraphical framework, and suggests the *D. tenuicostatum–D. hoelderi* boundary to be stratigraphically below the previously defined level. The new boundary supports a stratigraphically expanded expression of the *D. hoelderi* Zone, compared to the relatively condensed *P. largaense*, *P. pacificum* and *C. chilensis* zones.

The new $\delta^{13}C_{TOC}$ data from the Las Overas and Las Overas-C sections expands previous records from the Arroyo Serrucho sections, and provides a stratigraphically expanded record from the uppermost *D. tenuicostatum* Zone in the Lower Toarcian to the upper Toarcian *Dumortieria* Zone, interrupted by a stratigraphic gap in the *Phymatoceras* Zone. The studied interval is equivalent to the *D. tenuicostatum* to upper *pseaudoradiosa* European ammonite zones, and reveals a stratigraphically expanded ~6‰ negative excursion in the lower D. *hoelderi* Zone (=*serpentinum* Zone), representing the local expression of the T-OAE.

The correlation of the $\delta^{13}C_{TOC}$, TOC and Hg/TOC records to the same age strata in the Southern Neuquén Basin (Arroyo Lapa section) supports the likely complete nature of the negative excursion recorded in the lower *D. hoelderi* Zone of the Las Overas

section, although strata lower in the *D. tenuicostatum* Zone should be examined to confirm this interpretation.

The geochemical characterization of the section reveals the organic-lean character of the sediments. The extremely low TOC values (~0.4 wt%) corresponding to the negative CIE might be ascribed to basin subsidence and concomitant high sediment input and dilution due to increased continental weathering-rate, possibly induced by the warmer and wetter climate, at least locally, during the T-OAE. The contribution of reworked Carboniferous organic matter, indicated by palynology, appears not to have biased the bulk organic carbon-isotope signal, but supports the significance of continental weathering.

The correlation between the new Neuquén Basin and the stratigraphically expanded and continuous $\delta^{13}C_{TOC}$ record from the Mochras core, Cardigan Bay Basin, UK, suggests that both records represent the global carbon cycle signal of the Lower Toarcian. The Upper Toarcian correlation is compromised somewhat by very different stratigraphic characteristics of the sections, and the stratigraphic gap in the Neuquén Basin record corresponding to the *Phymatoceras* Zone. The approximate coeval appearance of siderite-bearing strata and concomitant negative carbon-isotope excursion in the Mochras core and the Las Overas section supports the existence of a low-sulphate ocean during the Early Toarcian and exemplifies the global extent of T-OAE and associated disturbance of the biogeochemical cycle.

Acknowledgements

The work presented in this thesis was shaped, supported and assisted by a wide variety of people. Firstly, I want to thank my supervisors Hugh Jenkyns, Stephen Hesselbo and Micha Ruhl for their contribution of knowledge, inspiring ideas and discussions, which have guided me through the course of my doctorate.

I want to thank Melanie Leng and Dan Condon for analytical support, and James Riding for the great help on sampling the Mochras core. Thanks to everyone who made the field work in Argentina possible: Susana Damborenea and Miguel Manceñido for guiding us through the Neuquén Basin, Aisha Al-Suwaidi for joining us in the field and sharing her knowledge, and Alberto Riccardi for providing great help on the biostratigraphical framework.

I want to thank Steve Wyatt for great technical support in the lab and for persistently fixing the Rock-Eval. Thanks for the very diverse lab support to Jonathan Welsh, Adian Woods and Gren Turner, Johan Weijers and Erik Tegelaar, Mabs Gilmore and Simona Nicoara and Jenny Huggett.

Special thanks go to Doctor Lawrence Percival, for the friendliest welcoming to Oxford, and the many, many discussions on the Jurassic and beyond. I also want to thank Alex Dickson for the sage advice along the way.

Very heartfelt thanks go out to the great people I met in Oxford. It became too many over the years to mention all of them. Most warmly thanks go to Jennifer Shurville for the amazing time in our home, Serjoscha Evers and Moritz Schulze Darup for the many pints, Victoria Elliot for all the outings, on the river and elsewhere, and to Lauren O'Conner, for giving me a temporary home and for last-minute proof-reading. Many thanks also to Tim Sweere, Leonardo Tedeschi and Jo Katchinoff for being great company in the office. I am also deeply grateful to have met Matthew Molteno during my time in Oxford, and his love, support and interest that carried me through this thesis.

I certainly want to thank my parents for shaping and supporting my scientific interest, and for financial support during my studies; and my brother, for visiting me in Oxford.

Importantly, I would like to acknowledge Shell, the Isotope Geosciences Facilities Steering Committee for the Natural Environment Research Council (NIGFSC), and the Burdett Coutts Fund of the Department of Earth Sciences, University of Oxford, for the financial support, and the British Geological Survey for the loan of samples.

Table of Contents

Abstract ..... **III**

Extended Abstract ..... **V**

Acknowledgements ..... **IX**

Chapter 1 : Introduction **1**

1.1. Background and hypotheses 3

1.1.1. Investigating carbon cycle perturbations 4

1.1.2. The Early Jurassic palaeoenvironment and carbon cycle 6

1.2. Aims of this study 7

1.3. Materials 9

1.3.1. The Llanbedr (Mochras Farm) drill-core 9

1.3.2 Outcrop samples from the Neuquén Basin, Argentina 10

1.4. Analytical Methods 12

1.4.1. Organic carbon isotope analysis ($\delta^{13}C_{TOC}$) 12

1.4.2. Organic carbon-isotope analysis on fossil wood fragments ($\delta^{13}C_{wood}$) 13

1.4.3. Rock-Eval analysis 13

1.4.4. Organic petrography 14

1.4.5. X-Ray fluorescence 14

1.4.6. QUEMSCAN 15

1.4.7. Palynology 16

1.4.8. Sedimentary mercury concentrations 16

1.4.9. Radioisotopic U-Pb dating 17

Chapter 2 : Geological settings and stratigraphical framework of the Llanbedr (Mochras Farm) drill-core, Cardigan Bay Basin, UK **19**

2. Introduction 21

2.1. Paleogeography and tectonic setting 21

2.2. Stratigraphy 24

2.2.1. Lithostratigraphy 27

2.3. Depositional environment 31

Chapter 3 : Continuous carbon-isotope ($\delta^{13}C_{TOC}$) record from the Lower Jurassic of the Llanbedr (Mochras Farm) borehole, Cardigan Bay Basin, UK **33**

3. Abstract 35

3.1. Introduction 35

3.2. Material and Methods 37

3.3. A high-resolution $\delta^{13}C_{TOC}$ record of the Hettangian, Sinemurian and Pliensbachian stages of the Mochras core 37

3.4. Correlation of NW European Lower Jurassic carbon-isotope records 40

3.5. Discussion and Conclusion 48

Chapter 4 : Orbital pacing of the Early Jurassic Hettangian to Pliensbachian $\delta^{13}C_{TOC}$ record 51
4. Abstract 53
4.1. Introduction 53
4.2. Spectral and time-series analysis 55
4.3. Results 59
4.4. Discussion 61
4.4.1. Correlation of dominant spectral peaks and small-amplitude CIEs 61
4.4.2. Towards an Early Jurassic floating Time-Scale 62
4.4.3. Towards an Early Jurassic absolute Time-Scale 67
4.4.4. Implications on the long-term Early Jurassic (Hettangian–Pliensbachian) $\delta^{13}C_{TOC}$ perturbations 73
4.4.5. Implications for the Upper Pliensbachian (upper margaritatus Zone and spinatum Zone) negative CIE 74
4.5. Conclusion 77

Chapter 5 : Characterization of the organic and inorganic sedimentary components of the Lower Jurassic Hettangian to Pliensbachian strata of the Llanbedr (Mochras farm) drill-core 79
5. Abstract 81
5.1. Introduction 81
5.2. Material and Methods 83
5.3. Organic-matter characterization 84
5.3.1. Rock Eval parameters 84
5.3.2. Validity of Rock-Eval data 87
5.3.3. Organo-facies 88
5.3.4. Characterization of the coal fragments 94
5.4. Effect of compositional changes of the organic matter on the $\delta^{13}C_{TOC}$ 95
5.4.1. Long-term and large-magnitude $\delta^{13}C_{TOC}$ trends 98
5.4.2. Eccentricity-paced small-amplitude $\delta^{13}C_{TOC}$ excursions 100
5.5. Inorganic geochemical characterization 101
5.6. Discussion 105
5.6.1. Depositional environment 105
5.6.2. Origin of the spores, pollen and coal fragments 107
5.6.3. Validity and Limitations of the interpretation of HI–$\delta^{13}C_{TOC}$ plots 107
5.6.4. Implications of changes in organic matter on the long-term carbon-isotope record 108
5.7. Conclusion 114

Chapter 6 : Stratigraphic framework of the Lower Jurassic of the northern Neuquén Basin, Mendoza Region, Argentina 117
6. Abstract 119
6.1. Palaeogeography and Tectonic Setting of the Neuquén Basin, Argentina 119
6.2. Lithofacies of the study area 125
6.3. Biostratigraphic framework of the study area 128
6.4. Discussion 129
6.5. Conclusion 133

Chapter 7 : Chemostratigraphic constraints of the Early Jurassic Toarcian stage in the Neuquén Basin, Argentina 135
7. Abstract 137
7.1. Introduction 137
7.2. Materials and Methods 141
7.3. $\delta^{13}C_{TOC}$ record of the Toarcian stage in the Northern Neuquén Basin 142
7.4. Geochemical organic-matter characterization 144
7.5. Mercury as a tracer for distal volcanism 147
7.6. Discussion 148
7.7. Conclusion 156

Chapter 8 : Conclusions and future work 159
8. Conclusions 161
8.1. Future work 164

Chapter 9 : Appendix 169

Chapter 10 : References 195

List of Figures

Figure 1.1: Basic steady-state model for the Phanerozoic exogenic carbon cycle. 5
Figure 1.2: Sample resolution for $\delta^{13}C_{TOC}$, Rock-Eval and HH-XRF analysis 11
Figure 2.1: Early Jurassic palaeogeography of the Mochras core 22
Figure 2.2: Simplified geological map of the Cardigan Bay 23
Figure 2.3: Stratigraphy of the Mochras drill-core 25
Figure 2.4: Stratigraphy of the uppermost Rhaetian–lower Hettangain 26
Figure 2.5: Comparative lithostratigraphic development of the Lower Jurassic 27
Figure 2.6: Core photographs. 29
Figure 3.1: $\delta^{13}C_{TOC}$ record of the Uppermost Rhaetian to Toarcian 38
Figure 3.2: Carbon-isotope excursions in Hettangian to Pliensbachian strata 41
Figure 3.3: Uppermost Rhaetian and lowermost Hettangian $\delta^{13}C_{TOC}$ record. 42
Figure 3.4: $\delta^{13}C_{TOC}$ record of the Hattangian to Toarcian of the Mochras core..... 46
Figure 4.1: $\delta^{13}C_{TOC}$ record spanning the Hettangian to Pliensbachian stages 58
Figure 4.2: MTM power spectra of individual data segments and corresponding dominant spectral peaks..... 60
Figure 4.3: MTM power spectra of the tuned $\delta^{13}C_{TOC}$ record 64
Figure 4.4: 405-kyr tuned $\delta^{13}C_{TOC}$ record..... 65
Figure 4.5: 405-kyr tuned $\delta^{13}C_{TOC}$ time series..... 68
Figure 4.6: Tuned $\delta^{13}C_{TOC}$ record relative to the absolute Early Jurassic time-scale .. 72
Figure 4.7: Correlation of the $\delta^{13}C_{carb}$ and $\delta^{13}C_{TOC}$ records of the upper Pliensbachian from different European localities..... 76
Figure 5.1: $\delta^{13}C_{TOC}$, Hydrogen Index, total organic-matter content and oxygen index of the uppermost Rhaetian to Pliensbachian stages.. 85
Figure 5.3: Maceral composition 91
Figure 5.4: Photomicrographs showing the organic facies of petrographically analyzed samples 92
Figure 5.5: photomicrographs of a Densospore and coal clast, $\delta^{13}C_{TOC}$ and $\delta^{13}C_{coal}$ record of the Upper Pliensbachian..... 95
Figure 5.6: HI–$\delta^{13}C_{TOC}$ plots 97
Figure 5.7: $\delta^{13}C_{TOC}$-HI plots of some small-amplitude CIEs 100
Figure 5.8: $\delta^{13}C_{TOC}$ record and elemental ratios 102

Figure 5.9: Petrographics of carbonate and other mineral facies 103
Figure 5.10: Photomicrographs showing the organo-mineral facies 104
Figure 5.11: $\delta^{13}C_{TOC}$ excursions with accompanied changes in HI 113
Figure 6.1: Toarcian paleogeography, Neuquén Basin during the Early Jurassic, and geological map indicating Jurassic and Cretaceous strata 120
Figure 6.2: Schematic evolution of the Neuquén Basin from the Late Triassic to the Early Cretaceous 121
Figure 6.3: Location of the study area 123
Figure 6.4: Andean ammonite zonation and biostratigraphy and correlation to the European zonation 124
Figure 6.5: Simplified lithological logs of the Sections Arroyo Serrucho E-E' and Arroyo Serrucho F-F', Las Overas and Las Overas-C 126
Figure 6.6: Field Photograph 127
Figure 6.7: Andean ammonite zonation and biostratigraphic intervals present within the herein studied sections and previously studies sections 131
Figure 6.8: Correlation of the provisional biostratigraphy of the Las Overas section and the nearby biostratigraphically calibrated sections 133
Figure 7.1: Comparison of Upper Pliensbachian and Lower Toarcian sections 140
Figure 7.2: $\delta^{13}C_{TOC}$ and TOC record of the four studied sections 143
Figure 7.3: Phytoclast assamblages in kerogen slides 146
Figure 7.4: bulk rock sedimentary mercury levels 148
Figure 7.5: Correlation of the $\delta^{13}C_{TOC}$ and TOC records of the biostratigraphically calibrated Las Overas section and Arroyo Serrucho sections 149
Figure 7.6: Correlation of the $\delta^{13}C_{TOC}$ and TOC records of the Northern and Southern Neuquén Basin 151
Figure 7.7: Correlation of the $\delta^{13}C_{TOC}$ record and siderite nodule occurrence of the Toarcian stage of the Neuquén Basin and the Cardigan Bay Basin. 155
Figure 8.1 Schematic illustrations of large- and small amplitude $\delta^{13}C_{TOC}$ trends recorded in the Mochras core. 167
Figure 8.2 Cathodoluminescence images of zircons 165

Appendix Figures

Figure A-1: Wavelet analysis and MTM power spectrum of the unsegmented $\delta^{13}C_{TOC}$ record 171
Figure A-2: Comparison of the $\delta^{13}C_{TOC}$ and elemental calcium concentrations 172
Figure A-3: Wavelet analysis of the tuned δ13CTOC record 173
Figure A-4: TOC-S_2 plot, cross-plot of Calcium concentrations calculated from Rock Eval and XRF analysis 174
Figure A-5: The SEM-EDS and QUEMSCAN analyses 175
Figure A-6: Correlation of Rock Eval parameter of bulk rock powders and decarbonated powders 176
Figure A-7: Cross-plots between HI and marine and terrestrial organic matter 176
Figure A-8: Stratigraphic log of section Arroyo Serrucho E–E' 178
Figure A-9: Stratigraphic log of section Arroyo Serrucho F–F' 180
Figure A-10: Stratigraphic log of section Las Overas 184
Figure A-10b: Stratigraphic log of section Las Overas - contuniued 185
Figure A-10c: Stratigraphic log of section Las Overas - contuniued 186
Figure A-11: Stratigraphic log of section Las Overas-C 189
Figure A-11b: Stratigraphic log of section Las Overas-C - contuniued 190
Figure A-12: Palynomorphs from Section Arroyo Serrucho and Las Overas 193

List of Tables

Table 4.1: Stratigraphic intervals of individual data segments..... 56

Table 4.2: Duration estimates based on cyclostratigraphic constraints of Hettangian, Sinemurian and Pliensbachian biostratigraphical units and stages 64

Table 7.1: Palynological content of Arroyo Serrucho and Las Overas sections 146

List of regularly used abbreviations

CAMP ..... Central Atlantic Magmatic Province
CIE…… ..... carbon-isotope excursion
DIC ..... dissolved inorganic carbon
$\delta^{13}C$ ..... carbon-13/carbon-12 ratio relative to PDB standard
Hg ..... mercury
kyr ..... thousand years
Myr ..... million years
LIP ..... large igneous province
OAE ..... Oceanic Anoxic Event
T-OAE ..... Toarcian Oceanic Anoxic Event
TOC… ..... total organic carbon
XRF ..... X-ray fluorescence

Chapter 1 : Introduction

1.1. Background and hypotheses

The coupling of atmospheric carbon dioxide concentrations and the global climate was proposed at the turn of the 19th century (Arrhenius 1896, Arrhenius and Sandström 1903), followed by the recognition of the long-term impact of anthropogenic greenhouse gas emissions (e.g. Callendar 1938, Revelle and Suess 1957). The magnitude of climatic and subsequent environmental change on the present day and future climate, in response to enhanced and rapid atmospheric carbon dioxide emissions, is still subject to ongoing research. Essential to this research is a comprehensive understanding of the dynamics of the global climate system, its sensitivities, feedback mechanisms, and the environmental responses in the marine, atmospheric, and terrestrial realm. It is therefore crucial to identify time intervals in the geological past characterized by climatic changes linked to elevated atmospheric carbon dioxide levels in order to examine consequences and the temporal framework of environmental response and recovery.

Much work has been done investigating individual short-lived extreme palaeoenvironmental changes, which may serve as analogues for present-day and future environmental transitions. Subject to ongoing studies are, for example, the Mesozoic oceanic anoxic events (OAEs), defined as short time periods during which global marine waters were relatively depleted in oxygen, and the enhanced burial of organic matter was widespread (Schlanger and Jenkyns 1976). The events were accompanied by major changes in the global climate and biogeochemical cycles (Jenkyns 2010). Leading hypotheses suggest increased atmospheric carbon dioxide levels as trigger mechanisms for these events, sourced from enhanced volcanic activity and/or thermogenic methane (CH_4) from sill intrusions into organic rich strata, and/or biogenic methane from the dissociation of gas hydrates (Rampino and Stothers 1988, Hesselbo *et al.* 2000, Courtillot and Renne 2003, McElwain *et al.* 2005, Kuroda *et al.* 2007, Svensen *et al.* 2007, Turgeon and Creaser 2008, Bond and Wignall 2014, Burgess *et al.* 2015). The sequential appearance of environmental perturbations in the Early Jurassic and the mid-Cretaceous have led to investigations of contributing mechanisms linking these events, such as autocyclicity of the biogeochemical cycle and orbital-scale productivity cycles (Handoh and Lenton 2003, Ikeda and Hori 2014).

However, the scattered and discontinuous nature of existing stratigraphic datasets has thus far hampered the study of transient global climatic and environmental changes in the context of longer timescales. A continuous geological record aggregating multiple events is needed to further investigate the timing, pacing, and possible causal links. Furthermore, the temporal correlation between OAEs and volcanic events must be better constrained in order to resolve the ultimate mechanisms.

1.1.1. Investigating carbon cycle perturbations

Atmospheric CO_2 levels and global temperatures co-varied throughout most of the Phanerozoic (Royer 2006) and are considered as the primary driving mechanism of the global climate. Several other factors control the average surface temperature of the Earth, such as the distribution of continents and vegetation, solar insolation, orbital variations and other greenhouse gases (Royer 2006). Key to determining pCO_2-related palaeoenvironmental events is the exogenic carbon cycle and changes in its mass and isotope signature. The exogenic carbon cycle comprises all carbon in the ocean, atmosphere, and biosphere (Kump and Arthur 1999, Figure 1.1). The exchange of carbon between the individual reservoirs, as well as external in- and outputs, such as volcanism, weathering and gas hydrate build-up and release, have a dominant control on the atmospheric CO_2 levels (Berner 1999, Kump and Arthur 1999, Dickens 2003).

The carbon-isotope composition ($\delta^{13}C$: ratio between ^{13}C and ^{12}C relative to PDB standard) of sedimentary materials that sequester from the exogenic carbon system, such as fossil organic carbon or biogenic carbonate, can be used to identify perturbations in the carbon cycle through time (e.g. Kump and Arthur 1999, Dickens 2003). Differences in the compound-specific fractionation of carbon during carbon-uptake, mainly due to the discrimination of ^{13}C in the carbon uptake by photosynthesis, lead to reservoir specific carbon-isotope compositions (see $\delta^{13}C$ values in Figure 1.1).

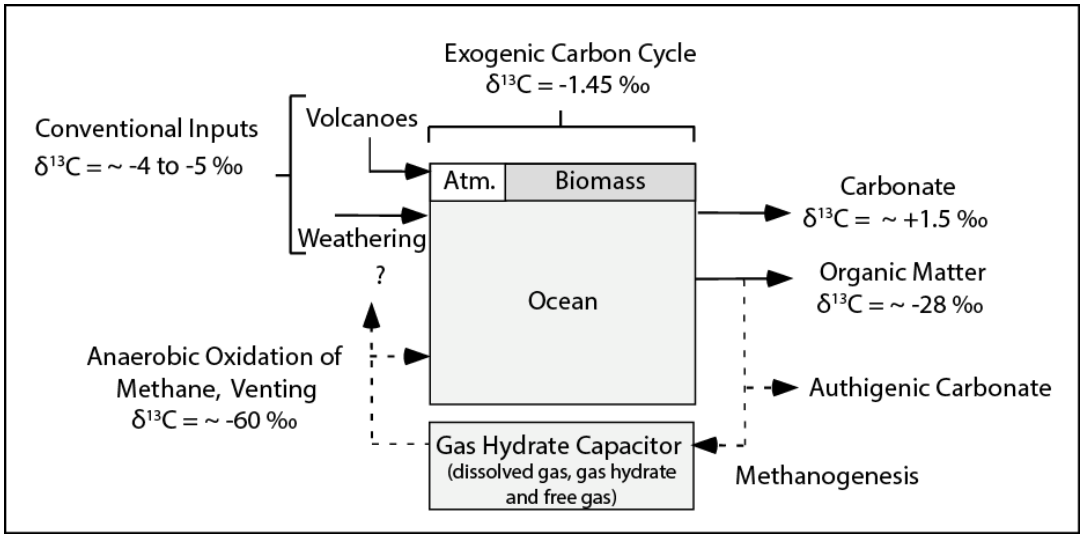

Figure 1.1: Basic steady-state model for the Phanerozoic exogenic carbon cycle (comprising ocean, atmosphere, and biomass), and external inputs and outputs, as well as carbon-isotope signatures, modified after Kump and Arthur (1999), Dickens (2003).

Increased atmospheric CO_2 levels and subsequent rise in global temperatures are thought to accelerate the hydrological cycle and weathering rates (Jenkyns 2003, Cohen *et al.* 2004, Percival *et al.* 2016, Them *et al.* 2017b). Enhanced riverine input of nutrients and freshwater into the oceans likely results in productivity- and stratification-driven shallow-water low-oxygen environments, supporting the burial of large amounts of organic matter (e.g. Jenkyns 2010). The increased burial of organic matter (enriched in ^{12}C) leaves the ocean-atmosphere relatively depleted in ^{12}C, producing a positive excursion in the $\delta^{13}C$ record (Kump and Arthur 1999, Jenkyns 2010). Conversely, the release of large amounts of isotopically light carbon, sourced e.g. from gas hydrates or the thermogenic alteration of organic-rich strata, shifts the isotope record to more negative values. Based on the isotope signature and estimated quantities of volcanically sourced CO_2, it is debated if enhanced volcanism likewise perturbs the carbon-isotope record (e.g. Dickens *et al.* 1995, Wignall 2001, Svensen *et al.* 2007).

Stratigraphic records of $\delta^{13}C$ can, however, be used as a proxy for changes in the global exogenic carbon cycle and associated palaeoenvironmental anomalies. In order to determine the global and coeval appearance of carbon-cycle perturbations, carbon-

isotope records from widely distributed locations and different carbon reservoirs, preferably from both the marine and terrestrial realm, are crucial. This requires a comprehensive stratigraphic control on studied intervals.

1.1.2. The Early Jurassic palaeoenvironment and carbon cycle

The Early Jurassic (201-175 Myr) was a time of extreme climatic and environmental changes. Most significant being the Toarcian oceanic anoxic event (T-OAE, ~183 Myr) marked by one of the most intense and geographically widespread development of anoxic/euxinic oceanic conditions of the Mesozoic Era; worldwide enhanced organic carbon burial (Jenkyns 2010); a transient rise in temperatures of up to ~7°C in mid-latitudes (Dera *et al.* 2009a, Korte *et al.* 2015), disturbance of the global carbon cycle (Jenkyns 1988); and an abrupt and major extinction of marine organisms (Little and Benton 1995, Harries and Little 1999, Caruthers *et al.* 2014).

The event is associated with increased atmospheric CO_2 levels, as indicated by fossil leaf stomatal frequency (McElwain *et al.* 2005) and disturbance of the global carbon cycle, evidenced by carbon-isotope records showing a positive excursion, interrupted by a sharp negative shift (Jenkyns 1988). Due to the apparent synchrony between the T-OAE and the emplacement of the Karoo-Ferrar Large Igneous Provinces (LIP), the rapid emission of isotopically light carbon into the atmosphere-ocean system has been linked to enhanced volcanic activity (Pálfy and Smith 2000, Wignall 2001, Pálfy et al. 2002, Caruthers *et al.* 2014, Sell *et al.* 2014, Burgess *et al.* 2015). Quantitative estimates of LIP volatiles and estimates on the duration of volcanic activity do not agree with the magnitude of the corresponding sharp negative carbon-isotope excursion and the short-lived nature of the T-OAE (Wignall 2001, Self *et al.* 2005, Self *et al.* 2006, Beerling and Brentnall 2007, Svensen *et al.* 2007, Kemp *et al.* 2011, Boulila *et al.* 2014, Huang and Hesselbo 2014, Sell *et al.* 2014). Further hypotheses suggest that initial volcanic CO_2 emissions and subsequent warming triggered the dissociation of large amounts of gas hydrates, which injected biogenic and therefore isotopically light carbon into the ocean–atmosphere system (Hesselbo *et al*. 2000). Alternatively, the degassing of organic-rich strata (Gondwana coals and shales), caused by thermogenic alteration triggered by sill intrusion during the onset of

the Karoo-Ferrar large LIP emplacement has been considered as source for the increased atmospheric CO_2 levels (McElwain *et al.* 2005, Svensen *et al.* 2007, Svensen *et al.* 2012). In any case, the onset of the Karoo-Ferrar LIP plausibly appears to have been the initial driving force. The accurate numerical dating of the onset of the T-OAE, crucial for the temporal correlation between the event and activity of the Karroo-Ferrar LIP, requires a well-defined geochemical and biostratigraphical framework to unambiguously define the T-OAE in the sedimentary record.

Other events of lesser magnitude preceding the T-OAE have been documented, such as short-lived warming events in the Late Sinemurian, Pliensbachian, and Pliensbachian–Toarcian boundary (e.g. Riding *et al.* 2013, Korte *et al.* 2015, Silva and Duarte 2015), and transient cold climates during the Late Pliensbachian (van de Schootbrugge *et al.* 2005, Korte *et al.* 2015). All these events are associated with excursions in the carbon-isotope record. There is, however, no comprehensive understanding of the timing of these events, trigger mechanisms or, possible causal links.

1.2. Aims of this study

This thesis aims to improve the overall understanding of the evolution of the Early Jurassic carbon-isotope composition of the bulk-organic carbon reservoir ($\delta^{13}C_{TOC}$), and to investigate the timing, pacing, and geochemical nature of excursion intervals (Chapters 2–5). The thesis further investigates the expression of the T-OAE in the Southern Hemisphere and develops the chemostratigraphical framework needed for the temporal correlation of the associated carbon-cycle perturbation with the onset of the Karoo-Ferrar LIP, and investigates the litho- and chemostratigraphic expression of the event in the Southern Hemisphere (Chapters 6–7).

Chapter 2

This chapter provides information on the geological, bio- and lithostratigraphical framework of the Lower Jurassic strata of the Llanbedr (Mochras Farm) drill-core (hereafter referred to as Mochras core), Cardigan Bay Basin, UK.

Chapter 3

A $\delta^{13}C_{TOC}$ record covering the Hettangian to Pliensbachian stages in Mochras core is generated to provide a continuous Lower Jurassic archive on a stratigraphically expanded and biostratigraphically well-defined section. The aim is to detect all isotope excursions recorded in the studied time interval, including events previously recognized in other locations, as well as so far unrevealed events. The record provides a new chemostratigraphic template for the Hettangian to Pliensbachian stages.

Chapter 4

Spectral and time-series analyses on the $\delta^{13}C_{TOC}$ record of the Mochras core are performed in order to investigate the role of orbital forcing on the carbon-isotope record, improve the temporal constraints of excursion events, and to better constrain the Early Jurassic time scale astronomically. Orbital tuning of the continuous Hettangian to Pliensbachian $\delta^{13}C_{TOC}$ record allows identification of potential mechanisms driving the Early Jurassic carbon cycle on the grounds of age correlation. The orbitally tuned $\delta^{13}C_{TOC}$ record, calibrated to previous astronomical constraints on the Hettangian and Pliensbachian stage, provides the first direct astronomical timescale for the Sinemurian stage.

Chapter 5

The composition of the bulk organic matter in the Hettangian to Pliensbachian strata of the Mochras core is investigated in order to determine the role of compositional changes on the bulk-organic carbon-isotope record. Non-organic detrital components are studied to investigate changes in the depositional environment.

Chapter 6 and 7

A stratigraphical framework is developed for Late Pliensbachian to Toarcian stratigraphic sections in the Northern Neuquén Basin, Argentina, based on bio- and lithostratigraphic information. A chemostratigraphic record ($\delta^{13}C_{TOC}$, TOC and Hg) of

the stratigraphically calibrated sections is generated and compared to other records from the southern Neuquén Basin, and to the coeval Northern Hemisphere record in order to identify the T-OAE and assess the local to global expression of the event. The biostratigraphically calibrated multi-proxy record offers the basis for future work on the radioisotopic dating of the multiple volcanic ash beds intercalated in the studied stratigraphic sections.

Chapter 8

Conclusion and future work.

1.3. Materials

1.3.1. The Llanbedr (Mochras Farm) drill-core

The Mochras drill-core and registered specimens are housed in the collections of the British Geological Survey (BGS), Keyworth, Nottingham, UK. The core sampling was performed as a team effort, including Hugh Jenkyns, Micha Ruhl, Weimu Xu (University of Oxford), Stephen Hesselbo (University of Exeter), James Riding (BGS) and myself. The core was originally labeled in Inch and Feet. Depth information given in this thesis is converted into meters. The Rhaetian to Pliensbachian in the Mochras core was sampled over the depth of 1910 to 863.3 meter below surface (mbs), where a total of 2860 samples were collected. Samples were taken in ~30 cm spacing between the depth 863.3 to 1290 mbs, where core slabs are reasonably well preserved. The Hettangian to Upper Sinemurian intervals were sampled from rubble bags, which each aggregates ~1.4 m intervals. A single sample has been taken from each bag, referring to the depth of the mid-point of the sampled interval.

Bulk-(total)-organic carbon-isotope ($\delta^{13}C_{TOC}$) analyses were performed on 1332 samples, 463 samples were analyzed for quantitative elemental composition using hand-held X-ray fluorescence and 673 samples were analyzed by Rock-Eval pyrolysis. The average sample spacing for each analysis is shown in Figure 1.2. Carbon-isotope analysis on fossil wood fragments ($\delta^{13}C_{wood}$) was performed on 12

samples, 8 samples have been analyzed for quantitative elemental composition using a Scanning Electron Microscope (QUEMSCAN), 14 samples for organic petrology and one sample was prepared for palynological analysis. Sample spacing and stratigraphic position is given in text.

1.3.2 Outcrop samples from the Neuquén Basin, Argentina

Samples from the Las Overas and Arroyo Serrucho sections from the Neuquén Basin, Argentina, were sampled during two field seasons, in spring 2014 and 2016. The reconnaissance, stratigraphic logging and sampling was performed as a team effort, including Hugh Jenkyns and Micha Ruhl from the University of Oxford, Stephen Hesselbo (University of Exeter), Susana Damborenea and Miguel Manceñido (University de la Plata, Argentina), Aisha Al-Suwaidi (Petroleum Institute, Abu Dhabi), and myself. A total of 1490 samples have been taken, of which 30 samples originate from the Arroyo Serrucho E–E' section (~50 cm sample spacing), 86 samples from the Arroyo Serrucho F–F' section (20 to 40 cm spacing), 1303 samples from the Las Overas section (1156 samples in 10 cm spacing between 0 and 89 m, and 147 in 20 cm spacing between 89 and 131 m), and 70 samples have been taken from the Las Overas-C section (1 m sample spacing).

A total of 592 of the bulk rock samples have been analyzed for $\delta^{13}C_{TOC}$ (40 cm to 1 m sample spacing), 347 by Rock-Eval pyrolysis (~ 80 cm to 1 m sample spacing), 67 for mercury content and 5 for palynology. Furthermore, a total of 17 volcanic ash beds have been sampled from the Las Overas section and one from the Las Overas-C section for radio-isotopic dating, and about 72 invertebrate fossils (cephalopods) were collected for ammonite biostratigraphy.

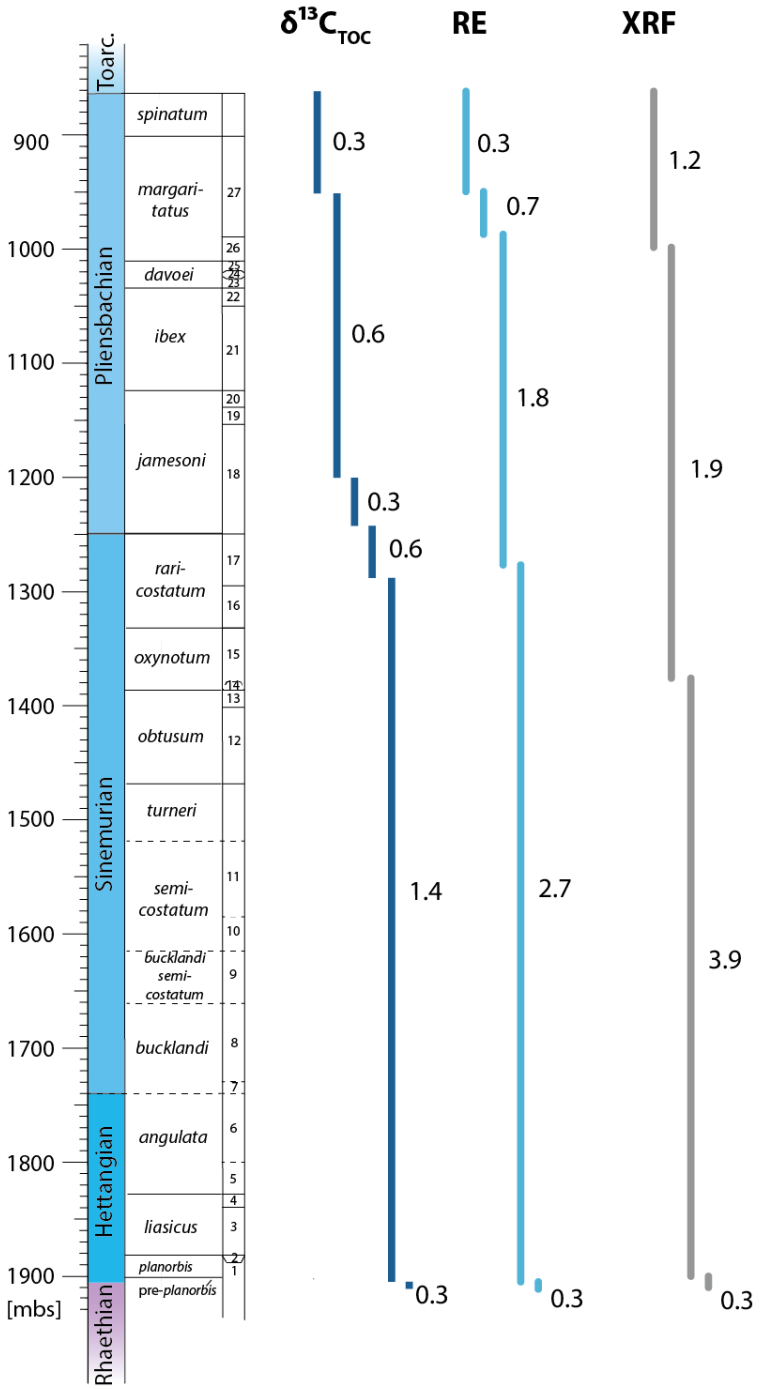

Figure 1.2: Sample resolution for $\delta^{13}C_{TOC}$, Rock-Eval (RE) and HH-XRF analysis. Values given in Figure are average values for each interval. Key for ammonite subzone numbering is given in Chapter 2, Figure 2.3.

1.4. Analytical Methods

1.4.1. Organic Carbon isotope analysis ($\delta^{13}C_{TOC}$)

The powdering of all samples has been performed at the Department of Earth Sciences, University of Oxford, using a rock hammer and a Fritsch mortar grinder Pulveridette as well as an agate mortar. The decarbonation process for the samples from the Neuquén Basin (Arroyo Serrucho and Las Overas sections) was performed at the Department of Earth Sciences, University of Oxford. Powdered samples from the Mochras drill-core were decarbonated at the NERC Isotope Geosciences Facilities, British Geological Survey (Keyworth, U.K.), following the same preparation procedure: To remove the calcium carbonate and sulfur from the powdered bulk rock samples, about 1-2 g of homogenized powdered bulk rock samples have been treated with ~30 ml of 3 M HCl in a warm water bath (~80°C) for about 24 hours. Samples were then centrifuged and the HCl decanted. Carbonate-rich samples have been treated with 3 M HCl a second time. The carbonate free samples were then rinsed with deionized water until neutral pH was reached, and dried in an oven over night at ~40°C. Dried samples were weighed into 8 x 6 mm tin capsules (~10 mg of sample, aiming for 25µg pure carbon).

The $\delta^{13}C_{TOC}$ analysis for the Mochras drill-core samples was also performed at the NERC Isotope Geosciences Facilities, British Geological Survey (Keyworth, U.K.). The nalysis was performed by combustion in a Costech Elemental Analyser (EA) on-line to a VG TripleTrap and Optima dual-inlet mass spectrometer. $\delta^{13}C$ values were calibrated to the VPDB scale using within-run laboratory standards for calibration (NBS18, NBS-19 and NBS-22). Replicate analysis of standards showed a precision of ± <0.1‰ (1 SD). Samples containing less than 0.2 wt% total organic carbon were analyzed using Liquid Nitrogen (cold-finger).

Samples from the Neuquén Basin (Las Overas and Arroyo Serrucho Section) were analyzed at the stable isotope facilities of the Open University, Milton Keynes, UK. The analysis was performed on a Thermo Finnigan MAT 253 mass spectrometer and a Thermo Flash HT elemental analyzer. $\delta^{13}C$ values were calculated using a three-point calibration with the in-house standards: IAEA-CH-6 sucrose, NIST8573 glutamic acid and IR-041 alanine. Replicate analyses showed a precision of ± <0.1‰ (1 SD).

1.4.2. Organic carbon-isotope analysis on fossil wood fragments ($\delta^{13}C_{wood}$)

Bulk rock samples from the Mochras core were carefully broken up to gravel size. The samples were treated with 3M hydrofluoric acid (HF) for several weeks to further break down the rock matrix silicates. The samples were rinsed with deionized water to remove HF until neutral pH was reached. Samples were then sieved to concentrate coal fragments, which were typically enriched in the <100µm fraction. Between 0.5-1µg fragments of coal were picked under an optical microscope using tweezers. To remove any carbonate and pyrite, the samples were then treated with hot HCL rinsed with deionized water. The dried samples were weighed into 3 x 5 mm tin capsules. Sample analysis was performed at the NERC Isotope Geosciences Facilities, British Geological Survey (Keyworth, U.K.). For analytical methods see section 1.4.1.

1.4.3. Rock-Eval Analysis

The Rock-Eval analysis was performed at the Department of Earth Sciences at the University of Oxford. The equipment used was a Rock-Eval 6 Standard Analyzer unit from Vinci Technologies, including a pyrolysis and oxidation oven, in which homogenized, powdered bulk rock samples (50–100 mg) are incrementally heated to 300–650 and 300–850°C for the pyrolysis and oxidation ovens, respectively. The flame ionization detector measures the quantity of free volatile hydrocarbons that are present in a sample before cracking (S1 peak) and the hydrocarbons and CO_2 produced during the thermal cracking of insoluble organic matter (kerogen, S2 and S3 peak). After pyrolysis, the residual organic carbon is heated under air in the oxidation oven to determine residual organic carbon and mineral carbon content (S4 and S5 peak), also using the flame ionization detector. The total organic carbon (wt%) is calculated as the sum of pyrolyzed organic C and residual organic C. The Hydrogen Index (mg HC/g TOC) represents the pyrolyzable organics relative to TOC and Oxygen Index (OI), whereby the OI represents the amount of oxygen relative to TOC. T_{max} (°C) is the temperature with the highest rate of hydrocarbon generation during pyrolysis temperature (recorded at S2 peak), and is used as a thermal maturity parameter. The mineral carbon (wt% of inorganic carbon present in bulk rock sample) is calculated from the sum of pyrolysed and oxidized mineral carbon. The in-house

SAB134 (Blue Lias organic-rich marl) standard were regularly measured (every 8 to 10 samples for the in-house standard). The standard deviation on TOC and HI of the in-house SAB134 was 0.11% and ±29.95 mg HC/g TOC, respectively. The standard deviation for T_{max}, Oxygen Index and Inorganic Carbon were at 1.9°C, 2.8 mg CO_2/g TOC and 0.25%, respectively. The long-term average TOC of the international reference standard IFP 160000 is 3.27%, with a standard deviation of 0.04% (the TOC content of the IFP 16000 standard is eferenced at 3.28±0.14 wt%).

1.4.4. Organic Petrography

Optical petrographic rock analysis was performed by Dr Olga Gorbanenko at the Department of Earth Sciences, University of Oxford, UK. The samples were mounted in epoxy resin and polished according to the method described in Gorbanenko (2017). The polished blocks were analyzed with an Leica DMRX – MPVSP microscope photometer, using both reflected white light and fluorescence illumination under oil immersion at a magnification of 500 X. Maceral analysis was undertaking with the point-count method (Peclon counting system) based on 1000 individual determinations per sample. The nomenclature of Taylor *et al*. (1998) was used for the macerals of the vitrinite and inertinite groups, and that of Hutton (1987) for the liptinite group macerals.

1.4.5. X-Ray fluorescence

Elemental concentrations (Al, Ca, Fe, S, Si, Ti, Rb, Zr) on Mochras samples were obtained by hand-held X-ray fluorescence (XRF) analysis. A handheld Olympus Innov-X Delta Premium DP6000C XRF Alloy Analyzer adjusted in a stand was used on the flat surface of bulk-rock samples. The analyzer uses a 4W X-ray tube and a large-area Silicon Drift Detector. X-ray absorption spectra were recorded in scanning mode from 3 to 40 keV and absorption peaks were automatically identified using the Innov-X “soil mode” software. Scanning time was set to 60 seconds for each light and heavy elements. All analyses were run in the Geochem Mode (DS-6000) and manufacturer delivered standards (metal coins) were used for calibration every time

the machine was restarted. The standard NIST 2710a was repeatedly measured for the analysis of the Mochras core. The results are as followed (x,y,z = average value %, standard deviation %, average internal error %). NIST2710a: Si (21.7, 1.7, 0.06), Ca (0.79, 0.17, 0.004), Al (5.5, 0.45, 0.05), Ti (0.29, 0.023, 0.005), Rb (0.1, 0.0008, 0.0001), Zr (0.21, 0.001, 0.0001).

1.4.6. QUEMSCAN

The quantitative evaluation of minerals (QUEMSCAN) in bulk rock samples allows the identification of the mineralogy and grain size distribution in bulk rock samples. For automated in-situ mapping of the petrography, backscattered electron and secondary electron signals of a scanning electron microscope (SEM) are combined with Energy-dispersive X-ray (EDX) spectroscopy and a mineral data database. This method is called QUEMSCAN. Bulk-rock samples from the Mochras core were analyzed for quantitative mineral composition at the research facilities of the Camborne School of Mines (CSM), University of Exeter, Penryn Campus. The CSM facilities are equipped with a Zeiss EVO® 50 scanning electron microscope, using a tungsten filament electron gun, and four light element X-ray EDS (Energy Dispersive Spectrometers) detectors and an electron backscatter detector. The bulk rock samples have been cut, polished, and cast in epoxy resin blocks and carbon coated to ensure conductivity. Depending on the position of the sample in the block, the scan area of ~ 2mm^2 has been defined around the centre of the block or by set coordinates. The scans were sub-divided in fields, with a field overlap of 15 μm, and grid spacing has been set at 2 μm. The electron beam was set on ~10kV accelerating voltage and 1000 counts were recorded on each analysis point. The Oil & Gas library provided by the FEI QUEMSCAN® software has been used to identify minerals from x-ray spectra. Due to the chemically similar composition of organic matter in the samples and the epoxy resin, both being primarily composed of carbon, organic matter in the samples has been detected as background.

1.4.7. Palynology

The single bulk-rock sample from the Mochras core (2961'6''=902.6 m), was prepared and analyzed by James Riding at the British Geological Survey. The palynology sample was prepared using the standard acid digestion method including mild oxidation with cold nitric acid (Wood 1996).

The sample preparation for kerogen and oxidized slides from the Neuquén Basin was performed by Malcolm Jones at the Palynological Laboratory Services Ltd, Anglesey. Carbonates and silicates were sequentially dissolved in hydrochloric acid (10% HCl) and hydrofluoric acid (40% HF). Preparations were sieved at 15 μm. Darkened, thermally mature wood fragment-dominated kerogens were recovered. Post-HF oxidative treatments (15 minutes warm nitric acid; 10 min. fuming nitric acid; 2.5 Schulze's solution) were used on splits of kerogens to lighten palynomorphs and to liberate palynomorphs from larger pieces of organic matter, including probable coal fragments. Kerogen counts of 100 pieces of organic matter were made, following the classification of Whitaker (1984) and Van der Zwan (1990). In addition, all palynomorphs present were counted.

1.4.8. Sedimentary mercury concentrations

Mercury analyses were performed by Dr Lawrence Percival at the Department of Earth Sciences, University of Oxford, using the RA-915 Portable Mercury Analyzer with PYRO-915 Pyrolyzer, Lumex as described by Bin *et al.* (2001). Powdered sample (50 ±2 mg) was weighed into a glass measuring boat and its precise mass determined. The sample was then placed into the pyrolyzer (set at Mode 1), which heated it to 700°C to volatilize the mercury in the sample. The resulting gas was analyzed spectrally to detect and calculate the elemental mercury concentration. As a standard, five 50 ± 2 mg samples of peat (NIMT/UOE/FM/001 – Inorganic Elements in Peat) with a known mercury concentration of 169 ±7mg/g were analyzed to calibrate the analyzer before the analysis of each sample-set. Reproducability of standard samples and repeat samples was at 10%. Additionally, a sample of peat was analyzed after approximately every tenth sample. A total of fifteen peat-standard samples (between 10 and 90 mg), were also used to calibrate the Lumex.

1.4.9. Radioisotopic U-Pb dating

The sample preparation and the U-Pb radio-isotopic work has been carried out at the NERC Isotope Geosciences Laboratory at the British Geological Survey, U.K by Dan Condon, Adrian Wood and partly myself.

Zircons were separated from each sample using conventional mineral separation techniques, include crushing, concentration of heavy minerals using a Rogers shaking table, magnetic separation and density separation by Di-Iodomethane. Zircons were hand-picked for each sample, choosing euhedral, prismatic crystals. To examine the internal structures like zonation patterns and inclusions of the zircon population of each sample, a cathodoluminescence detector is combined with standard SEM detectors. The work has been performed at the British Geological Survey, on a FEI quanta 600 environmental scanning electron microscope with both a Centraurus cathodoluminescence and backscatter detector. Hand-picked zircons (euhedral, high aspect ratio) were mounted in epoxy blocks and polished to a flat surface. The polished blocks have been carbon coated for enhanced conductivity.

In order to eliminate the discordance caused by Pb loss, all zircons selected for analysis were chemically abraded to remove radiation damaged crystal volumes, using a modified version of Mattinson (2005). Samples were placed in a quartz dish and annealed at 900°C for 60 h in a muffle furnace. Zircons were then loaded in individual Teflon beaker and refluxed in 4 M HNO_3 at 120°C, before being ultrasonically cleaned for about 20 min. The individual zircons were rinsed in acetone and 4M HNO_3 before being loaded into 300 µl FEP Teflon microcapsules. The crystals were leached in 29 M HF in a Parr vessel (self sealing stainless steel vessel) at 180˚C for 10 to 12 h, and subsequently rinsed with 6 M HCL and refluxed on a hotplate for 2 to 5 h at 120˚C. Finally the chemically abraded zircons were rinsed several times with 4 M HNO_3.

The leached zircons were spiked with ^{202}Pb-^{205}Pb-^{233}U-^{235}U (ET2535) EARTHTIME tracer solution and dissolved in c. 150 µl 29 M HF and trace HNO_3 in a Parr vessel at 220˚C over 60 hours, assuming the complete dissolution of he individual rains within this timeframe. The dissolved samples were dried as fluorides before re-dissolved in 3M HCL overnight at 180˚C in a Parr vessel. A HCL anion

exchange column was used to isolate U and Pb. The re-combined U and Pb fractions were subsequently dried down and loaded in a silica gel.

The isotope ratio measurement was performed using a Thermo-Electron Triton thermal ionization mass spectrometer (TIMS). The Pb analyses was performed in dynamic mode on a MassCom secondary electron multiplier (SEM) detector and corrected for mass bias using a 0.14 ± 0.02 % / amu (1 σ) fractionation factor for samples spiked with the ET2535 tracer. Linearity and dead time corrections on the SEM were monitored by repeated analysis of standards (NBS 982, NBS 982, U 500). Uranium oxide (UO_2) was run in dynamic mode and corrected for isobaric interferences using a $^{18}O/^{16}O$ value of 0.00205 (IUPAC value, also determined through direct measurement at NIGL).

U beams were analyzed in static mode, on Faraday detectors equipped with 10^{12} Ω resistors for intensities greater than 4 mV. Dynamic mode was used for lower intensities. The mass fractionation of U was calculated in real-time based on the isotopic composition of the ET535 and ET2535 tracer.

Chapter 2 : Geological settings and stratigraphical framework of the Llanbedr (Mochras Farm) drill-core, Cardigan Bay Basin, UK

2. Introduction

The Llanbedr (Mochras Farm) borehole (hereafter referred to as Mochras core) was drilled onshore on the coast of West Wales from 1967 to 1969. The drilling penetrated, and fully cored, a biostratigraphically complete Lower Jurassic succession of ~1300 m thickness, recovered from 601.83 to 1906.78 meter below surface (mbs), and an additional 32.05 m of Upper Triassic strata between 1906.78 and 1938.8 mbs (Woodland 1971, Dobson and Whittington 1987). The recovered interval is preserved and archived as aggregated core fragments (Hettangian to upper Sinemurian strata) and continuous core slabs (Upper Triassic, upper Sinemurian to Toarcian), housed at the core store facilities on the British Geological Survey. The drill-core offers a remarkably expanded, biostratigraphically calibrated and lithologically uniform Lower Jurassic succession, dominated by calcareous mudstones and clay-rich limestones.

2.1. Paleogeography and tectonic setting

The Mochras drill-site is located at the NE margin of the SW oriented Cardigan Bay Basin, onshore West Wales, UK (52°48’32’’N, 4°08’44’’W, Figure 2.1 and 2.2, Woodland 1971, Tappin 1994). The Cardigan Bay Basin forms the northeastern end of the North Celtic Sea Trough, an extensive intracratonic rift (Dobson and Whittington 1987). The rifting initiated in the earliest Triassic, likely related to crustal extension in the North Atlantic and the opening of the Tethys Ocean in the South (Ziegler 1982). During the Early Jurassic, the basin was located within the northern Tethys, the so-called Laurasian Seaway, between the paleolatitudes 30-45° N (Coward 2003). The Viking corridor, an N-S trending seaway connected the Laurasian seaway to the Boreal ocean in the North (Ziegler 1990, Bjerrum *et al.* 2001, Figure 2.1). The opening of the Hispanic corridor during the Early Jurassic progressively connected the region to the Panthalassa Ocean in the SW (Porter *et al.* 2013).

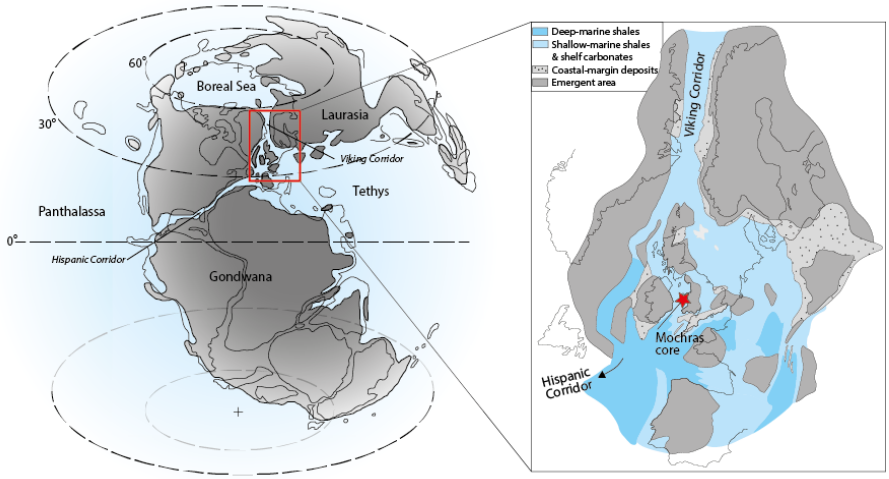

Figure 2.1: Early Jurassic palaeogeography showing the location of the Mochras core (red star) within the northwestern Tethys Ocean (red rectangle). The figure is modified after Dera *et al.* (2011), Korte *et al.* (2015), Ruhl *et al.* (2016).

The Cardigan Bay Basin was surrounded by nearby landmasses (see Figure 2.1), such as Cornubia to the South, the Irish Massif toward the west, and the London-Brabant Massif toward the east (Bradshaw *et al.* 1992). The Welsh Massif in close proximity to the south was possibly emerged during the Early Hettangian and Late Pliensbachian and Toarcian stages (Bradshaw *et al.* 1992).

The stratigraphic thickness of the Lower Jurassic in the Mochras drill-core (~1300 m) is about two times more expanded compared to other Lower Jurassic biostratigraphically complete UK drill-cores, and comprises about 3 to 4 times of the sedimentary thickness of the well studied Dorset coast succession (Wessex Basin, ~360 m), Yorkshire coast (Cleveland Basin, ~450m) or the Sancerre-Couy core (~250 m) from the Paris Basin, France (Tappin 1994, Hesselbo *et al.* 2013, Boulila *et al.* 2014, Ruhl *et al.* 2016, see Figure 2.2). The immense thickness of the sedimentary half-graben infill of the Cardigan Bay Basin was linked to high subsidence rates (Woodland 1971). The uniformity of the basin infill sediments and the lack of turbidites or slumped strata in the Lower Jurassic succession suggest a steady and sustained subsidence rate, rather than synsedimentary fault activity along the major fault system, comprising the Bala, Mochras and Tonfanau Faults (eastern and south-

eastern basin margins, Woodland 1971). However, synsedimentary fault activity has been also been proposed (Tucker and Arter 1987, Tappin 1994).

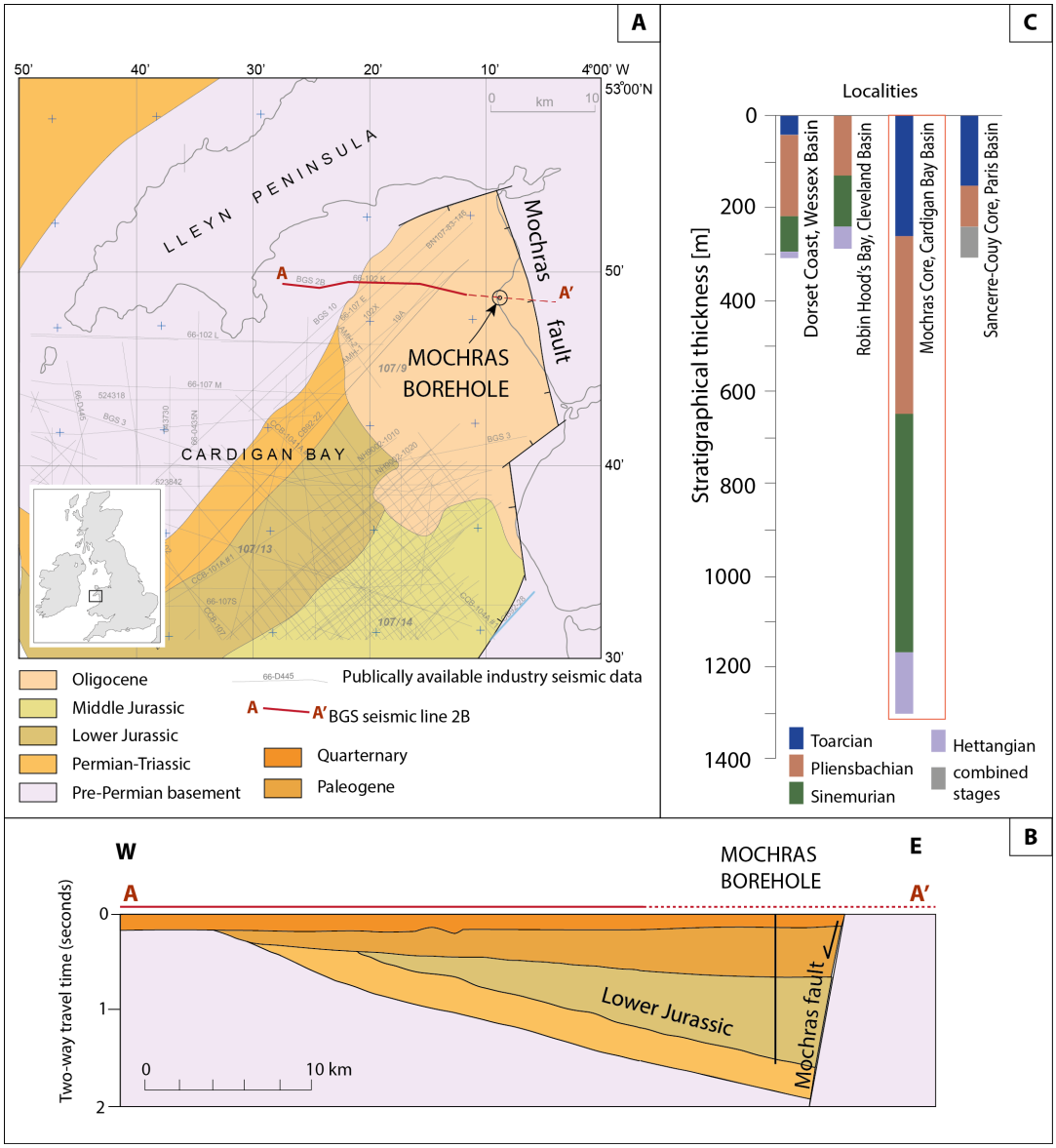

Figure 2.2: **A:** Simplified geological map of the Cardigan Bay onshore and offshore area showing the location of the Mochras drill site, modified from Hesselbo *et al*. (2013), based on Dobson and Whittington (1987), Tappin *et al*. (1994), and the British Geological Survey 1:25,000 map of Cardigan Bay, Solid Geology. **B:** Interpretation of the British Geological Survey reflection profile 2B, modified from Tappin *et al*. (1994) and Hesselbo *et al*. (2013). **C:** Relative thickness of the Early Jurassic succession in the Mochras drill-core compared to the Dorset Coast (Lyme Regis to Bridport, Wessex Basin), Robin Hood's Bay (Whitby to Robin Hood's Bay, Cleveland Basin) and Sancerre-Couy core (Paris Basin), modified from Ruhl *et al*. (2016), based on Ivimey-Cook (1971), Peti *et al*. (2017).

2.2. Stratigraphy

The sedimentary succession of the Mochras drill-core comprises continental Triassic deposits (1938.8–1906.79 mbs) and Lower Jurassic Hettangian to Toarcian marine strata (1906.78–601.83 mbs), unconformably overlain by Paleogene–Neogene sandstones and glaciogenic sediments (601.83–0 mbs).

The ammonite biostratigraphy of the Lower Jurassic of the Mochras core has been studied by Ivimey-Cook (1971) based on the ammonite zonation of Dean *et al.* (1961) and was revised by Page in Copestake and Johnson (2014), based on the standard ammonite chronozones and sub-chronozones for the European Lower Jurassic defined in Simms *et al*. (2004). The revision of ammonite zonation has been based on the original, brief description of biostratigraphy and ammonite species. The Early Jurassic ammonite biostratigraphy was largely determined to the subzone level (see Figure 2.4). Foraminifera biostratigraphy in the Mochras core succession was studied in detail by Copestake and Johnson (2014) and supports the ammonite biostratigraphical framework.

According to ammonite biostratigraphy, the Lower Jurassic succession appears stratigraphically nearly complete. A possible stratigraphic gap occurs at the Triassic-Jurassic boundary (1906.78 mbs). The Triassic–Jurassic boundary is defined globally by the appearance of the ammonite *Psiloceras spealae tirolicum*, indicating the base of the *tillmani* chronozone, as seen in the global stratotype section at Kuhjoch, Eiberg Basin, Austria (Hillebrandt *et al.* 2009, 2013, Ruhl *et al.* 2009). *Psiloceras spealae,* however, is not known to appear in any UK section. Due to the lack of a biostratigraphical marker, the Triassic-Jurassic boundary in the Mochras core has been placed at the sharp lithological change from grey-green dolomitic siltstone to calcareous mudstone at 1906.78 mbs (Figure 2.5). The boundary lies about 1.7 m below the first appearance of *Psiloceras planorbis* (1905 mbs, Ivimey-Cook 1971), which defines the base of the *planorbis* Zone.

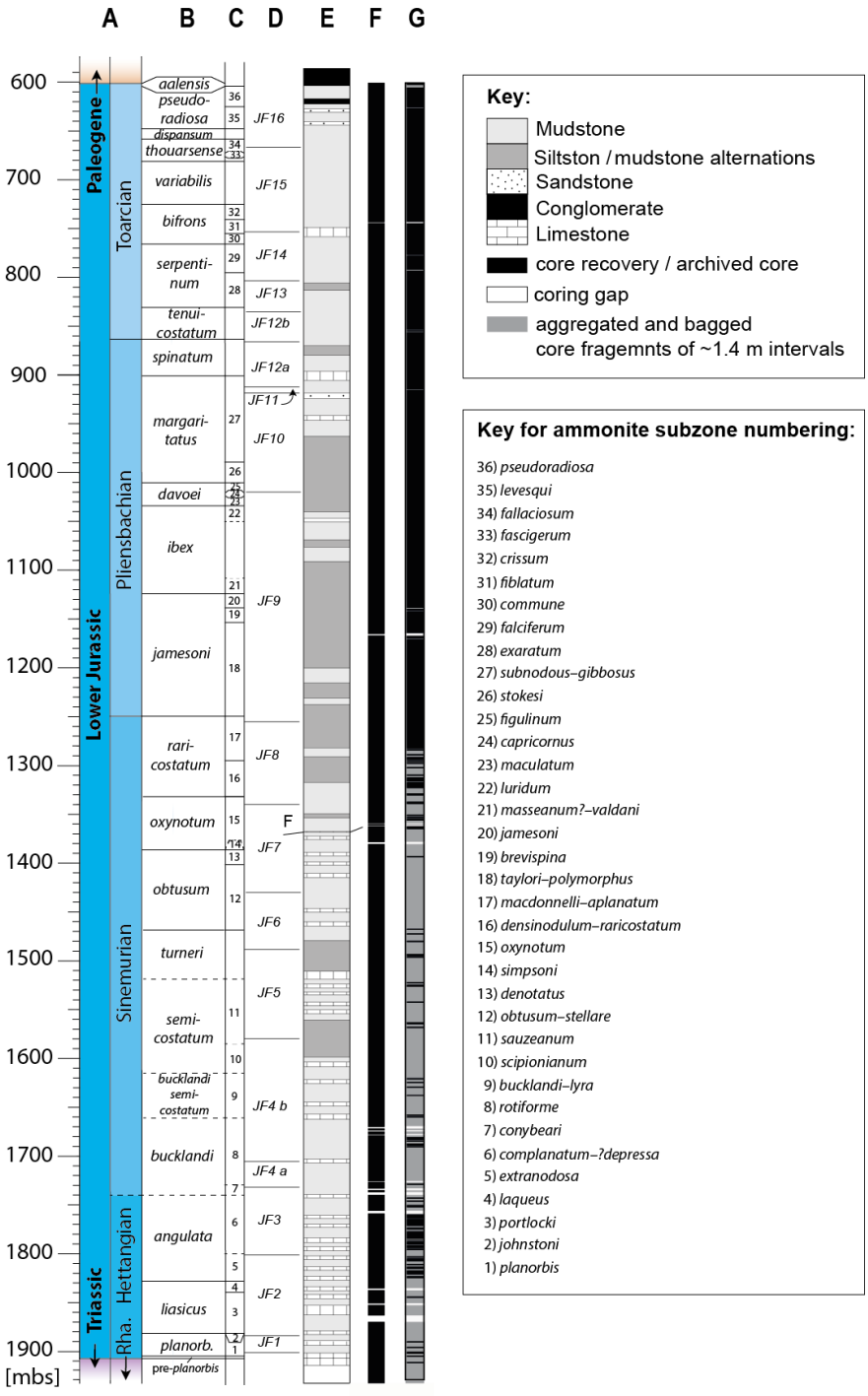

Figure 2.3: Stratigraphy of the Mochras drill-core, modified from Tappin *et al*. (1994) and Hesselbo *et al*. (2013). **A:** Stratigraphy. **B–C:** Ammonite zonation and subzonation after Ivimey-Cook (1971), revised by Page in Copestake and Johnson (2014). Key for subzone numbering given in figure. **D:** Foraminifera biostratigraphy after Woodland (1978) and Copestake and Johnson (2014). **E:** Litholog, key for lithologies given in figure, F – fault. **F:** reported core recovery (97.6 %) and **G:** archived preserved core (black, 59.1 %) and core preserved as aggregated bagged core fragments (grey).

The biostratigraphically undefined interval between the lithologically defined boundary and the base of the *planorbis* Zone (1906.78 to 1905 mbs) suggests the presence of 'pre-*planorbis* beds', likely equivalent to the *tillmani* zone (Copestake and Johnson 2014, see Figure 2.4). However, there is no evidence if the pre-*planorbis* beds are stratigraphically complete.

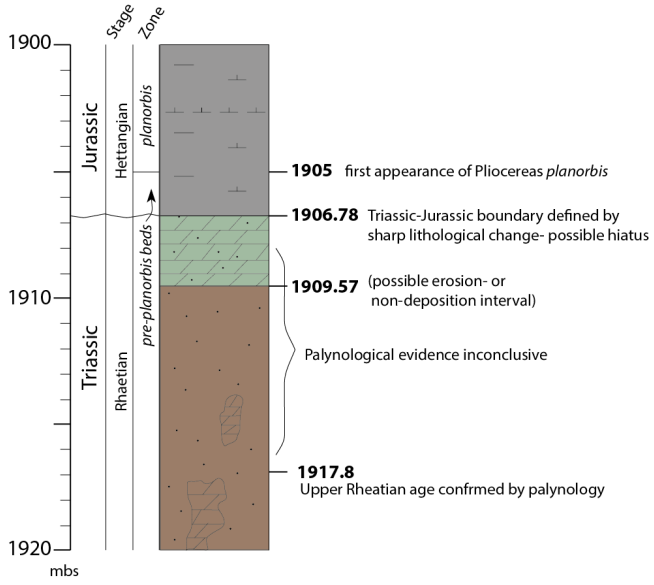

Figure 2.4: Stratigraphy of the uppermost Rhaetian–lower Hettangain of the Mochras core succession. Ammonite zonation after Ivimey-Cook (1971), revised by Page in Copestake and Johnson (2014), palynology after Warrington in Woodland (1971).

Following the possible stratigraphic gap, every stage and zone of the NW European Early Jurassic ammonite zonation is present in the Mochras core. Due to poor preservation of ammonite specimens and apparent overlap between the zones, the boundaries between upper Hettangian and lower Sinemurian *angulata*, *bucklandi*, *semicostatum* and *turneri* zones were defined provisionally. The *bucklandi-semicostatum* Zone boundary is defined as a transition Zone (see Figure 2.3). A clear unconformity was recognized at the top of the Lower Jurassic strata, where the *aalensis* Zone is unconformably overlain by Paleogene sediments.

2.2.1. Lithostratigraphy

The Lower Jurassic succession of the Mochras core has not been assigned to any formations or members, as there was no lithostratigraphic scheme for the Cardigan Bay Basin when the succession was cored. The lithology of the Lower Jurassic succession of the Mochras drill-core is remarkably uniform compared to the same age strata in the UK, where thick limestone and sandstone formations developed (e.g. Upper Pliensbachian Cleveland Ironstone Formation in the Cleveland Basin, Upper Toarcian Britport sands in the Wessex Basin, see Figure 2.5). The Mochras succession is primarily comprised of calcareous mudstone with varying silt and clay content, alternating with strongly bioturbated calcareous siltstones and silty limestones (Ivimey-Cook 1971).

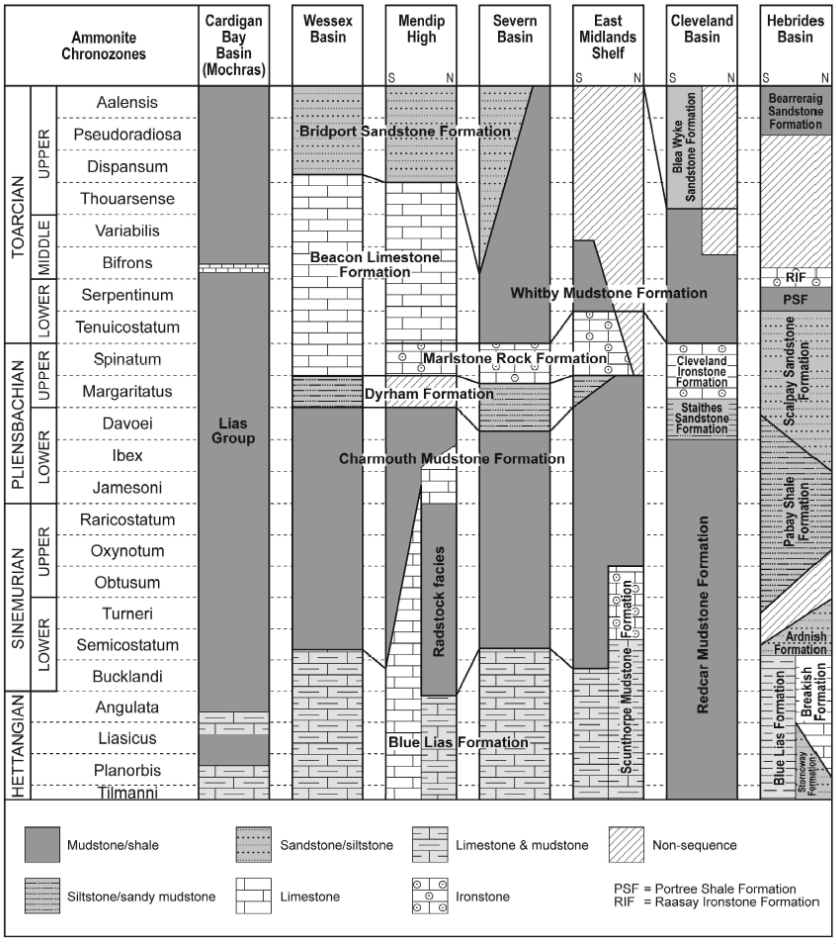

Figure 2.5: Comparative lithostratigraphic development of the Lower Jurassic in the UK, modified from Copestake and Johnson (2014)

Due to the poor core preservation of the lower (Hettangian to upper Sinemurian) part of the core, descriptions in the following are based on the drilling report (Woodland 1971), whereby the uppermost Sinemurian, Pliensbachian and Toarcian part of the core have been viewed, logged, photographed and sampled by the science party (including Stephen Hesselbo, Hugh Jenkyns, Micha Ruhl, Weimu Xu and James Riding) for the purpose of this study and other studies (see Ruhl *et al*. 2016, Xu *et al*. 2018). A detailed log of the well preserved uppermost Sinemurian to Pliensbachian succession (1281.8–863 mbs) can be found in the digital appendix (D-A-1).

The Early Jurassic succession is underlain by Upper Triassic sediments, of which the upper 32.05 m (1906.78 to 1938.83 mbs) have been penetrated and cored. The lower ~29 m comprise bedded and laminated sandstones and clay, dominated by reddish to brown colour, suggesting a terrigenous origin. A sharp, irregular surface and a change in sedimentation appears at the 1909.57 mbs, suggesting a non-deposition interval. The upper ~3 m of cored Upper Triassic are comprised of grey-green coloured, partly dolomitized shallow marine carbonates, interrupted by terrestrial hematitic depositions, that have been attributed to instability and soft-sediment slumping (Harrison 1971).

The boundary from Triassic to Lower Jurassic sedimentation (1906.78 mbs) is marked by a sharp and irregular change to grey calcareous mudstone in the lower Hettangian (lithology similar to ‘A’ in Figure 2.5). The Hettangian (1906.78 – 1741.1 mbs) to upper Sinemurian (1741.1 – 1277 mbs) strata generally comprise alternating calcareous argillaceous siltstones and softer, dark grey calcareous silty mudstone (Woodland 1971). Argillaceous limestone bands and nodules occur irregularly. Fossil occurrence is generally rare, but some beds of calcareous mudstone and limestone appear shelly (Woodland 1971).

The interval between the base Hettangian up to Sinemurian lower *semicostatum* zone (1906.78 mbs to ~1600 mbs) appears soft and friable with common slickensides, suggesting highly shared bands of up to 0.6 m, without evidence that the shear planes were of stratigraphic significance (Woodland 1971). The interval between the 1560 mbs and 1370 mbs (Sinemurian upper *semicostatum* to mid-*oxynotum*) has been described to be rich in relatively small ferruginous carbonate nodules (Woodland

1971). Pyrite is common within the entire succession but most abundant in nodules, streaks and shelly bands.

The lithology of the upper Sinemurian (~1277–1249.7 mbs) and Pliensbachian (1249.7–863.5 mbs) strata is characteristically harder and comprises a higher proportion of pale calcareous argillaceous siltstone, which is partly heavily bioturbated (see Figure 2.6). The Upper Sinemurian to Pliensbachian strata are generally fossiliferous, with abundant crinoid ossicles, belemnites, ammonites and bivalve shells. Laminated intervals occur commonly in the *jamesoni* to mid-*margaritatus* Zone (1259–1194 mbs, 1157–1152 mbs, 1108–1072 mbs, 1006–1004 mbs, 988–985mbs, see Figure 3.7). Macroscopic wood fragments appear occasionally throughout the Pliensbachian strata, and are abundant in the Upper Pliensbachian.

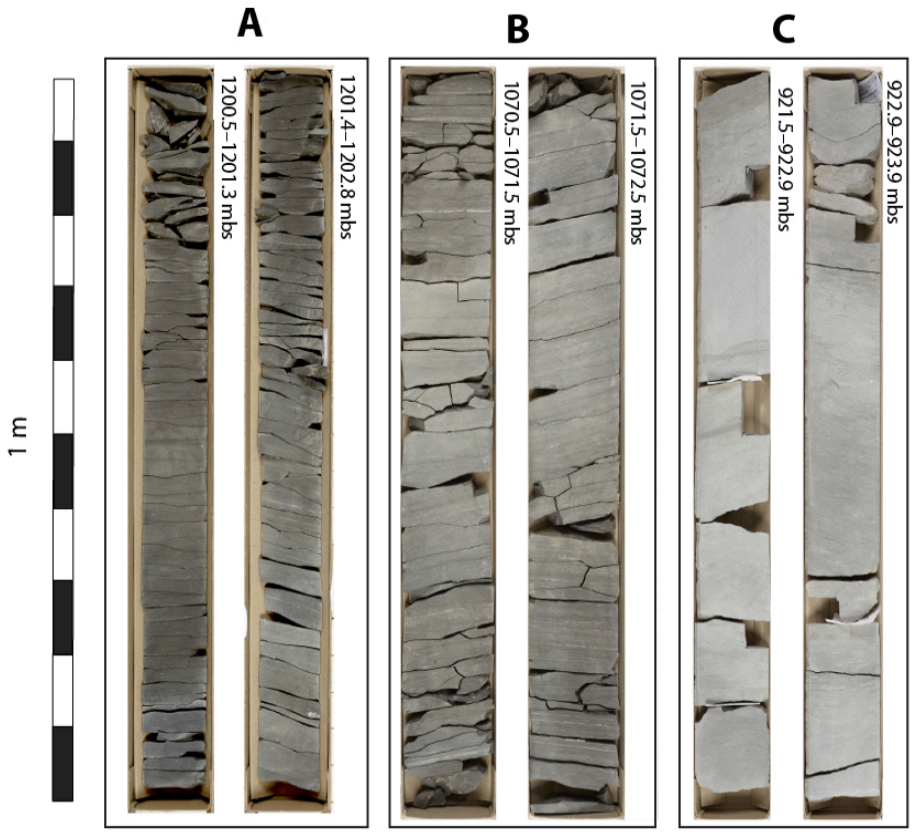

Figure 2.6: Core photographs of **A:** the lower Pliensbachian *jamesoni* Zone (1201.8–1200.5 mbs), representative for the dark and soft mudstones as they also occur in the Hettangian and lower Sinemurian strata **B:** the lower Pliensbachian *ibex* Zone, showing a gradual transition from pale grey limestone into darker brown to grey mudstone within each core. Mudstones show faint laminations in this core interval **C:** the upper Pliensbachian *margaritatus* Zone, representative for the pale grey limestones common in the Pliensbachian succession.

Ruhl *et al*. (2016) described lithological couplets of pale grey limestone gradually transitioning in darker brown to grey mudstone throughout the Pliensbachian (1249.7–863.5 mbs). The individual couplets span ~90 cm throughout the lower Pliensbachian (1249.7 to ca. 916 mbs) and ~30 cm in the uppermost Pliensbachian (~916–863.5 mbs) and are most clearly pronounced along the Sinemurian–Pliensbachian boundary and the top *ibex* to base *margaritatus* zones. The lithological couplets correlate with changes in the $CaCO_3$ content, TOC and HI index and are interpreted as climatically controlled periodic fluctuations in the supply of organic and inorganic matter, driven by astronomical forcing (Ruhl *et al*. 2016). A distinctive coarse grained band at ~919 mbs (uppermost *margaritatus* zone) has been defined by Woodland (1971), comprising sandstone with subangular fragments, and a 5 cm thick pebble bed with well rounded silt pebbles in shelly calcareous silty matrix has been observed at 908 mbs depth (*margaritatus* Zone), which suggests autochthonous origin.

The mudstone facies of the upper Pliensbachian *spinatum* zone in the Mochras drill-core is unique for same age strata in Britain, where the *spinatum* lithology is found as sandstone, ironstone or limestone facies (i.e. Cleveland Ironstone, Marlstone Rock formations, see Figure 2.5).

The Toarcian lithology comprises alternating successions of marly limestone and carbonate rich marl to mudstone and appears generally more fossiliferous compared to Pliensbachian strata (Woodland 1971, Xu *et al*. 2018). The same lithological couplets as described for the Pliensbachian are present in the Toarcian succession, which are well pronounced in the *bifrons*, *variabilis* and lower *thouarense* ammonite zones (Xu *et al.* 2018). Siderite nodules occur regularly throughout the *D. tenuicostatum* and *falciferum* zone (Woodland 1971, Xu *et al*. 2018). The Lower Toarcian in the Mochras core covering the Upper *tenuicostatum* ammonite zone and the *exaratum* ammonite subzone of the *serpentinum* ammonite zone (863.5 to 750 mbs) is marked by carbonate-poor mudstone with local centimetre-thick laminated black shale. The *exaratum* subzone exhibits several intervals of coarser grained (silty) sediments, commonly with macroscopic wood fragments, as well as sedimentary structures such as wave ripples and levels of soft- sediment deformation (Xu *et al*. 2018). The upper *D. tenuicostatum* ammonite zone and the *exaratum* ammonite subzone of the *serpentinum* ammonite zone are marked by carbonate-poor mudstone with local

centimeter-thick laminated black shale, representing the local lithological expression of the Toarcian oceanic anoxic event. A distinct limestone unit in the Toarcian *bifrons* zone correlates well with same age strata in south and central England (Beacon Limestone Formation).

2.3. Depositional environment

In the Hettangian and Sinemurian strata, fossil and microfossil assemblages in the Mochras core suggest poorly oxygenated bottom waters due to sluggish circulation, and stratified surface waters poor in nutrients, due to low continental freshwater run-off (van de Schootbrugge *et al.* 2005). The occasional appearance of laminated facies also indicates intervals of less oxygenated bottom-water in the upper Sinemurian to Pliensbachian, which are generally well-oxygenated as indicated by the occurrence of and crinoid ossicles (mainly in the Pliensbachian). The predominant occurrence of acritarchs throughout the studied interval suggests a low-nutrient environment, which appears to be interrupted by two phases of mesotrophic conditions in the upper Sinemurian and upper Pliensbachian strata, as indicated by the occurrence of cyst-forming dinoflagellates (van de Schootbrugge *et al.* 2005). The intervals marked by dinoflagellate occurrence correlate with regionally cooler climates and/or cold and saline waters (van de Schootbrugge *et al.* 2005, Korte *et al.* 2015). Opening and closing of the connection seaways (Hispanic corridor and Viking corridor) likely affected the oceanic heat flow patterns and are debated as potential driving mechanism for Early Jurassic climatic transitions as they are recorded from the Pliensbachian and Toarcian stages in the NW European realm (Porter *et al.* 2013, Korte *et al.* 2015).

The siliciclastic (quartz, autochtonous clay) in the sediments, as well as the abundant fossil plant and wood debris in the upper Pliensbachian and lower Toarcian strata, were likely sourced from nearby landmasses, i.e. the Irish Massivf to the west and Cornubia to the south (Ruhl *et al.* 2016, Xu *et al.* 2018). The depositional environment throughout the Toarcian stage was evidently open marine as shown by Mo and U enrichments in the sediments (Percival *et al*. 2016). Elevated sedimentary organic carbon values indicate increased continental weathering rates at the the Pliensbachian–Toarcian boundary and the Toarcian *D. tenuicostatum* and *serpentinum*

zones, concomitant with the negative carbon-isotope excursion associated with the Toarcian oceanic anoxic event (Xu *et al*. 2018). The Pliensbachian-Toarcian boundary up to the Toarcian *serpentinum* ammonite Zone show less favorable bottom water conditions, as crinoid ossicles disappear. Nodular siderite beds in the same interval suggest intensified continental weathering and widespread large-scale pyrite fixation during the Toarcian oceanic anoxic event (Xu *et al.* 2018). The interval is also marked by brief anoxic to euxinic conditions and unfavorable conditions for marine organisms, although increased algal marine productivity likely accounts for slightly increased sedimentary organic matter (Xu *et al.* 2018).

Chapter 3 : Continuous carbon-isotope ($\delta^{13}C_{TOC}$) record from the Lower Jurassic of the Llanbedr (Mochras Farm) borehole, Cardigan Bay Basin, UK

3. Abstract

The lack of a continuous high-resolution carbon-isotope record based on a single material, and thus a single carbon reservoir, has so far inhibited investigation of the secular evolution of the Early Jurassic ocean-atmosphere carbon cycle. This study presents a continuous high-resolution $\delta^{13}C_{TOC}$ record from the Lower Jurassic comprising new data from the Hettangian to Pliensbachian interval combined with pre-existing data from the Toarcian. The record derives from biostratigraphically well-calibrated hemipelagic limestones and marls of the Llanbedr (Mochras Farm) borehole, Cardigan Bay Basin, UK. The new record from the Mochras core exhibits some of the carbon-isotope excursions previously identified in various sedimentary basins, but here aggregated in a continuous record from a single location. The record further reveals the consecutive appearance of small-amplitude excursions of comparable magnitude and stratigraphic thickness, well expressed through certain intervals of the Hettangian to Pliensbachian section, including several isotopic events that have not been identified elsewhere. The new $\delta^{13}C_{TOC}$ record provides a chemostratigraphic template for the identification and correlation of Early Jurassic carbon-isotope events, and brings new insights into possible causal mechanisms behind small-amplitude carbon-isotope excursions.

3.1. Introduction

Stratigraphic records of $\delta^{13}C$ are used as proxies for the carbon-isotope composition of ocean–atmosphere carbon, as well as to detect intervals of change in the global exogenic carbon cycle and palaeoenvironmental anomalies, such as globally increased organic-carbon burial and the release of isotopically light carbon into the ocean–atmosphere system (Kump and Arthur 1999). The most prominent carbon-isotope events identified in Lower Jurassic strata are associated with the Triassic–Jurassic boundary (~201 Myr) and the Toarcian Oceanic Anoxic Event (T-OAE; ~183 Myr), both of which are expressed in the $\delta^{13}C$ values derived from oxidized and reduced

carbon reservoirs (e.g. Hesselbo *et al.* 2000, Hesselbo *et al.* 2002, Jenkyns *et al.* 2002, Ruhl *et al.* 2009, Al-Suwaidi *et al.* 2010, Whiteside *et al.* 2010, Caruthers *et al.* 2011) and associated with the globally increased emission of isotopically light volcanic, themogenic, or biogenic carbon into the ocean–atmosphere system (Hesselbo *et al.* 2002, McElwain *et al.* 2005, Svensen *et al.* 2007, Svensen *et al.* 2012). Bracketed by these distinct very large-amplitude isotopic events, numerous carbon-isotope excursions of lesser magnitude have been identified in the Hettangain to Pliensbachian interval, such as the negative shift at about the Sinemurian–Pliensbachian boundary (e.g. Jenkyns *et al.* 2002, Woodfine *et al.* 2008, Korte and Hesselbo 2011, Duarte *et al.* 2014), or the widespread positive carbon-isotope excursion (CIE) in the upper *magraritatus* Zone (Jenkyns and Clayton 1986, Korte and Hesselbo 2011, Silva *et al.* 2011, Peti *et al.* 2017).

The existing records for the Lower Jurassic Series tend to cover short stratigraphic intervals, originate from a variety of different sedimentary basins and different carbon archives (bulk organic matter, bulk carbonate, fossil calcite, fossil wood, palynomorphs), or are of relatively low stratigraphic resolution. Causal mechanisms for carbon-isotope excursions found in Lower Jurassic sediments have been proposed on the assumption of stand-alone events, similar to the T-OAE, being linked to exceptional increased release or burial of isotopically light carbon of yet undefined source (e.g. Silva *et al.* 2011, Riding *et al.* 2013, respectively), or changes in productivity or sea-level (Jenkyns and Weedon 2013, Porter *et al.* 2014). Alongside such event-focused interpretations, orbital pacing of the exogenic carbon-cycle, or regional to global environmental conditions have also been proposed to drive cyclic fluctuations in the organic carbon-isotope record on the scale of Milancovitch cyclicity (10^4 to 10^5 years) (i.e. Bonis *et al.* 2010, Clemence *et al.* 2010, Ruhl *et al.* 2010, Hüsing *et al.* 2014, Xu *et al.* 2017a) to grand orbital cycles Myr-scale amplitude modulations (Myr-scale amplitude modulations, also referred to as great eccentricity cycles, Martinez and Dera 2015).

Up until now, there has been no overall understanding of the evolution of the entire Early Jurassic regional and global carbon-isotope record, causal mechanisms driving individual shifts, or possible links between individual excursion intervals. The new $\delta^{13}C_{TOC}$ record of the Mochras core provides the required Lower Jurassic archive on a

stratigraphically expanded and biostratigraphically well-defined section that is necessary for integration of the disparate existing studies.

3.2. Material and Methods

A total of 1330 samples form the uppermost Rhaetian to Pliensbachian strata (1909.8 to 863.65 mbs) have been analyzed for bulk organic carbon-isotope composition ($\delta^{13}C_{TOC}$). Detailed information on sample resolution and analytical methods can be found in Chapter 1, sections 1.3.1 and 1.4.1, respectively.

3.3. A high-resolution $\delta^{13}C_{TOC}$ record of the Hettangian, Sinemurian and Pliensbachian stages of the Mochras core

The new high-resolution $\delta^{13}C_{TOC}$ record (Figure 3.1) presented here for the uppermost Rhaetian, largely complete Hettangian and complete Sinemurian and Pliensbachian stages of the Mochras core are combined with new data for the Toarcian (*tenuicostatum* to lower *aalensis* zones) from the same core (Xu *et al.* 2018). The new dataset illustrates significant long- and short-term fluctuations in the bulk organic carbon-isotope evolution with, overall, values ranging between −29.3‰ and −23.3‰, with an average of −26.6‰ (n = 1333) in the Hettangian to Pliensbachian record, and −31.2‰ to −23.7‰, with an average of −27.1‰ in the Toarcian dataset (n=433, Xu *et al.* 2018)

At a large scale, the record comprises a long-term 5‰ positive trend in $\delta^{13}C_{TOC}$ from the base of the Hettangian through to the upper Sinemurian (from ~ −28.6 to −23.3‰, 1906.7 to 1500 mbs, see Figure 3.1). The Sinemurian–Pliensbachian boundary is characterized by a more or less symmetrically shaped 5‰ negative CIE (upper *oxynotum* to upper *ibex* zone, ca. 1360 to 1060 mbs, reaching the most negative values in the lower *jamesoni* zone).

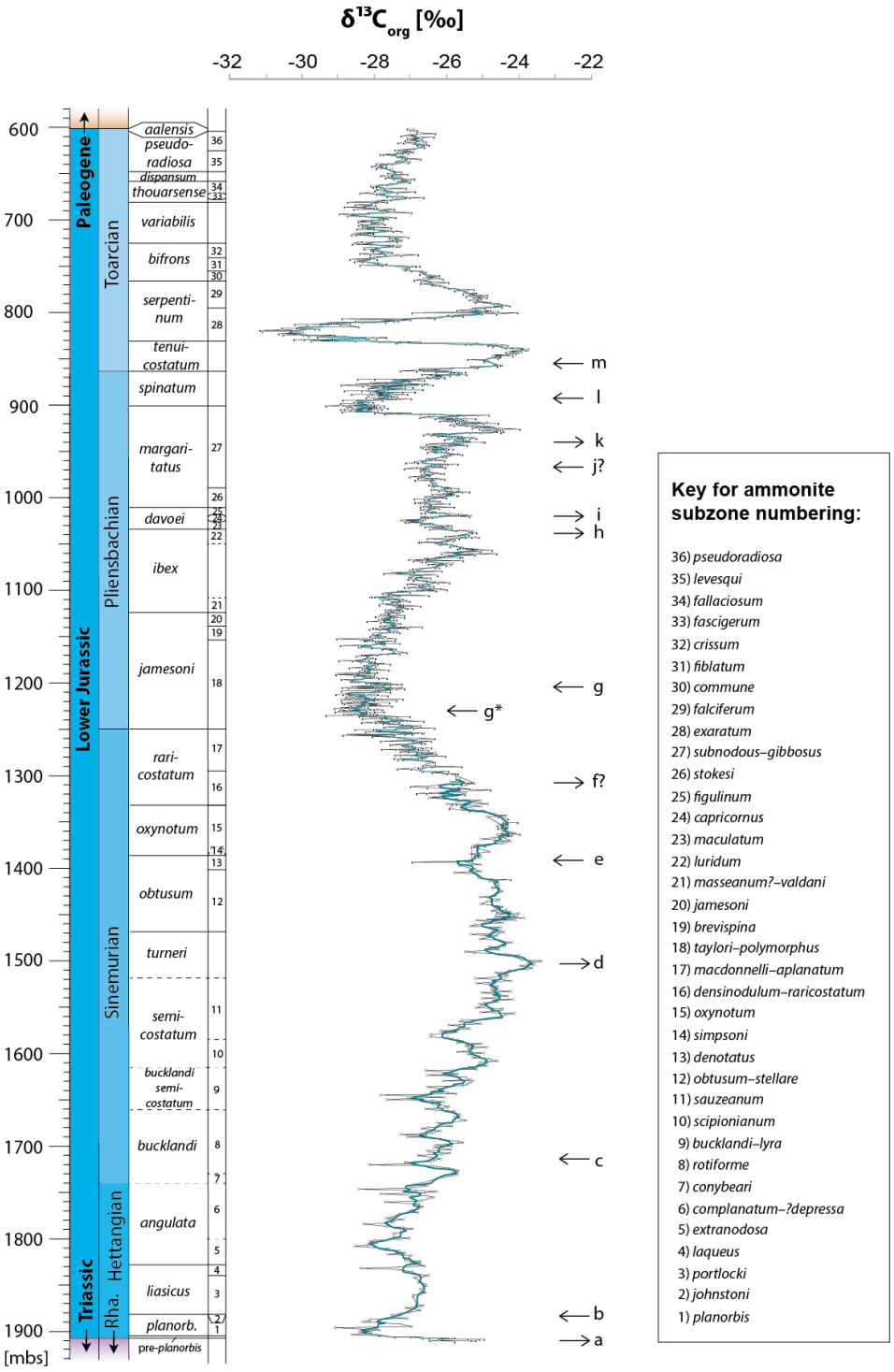

Figure 3.1: $\delta^{13}C_{TOC}$ record of the Uppermost Rhaetian to Toarcian of the Mochras core. Toarcian $\delta^{13}C_{TOC}$ data from Xu *et al.* (2018). Blue line represents a 9-point moving average for data from the Hettangian to Upper Sinemurian, and 7-point moving average for the Upper Sinemurian to Toarcian. Filled symbols = samples from core slabs; open symbols = samples from interval averaged (~1.4 m) bags of broken core rubble. Ammonite biostratigraphy based on Ivimey-Cook (1971) and Page in Copestake and Johnson (2014). Key for subzone numbering given in Figure. Characters **a** to **l** mark the

stratigraphic position of isotope excursions discussed in the text. Corresponding arrows indicate the negative excursions (pointing left) and positive excursions (pointing right).

The middle Pliensbachian interval presents overall a positive plateau, with the record of the upper *margaritatus* Zone (*subnodosus* and *gibbosus* subzones) rising gradually to a positive peak (~980 to 930 mbs), followed upwards by a very abrupt and sharp 2‰ positive shift in the upper *margaritatus* zone (between 930 and 926 mbs). The upper *margaritatus* to *spinatum* zone is marked by an asymmetrical 4‰ negative excursion, with a stratigraphically sharp onset and more expanded 'recovery'. The Toarcian record comprising a lower Toarcian overarching positive excursion interrupted by the large negative carbon-isotope excursion of the T-OAE (Figure 3.1), as described previously (Jenkyns and Clayton 1997, Jenkyns *et al.* 2002, van de Schootbrugge *et al.* 2005, Xu *et al.* 2018).

At a smaller scale, the $\delta^{13}C_{TOC}$ record is further characterized by a consecutive series of metre- to tens-of-metres scale alternating positive and negative shifts of ~0.5 to 2‰ magnitude, superimposed on the long-term isotope trends. These cyclic changes in $\delta^{13}C_{TOC}$ gradually change in stratigraphic thickness (from 8 to 40 m) and are particularly well defined in the Hettangian and Sinemurian interval (between 1906.78 mbs and 1340 mbs), as well as in the mid-Pliensbachian upper *ibex* to lower *margaritatus* zones (1055 to 930 mbs). Individual cycles appear larger in magnitude and stratigraphical thickness in the lower Hettangian, and in the Sinemurian *obtusum* to *oxynotum* zones compared to the carbon-isotope fluctuations occurring in the Pliensbachian strata.

Within the Pliensbachian, on very small-scale of 30 cm to 1 m, the $\delta^{13}C_{TOC}$ values show cyclic variations of up to ~2‰. In the Hettangian and Sinemurian stages, where sample resolution was generally restricted to 1.4 m, the cyclic variations are relatively small (<1‰), with outliers of larger magnitude occurring on the most negative interval of an individual metre- to tens-of-metre scale small-amplitude shifts. However, it is unclear whether this difference between Hettangian–Sinemurian and Pliensbachian is an artifact due to the relatively coarse sample spacing.

3.4. Correlation of NW European Lower Jurassic carbon-isotope records

Several long-term trends and small-amplitude positive and negative excursions recorded in the new high-resolution $\delta^{13}C_{TOC}$ record of Mochras have previously been recorded in the low-resolution isotope record published for the same core (Katz *et al.* 2005), and various other European basins (references cited in Figure 3.2 and Jenkyns and Clayton (1997)).

Two pronounced negative CIEs mark the record of the Triassic–Jurassic boundary in marine and terrestrial proxy-records of several locations around the world e.g. in the Eiberg Basin, Austria (Ruhl *et al.* 2009), Bristol Channel Basin, UK (Hesselbo *et al.* 2002, Ruhl *et al.* 2009), Jameson Land Basin, Greenland (Hesselbo *et al.* 2002), Newark Basin, USA (Whiteside *et al.* 2010), and New York Canyon, USA (Bartolini *et al.* 2012). An initial, stratigraphically short, negative CIE occurs in the uppermost Rhaetian, associated with the end-Triassic mass extinction, and a main, stratigraphically longer-lasting, negative CIE onsets around the Triassic–Jurassic boundary itself. The negative CIEs are thought to result from the massive release of CO_2 as they are simultaneously recorded in various carbon reservoirs and correlate in time with volcanic pulses linked to the Central Atlantic Magmatic province (see Deenen *et al.* 2010, Davies *et al.* 2017).

The precise correlation of the Mochras $\delta^{13}C_{TOC}$ record to the well-studied GSSP section in the Eiberg Basin (Kuhjoch section, Austria) and the St Audries Bay section (Bristol Channel Basin, UK, see Figure 3.3) is problematic due to stratigraphic uncertainties in a) the pre-*planorbis* beds in Mochras and their accurate correlation to the *tilmanni* ammonite Zone (defined by the first occurrence of *P. spalae*, which has not been found in stratigraphic sections in Britain), b) the unknown stratigraphic gap associated with the hiatus at the lithostratigraphically defined Triassic–Jurassic boundary in the Mochras core, and c) the present lack of high-resolution palynological data, which would allow usage of the lowest occurrence of *Cerebropollenites thiergartii* as a alternative terrestrial stratigraphic marker for the Triassic–Jurassic boundary, as suggested by (Bonis *et al.* 2010).

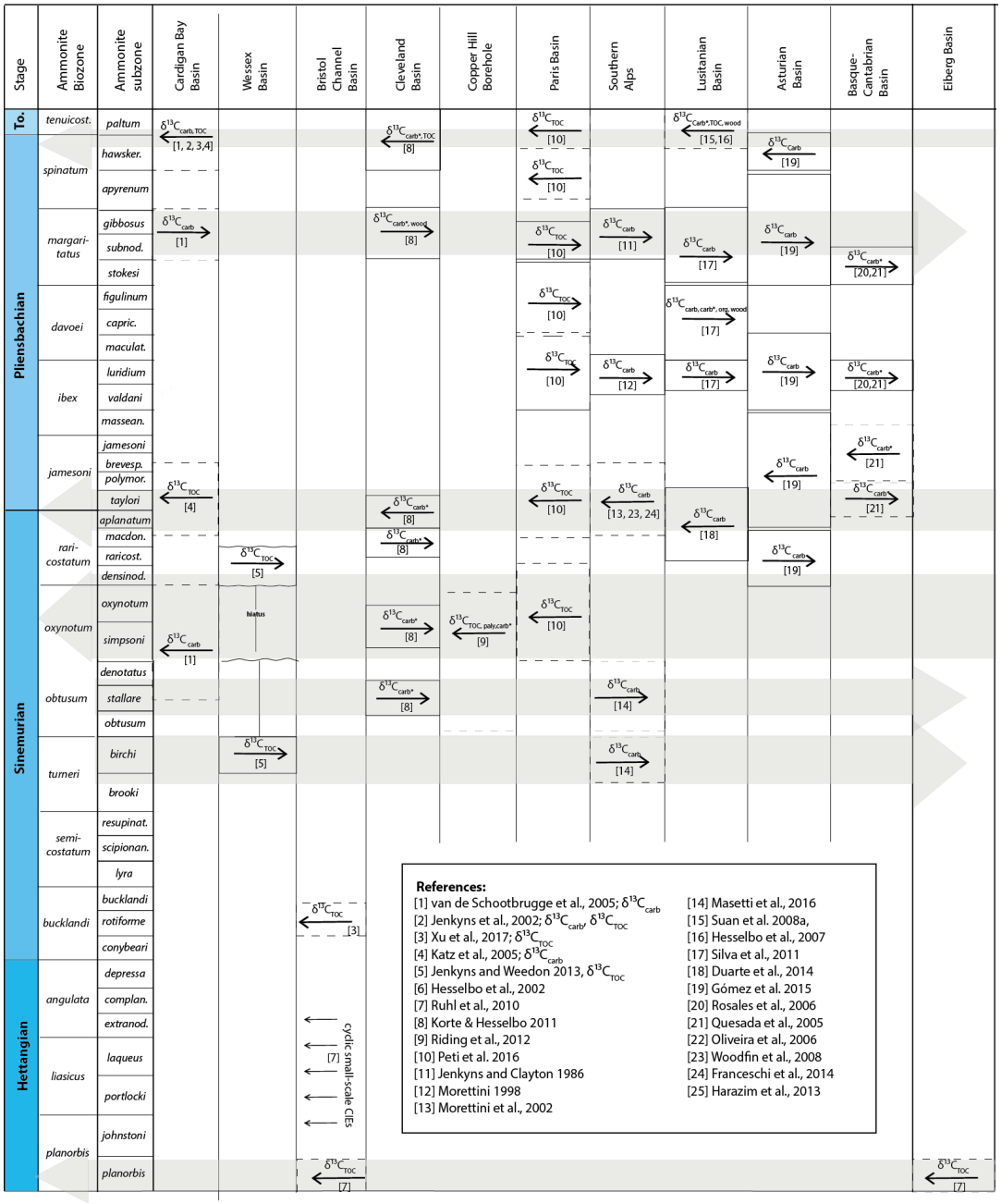

Figure 3.2: Carbon-isotope excursions identified in Hettangian to Pliensbachian strata in $\delta^{13}C_{TOC}$ (bulk organic), $\delta^{13}C_{carb}$ (bulk carbonate), $\delta^{13}C_{carb*}$ (fossil calcite), $\delta^{13}C_{wood}$ (fossil wood), $\delta^{13}C_{pal}$ (palynomorphs). Arrows pointing to the right: positive $\delta^{13}C$ excursion; arrows pointing to the left: negative $\delta^{13}C$ excursion. Dotted lines indicate biostratigraphical uncertainties at the subzone level. References given in table.

However, the first occurrence of *Psiloceras spelae* Guex, defining the basal Jurassic boundary *tilmanni* chronozone at the GSSP section, at Kuhjoch, Austria (Hillebrandt *et al.* 2007) correlates with a small positive isotope shift in between the initial and main CIE ('a' in Figure 3.1 and 3.3). The carbon-isotope record of the lowermost Hettangain pre-*planorbis* bed could represent this positive shift, supporting the presence of a largely complete lowermost Hettangian record. The negative CIE occurring in the lowest Hettangian ('b' in Figure 3.1 and 3.3) in the Mochras core therefore likely represents the upper part of the 'main CIE', associated with the Triassic–Jurassic boundary negative excursion.

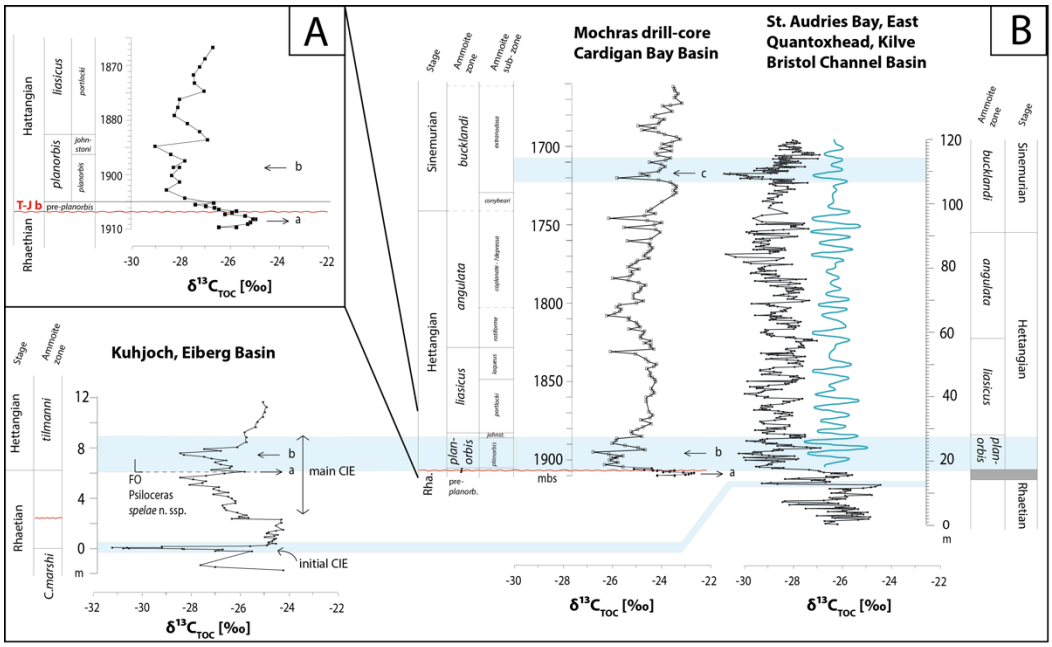

Figure 3.3: **A:** Uppermost Rhaetian and lowermost Hettangian $\delta^{13}C_{TOC}$ record of the Mochras core, indicating the stratigraphic position of the Triassic–Jurassic boundary and associated hiatus (red line) and the base of the *planorbis* Zone (black line). **B:** Proposed correlation between the Triassic–Jurassic boundary $\delta^{13}C_{TOC}$ record of the Kuhjoch section, Eiberg Basin, Austria (data from Ruhl *et al*. 2009, 2010 (red line represents hiatus, dotted line represents level of the first occurrence of *Psiloceras spelae* Guex), the Mochras core, and the Bristol Channel Basin (St Audries Bay, East Quantoxhead and Kilve sections; data from Ruhl *et al*. 2010, Hesselbo *et al*. 2002, Hüsing *et al*. 2014, Xu *et al*. 2017a). Blue line represents band-pass filters (~263-727 cm) and reflects interpreted ~100-kyr eccentricity oscillations in the $\delta^{13}C_{TOC}$ record (modified from Ruhl *et al*. 2010).

Following the negative CIE associated with the Triassic–Jurassic boundary, a series of fluctuations in the Hettangian and lower Sinemurian $\delta^{13}C_{TOC}$ record of 1 to 2 ‰ magnitude have been reported from St Audries Bay, East Quantoxhead and Kilve sections (Bristol Channel Basin; Ruhl *et al.* 2009, Clemence *et al.* 2010, Hüsing *et al.* 2014, Xu *et al.* 2017a). A ~2.5 ‰ negative CIE is also observed in the lower Sinemurian *bucklandi* ammonite zone (*rotiforme* subzone) of East Quantoxhead, both in $\delta^{13}C_{TOC}$ and in $\delta^{13}C_{Carb}$ (Ruhl *et al.* 2009, Xu *et al.* 2017a). These CIEs have been interpreted as orbitally paced 405 kyr modulated short (~100 kyr) eccentricity cycles (see Ruhl *et al.* 2009, Clemence *et al.* 2010, Hüsing *et al.* 2014, Xu *et al.* 2017a). The fluctuations in the $\delta^{13}C_{TOC}$ possibly reflect changes in the exogenic carbon cycle and/or intensified regional to global changes in the palaeo- and depositional environment (Ruhl *et al.* 2009, Hüsing *et al.* 2014, Xu *et al.* 2017a). The changes in the isotopic composition are thereby possibly controlled by changes in the source of sedimentary organic matter, the magnitude of marine and/or terrestrial isotope fractionation, or changes in the hydrology, affecting the isotopic composition of the dissolved inorganic carbon (DIC, Xu *et al*. 2017). Compared to the Bristol Channel Basin, the resolution of the Mochras $\delta^{13}C_{TOC}$ record is comparably low, hindering a correlation of the individual ~100 kyr short eccentricity fluctuations in the $\delta^{13}C_{TOC}$ record. However, a possible correlation of the negative CIE and the *bucklandi* Zone (*rotiforme* Subzone) negative excursion, based on biostratigraphic correlation, is suggested (see excursion marked as ‘c’ in Figure 3.1 and 3.3). For in-depth discussion on the orbital pacing of the Mochras $\delta^{13}C_{TOC}$ record see Chapter 4.

A positive shift in the Sinemurian *turneri* Zone was previously recorded in the Wessex Basin (Jenkyns and Weedon 2013) and correlated to a positive excursion in the Last Creek section in North America (Porter *et al.* 2014). Due to the widespread appearance, the event has been interpreted to reflect a global increase in productivity and carbon burial. In the Mochras core, a similar, distinct positive CIE can be observed in the *turneri* Zone, superimposed on the gradual positive long-term Hettangian to Upper Sinemurian positive shift (excursion marked as ‘d’ in Figure 3.1).

A distinct negative shift in the Sinemurian *obtusum–oxynotum* zones is recorded in both, $\delta^{13}C_{carb}$ and $\delta^{13}C_{TOC}$ of the previous isotope-record of the Mochras core and this study (van de Schootbrugge *et al.* 2005, excursion marked as 'e' in Figure 3.1), and

likely stratigraphically correlates with the CIE present in the marine and terrestrial record ($\delta^{13}C_{TOC}$ and $\delta^{13}C_{palynomorph}$) of the Copper Hill borehole, Linconshire, UK (Riding *et al.* 2013), as well as in the southern Alps (Masetti *et al.* 2016), the Dorset coast, Wessex Basin, UK ($\delta^{13}C_{TOC}$, Jenkyns and Weedon 2013), and the Sancerre-Couy core, Paris Basin (Peti *et al.* 2017, see Figure 3.4). Most of the previously studied successions have stratigraphical uncertainties due to the widespread hiatus at about the *obtusum–oxynotum* zonal boundary, leaving the true stratigraphical extent of the excursion in question. However, the *obtusum–oxynotum* zones CIE in the Copper Hill borehole is accompanied by an increase in thermophilic pollen, and has been interpreted as a hyperthermal event, proposed to have been triggered by volcanic degassing (Riding *et al.* 2013).

A positive CIE in the *raricostatum* Zone has been identified in the sedimentary record of several European basins (Korte and Hesselbo 2011, Jenkyns and Weedon 2013, Gómez *et al.* 2016). This excursion is not clearly expressed in the Mochras core, although a small-amplitude positive shift appears in the lower *raricostatum* Zone (proposed stratigraphic position in the Mochras record marked as 'f?' in Figure 3.1), overshadowed by the broad negative CIE across the Sinemurian–Pliensbachian transition. Jenkyns and Weedon (2013) linked the positive excursion to increased organic-matter burial in expanded shelf-sea areas along the proto-Atlantic margins during intervals of elevated sea levels.

The negative excursion at the Sinemurian–Pliensbachian boundary appears in the $\delta^{13}C_{TOC}$ record of the Paris Basin (Peti *et al.* 2017), as well as in $\delta^{13}C_{carb}$ and $\delta^{13}C_{wood}$ in the Cleveland Basin (Robin Hood's Bay, UK; Korte and Hesselbo 2011), the $\delta^{13}C_{carb}$ record of the Lusitanian Basin (Duarte *et al.* 2014) and Basque-Cantabrian Basin and the Southern Alps (Quesada *et al.* 2005, Woodfine *et al.* 2008, Franceschi *et al.* 2014). The concomitant occurrence of the excursion in several carbon reservoirs and several basins indicates a global change in the ocean-atmospheric $\delta^{13}C$ ratios. Ruhl *et al*. (2016) suggested the atmospheric release of CO_2 emitted during a late phase of CAMP volcanism as a potential source for isotopically light carbon, driving the isotope record towards a prolonged negative shift. The Mochras core exhibits a sustained and gradual ~4.5 ‰ negative CIE across the Sinemurian–Pliensbachian transition (stratigraphic position marked as 'g' in Figure 3.1). This observed negative

CIE onsets at the *oxynotum–raricostatum* zonal boundary, reaches a minimum in the lower *jamesoni* Zone and reaches a return to positive values in the upper *ibex* Zone. The absence of a similar signal in the $\delta^{13}C_{carb}$ record of Mochras (Katz *et al.* 2005) suggests a possible diagenetic overprint here. However, a stratigraphically less expanded ~1.5 ‰ drop in isotope values superimposed on the gradual negative shift and marking the most negative values of the overarching negative excursion in the lowermost *jamesoni* Zone (see 'g*' in Figure 3.1) is documented in the $\delta^{13}C_{carb}$ record of the Mochras core (van de Schootbrugge *et al.* 2005). Notably, the negative CIE in the $\delta^{13}C_{belemnite}$ record of the Basque-Cantabrian basin (Quesada *et al.* 2005) appears in the *jamesoni* to early *ibex* zones and is preceded by a positive shift. The Sancerre-Couy core record reveals two sharp and apparently short-lived negative spikes located in the lowermost *jamesoni* zone (see Figure 3.4).

A ~2 ‰ positive CIE associated with organic-rich strata in the *ibex* Zone has previously been detected in $\delta^{13}C_{carb}$ in several sedimentary basins (Basque-Cantabrian Basin: Quesada *et al*. 2005, Rosales *et al*. 2006; Lusitanian Basin: Silva *et al*. 2011; Cardigan Bay Basin: Katz *et al*. 2005, van de Schootbrugge *et al*. 2005; Umbria-Marche: Morettini 1998). The Basque-Cantabrian Basin and Lusitanian Basin records are biostratigraphically well defined to a subzone level, placing the positive CIE in the *luridium* Subzone. A concomitant positive peak appears in the *luridium* Subzone in the Mochras $\delta^{13}C_{TOC}$ record (marked as 'h' in Figure 3.1). A positive carbon-isotope event is also recorded in the Sancerre-Couy record from the Paris Basin (Peti *et al.* 2017), although with uncertainties in the age constraints (see Figure 3.4). The relatively low sample resolution and low biostratigraphic resolution of the Paris Basin record hamper the exact correlation of the two positive shifts occurring in the mid-*ibex* to lower *davoei* zones, and the $\delta^{13}C$ positive excursion in the Paris Basin likely represents both events lumped into a single excursion event.

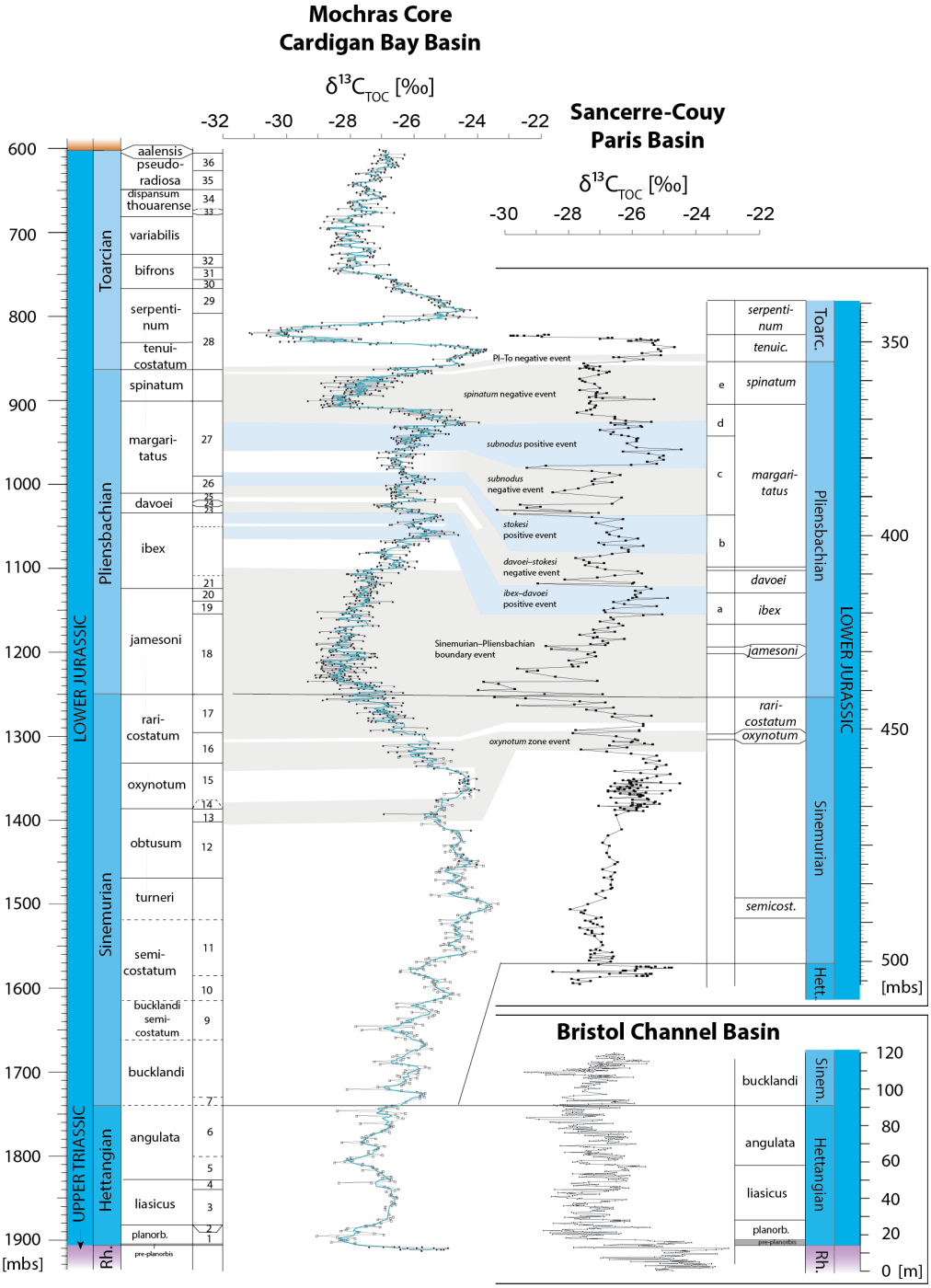

Figure 3.4: $\delta^{13}C_{TOC}$ record of the Hattangian to Toarcian of the Mochras core (Toarcian data from Xu *et al*. (2018)), upper Hettangian to Pliensbachian of the Sancerre-Couy core, Paris Basin (Peti *et al*. 2017) and Hettangian to lower Sinemurian record from the Bristol Channel Basin (St Audries Bay, data composite from Hesselbo *et al*. 2002, Ruhl *et al*. 2010, and Xu *et al*. 2017a) Identified Ammonite subzones in Mochras stratigraphy see Figure 3.1. Identified Ammonite subzones in the Sancerre-Couy stratigraphy: a) *valandi*, b) *stokesi*, c) *subnodus*, d) *gibbosus*, e) *solare*. Blue line represents a 9-point moving average for data from the Hettangian to Upper Sinemurian, and 7-point moving average for the Upper Sinemurian to Toarcian.

A further positive CIE has been recorded in the *davoei* Zone (marked as 'i' in Figure 3.1) of the Lusitanian Basin (Silva *et al.* 2011), present in the $\delta^{13}C$ record of carbonate, fossil calcite, bulk organic matter and wood. The excursion is also recorded in the $\delta^{13}C_{TOC}$ record of the Paris Basin (Peti *et al.* 2017), although the correlation to the Paris Basin record is hampered by the inexact biostratigraphical assignments (see Figure 3.4). In the Lusitanian Basin, both the *ibex* and *davoei* excursions are associated with organic-rich facies indicating the drawdown of isotopically light carbon (Duarte *et al.* 2011, Silva *et al.* 2011).

A negative event in the lower *margaritatus* Zone (*subnodus* Subzone) has so far only been reported from the Sancerre-Couy core, Paris Basin (Peti *et al.* 2017). The *subnodosus* and *gibbosus* subzones are not individually defined in the Mochras core. Several isotope shifts, both positive and negative, are recorded in the lumped *subnodosus* and *gibbosus* subzones (see 'j?' in Figure 3.1), wherefore it is not possible to identify the event recorded in the Paris Basin.

The overarching positive CIE in the upper *margaritatus* Zone (*subnodosus* and *gibbosus* subzones, marked as 'k' in Figure 3.1) has been reported from a variety of datasets from the Upper Pliensbachian (Jenkyns and Clayton 1986, Oliveira 2006, Rosales *et al.* 2006, Korte and Hesselbo 2011, Ruhl *et al.* 2016, Peti *et al.* 2017), except for the diagenetically overprinted $\delta^{13}C_{carb}$ record from the Fontaneilles section (southern France, van de Schootbrugge *et al.* 2010). The positive shift is associated with widespread (globally) increased sedimentary organic-matter preservation evidenced by the occurrence of lack shales, possibly leading to cooling climates during a falling sea-level change associated with regressive facies successions (Suan *et al.* 2010, Silva *et al.* 2011 and references therein). Rosales *et al.* (2006) linked the *ibex* and *margaritatus* Zone positive peaks to regional transgression events and the organic-matter preservation due to the increase of shelf areas. The occurrence of comparable carbon-isotope shifts in multiple basins again suggests a trans-regional causative mechanism, similar to the *raricostatum* and *turneri* Zone positive CIEs. This positive CIE is well expressed in the Mochras record ('k' in Figure 3.1) and further characterized by an abrupt and sharp positive shift in the upper *margaritatus* Zone.

The negative ~4.5‰ CIE recorded in the uppermost *margaritatus* and *spinatum* zones of the Mochras core, following the *margaritatus* Zone positive trend ('l' in Figure 3.1), was also reported from the Paris Basin (Peti *et al.* 2017), however, there recorded with a smaller (~2‰) magnitude. Although not discussed in detail in other studies, the negative excursion can potentially also be observed in various additional isotope records (Quesada *et al.* 2005, Oliveira 2006, Suan *et al.* 2010, Korte and Hesselbo 2011, Harazim *et al.* 2013, Martinez and Dera 2015, Silva and Duarte 2015, Gómez *et al.* 2016). A trigger mechanism or possible source for increased ocean-atmosphere ^{12}C-enrichment has not yet been proposed for this event.

The negative CIE at the Pliensbachian–Toarcian boundary, known from the Cleveland Basin (Kemp *et al.* 2005, Littler et al. 2009) and Lusitanian Basin (Hesselbo *et al.* 2007) has recently been suggested to be coincident with an early pulse of the Karoo-Ferrar volcanic activity; it is associated with increased volcanically sourced elemental mercury in sedimentary organic matter, and increased weathering rates based on osmium-isotope analysis (Percival *et al*. 2016). The boundary ~2 ‰ negative CIE is well expressed in the Mochras core (marked as 'm' in Figure 3.1) and is similar in size to that recorded in other sections (e.g. Cleveland Basin, Kemp *et al.* 2005, Littler *et al*. 2009).

3.5. Discussion and Conclusion

The new Mochras $\delta^{13}C_{TOC}$ record aggregates features that have previously been recorded in the Hettangian to Toarcian record of several NW European sedimentary basins. Individual small-scale CIEs identified and characterized in previous datasets appear less singular in the collective context of the continuous and stratigraphically expanded Mochras record, where CIEs of similar magnitude and stratigraphical thickness appear consecutively, some of which have not previously been identified. The sequence of similar excursion intervals hampers the accurate correlation to other records, which provide relatively low sample resolution and biostratigraphical discrimination, as they may merge several individual events (e.g. the *ibex–davoei* and *davoei–stokesi* positive events, Paris Basin, see Figure 3.4). Furthermore, widespread

non-depositional levels in localities outside the Cardigan Bay Basin, especially in the upper Sinemurian *obtusum*, *oxynotum* and *raricostatum* zones, hamper the identification of the correlating cycles between the Cardigan Bay Basin, the Wessex Basin and the Copper Hill borehole.

However, a large number of larger and smaller amplitude carbon-isotope fluctuations observed in the Mochras core appear approximately coeval in multiple carbon reservoirs ($\delta^{13}C_{TOC}$, $\delta^{13}C_{carb}$, $\delta^{13}C_{fossilCarb,}$ $\delta^{13}C_{wood}$) in a variety of different NW European basins. The Mochras dataset therefore likely represents a regional to global $\delta^{13}C_{TOC}$ signal that, due to the temporal correlation with isotope events in marine carbonate and terrestrial organic matter, possibly reflects changes in the global ocean–atmosphere CO_2 carbon-isotope signal. The Mochras $\delta^{13}C_{TOC}$ record is therefore proposed as a chemostratigraphic template for all the Lower Jurassic stages, onto which disparate datasets may be matched in the future.

Regardless of the regional or global nature of the isotope shifts, the new Mochras $\delta^{13}C_{TOC}$ record indicates a repetitively acting mechanism to be considered as the driver behind the reoccurring small-amplitude carbon-isotope fluctuations, either affecting the global exogenic carbon cycle, changes in biological fractionation, local changes in the DIC pool or the primary source of sedimentary organic matter.

Further study is suggested on the pacing of the observed small-amplitude CIEs throughout the Lower Jurassic sequence in the Mochras core. The characterization of the total organic matter composition within the Hettangian to Pliensbachian sediments will also consider the role of changes in the source of organic matter in the isotope evolution of the Early Jurassic and lead to insight into possible mechanisms that link orbital forcing and specific palaeoenvironmental changes.

Chapter 4 : Orbital pacing of the Early Jurassic Hettangian to Pliensbachian $\delta^{13}C_{TOC}$ record

4. Abstract

The $\delta^{13}C_{TOC}$ record of the Lower Jurassic Hettangain to Pliensbachian stages of the Llanbedr (Mochras Farm) drill-core (Cardigan Bay Basin, UK) is characterized by the consecutive appearance of small-amplitude (~0.5-2 ‰) fluctuations of comparable magnitude and stratigraphic thickness. These fluctuations are regularly cyclic and suggested to be orbitally paced, corresponding to 405-kyr long-eccentricity cycles. Orbital tuning of the continuous Hettangian to Pliensbachian $\delta^{13}C_{TOC}$ record allows assessment of the time scales of the isotope excursions, and identification of potential mechanisms driving the Early Jurassic carbon cycle on the grounds of age correlation. The results established herein closely agree with previous astrochronological time scales for the Hettangian and Pliensbachian stages, and provide a new basis for a Sinemurian chronology.

4.1. Introduction

In order to understand the secular evolution of the Early Jurassic carbon cycle, sporadic perturbations in the global carbon cycle must be distinguished from periodic fluctuations. Identification of periodicities in carbon-isotope records can further provide information about the pacing and durations of identified isotope excursions, add constraints to the geological timescale, and allow age-correlation to palaeoenvironmental and palaeoceanographic events, giving insights into possible driving mechanisms of the $\delta^{13}C_{TOC}$ record.

Cyclic changes in the Earth's axial and orbital parameters, comprising the axial precession (~20 kyr), axial obliquity (~40 kyr) and orbital eccentricity (~95-125 and 405 kyr), control the seasonal and latitudinal solar insolation and consequent fluctuations in the Earth's climate (Laskar 1993). These cyclic fluctuations, also often referred to as astronomical or Milankovitch cycles, can be recorded in the stratigraphic records of palaeoenvironmental geochemical proxies. Several sedimentary parameters are sensitive to astronomical forcing and associated climatic

changes, such as e.g. oxygen and carbon isotopes, magnetic susceptibility and $CaCO_3$ (Hinnov and Hilgen 2012). Although carbon-isotope records are not commonly used in cyclostratigraphic studies, orbital pacing of small-amplitude (0.1-2 ‰) fluctuations in the carbon-isotope record (both bulk carbonate and bulk organic matter) have been reported for numerous time intervals, e.g. the Miocene (Zachos *et al.* 2001, Ma *et al.* 2011), the Paleocene and Eocene (Zachos *et al.* 2001, Cramer *et al.* 2003, Lourens *et al.* 2005, Zachos *et al.* 2010), the Cretaceous (e.g. Sprovieri *et al.* 2006, Voigt *et al.* 2007, Giorgioni *et al.* 2012, Sprovieri *et al.* 2013) and the Early Jurassic (Hettangian to Sinemurian, e.g. Ruhl *et al.* 2009, Whiteside *et al.* 2010, Hüsing *et al.* 2014, Xu *et al.* 2017a). Furthermore, eccentricity amplitude modulations, with a ~9-Myr periodicity, have also been suggested for the Jurassic to Early Cretaceous carbon cycle based on analysis of carbon-isotope records (Martinez and Dera 2015). Although the above records originate from very different time periods with different climatic and palaeoceanographic conditions, and different environmental and depositional (sedimentary) settings (e.g. boreal and Tethyan realm, shallow - and deep-sea sediments), a short-term (~100-kyr) and long-term (~400-kyr) periodicity, corresponding to eccentricity orbital cycles, have been discovered in all of the archives. It is to be expected, therefore, that similar orbitally paced, small-amplitude $\delta^{13}C$ excursions are recorded in other time intervals and palaeogeographic locations. If not recorded in a consecutive order within a stratigraphically expanded and continuous record, these orbitally paced cyclic fluctuations in the $\delta^{13}C$ record can, however, potentially be misinterpreted as stand-alone events.

The Hettangian to Toarcian $\delta^{13}C_{TOC}$ record from the Llanbedr (Mochras Farm) borehole, hereafter simply referred to as Mochras core, exhibits carbon-isotope excursions (CIEs) of different magnitudes and stratigraphical extent (see Chapter 3 and Xu *et al.* 2018). Large-amplitude CIEs recorded in the Mochras record, appearing in the lower Hettangian, the Sinemurian-Pliensbachian boundary (this study), and the lower Toarcian (Xu *et al.* 2018), have been recorded in various sedimentary basins, and are thought to record the increased emission of isotopically light carbon, sourced from volcanic activity and/or biogenic and thermogenic methane (e.g. Hesselbo *et al.* 2000, Hesselbo *et al.* 2002, Svensen *et al.* 2007, Svensen *et al.* 2012, Ruhl *et al.* 2016). Carbon-isotope fluctuations of smaller magnitude (~0.5-2‰) appear as

consecutive small-amplitude excursions of comparable magnitude and stratigraphic thickness, well expressed through certain intervals of the Hettangian to Pliensbachian record. Some of these small-scale CIEs have previously been identified in various sedimentary basins (e.g. positive CIEs in the turneri, ibex and davoei ammonite zones, recorded in the Paris and Lusitanian Basin, Silva *et al.* 2011, Peti *et al.* 2017). Several other small-amplitude $\delta^{13}C_{TOC}$ excursions appear in the Lower Jurassic record of the Mochras core, which were so far unrevealed. All these excursions aggregated in a continuous record suggest a causal driving mechanism, such as orbital forcing.

This chapter investigates the potential role of eccentricity orbital forcing on the Early Jurassic Hettangian to Pliensbachian small-amplitude (~0.5-2‰) excursions in the $\delta^{13}C_{TOC}$ record of the Mochras core using spectral and time-series analysis. This work aims to improve the understanding of the nature and causal mechanisms and to use astrochronology to better constrain the Early Jurassic time scale.

4.2. Spectral and time-series analysis

The Hettangian to Pliensbachian $\delta^{13}C_{TOC}$ record presented in Chapter 3 has been used for the following spectral and time-series analysis. Data preparation and analysis for this chapter was performed using the R Package for Astrochronology, version 0.3.1 (Meyers 2014). The pre-*planorbis* beds (equivalent to the *tilmanni* Zone) and the *planorbis* Zone (24 m; 1906.7 to 1882 mbs, based on Page in Copestake and Johnson 2014) were excluded from the spectral analysis, due to their relative thinness, and possible stratigraphic gap associated with the inferred Triassic-Jurassic boundary (see Chapter 2, 3).

The spectral analysis requires data sets with equal sample spacing. In order to reduce artefacts such as aliasing during linear interpolation (manipulation of the data set to equal sample spacing) due to the considerable differences of the original sample spacing (see table 4.1), the $\delta^{13}C_{TOC}$ record has been divided into 3 segments ('iso' function): segment 1: 1882 to 1250 mbs, segment 2: 1260 to 900 and segment 3: 920 to 863.5mbs (see Figure 4.1, also see Figure A-1 in appendix for wavelet and MTM spectra on unsegmented dataset). Furthermore, the interval comprised by segment 3

was separated as the corresponding stratigraphical interval is marked by a 40-60% reduced sedimentation rate compared to the underlying Pliensbachian strata, as reported by the study of Ruhl *et al.* (2016). The individual segments overlap slightly to avoid artificial peaks at the end points during spectral analysis. Each segment has been manipulated to equal sample spacing using linear interpolation ('linterp' function, see Table 4.1).

Table 4.1: Stratigraphic intervals of individual data segments, number of samples and sample spacing of the original and manipulated datasets

	Depth Interval [mbs]	Stratigraphic thickness [m]	Original Number of Data Points	Average Sample Spacing [m]	Interpolated Sample Spacing [m]	Interpolated Number of Data Points
Segment 3	920-863.5	56.1	186	0.34	0.33	170
Segment 2	1260-900	360	680	0.54	0.52	673
Segment 1	1882-1250	632	493	1.36	1.4	452

The linear trend of each segment has been removed ('detrend' function) and in order to emphasize short periodicities corresponding to eccentricity cycles, long periodicities have been removed from each segment ('bandpass' filter function). To ensure that no bandwidth attributable to eccentricity cyclicity was removed, the band-pass width was selected based on previous studies on the uppermost Sinemurian to Pliensbachian of the Mochras core: The spectral analysis of elemental calcium concentrations (Ruhl *et al.* 2016), and the digitized gamma ray log (Hesselbo *et al.* 2013). Both studies identified dominant spectral peaks interpreted as eccentricity cycles. These peaks were identified between ca. 8–45.4 m and 32 m, respectively.

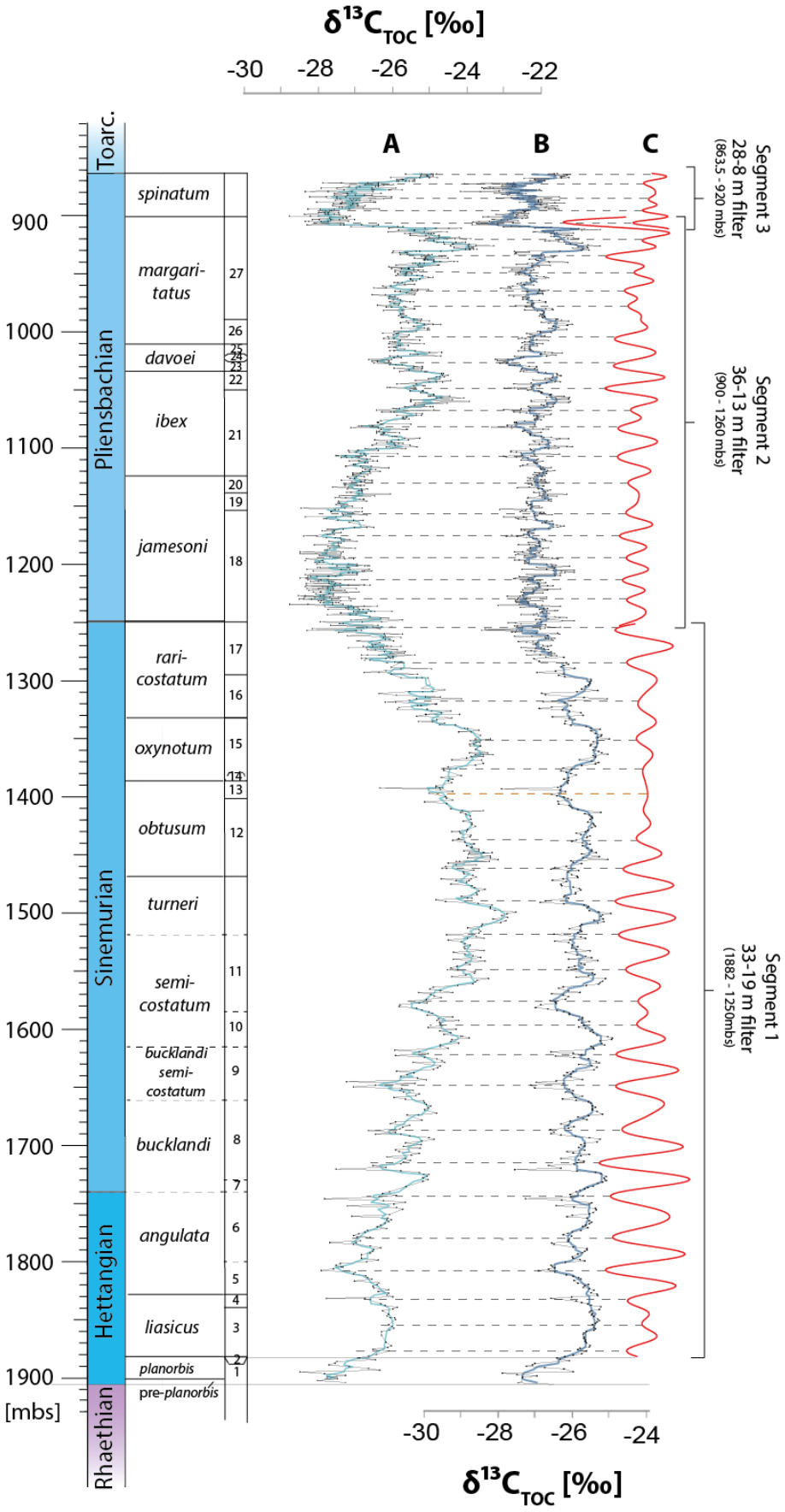
δ13CTOC [‰]
-30 -28 -26 -24 -22
A B C
Segment 3
28-8 m filter
(863.5 - 920 mbs)
Segment 2
36-13 m filter
(900 - 1260 mbs)
Segment 1
33-19 m filter
(1882 - 1250mbs)
Toarc.
Pliensbachian
Sinemurian
Hettangian
Rhaethian
spinatum
margari-tatus
davoei
ibex
jamesoni
rari-costatum
oxynotum
obtusum
turneri
semi-costatum
bucklandi semi-costatum
bucklandi
angulata
liasicus
planorbis
pre-planorbis
900
1000
1100
1200
1300
1400
1500
1600
1700
1800
1900
[mbs]
27
26
25
24
23
22
21
20
19
18
17
16
15
14
13
12
11
10
9
8
7
6
5
4
3
2
1
-30 -28 -26 -24
δ13CTOC [‰]

Figure 4.1: $\delta^{13}C_{TOC}$ record spanning the Hettangian to Pliensbachian stages **A**) original $\delta^{13}C_{TOC}$ record, **B**) detrended, high band-pass filtered and interpolated dataset. **C**) band-pass filter of dominant spectral peaks (2.6-19.4 m filter for segment 1, 35.5-13.3 m filter for segment 2, 14.1-8.4 m filter for segment 3) in the depth-domain. Grey dashed lines indicate cycles assigned based on dominant spectral peaks, orange dashed line indicates cycle assigned by visual interpretation. Key to ammonite subzone numbering given in Chapter 2, Figure 2.3.

For segments 2 and 3, which both correspond to the stratigraphical interval analyzed in the previous studies, periodicities above 50 m have been removed. In order to consider the possibility of a higher sedimentation rate, and hence thicker cycles in the Hettangian to upper Sinemurian strata, the low-frequency band-pass filter was set to 80 m on segment 1. Spectral analysis on individual segments was then performed using 3π multi-taper spectral analysis ('MTM' function) with robust red-noise model (Mann and Lees 1996). Dominant spectral components were filtered ('bandpass' function) and compared to the raw $\delta^{13}C_{TOC}$ record and edited (interpolated, detrended and long-band-pass filtered) dataset (see Figure 4.1).

In order to generate a relative (floating) timescale, individual cycles were defined based on the dominant spectral components (grey lines in Figure 4.1), and visual assignment in intervals where data gaps hampered clear peak identification (orange line in Figure 4.1, discussed further below). Each cycle was interpreted to correspond to a 405-kyr long eccentricity cycle, in conformance with the interpretation of dominant spectral peaks of comparable thickness in previous studies on the uppermost Sinemurian and Pliensbachian strata (corresponding to Segment 2 and 3, Hesselbo *et al.* 2013, Ruhl *et al.* 2016). The $\delta^{13}C_{TOC}$ record from Mochras was subsequently time-calibrated by allocating 405-kyr periodicities to each cycle, using the 'tune' function.

Dominant spectral peaks (see Figure 4.2) in the time calibrated (tuned) data series have been identified by multi-taper spectral analysis and the dominant 405-kyr and 1.4 Myr periodicities have been band-pass filtered ('bandpass' function, Figure 4.3, 4.4). Numerical ages were assigned to the Mochras tuned time series and band-passed cycles at the Triassic-Jurassic boundary, as this level can be confidently correlated to successions elsewhere where radioisotopically dated ash beds occur (radioisotopic constraints from: Schaltegger *et al.* 2008, Schoene *et al.* 2010, Guex *et al.* 2012,

Blackburn *et al.* 2013, Wotzlaw *et al.* 2014, Davies *et al.* 2017). As the pre-*planorbis* beds and the *planorbis* Zone were excluded from the spectral analysis due to the stratigraphically thin appearance and the possible incomplete nature of the pre-*planorbis* beds, the duration of this interval was inferred from cyclostratigraphic constraints of same age strata of the Bristol Channel Basin (St Audries Bay, Xu *et al*. 2018, details are further discussed below). In order to compare the Mochras record to astronomical solutions, the late Rhaetian to early Toarcian (202-183 Myr) interval has been isolated from the solutions proposed by Laskar *et al.* (2011) ('iso' function') and band-pass filtered to extract the 405-kyr cycles ('bandpass' function). The 405-kyr filtered records have been compared to the 405-kyr band-passed of the Mochras core (Figure 4.5).

4.3. Results

The MTM power spectrum estimates show dominant spectral peaks (>90% confidence) between 32.6 and 19.4 m for segment 1, 35.5 and 13.3 m for segment 2 and 14.1 and 8.4 m for segment 3 (>80% confidence) (Figure 4.1 and 4.2). The band-pass filter corresponding to these dominant spectral peaks mostly compares closely with the appearance of ~0.5-2 ‰ small-amplitude excursions of the $\delta^{13}C_{TOC}$ record (see Figure 4.1). The filtered spectral peaks appear comparably less pronounced and offset to the small-amplitude excursion in the upper *obtusum* Zone to lower *oxynotum* Zone (see red line in Figure 4.1). Furthermore, the dominant spectral peaks in segment 3 (uppermost *margaritatus* Zone and *spinatum* Zone) are only determined with an 80% significance level (see Figure 4.2).

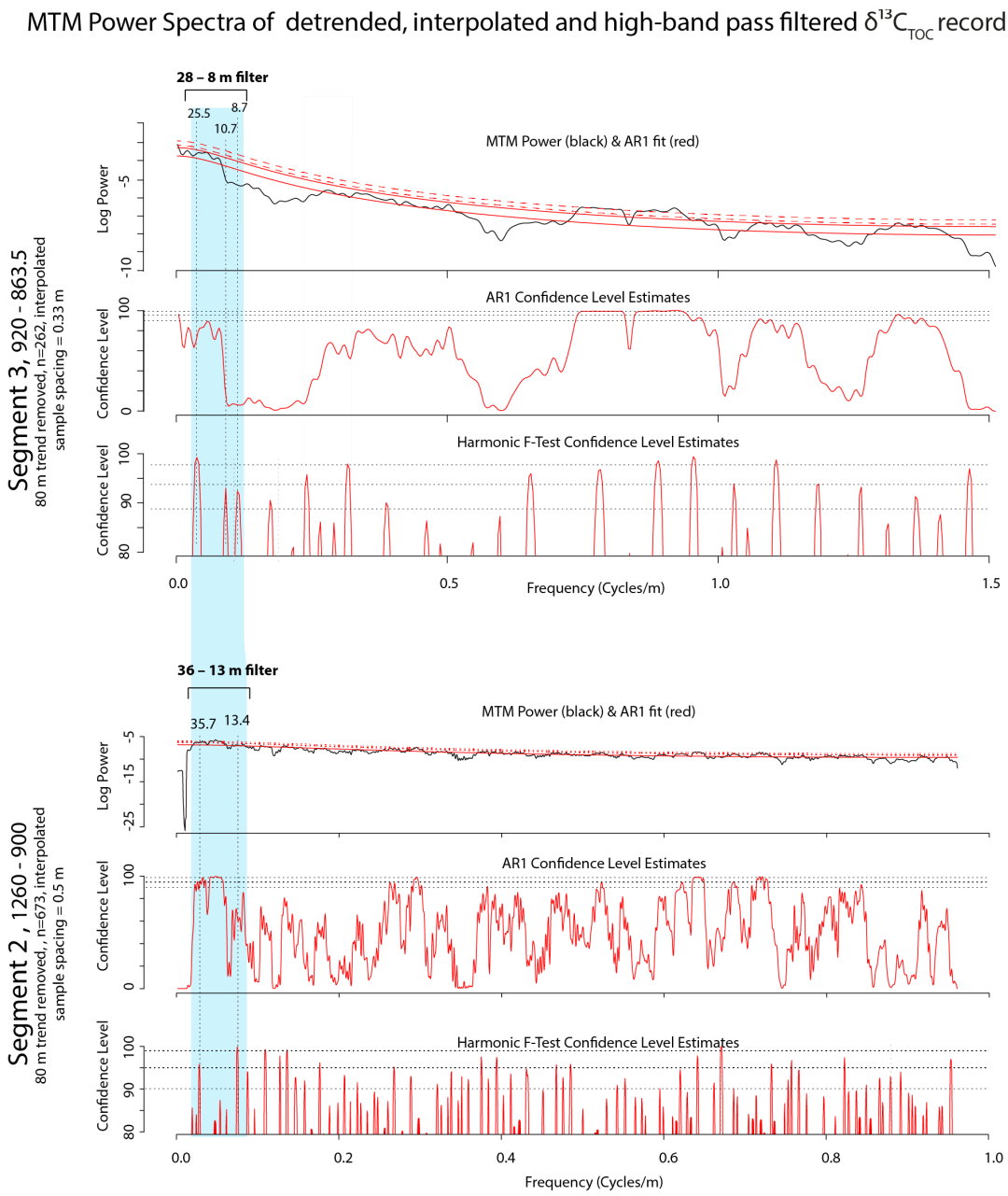

Figure 4.2: MTM power spectra of individual data segments and corresponding dominant spectral peaks

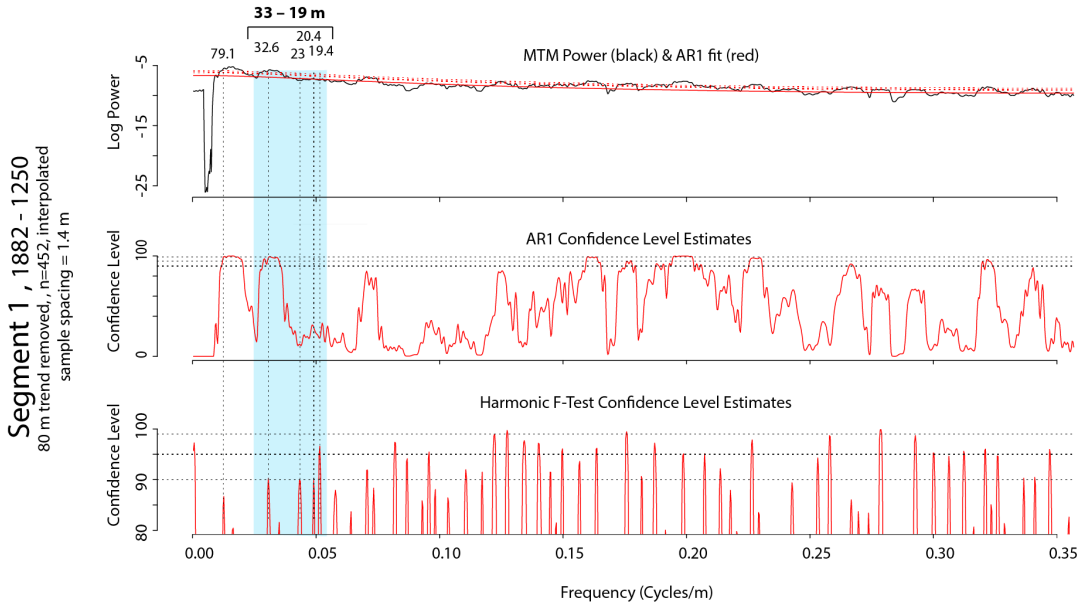

Figure 4.2 - continued: MTM power spectra of individual data segments and corresponding dominant spectral peaks

4.4. Discussion

4.4.1. Correlation of dominant spectral peaks and small-amplitude CIEs

The dominant spectral peaks determined in the upper Sinemurian to Pliensbachian $\delta^{13}C_{TOC}$ record of the Mochras core (segment 2: 36 to 13.5 m; segment 3: 8.4 to 14.1 m) are in close agreement with the bandwidth of dominant spectral peaks previously determined in the high band-pass filtered elemental calcium concentrations (segment 2: ~13.5 to 45.4 m and segment 3: ~6 to 40 m, Ruhl *et al.* 2016) and the digitized downhole gamma ray log (32 m, Hesselbo *et al.* 2013) within the same stratigraphic interval, supporting the statistical significance of the peaks determined in segment 2 and 3, despite the relatively low confidence level for the $\delta^{13}C_{TOC}$ record of the upper Pliensbachian (segment 3) alone. Both previous studies assigned the dominant frequencies to long eccentricity (405-kyr) Milankovitch cycles, and the interpretation has further been validated by correlation of the time-converted (tuned) record to radioisotopic age constraints (see Ruhl *et al.* 2016). The filtered dominant spectral peaks and corresponding small-amplitude isotope excursions in segment 2 and 3 of

the Mochras $\delta^{13}C_{TOC}$ record can therefore, with certainty, be interpreted to correspond to ~405-kyr orbital cycles.

This interpretation can be extrapolated to the dominant spectral peaks in the Hettangian to upper Sinemurian $\delta^{13}C_{TOC}$ record (segment 1) if a comparable sedimentation rate is assumed, as the frequencies are comparable to those of the above record. The determination of cycles corresponding to dominant spectral peaks in the upper part of segment 1 (upper *obtusum* Zone to *oxynotum* Zone) is complicated by mis-match of visually defined shifts in the $\delta^{13}C_{TOC}$ record, and dominant spectral peaks, which are expressed in a relatively low amplitude (see Figure 4.1). The low sample resolution in this interval, due to coring gaps of 2.8 to 4.3 m (between 1428-1425.1 mbs, 1416.4-1414.9 mbs and 1410.6- 1406.3 mbs, see core recovery plot in Chapter 2, Figure 2.3) impede the determination of a clear spectral peak within this stratigraphic interval. The upper *obtusum* Zone cycle has therefore been assigned visually (orange line in Figure 4.1). However, the low sample resolution and weakening amplitude of spectral peaks might have led to a misidentification (splitting/lumping) of cycles, in which case an uncertainty of at least 405-kyr is possible.

4.4.2. Towards an Early Jurassic floating time-scale

The time-converted (tuned) $\delta^{13}C_{TOC}$ record comprises a dominant spectral component at periodicity of ~405 kyrs, which, as expected, is consistent with the tuning parameter. The MTM power spectrum of the tuned data series shows further dominant peaks of >90% significance corresponding to 9.1, 2.6, 1.8, 1.4 and 0.9 Myrs (Figure 4.3). These periodicities likely correspond to amplitude modulations. The 405-kyr and 1.4 Myr cycles are the most prominent cycles, and are well expressed in the lower Hettangian and Pliensbachian strata (see Figure A-3 in Appendix). Periodicities corresponding to short eccentricity cycles (~ 100 kyrs) and obliquity cycles (~40 kyrs) also appear in the power spectrum of tuned $\delta^{13}C_{TOC}$ record with a significance of >90% (see Figure 4.3). Periodicities corresponding to precession cycles (20 kyrs) could not be detected in the record due to the sample resolution. Significant spectral peaks at 24 and 25 kyrs could potentially represent parts of the precession frequency

spectrum, although this needs to be tested and validated on a higher resolution data set.

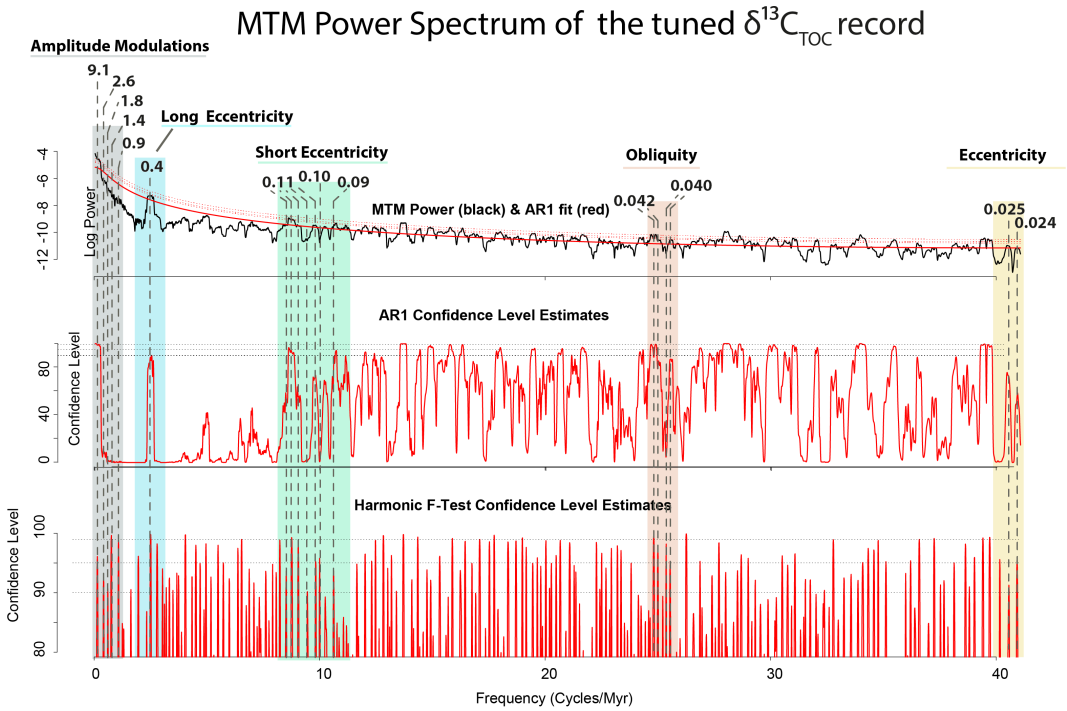

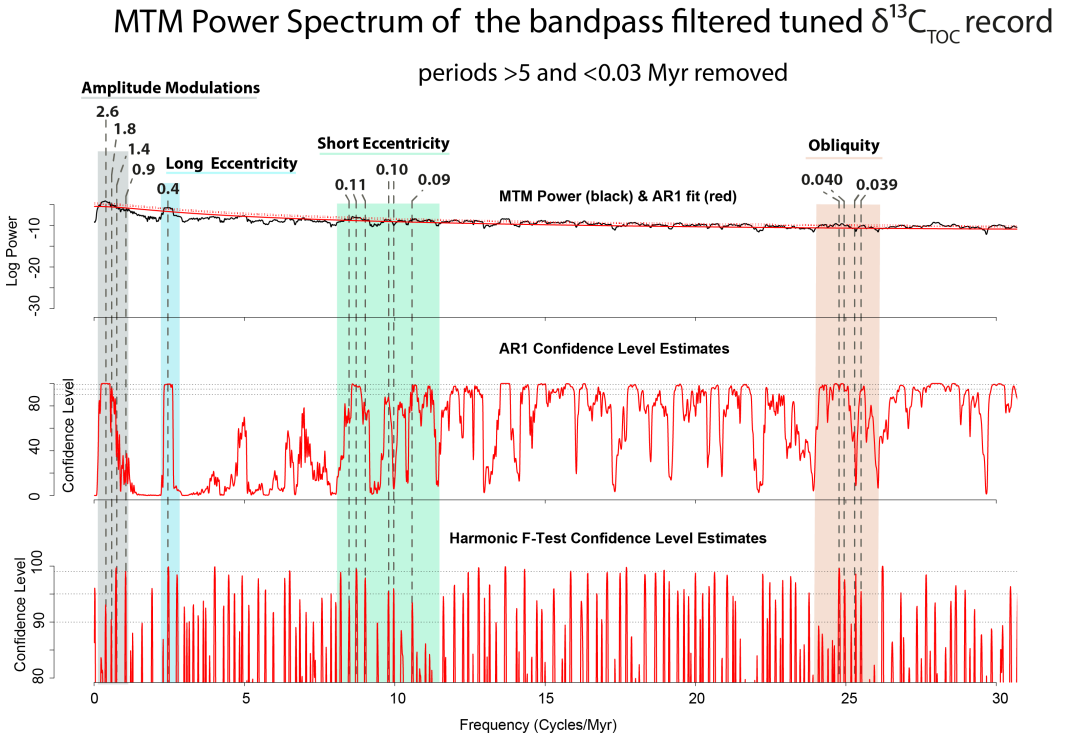

Figure 4.3: MTM power spectra of the tuned $\delta^{13}C_{TOC}$ record and the bandpassed $\delta^{13}C_{TOC}$ record (periodicities >5 and >0.03 Myrs removed). Dominant spectral peaks corresponding to Myr scale amplitude modulations (~1 Myr, 1.4 Myr, 2.6 Myr and 9.1, 2.6, 1.8, 1.4 and 1 Myr, gray), long eccentrixity (405 kyrs, blue), short eccentricity (~100 kyrs, green), obliquity (~40 kyrs, red) and possibly the spectral peaks corresponding to eccentricity orbital forcing (~20 kyrs, yellow) are marked in color.

The time-converted, 405-kyr tuned, $\delta^{13}C$ record provides a floating timescale allowing duration estimates for the biostratigraphical units and stages of the studied interval (see Table 4.2, Figure 4.4). The Lower Hettangian *planorbis* Zone and pre-*planorbis* beds (which were excluded from the analysis, see above) were assigned to a duration of 350 kyr, based on the astrochronological constraints of the same age strata of the Blue Lias Formation exposed in Somerset (St Audries Bay, Xu *et al.* 2017a).

Table 4.2: Duration estimates based on cyclostratigraphic constraints of Hettangian, Sinemurian and Pliensbachian biostratigraphical units and stages. Data from Ruhl *et al*. 2016, Xu *et al*. 2017 and this study. Radiometric ages from (Schaltegger *et al.* 2008, Schoene *et al.* 2010, Guex *et al.* 2012, Blackburn *et al.* 2013, Riccardi and Kamo 2014, Wotzlaw *et al.* 2014, Davies *et al.* 2017, Them *et al.* 2017b)

Stage/ Event	Ammonite Zone	Inferred absolute age at base (Myr) (this study)	Radiometric age constraints (Myr)	relative duration of biostratigraphical units and stages (Myr)		
				Mochras core: this study	Mochras core: Ruhl et al., 2016	St. Audrie's Bay: Xu et al., 2017
Toarcian	tenuicostatum	**183.10±0.57**	**~183.16±0.11**			
Pliensbachian	spinatum			1.4 **Σ 8.8**	1.4 **Σ 8.7**	
	margaritatus			2.8	2.4	
	davoei			0.4	0.4	
	ibex			1.8	1.8	
	jamesoni	**191.89±0.57**		2.4	2.7	
Sinemurian	raricostatum			1.2 **Σ 7.4±0.405**	**Σ 6.93 (+0.75/–0.65)**	
	oxynotum			0.8		
	obtusum			1.4 ±0.405		
	turneri			0.6		
	semicostatum			1.6		
	semicostatum/ bucklandi			1.7		
	bucklandi	**~199.29±0.17**	**199.43±0.10/ 199.53±0.19**	1.0		>1.1
Hettangian	angulata			1.2 **Σ 2.1**		0.8 **Σ 1.9**
	liasicus			0.52		0.7
	planorbis		**201.36±0.17**	0.35		0.35

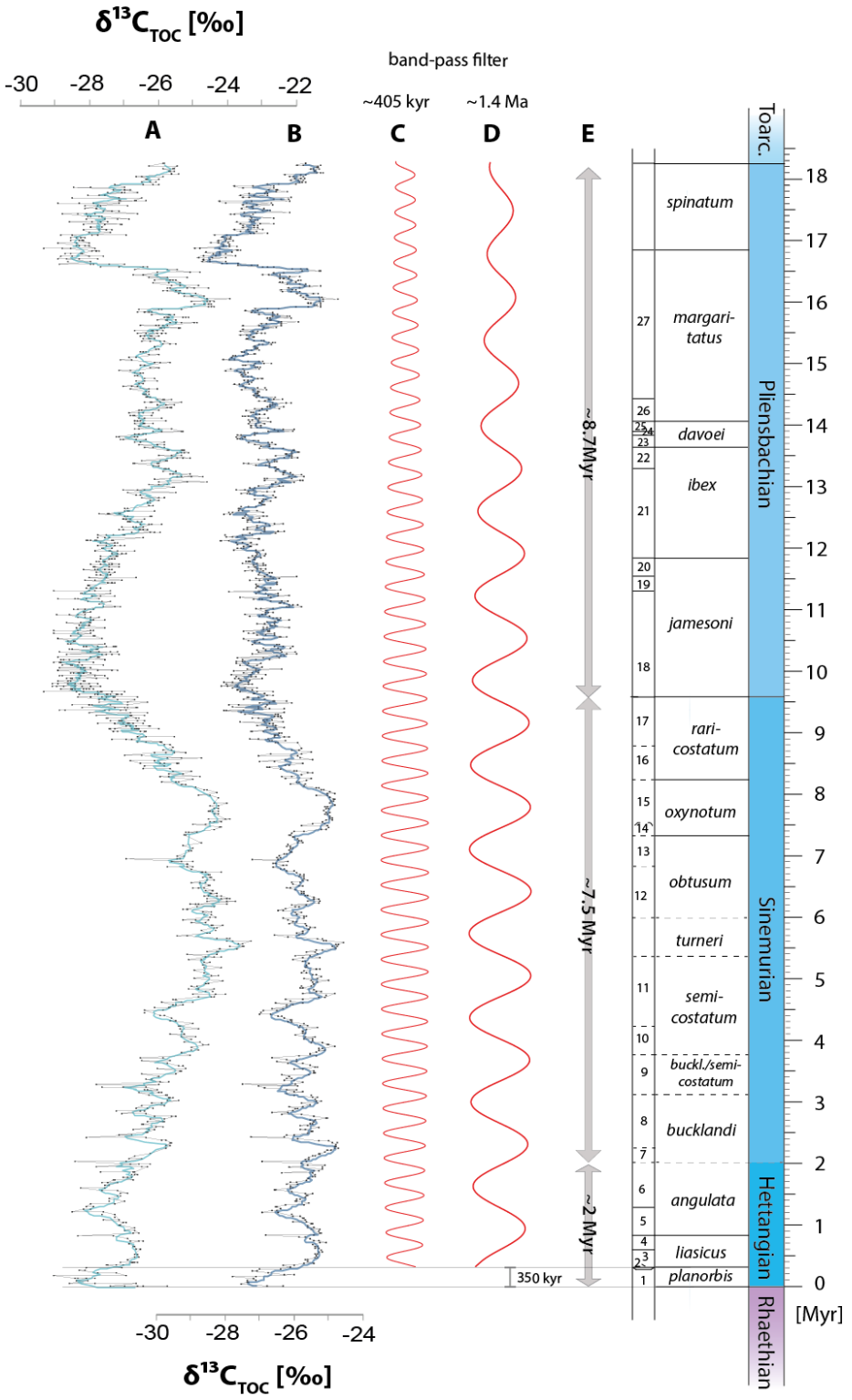

Figure 4.4: 405-kyr tuned $\delta^{13}C_{TOC}$ record. **A**) original dataset and **B**) detrended, interpolated and high-bandpass filtered dataset, compared to dominant spectral peaks: **C**) 405 kyr, **D**) 1.4 Myr. Duration estimates of individual stages marked as grey arrows (**E**). Key to ammonite subzone numbering given in Chapter 2, Figure 2.3.

The floating time scale slightly deviates from the duration estimated of the cyclostratigraphic interpretation from St Audries Bay for the Hettangian *liasicus* and *angulata* zones (~1.9 vs 2.1 Myrs) above the pre-*planorbis* beds and *planorbis* Zone (see Table 2, Xu *et al.* 2017a), likely due to the much lower sample resolution in the Mochras dataset, and subsequent inaccurate determination of individual cycles (~20 kyr resolution in Mochras vs. ~6 kyr resolution in St Audries Bay). For the Pliensbachian stage, the new Mochras $\delta^{13}C_{TOC}$ time series suggests the duration of 8.8 Myr for the Pliensbachian stage, and between 0.4 to 2.4 Myr for the individual ammonite zones (see Table 4.2). The duration estimates agree closely with the previous (higher resolution) astrochronological constraints based on the elemental calcium record of the Mochras core (Ruhl *et al.* 2016, see Table 4.2), as expected from the comparable tuning parameters used. The additional ~100 kyr in the estimated duration of the Pliensbachian stage within in this study compared to the study from Ruhl *et al*. (2016) likely results from the lower resolution of the $\delta^{13}C_{TOC}$ dataset (~60 to 30 cm in $\delta^{13}C_{TOC}$ dataset vs ~12 cm resolution in calcium concentrations dataset) and resulting inaccurate cycle determination. A comparison of both datasets and filtered dominant spectral peaks in the depth domain is shown in the Appendix (Figure A-2). However, the overall broad agreement between the timescale generated herein compared to the previous time scale studies validates the interpretation that small-amplitude isotope excursions represent 405-kyr eccentricity cycles, and allows extension of the time-scale to the Sinemurian stage.

The estimated duration of the Sinemurian Stage was previously based on assumed constant linear decrease in $^{87}Sr/^{86}Sr$ (~7.62 Myr^{-1}), determined cyclostratigraphically from the lower Pliensbachian in Dorset, UK (Weedon and Jenkyns 1999), and further revised from radioisotopic constraints on the Hettangian–Sinemurian and Pliensbachian–Toarcian boundary, combined with astronomical constraints on the duration of the Pliensbachian Stage (6.93 +0.75/−0.65 Ma, Ruhl *et al*. 2016). Here we provide the first direct astronomical timescale for the Sinemurian Stage and individual ammonite zones, proposing a total Stage duration of 7.4 Myr (see Table 4.2). The duration estimates of the individual ammonite zones are complicated by the currently poorly defined boundary between the *bucklandi* and *semicostatum* zones, which in Mochras are lumped as a '*bucklandi–semicostatum'* transition Zone (Page, in

Copestake and Johnson 2014). Further uncertainty is added through the visually defined cycle in the upper Sinemurian *obtusum* Zone. However, the total duration of the combined Hettangian, Sinemurian and Pliensbachian stages, based on the cyclostratigraphically calibrated floating time scale generated in this study is proposed to be 18.28±0.4 Myr.

4.4.3. Towards an Early Jurassic absolute Time-Scale:

The floating timescale, including the estimated duration for the pre-*planorbis* beds and *planorbis* Zone (see above), tied to the absolute age of the Triassic–Jurassic boundary at the base of the Mochras record facilitates further validation of the floating timescale as it allows the correlation to biostratigraphically calibrated radioisotopic ages corresponding to stratigraphically higher levels, and a comparison to the proposed astronomical solutions (Laskar *et al*. 2011; Figure 4.5).

Radioisotopic dates obtained from volcaniclastic material intercalated in a biostratigraphically calibrated sedimentary succession in the Pucara Basin (North Peru) date the Triassic–Jurassic boundary to 201.36±0.17 Myr (Wotzlaw *et al.* 2014, recalculated from Schoene 2010, Guex *et al*, 2012). A similar age was obtained for the biostratigraphically calibrated Triassic–Jurassic boundary in the New York Canyon, Nevada (201.22±0.13 Myr, Schoene *et al.* 2010). Astronomical constraints on the Newark/Hartford succession, however, infer a slightly older age of 201.42±0.02 Myr (Blackburn *et al.* 2013), and approximately ~201.48±0.01 Myr based on the astronomical constraints of the uppermost Triassic and lowermost Jurassic in the Bristol Channel Basin (St Audries Bay section, Xu *et al.* 2017a) when anchored to the precise age of the End-Triassic Mass Extinction (201.56±0.001, Davies *et al.* 2017). For this study, 201.36±0.17 Myr is used as the absolute age for the Triassic-Jurassic boundary (based on the calculations in Wotzlaw *et al*. 2014).

The age of the Hettangian–Sinemurian boundary given on the basis of the herein generated time-scale agrees (within uncertainties) with the radiometric age generated from the boundary at Pucara Basin section in N Peru (199.53±0.19/199.43±0.1 Myr, Schaltegger *et al.* 2008, Guex *et al.* 2012, Guex *et al.* 2012; Figure 4.5). The estimated age of the (upper mid) *margaritatus* Zone agrees with the radioisotopic (U-Pb) age

from the Pliensbachian (mid) *margaritatus* Zone in the Fernie Formation (East Tributary of Bighorn Creek, Alberta, Canada), dated to 185.49±0.17 Myr (Them *et al.* 2017b, see Figure 4.5). Furthermore, the absolute time scale generated herein is in approximate agreement with the Pliensbachian–Toarcian boundary age date from a volcanic ash layer at the biostratigraphically well defined Chacay Melehue Section, Neuquén Basin, Argentina (183.16±0.1 Myr, Riccardo and Kamo 2014). There, the dated volcanic ash bed lies stratigraphically close to the Pliensbachian-Toarcian boundary (~4.6 m above boundary defined by the first occurrence of *Dactylioceras (Eodactylites) simplex*), considering the boundary to be marginally older. In the Mochras core, the boundary is suggested to be dated 183.1 Myr and potentially younger than the numerical age indicates. However, incorporating the uncertainties regarding the floating time scale (see above) and the exact age of the Triassic–Jurassic boundary anchored age, the model fits the radiometric age constraints considerably well.

The anchored and filtered 405-kyr cycles of the tuned Mochras record further agree with the 405-kyr-filtered eccentricity orbital solution (La2010 a to d, Figure 4.5). However, due to the uncertainties in the radiometric and astrochronological constraints, the correlation, and especially the phase relationship between the periodic changes in $\delta^{13}C_{TOC}$ and the astronomical solutions, should be considered with caution. The floating time scale of the Mochras core is therefore not matched with a specific solution, nor anchored to the absolute timescale proposed by Laskar *et al*. (2011).

Figure 4.5: 405-kyr tuned $\delta^{13}C_{TOC}$ Mochras time series (**A**), original and detrended, interpolated and high-bandpassed $\delta^{13}C_{TOC}$ record (**B**), 405-kyr band-passed time series (**C**), all datasets anchored to the Triassic-Jurassic boundary (201.36±0.17), compared to the 405-kyr eccentricity series filtered from the astronomical solutions (**D**) (Laskar *et al*. 2011). Radiometric age constraints from: Schaltegger *et al*. (2008); Schoene *et al*. (2010), Guex *et al*. (2012); Blackburn *et al*. (2012); Wotzlaw *et al*. (2014), Riccardi and Kamo (2014), Them *et al*. (2017), Davis *et al*. (2017).

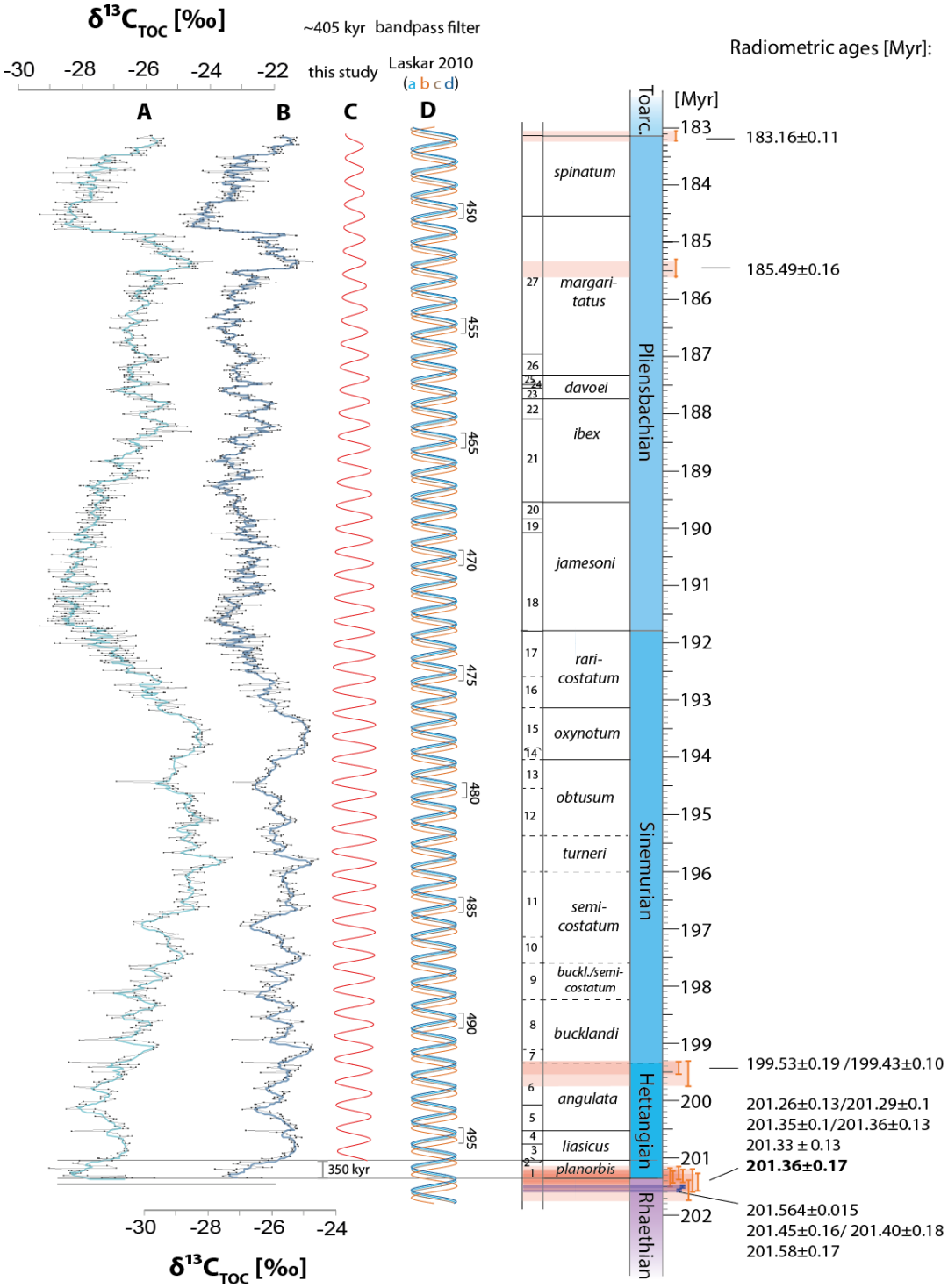
δ13CTOC [‰]
~405 kyr bandpass filter
this study
Laskar 2010
(a b c d)
A
B
C
D
350 kyr
δ13CTOC [‰]
Radiometric ages [Myr]:
[Myr]
Toarc.
Pliensbachian
Sinemurian
Hettangian
Rhaethian
spinatum
margari-tatus
davoei
ibex
jamesoni
rari-costatum
oxynotum
obtusum
turneri
semi-costatum
buckl./semi-costatum
bucklandi
angulata
liasicus
planorbis
183.16±0.11
185.49±0.16
199.53±0.19 /199.43±0.10
201.26±0.13/201.29±0.1
201.35±0.1/201.36±0.13
201.33 ± 0.13
201.36±0.17
201.564±0.015
201.45±0.16/ 201.40±0.18
201.58±0.17

Implications for the short-term Early Jurassic carbon-isotope perturbations

The predominant expression of eccentricity-paced changes in the carbon-isotope record, but, more importantly, also in other records of higher temporal resolution, is likely related to the long residence time (10^5 years) of inorganic carbon in the ocean (Cramer *et al.* 2003), as well as the stability of the 405-kyr long eccentricity cycle throughout the Phanerozoic (Laskar *et al.* 2004, Laskar *et al.* 2011, Westerhold *et al.* 2012). The palaeoenviromental and palaeoceanographic mechanisms, however, which link changes in the organic and inorganic marine carbon reservoirs and their isotopic compositions to eccentricity forcing, are still debated. A direct relation to changes in the Earth's climate is doubtful, because changes in the Earth's orbit result in minor changes in energy received per unit area (W/m^2) and may therefore have a negligible direct effect on the climate (Paillard 2010). However, eccentricity modulates the effect of precessional changes, affecting the intensity of seasonal contrasts (Paillard 2010).

The eccentricity modulated seasonal changes likely affect precipitation patterns, continental weathering rates, freshwater and nutrient input, and alkalinity of ocean basins. Consequently, marine productivity and terrestrial organic matter input, oxidation and preservation of organic matter, as well as precipitation and dissolution of inorganic carbon, and the build-up and release of carbon in continental wetlands and peats, are indirectly acting on eccentricity-paced timescales (e.g. Zachos *et al.* 2010, Ma *et al.* 2011). The orbital forcing in the $\delta^{13}C_{TOC}$ record can therefore reflect the distinctly different partitioning of carbon between oxidized (^{12}C depleted) and reduced (^{12}C enriched) carbon reservoirs during high- and low-eccentricity phases.

These cyclic environmental changes, induced by seasonal climatic variations, have different effects on individual carbon-isotope reservoirs. A global signal affecting the entire ocean-atmosphere carbon pool can be produced by e.g. orbitally paced build-up and subsequent subaerial release of wetlands and peats, as suggested by Zachos *et al*. (2010). A more local or regional change in the carbon-isotope record might occur when the effects restricted to the marine realm, as e.g. by changes in the $\delta^{13}C_{DIC}$ due to freshwater input or carbonate precipitation/dissolution. Isotopic changes of the bulk organic carbon reservoir alone can be induced by changes in the nutrient or terrestrial organic matter input, and changes in the oxygenation/preservation of organic matter,

as changes in the relative amount of individual organic matter constituents with distinctively different isotope signatures bias the bulk organic carbon-isotope record (e.g. Schouten *et al.* 2007, Sluijs and Dickens 2012, Suan *et al.* 2015). Changes in the bulk organic matter composition in the Lower Jurassic Mochras strata are identified and discussed in detail in Chapter 5.

The eccentricity paced isotope excursions in the $\delta^{13}C_{TOC}$ record of the Mochras core can therefore not, on their own, be interpreted as global isotope signals. In order to identify global carbon-cycle changes, isotopic changes should appear coeval in the marine (organic and inorganic) and terrestrial carbon reservoirs. The correlation between the $\delta^{13}C_{TOC}$ record and the low-resolution $\delta^{13}C_{carb}$ record (van de Schootbrugge *et al*. 2005, tuned to the herein developed timescale) reveals that only individual eccentricity paced small-amplitude CIEs in the Mochras $\delta^{13}C_{TOC}$ record appear coeval to CIEs in the $\delta^{13}C_{carb}$ (e.g. in the *semicostatum* and upper *obtusum*, lower *jamesoni* and *davoei* zones, see Figure 4.6). This observation is, however, extremely biased by the low sample resolution of the $\delta^{13}C_{carb}$ record. Some CIEs present in the $\delta^{13}C_{TOC}$ and $\delta^{13}C_{carb}$ record in Mochras were also recognized in the Hettangian to Pliensbachian record of other NW European basins and even global extent, i.e. the positive CIEs in the Sinemurian *turneri* Zone (Wessex basin and N America, Jenkyns and Weedon 2013, Porter *et al.* 2014, respectively), Pliensbachian *ibex* Zone (Basque Cantabrian Basin, Lusitanian Basin; Quesada *et al.* 2005, Rosales *et al.* 2006, Silva *et al.* 2011) and *davoei* Zone (Lusitanian Basin, Silva *et al.* 2011, Peti *et al.* 2017). The apparent coeval occurrence of some carbon-isotopic changes in organic and inorganic marine substrates over a regional extent suggest a wider impact than local changes in the Cardigan Bay Basin.

With the current lack of a diagenetically unaltered $\delta^{13}C_{carb}$ record equivalent in resolution and stratigraphic extent to the Mochras $\delta^{13}C_{TOC}$ record, it is, however, not evident if fluctuations in $\delta^{13}C_{carb}$ appear concomitant with every single 405-kyr paced shift in $\delta^{13}C_{TOC}$. Alternatively, CIEs in $\delta^{13}C_{carb}$ might correspond other periodicities (e.g. 1.4 Myr amplitude modulations), or appear sporadically.

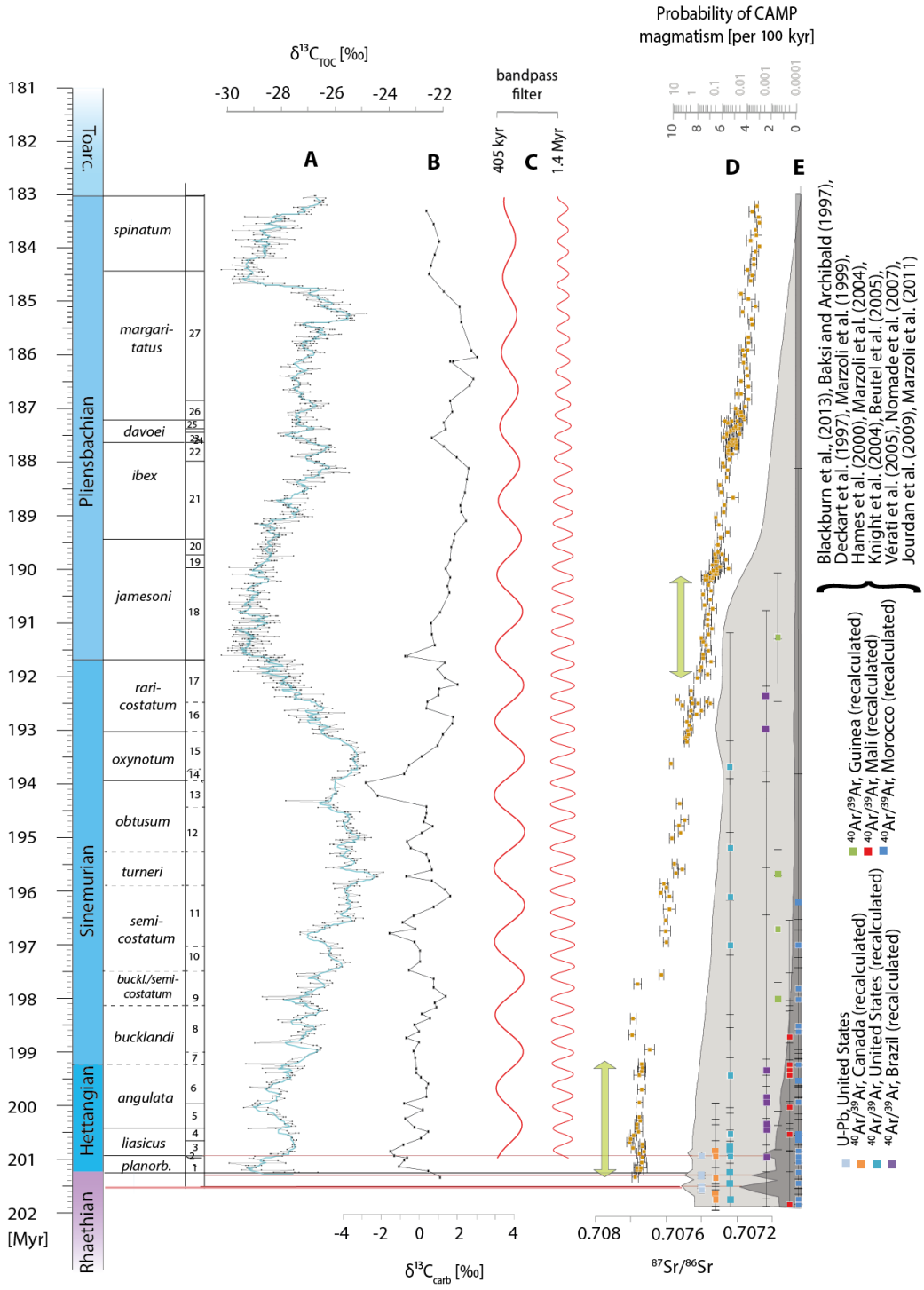

Figure 4.6: Tuned $\delta^{13}C_{TOC}$ record (**A**), relative to the absolute (numerical) Early Jurassic time-scale, correlated to the tuned $\delta^{13}C_{carb}$ record of the Mochras core (van de Schootbrugge *et al*. 2005) (**B**), 405 kyr and 1.4 Myr band-pass filter of the tuned $\delta^{13}C_{TOC}$ record of the Mochras core (**C**), sea-water strontium-isotope data (Jones *et al*. 1994, Jenkyns *et al*. 2002, data were normalized to a value of the NBS987 standard of 0.710250, with 24 $*10^{-6}$ added to the published data of Jones *et al*. 1994, which was normalized to a different standard). Green arrows indicate plateaus in the strontium-isotope curve, indicating a balance between radiogenic and radiogenic Strontium input (modified from Ruhl *et al*.

(2016) (**D**) and probability of magmatic activity (**E**). Dark grey area shows the cumulative probability of CAMP magmatism through time, following uncertainties on U–Pb ages and the recalculated $^{40}Ar/^{39}Ar$ radiometric dates of individual basalt formations, light gray area shows same data on log scale. Modified after Ruhl *et al*. 2016, references for radio-isotopic ages in figure.

4.4.4. Implications on the Long-term Early Jurassic (Hettangian–Pliensbachian) $\delta^{13}C_{TOC}$ perturbations

Very long-eccentricity (Myr-scale) amplitude modulations (sometimes also termed 'grand orbital cycles') have been proposed as driving mechanisms of long-term, large magnitude carbon fluxes in the Cenozoic and Mesozoic (Boulila *et al.* 2012, Martinez and Dera 2015). This may suggest long-scale and large magnitude CIEs, such as at the Sinemurian-Pliensbachian boundary, are potentially controlled by orbital parameters and processes. The Hettangian to Pliensbachian $\delta^{13}C_{TOC}$ time series of the Mochras core exhibits a marked spectral peak corresponding to a 9.1 Myr cycle (see Figure 4.3), similar to the proposed (considerably fluctuating) ~9 Myr cycle in the $\delta^{13}C_{carb}$ compilation for the Jurassic to Early Cretaceous (Martinez and Dera 2015). However, the total duration of the time series here presented (18.28 Myr) is too short to validate such a periodicity with sufficient certainty.

Leading hypotheses link the Hettangian negative CIE to increased emission of isotopically light carbon into the ocean-atmosphere system (e.g. Pálfy *et al.* 2001, Hesselbo *et al.* 2002). The relatively negative carbon-isotope values in the earliest Jurassic Hettangian stage associated with the 'main' CIE at the Triassic-Jurassic boundary, have been linked to the emission of isotopically light carbon from volcanic sources, and/or biogenic and thermogenic methane from continental shelf clathrates and organic-rich strata, following the flood basalt and dyke and sill emplacement of the main phase of CAMP (e.g. Pálfy *et al.* 2001, Hesselbo *et al.* 2002, Schoene *et al.* 2010, Whiteside *et al.* 2010, Blackburn *et al.* 2013, Davies *et al.* 2017). The Sinemurian-Pliensbachian boundary negative CIE was similarly suggested to coincide with a possible late second phase of CAMP magmatism (Ruhl *et al.* 2016). According to the new absolute timescale for the Hettangian to Pliensbachian based on the orbitally tuned $\delta^{13}C_{TOC}$ record from the Mochras core, the Sinemurian–Pliensbachian

boundary negative excursions correspond to phases of increased volcanic activity (see Figure 4.6).

4.4.5. Implications for the Upper Pliensbachian (upper margaritatus Zone and spinatum Zone) negative CIE

Volcanigenic CO_2 as source for the distinct negative carbon-isotope excursion in the upper *margaritatus* Zone appears unlikely. The CIE event post-dates the activity of CAMP (see Figure 4.6), and pre-dates initial intrusive phase of the Karoo-Ferrar Large Igneous Province (between 183.246±0.045 and 182.2 Myr; Svensen *et al.* 2007, Svensen *et al.* 2012, Sell *et al.* 2014, Burgess *et al.* 2015). Furthermore, the subaerial release of volcanically sourced isotopically light carbon as a source for the ^{13}C-depleted carbon is not evident in sedimentary elemental mercury data prior to the Pliensbachian–Toarcian boundary (Percival *et al.* 2015). However, submarine volcanism, such as increased mid ocean ridge spreading rates and/or the increase in the spatial extent of mid-ocean ridges are thought to emit significant amounts of CO_2 (Brune *et al.* 2017), without subaerial release of mercury.

The emission of large amounts of CO_2 would likely have led to an increase in atmospheric pCO_2, subsequently leading to global warming and increased weathering rates as observed at e.g. the Pliensbachian–Toarcian boundary (Percival *et al*. 2016). The seawater strontium-isotope composition of the late Pliensbachian, however, does not indicate a significant input of radiogenic Sr from the weathering of juvenile basalts, nor a distinct change to radiogenic values induced by increased continental weathering as it is seen concomitant with the Early Hettangian and Sinemurian–Pliensbachian boundary negative excursion events (see Figure 4.6). Conversely, the late Pliensbachian is likely associated with climatic cooling, linked to either preceding increased organic carbon burial and subsequent atmospheric cooling, leading to a stronger influence of cold and saline boreal waters (van de Schootbrugge *et al.* 2005), or regional lithospheric up-doming of the North Sea region obstructing a northward heat transport through the Viking corridor and subsequent overall cooling (e.g. Korte *et al.* 2015). The general decline in seawater temperatures during the upper *margaritatus* and *spinatum* Zone is supported by oxygen-isotope studies, fish tooth

apatite and the appearance of glendonites and dropstones (i.e. Price 1999, Bailey *et al.* 2003, Rosales *et al.* 2004, van de Schootbrugge *et al.* 2005, Dera *et al.* 2009b, Dera and Donnadieu 2012, Korte *et al.* 2015). Furthermore, increased aridity and decreased continental run-off in the Laurasian Seaway were inferred from low amounts of kaolinite (Dera *et al.* 2009b).

Mechanisms driving the negative carbon-isotope shift on a regional scale appear more likely due to the considerably variable regional expression of the carbon-isotope shifts in the upper *margaritatus* Zone and *spinatum* Zone. Although the organic and inorganic carbon isotope-records of the upper *margaritatus* and *spinatum* isotope event correlate in the overall shape, the magnitude of individual shifts varies significantly between different compounds and in different European basins (Harazim *et al.* 2013, Peti *et al.* 2017, see Figure 4.7). A change in the bulk organic-matter assemblage towards a larger relative amount of isotopically light carbon is, at least in Mochras, not contributing to the magnitude of the negative excursion (see Chapter 5). Alternatively, palaeoceanographic mechanisms, such as localized methane seepage, could potentially have led to local/regional differences in the magnitude of isotope shifts.

Large-scale methane seepage during the late Pliensbachian (*margaritatus* Zone and *spinatum* Zone) has previously been proposed, based on the widespread occurrence of authigenic seep carbonate formation (*Tisoa siphonalis* and glendonites) in southern and northern France, Luxemburg and Germany (and references therein, van de Schootbrugge *et al.* 2005, Teichert and Luppold 2013). A possible trigger mechanism inducing the dissociation of gas hydrates is the abrupt lowering of the sea level. The decreasing hydraulic pressure can decrease the thickness of the methane hydrate stability zone, leading to decomposition of gas hydrates in deeper sediments (Teichert *et al.* 2003, Kiel 2009). Indeed, a late Pliensbachian large amplitude sea-level changes are documented for the European realm (Haq *et al.* 1987, Hesselbo 2008, Haq 2017), and regression is witnessed by increased detrital sedimentation and erosion, widespread decrease in sedimentation rates, ironstone formation, and carbonate production crisis (e.g. Curtis and Spears 1968, Sellwood 1971, Haq *et al.* 1987, Partington *et al.* 1993, Blomeier and Reijmer 1999, Cobianchi and Picotti 2001, Mallarino *et al.* 2002, Léonide *et al.* 2007, Hesselbo 2008, Haq 2017). The anaerobic

oxidation of methane (coupled with sulfate reduction), indicated by the formation of seep carbonates, generally accounts as sink for methane in marine sediments. Different redox states in the sediment and bottom waters could account for local differences in the relative amount of methane seepage and carbonate formation. Diminished water circulation in the Tethyan realm due to the low sea-level and the emergence of landmasses, such as the Welsh massive to the south of the Cardigan Bay Basin may have led to locally different expression of the negative excursion. However, this is highly speculative and needs further investigation.

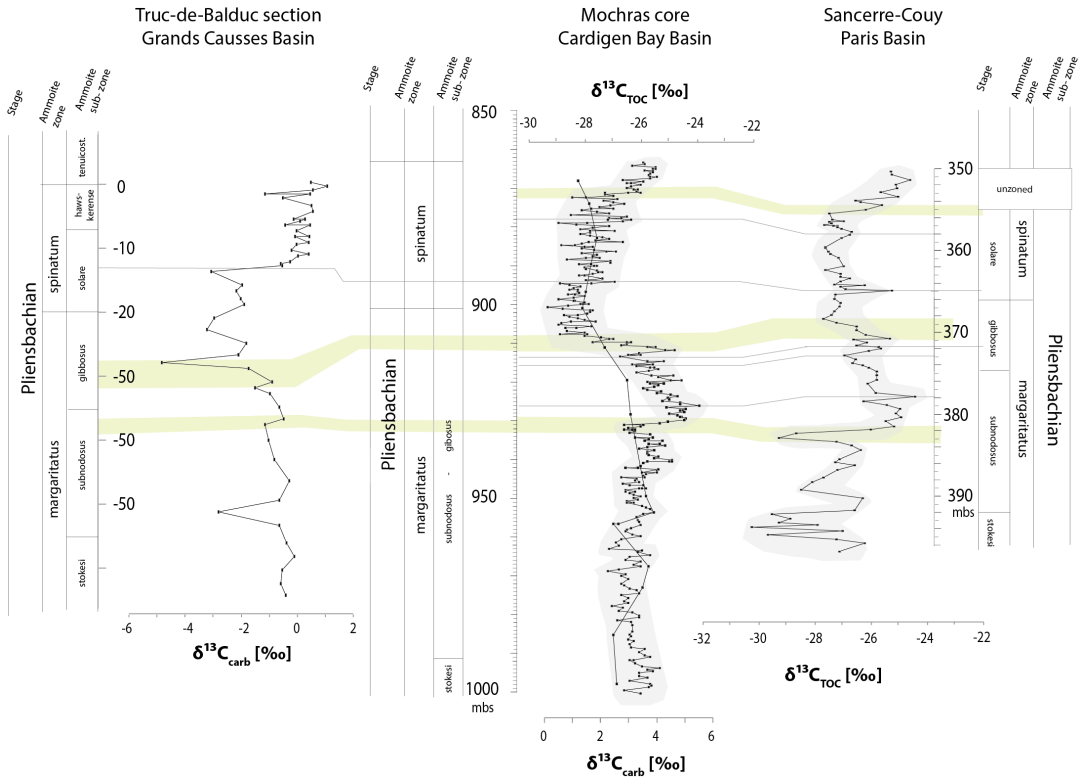

Figure 4.7: Upper Pliensbachian *margaritatus* and *spinatum* zones core $\delta^{13}C_{carb}$ data (Katz *et al*. 2005) and $\delta^{13}C_{TOC}$ record (this study) correlated to the $\delta^{13}C_{carb}$ Truc-de-Balduc section, Grands Causses Basin (Harazim *et al.* 2013) and $\delta^{13}C_{TOC}$ record of the Sancerre-Couy drill-core, Paris Basin (Peti *et al.* 2017).

Similar to the late Pliensbachian upper *margaritatus* Zone and *spinatum* Zone event, the negative excursion recognized at the Campanian–Maastrichtian boundary (Late Cretaceous) appears to be associated with cool climates and low sea-level (Jarvis *et al*. 2002, Linnert *et al*. 2014). For the Campanian–Maastrichtian boundary

event several causal mechanisms were suggested to have led to the negative carbon-isotope excursion: eustatic sea-level fall promoting lowland erosion and the recycling and oxidation of organic matter (Jarvis *et al*. 2002, 2006), changes in the deep-water formation leading to changes in the ratio between carbonate and organic carbon burial (Friedrich *et al*. 2009, Linnert *et al*. 2017), reduced rate of organic matter flux (Friedrich *et al*. 2009), and tectonic processes affecting oceanic bathymetry and shelf-sea size, and potentially the exchange of deep waters between oceanic basins (Voigt *et al*. 2012). A closer comparison between the Campanian–Maastrichtian boundary event (and other similar negative CIEs) and the Late Pliensbachian negative excursion and associated palaeoenvironmental conditions are needed to understand the wider relevance of such mechanisms in driving these sort of CIEs.

4.5. Conclusion

The ~18.28 Myr long orbitally-tuned carbon-isotope record of the Hettangian to Pliensbachian of the Mochras core provides the most expanded Early Jurassic astronomical timescale to date. Orbital tuning of dominant spectral peaks to long eccentricity cycles (405 kyr) provides a floating timescale which agrees roughly with previous timescales on the Hettangian and Pliensbachian, and provides the first astronomical time scale for the Sinemurian Stage and constituent biostratigraphical zones, suggesting a total duration of 7.4 Myr. The time scale, anchored to the Triassic-Jurassic boundary, further agrees with biostratigraphically calibrated radioisotopic ages for the Hettangian-Sinemurian boundary, the late Pliensbachian (mid-*margaritatus* Zone) and the Pliensbachian-Toarcian boundary.

According to the interpretation of dominant spectral peaks corresponding to long-eccentricity orbital cycles, the small-amplitude (~0.5-2‰) variations in the Mochras $\delta^{13}C_{TOC}$ record are largely paced by orbital forcing. Although several eccentricity paced isotope excursions occur in the multiple carbon-isotope reservoirs, and some with a regional spatial extent, it is not evident if eccentricity-paced fluctuations in $\delta^{13}C_{TOC}$ record of the Mochras core indicate changes in the global carbon cycle.

The herein established time-scale supports previous work, suggesting a temporal

link between the large-amplitude negative CIEs at the Sinemurian-Pliensbachian and volcanic activity.

The upper Pliensbachian upper *margaritatus* Zone and *spinatum* Zone negative CIE is associated with markedly different palaeoenvironmental conditions and changes compared to the preceding Hettangian and Sinemurian–Pliensbachian boundary events, suggesting different causal mechanisms underlying the isotope excursion, as i.e. large-scale methane seepage triggered by the Late Pliensbachian regression.

Chapter 5 : Characterization of the organic and inorganic sedimentary components of the Lower Jurassic Hettangian to Pliensbachian strata of the Llanbedr (Mochras farm) drill-core

5. Abstract

The characterization of the bulk organic matter in the Hettangian to Pliensbachian strata of the Mochras core reveals the sediments as immature to early mature, organic-lean and dominated by terrestrial organic matter. Changes in the relative abundance of isotopically light organic constituents appears to be a subordinate driving mechanism of long- and short-term bulk $\delta^{13}C_{TOC}$ carbon-isotope excursions. Notably, changes in the source of organic matter occur in some cases concomitantly with isotopic shifts that took place on astronomically/orbitally modulated (eccentricity) time scales, and along the Sinemurian-Pliensbachian boundary.

5.1. Introduction

Bulk organic carbon-isotope records ($\delta^{13}C_{TOC}$) of major perturbations in the carbon cycle, associated with climatic and palaeoceanographic events, are potentially biased by changes in the relative contribution of organic constituents. Differences in isotopic fractionation during carbon uptake by photosynthesis can cause differences in the specific carbon-isotope signature of marine and terrestrial organic matter. Variations in the relative abundance of marine versus terrestrial constituents in the sedimentary bulk organic matter can therefore lead to changes in the $\delta^{13}C_{TOC}$ record, independently of changes in the isotopic composition of the ocean–atmosphere carbon reservoir. Such changes can account for differences in the shape and magnitude of isotope excursions in $\delta^{13}C_{TOC}$ and $\delta^{13}C_{carb}$ records (e.g. Sluijs and Dickens 2012). The nature of bulk organic matter, and the relative proportions of its constituent macerals and biomolecules is, however, closely linked to palaeoenvironmental conditions, which may all change simultaneously, making it difficult to de-convolve the larger reservoir and ecological signals.

Previous work on the Toarcian Anoxic Event (T-OAE) and the Paleocene Eocene Thermal Maximum (PETM) have shown that the amplitude of negative CIEs in marine sediments can be considerably exaggerated by coeval changes in the source of

organic matter (Sluijs and Dickens 2012, Schootbrugge *et al.* 2013, Suan *et al.* 2015). In general, a 3 to 4 ‰ enrichment of ^{13}C in terrestrial organic matter (fossil wood) compared to algal-dominated sediment is recorded from Jurassic and Cretaceous sediments (Tyson 1995). The study of specific compounds and specific organic compounds from Toarcian sediments sampled from the same lithological horizon suggests a similar relationship (Hesselbo *et al.* 2000, Hesselbo *et al.* 2007, Al-Suwaidi *et al.* 2010, French *et al.* 2014) In order to identify the contribution of organic matter changes to the shape and magnitude of bulk organic carbon-isotope ($\delta^{13}C_{TOC}$) excursions, it is crucial, therefore, to investigate the composition of the bulk organic matter, and changes in the relative contribution of individual constituents.

The $\delta^{13}C_{TOC}$ record of the Hettangian to Pliensbachian strata of the Llanbedr (Mochras Farm) borehole, Cardigan Bay Basin, hereafter referred to as Mochras core, illustrates several long-term and orbitally paced carbon-isotope excursions (CIEs) in the bulk organic carbon-isotope record (see Chapters 3 and 4). Large-scale carbon-isotope changes appear concomitantly with sediments deposited coincidently with palaeoenvironmental and palaeoceanographic changes: e.g. the opening of the Hispanic corridor during the late Sinemurian, and climatic cooling in the late Pliensbachian (Porter *et al.* 2013, Korte *et al.* 2015). In this context, large-scale $\delta^{13}C_{TOC}$ excursions are potentially accompanied and, possibly, exaggerated by parallel changes in the source of organic matter. Small-amplitude eccentricity-paced excursions appear throughout the record, but it is not established whether these cyclic fluctuations were driven by changes in the source of organic matter, as a function of productivity and preservation, or represent changes in the overall isotopic compositions within the larger ocean-atmosphere reservoir. This chapter aims to characterize the changing composition of the bulk organic matter in the Hettangian to Pliensbachian strata of the Mochras core, and investigate the secular evolution of the $\delta^{13}C_{TOC}$ record on long- and short-term time scales. Additionally, the chapter makes a preliminary assessment of changes in non-organic detrital input through the Hettangian to Pliensbachian stages at Mochras and considers whether changes in organic matter sourcing may have affected the observed trends in organic matter composition and $\delta^{13}C_{TOC}$ values.

5.2. Material and Methods

- Coal fragments from 12 samples from the Upper Pliensbachian (956.2, 943.8, 929.4, 918.5, 916.2, 909.9, 907.7, 904.6, 988.05, 880.3, 873.6, 864.6 mbs) have been analyzed for $\delta^{13}C$. For analytical method see Chapter 1.4.2.
- A total of 714 powdered bulk-rock samples have been analyzed for total organic carbon content (TOC, wt%), Hydrogen Index (HI, mg HC/g TOC), Oxygen Index OI (mg CO_2/g TOC), T_{max} (°C) and Total Inorganic Carbon (TIC, wt%), obtained from Rock-Eval analysis. For details on the sample resolution see Chapter 1.3, Figure 1.2, for analytical method see Chapter 1.4.3.
- In order to identify and quantify individual organic and inorganic components in detail, petrographic maceral analysis has been performed on 16 samples (1747.2, 1758.6 , 1656.3 mb, 1392.9 , 963.2, 957.4, 941.9, 930.2, 920.9, 907.6, 906.2, 901.9, 884.7, 873.9 mbs). The analytical work was performed by Dr Olga Gorbanenko at the Department of Earth Sciences at the University of Oxford. For analytical method see Chapter 1.4.4. The interpretation of the qualitative and quantitative assessment was performed by myself.
- A total of 350 bulk-rock samples have been analyzed for quantitative elemental concentrations using a hand-held XRF scanner (InnovX). For analytical method see Chapter 1.4.5.
- A total of 8 samples from (1394.3, 1392.4, 940.6, 932.4, 909.5, 907.6, 900.8, 894.2 mbs) have been analyzed for quantitative evaluation of minerals (QUEMSCAN). For analytical method see Chapter 1.4.6.
- One bulk-rock sample, located at 902.6 mbs, was analyzed to assess the Paleozoic pollen content. For analytical method see Chapter 1.4.7.
- Data tables attached in digital appendix D-A-2.

5.3. Organic-matter characterization:

5.3.1. Rock Eval parameters

Average T_{max} values of 429°C and vitrinite reflectance of R_0= 0.38–0.63 (Holford *et al.* 2005) suggest an immature to early mature nature of the sedimentary organic matter in the Mochras core. The bulk-rock total organic carbon content (TOC) fluctuates between 0.1 and 3.3 wt% (Figure 5.1). The lowermost Hettangian negative CIE interval (pre-*planorbis* beds to lower *liasicus* Zone, 1906.7 to 1880 mbs) is marked by TOC contents of up to 3.3 wt%. The superjacent strata of the *liasicus* to mid-*turneri* zones (ca. 1880 to 1500 mbs) have generally rather low TOC, with average values of 0.75 wt%, concomitant with the gradual long-term increase in $\delta^{13}C_{TOC}$; and, in the mid-*turneri* Zone to upper *oxynotum* Zone (ca. 1500 to 1350 mbs), TOC runs at ~1 wt% on average in parallel with a slight decrease in $\delta^{13}C_{TOC}$. The low TOC is interrupted by stratigraphically limited intervals of relatively elevated TOC values (1.7 to 3.3 wt%), corresponding to small-amplitude negative shifts in the $\delta^{13}C_{TOC}$ record. The TOC increases gradually in the upper Sinemurian (mid-*oxynotum* to lowermost *jamesoni* zones), reaching up to ca. 2 wt%. The TOC tends to slightly lower values in the upper *ibex* Zone, increases in the lower *margaritatus* Zone with highest values corresponding with upper positive $\delta^{13}C_{TOC}$ shift in the upper *margaritiatus* Zone. Concomitantly with the sharp increase in $\delta^{13}C_{TOC}$ and the onset of the sharp negative CIE in the upper *margaritatus* Zone, TOC values decrease to values <1.4 wt%, and increase again towards the Pliensbachian–Toarcian boundary where they reach values of ~1%. Similar to the Hettangian and Sinemurian record, some individual maxima in TOC correlate with negative shifts in $\delta^{13}C_{TOC}$, as for example in the mid-*ibex* Zone and *davoei* Zone. On a smaller scale (<1 m), the TOC values fluctuate by up to 0.5 wt% in the Hettangian to upper Sinemurian, and by 1.5 wt% in the Pliensbachian. These cyclic small-scale fluctuations in the Pliensbachian strata have been linked to precession-paced lithological changes as a function of sediment dilution (Ruhl *et al.* 2016).

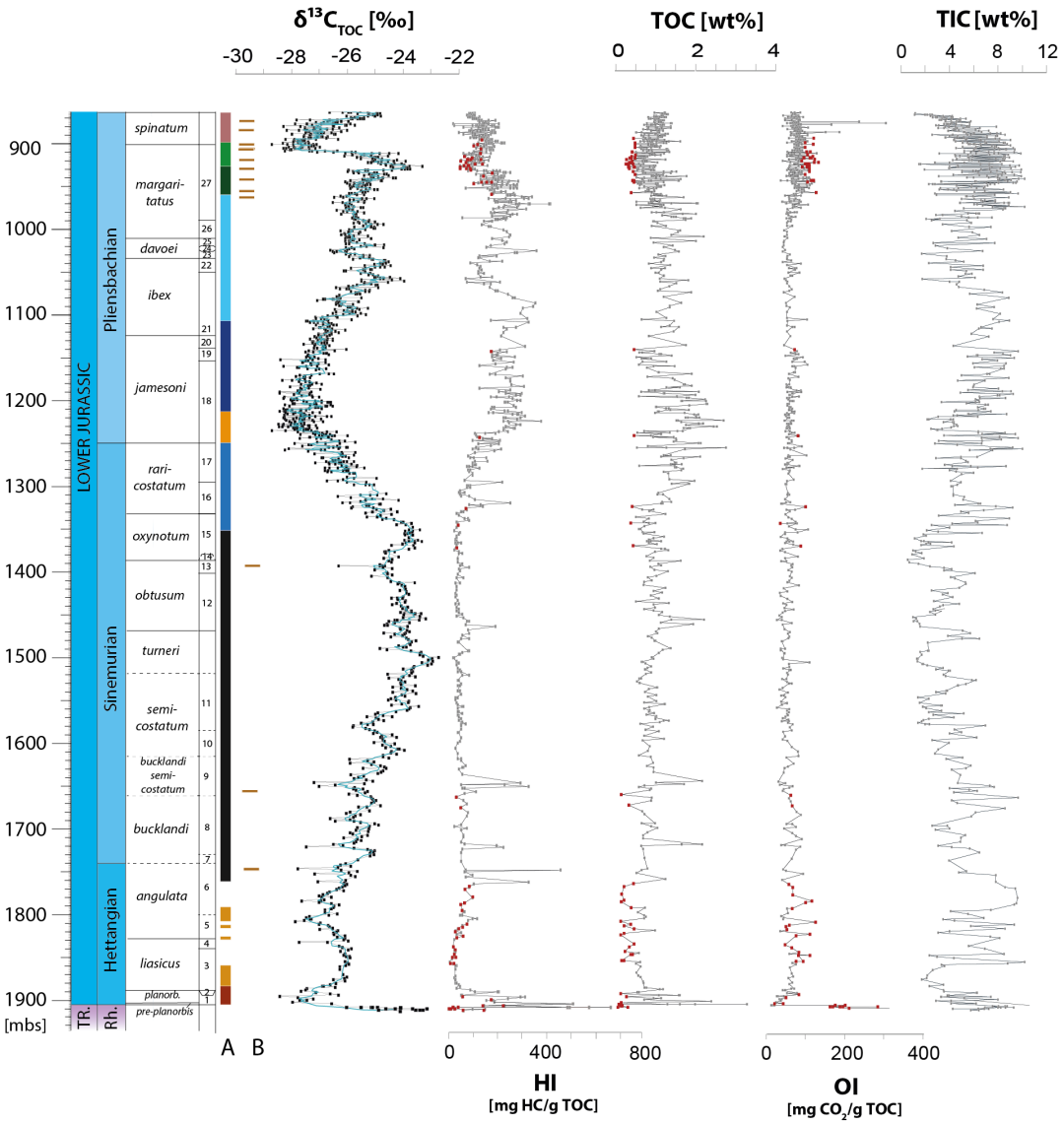

Figure 5.1: $\delta^{13}C_{TOC}$, Hydrogen Index, total organic-matter content and oxygen index of the uppermost Rhaetian to Pliensbachian stages. Samples with TOC values < 0.5 wt% and corresponding Hydrogen Index and Oxygen Index are marked in red. For ammonite subzone nomenclature, see Chapter 2, Figure 2.3. A) Stratigraphic position of samples plotted in Figure 5.6. For colour code too Figure 5.6. B) Orange bars in *angulata*, *bucklandi-semicostatum*, *obtusum*, *margaritatus* and *spinatum* zones indicate the stratigraphic position of organic and non-organic petrology samples.

The Total Inorganic Carbon content (TIC) are similarly variable in the Hettangian and Sinemurian, fluctuating between ~0 and 11 wt% (Figure 5.1). Due to the presence of both dolomite and calcite (discussed below, and see Appendix, FigureA–4), inorganic carbon content obtained by Rock-Eval Pyrolysis is not converted into

$CaCO_3$. However, calcium carbonate content calculated from mineral carbon (assuming that all mineral carbon was sourced from $CaCO_3$) and elemental calcium content obtained by hand-held XRF measurements show a good correlation (R^2=0.75) (see Appendix, Figure A-5), indicating a subordinate role of dolomite. Due to the highly variable TIC (see Figure 5.1), the TOC is evidently affected by fluctuating sediment dilution along the entire study interval. The TOC of the carbonate-free fraction (TOC_{cff}, calculated and validated through a comparison to Rock-Eval data from decarbonated samples, see Appendix, Figure A-6), shows less small-scale variability in the organic-carbon content, with values ~ 0.95 wt% higher on average.

The Hydrogen Index (HI, Figure 5.1) recorded in the Hettangian to Pliensbachian strata follows a similar pattern to the TOC. HI values of the uppermost Rhaetian strata are low (0–47 mg HC/g TOC), followed by a sharp increase (up to 660 mg HC/g TOC) in the pre-*planorbis* beds, corresponding to the onset of the lower Hettangian negative $\delta^{13}C_{TOC}$ excursion and elevated TOC values. HI values remain relatively elevated (200–300 mg HC/g TOC) in the *planorbis* and lower *liasicus* zones, in parallel with the main part of the negative CIE. The Hydrogen Index values are generally subdued in the stratigraphically higher Hettangian to upper Sinemurian section (1880 to 1350 mbs; ~80 mg HC/g TOC), a state interrupted by individual peaks reaching up to 420 mg HC/g TOC. The individual peaks correspond to high values in TOC and lowest negative values of individual small-amplitude $\delta^{13}C_{TOC}$ excursions. The HI values gradually increase through the *raricostatum* Zone in parallel with the negative limb of the Sinemurian–Pliensbachian boundary $\delta^{13}C_{TOC}$ excursion. The HI values reach up to 200 mg HC/g TOC at the Sinemurian–Pliensbachian boundary (1249 mbs), followed by an abrupt shift to higher HI values (~250 to 300 mg HC/g TOC), coincident with the most negative values of the Sinemurian–Pliensbachian boundary negative CIE in the lowermost *jamesoni* Zone. The HI values stay elevated throughout the *jamesoni* Zone to mid-*margaritatus* Zone, albeit fluctuating on a smaller (tens of metre) scale, with higher values corresponding to small-amplitude negative $\delta^{13}C_{TOC}$ CIEs in the mid-*ibex*, *davoei* and mid-*margaritatus* zones (up to 280 mg HC/g TOC), and intervals with lower values (100–180 mg HC/g TOC) corresponding to positive shifts in the $\delta^{13}C_{TOC}$ record (upper *jamesoni*, upper *ibex*, lower *margaritatus* zones). The overarching trend of HI values

in the mid-*margaritatus* Zone (968–929 mbs) decreases from 410 to 195 mg HC/g TOC at 930 mbs, followed by a sharp decrease to 81 at 929 mbs, coincident with the gradual positive CIE and abrupt increase in $\delta^{13}C_{TOC}$ values. The superjacent HI record slightly increases to ~105 mg HC/g TOC at 908 mbs, followed by a sharper increase to average values of 200 mg HC/g TOC up to 904 mbs, parallel with the very sharp negative shift in $\delta^{13}C_{TOC}$. The HI values fluctuate in the stratigraphically higher strata up to 977 mbs, with values between 80 and 220 mg HC/g TOC, and individual low HI values falling to 25 mg HC/g TOC. The uppermost *spinatum* Zone is characterized by generally falling HI values to a minimum of 74 mg HC/g TOC at the Pliensbachian–Toarcian boundary.

Some individual high Oxygen Index (OI, Figure 5.1) values appear in the uppermost Rhaetian (>160 mg CO_2/g TOC). The OI values are then generally low throughout the Hettangian, Sinemurian and lower Pliensbachian record (average <50 mg CO_2/g TOC). OI gradually increases in the *ibex* Zone, remaining slightly elevated (~ 80 mg CO_2/g TOC) throughout the upper Pliensbachian. A series of higher OI peaks (>100 mg CO_2/g TOC) appear in the *spinatum* Zone of the uppermost Pliensbachian.

5.3.2. Validity of Rock-Eval data

TOC values, Hydrogen Index, and Oxygen Index obtained by Rock Eval analysis from organic-lean samples (<0.5 wt% TOC) are considered to be unreliable (Tyson 1995) due to possible analytical uncertainties (no clear S_2, S_3 peak is generated). Hence, TOC, HI and OI values corresponding to samples with TOC <0.5 wt% are indicated in Figure 5.1 (red squares) and were excluded from the organo-facies interpretation.

A common factor artificially reducing TOC and Hydrogen Index is the matrix retention of hydrocarbons in the presence of clay minerals (mineral matrix effect; Espitalie *et al.* 1980). The mineral matrix effect is largest in organic-lean samples and those containing abundant clay minerals (especially illite) in the mineral matrix (Espitalie *et al.* 1980, Dahl *et al.* 2004). Based on lithological descriptions (see Chapter 2), higher amounts of clay minerals are likely to occur in the mudstones

present in the lower (Hettangian and lower Sinemurian) succession of the Mochras core. Quantitative assessment of the mineral content (see Appendix A-5) suggests a slightly higher amount of clay minerals illite (see Appendix A-5) in the darker mudstone lithology. This suggests a likely greater mineral matrix effect compared to the carbonate-rich samples of the upper Sinemurian and Pliensbachian. The low HI values in the lower part of the Mochras core, and the gradual increase in HI concomitantly with increasing TOC values, could therefore be a function of increasing TOC values gradually saturating the mineral matrix. The S_2–TOC plot (after Dahl *et al*. 2004) indicates, however, a minimal matrix effect (S_2 = ~0.5 mg HC/g rock retained) for the Hettangian to upper Sinemurian samples (see Apendix, Figure A-6). The mineral matrix effect is therefore unlikely to account for the low TOC values in the Hettangian to upper Sinemurian strata. Furthermore, the pyrolpysis of acid treated, decarbonated, samples, with TOC values up to 1% higher compared to bulk rock samples, yielded similar HI values (R^2=0.89, see Appendix A-5). The organic-lean and low HI character of the Mochras sediments is therefore a likely an inherent sediment characteristic, rather than being due to analytical bias.

5.3.3. Organo-facies

Hydrogen and Oxygen indices provide information about the source and source mixture of sedimentary organic matter, as marine organic matter is enriched in hydrogen compared to terrestrial organic components. Hydrogen indices between 0 and 200 are considered to represent organic matter sourced from hydrogen-poor land plants (Kerogen Type III), and HI values of about 400 to 600 corresponding to well-preserved planktonic organic matter (Kerogen Type II) (Tissot and Welte 1978). HI values between 200 and 400 are interpreted to correspond to mixed sources (Tissot and Welte 1978). According to this classification, the lowermost Hettangian is marked by the occurrence of very hydrogen-rich organic matter (green squares, Figure 5.2). The persistent low HI in the superjacent Hettangian to upper Sinemurian strata suggest a dominant contribution of hydrogen-poor land-sourced organic matter to the bulk organic carbon, and can be classified as Type III kerogen (dark blue squares, Figure 5.2). The relative amount of marine hydrogen-rich organic compounds in the

bulk organic matter increases through the upper Sinemurian. The Pliensbachian organic matter comprises a mixed Type II/Type III kerogen type (light blue squares, Figure 5.2).

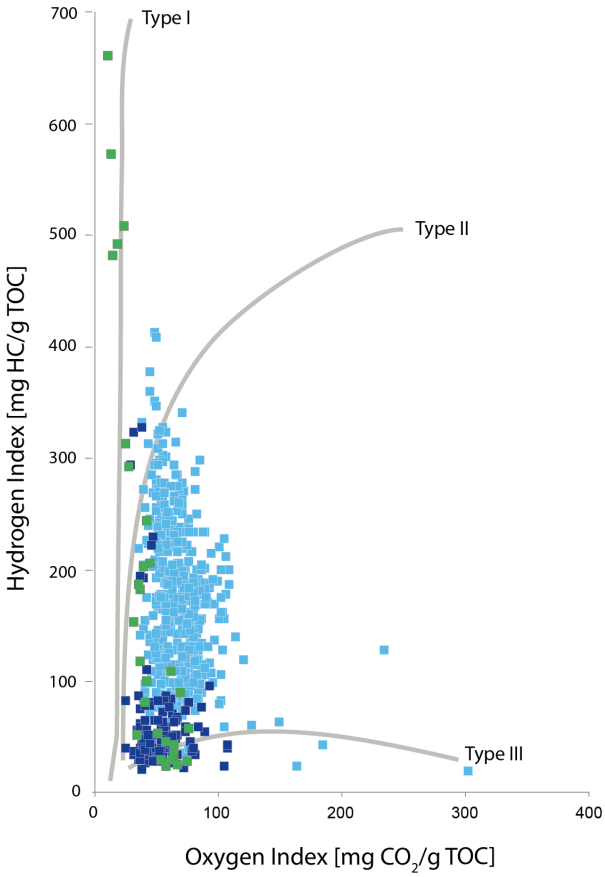

Figure 5.2: Modified van Krevelen diagram. Lowermost Hettangian pre-*planorbis* beds and *planorbis* Zone (1906.7–1887 mbs, green squares) shows mainly Type II and Type I organic matter. Hettangian to upper Sinemurian strata (1887– 1350 mbs, dark blue squares) is characterized by Type III organic matter with individual peaks comprising Type II organic matter. Upper Sinemurian and Pliensbachian strata (1350–863.5 mbs, pale blue squares) have a mixed Type II and Type III composition.

Another process affecting the Hydrogen Index, that is unrelated to the source of organic matter, is the biochemical (bacterial) degradation of organic matter (Demaison and Moore 1980). In a well-oxygenated water column, the oxidation of organic matter by aerobic bacteria is a very efficient and fast acting process, taking place while dead

organic matter descends through the water column before it is deposited. The oxidation results in lipid- and hydrogen-poor organic residues, and, consequently, Hydrogen Indices of the oxidized organic matter are not indicative of the primary source. The anaerobic degradation of organic matter is thermodynamically less efficient, resulting in organic residues that preserve the primary lipids and hydrogen composition (Claypool and Kaplan, 1994 and references therein), and additionally comprises the remains of the hydrogen-rich bacterial biomass itself (Lijmbach 1975). The low HI values in the Hettangian to upper Sinemurian strata might therefore be a result of organic matter degradation due to relatively well-oxidized water conditions, whereby the Pliensbachian organic mater represents better preserved organic residues due to the deposition under low oxygen conditions. In order to investigate the impact of organic matter degradation on the Mochras sediments, further investigations on the the preservation and oxidation state of the organic matter, e.g. by detailed maceral or biomarker analysis, are needed.

In order to identify and quantify individual organic components in detail, petrographic maceral analysis has been performed on 16 samples, of which two are from the upper Hettangian (upper *angulata* Zone, 1747.2 and 1758.6 mbs), 2 from the Sinemurian (*bucklandi* and *semicostatum* transition Zone and upper *obtusum* Zone), and 12 samples from the upper Pliensbachian (*margaritatus* and *spinatum* zones, stratigraphic position of samples marked in Figure 5.1). Maceral analysis was performed by Dr Olga Gorbanenko by point-count method based on 1000 individual determinations per sample (polished blocks). The nomenclature of Taylor *et al*. (1998) was used for the macerals of the vitrinite and inertinite groups, and that of Hutton (1987) for the liptinite group macerals (data table see digital Appendix D-A-2). The results were normalized to the total organic carbon content (vol.%) of each sample to compare the relative abundance of each component (Figure 5.3, and 5.4).

The dominant fraction of the organic facies of the Hettangian and Sinemurian samples are macerals of the liptinite group, comprising between 71.7 and 96.7 vol.%. liptodetrinite, derived from degraded liptinitic maceral remains, is the predominant maceral of the liptinite group (see Figure 5.3, and 5.4).

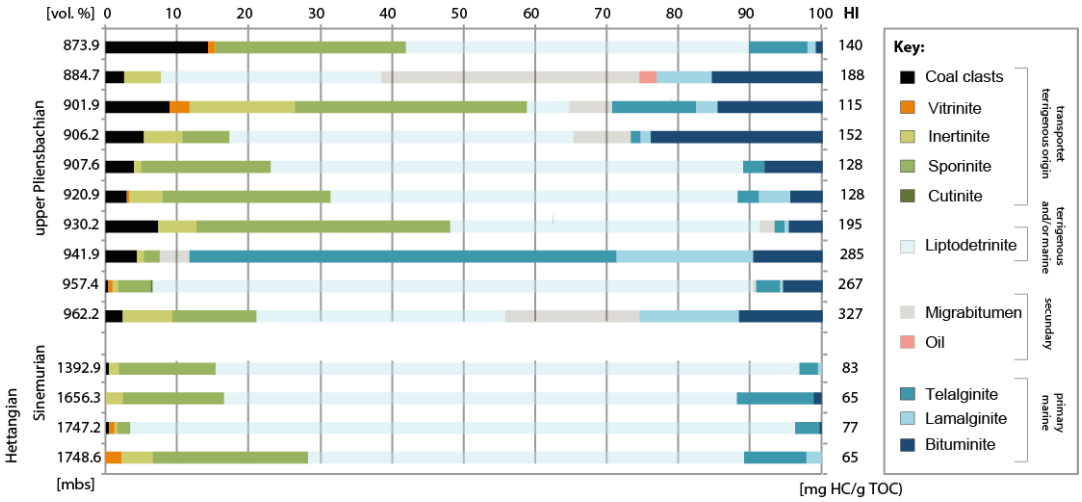

Figure 5.3: Maceral composition and Hydrogen Index of the studied samples from the Hettangian and Sinemurian, and Upper Pliensbachian of the Mochras core, normalized to total organic matter (vol.%).

The formation of liptodetrinite is likely associated with high oxygen availability and increased circulation of the water masses (Gorbanenko and Ligouis 2015). The bacterial degradation of liptinite and subsequent formation of liptodetrinite within a well-oxygenated water column is a likely mechanism to explain the low HI values as comprised by the four samples analyzed (HI between 65 and 83 mg HC/g TOC, see Figure 5.3). Alternatively, a contribution of terrestrial liptinitic precursors, such as sporinite and cutinite derived from the outer wall of spores and pollen, as well as leaves and stems (Tyson 1988) could account for the low HI vales of the studies samples. Liptinite macerals of marine origin (3.1 to 10.9 %) are predominantly represented by telalginite and small amounts of lamalginite. Both macerals are derived from algae and are grouped as alginate (Tyson 1998). Bituminite, also known as amorphous organic matter (AOM), the product of bacterial decomposition of algae and faunal plankton (Teichmüller 1989) under quiet and anoxic conditions (Gorbanenko and Ligouis 2015), only appears in trace amounts. Macerals of evident terrigenous origin are predominantly represented by sporinite (3.3 and 28.3 vol.%, see Figure 5.4). Only minute amounts of cutinite (see Figure 5.3 and 5.4), vitrinites (an alteration product of lignin and cellulose), coal fragments, and inertinite (degraded vitrinites) appear (see figure 5.3, 5.4). No secondary organic products such as migrabitumen or oil are present.

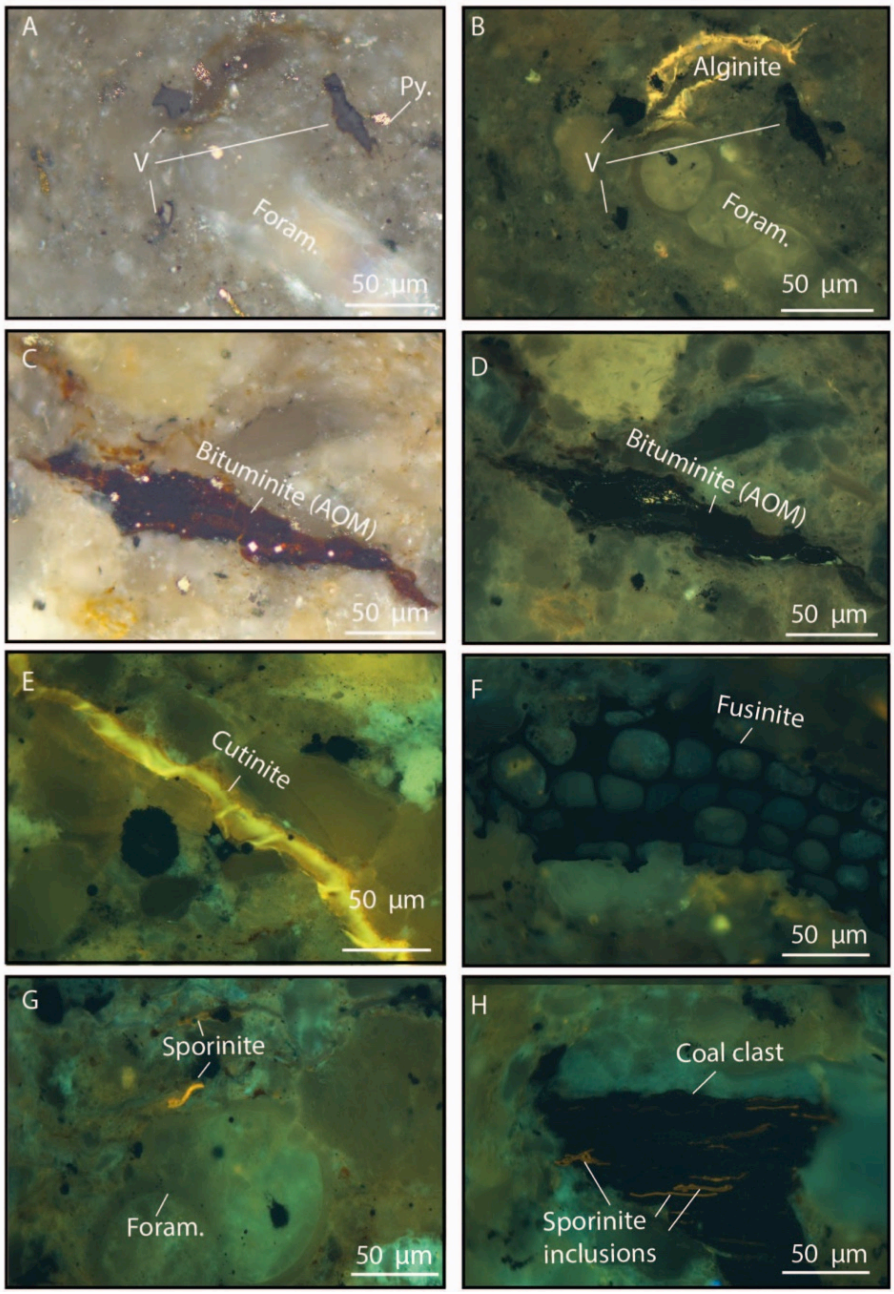

Figure 5.4: Photomicrographs showing the organic facies of petrographically analyzed samples. **A:** reflected white light photomicrographs of sample 1748.6, showing vitrinite macerals (V) and zooclast (foraminifera) **B:** same view in fluorescence mode, oil emersion, showing degraded alginate and internal structure of foraminifera. Typical microfacies of the Hettangian and Sinemurian samples. **C:** Bituminite (Amorphous organic matter, AOM) in reflected white light, sample 973.9 mbs **D:** same view in fluorescence mode, oil emersion **E:** Cutinite in fluorescence mode, oil emersion (sample 901.9 mbs) **F:** well preserved intertinite (fusinite) fluorescence mode, oil emersion (sample 962.2 mbs) **G:** sporinite in typical microfacies for the Upper Pliensbachian strata, fluorescence mode, oil emersion **H:** coal fragment with sporinite inclusions, typical for the Pliensbachian organo-facies.

The upper Pliensbachian samples comprise a larger variety of different macerals of the liptinite, vitrinite and inertinite group, and the relative organic composition of the samples is more variable (see Figure 5.3). Similar to the Hettangian and Sinemurian samples, liptodetrinite is the predominant liptinite maceral (30.8 to 83.7 vol.%), and the main organic component, with exception of sample 901.9 mbs (5.9 vol.%), and, especially, 941.9 mbs, which does not contain any liptodetrinite. Liptinites of certain marine origin (alginate and Bituminite) comprise 6.7 to 29.4 vol.% of the total organic matter (see Figure 5.3 and 5.4). Unlike the Hettangian and Sinemurian samples, bituminite is present in quantities between 1 and 24 vol.%, and represents the predominant marine organic component in most of the samples. Alginite accounts for 2 to 14.7 vol.% of the organic matter. However, sample 941.9 mbs comprises 78.7 vol.% alginate, and is the only sample with a predominantly primary marine organic-matter assemblage. The generally higher relative amount of marine organic matter in the Pliensbachian samples suggests that the liptodetrinite could be derived from a relatively large amount of marine liptinite macerals compared to the Hettangian and Sinemurian samples. However, variable amounts of terrestrial and marine precursors are supported by the poor correlation between marine and terrestrial organic matter and Hydrogen Indices of the corresponding sample (see Appendix, Figure A-7).

Terrestrial organic matter comprises 2.4 to 44 vol.% of the upper Pliensbachian total organic-matter assemblage. Sporinite (2.1 to 35.3 vol.%) is the dominant terrigenous organic component in most of the samples, but is absent in sample 884.1 mbs. The relative amounts of coal fragments and inertinite macerals in Pliensbachian samples are variable (0.3 to 14.3 vol.% and 0.7 to 14.7 vol.% of the total organic matter, respectively), but generally higher compared to Hettangian and Sinemurian samples. Based on the visual core descriptions (Woodland 1971 and this study), the quantity of macroscopic wood/coal fragments increases significantly at ~929 mbs compared to the lower strata. Vitrinite occurs in small amounts only (indigenous and recycled, 0.5 to 2.9 vol.%). Sporinite appears to be derived solely from terrestrial spores, as no pollen grains were found in the analyzed samples. However, previous palynological studies on the Mochras core have identified pollen in the microfossil assemblage (see van de Schootbrugge *et al.* 2005). Secondary macerals, migrabitumen and oil, sourced from cracking, deasphalting and

biodegradation of organic matter, are present in varying amounts (0.1 to 35 vol.%, see Figure 5.3).

The identification of trends in the relative abundance of marine versus terrestrial organic matter based on the maceral identification is largely hampered by the large amount of liptodetrinite in the organo-facies, which can be the product of marine and/or terrestrial liptinite macerals. The generally low Hydrogen indices and TOC values of the Hettangian to Sinemurian sediments may be the result of either bacterial degradation of marine liptinite in a well-oxygenated water column, or derive from terrestrially dominated sedimentary organic matter. The presence of Liptodetrinite and absence of Bituminite in the Hettangian and Sinemurian samples, however, implies well-oxygenated conditions in the water column above the sediment (Gorbanenko and Ligouis 2015), supporting a marine origin of the Liptodetrinite precursor. The Pliensbachian samples, which are characterized by slightly lower amounts of Liptodetrinites but higher amounts of Bituminite, suggest lower-oxygen environments and therefore better conditions for organic matter preservation. Due to the better preservation of lipids and hydrogen bonds in Pliensbachian strata, HI values and changes in HI are more likely to represent changes in the source of organic matter rather than being linked to changes in the oxidation state of the preserved organic matter.

5.3.4. Characterization of the coal fragments

The coal fragments present in the analyzed samples were distinguished from charcoal by their dark appearance in fluorescent light and the well-preserved sporinite inclusions (see Figure 5.4, 5.5). Palynological analysis of a single bulk-rock sample located at 902.6 mbs (lowermost *spinatum* Zone) indicates the presence of reworked spores (Densopsores, Figure 5.5), suggesting Paleozoic reworking. However, it is not evident if these spores were liberated from the coal inclusions during oxidation, or if the spores were derived from the bulk-rock sediment.

Component specific carbon-isotope analyses of coal fragments ($\delta^{13}C_{coal}$) from the upper Pliensbachian (upper *margaritatus* to *spinatum* zones) comprise values between −23 and −24.5‰ (Figure 5.5). The isotope signature is following the overall evolution

of the bulk organic isotope record, although the broad positive and subsequent negative excursion appears with a much smaller (~1‰) magnitude.

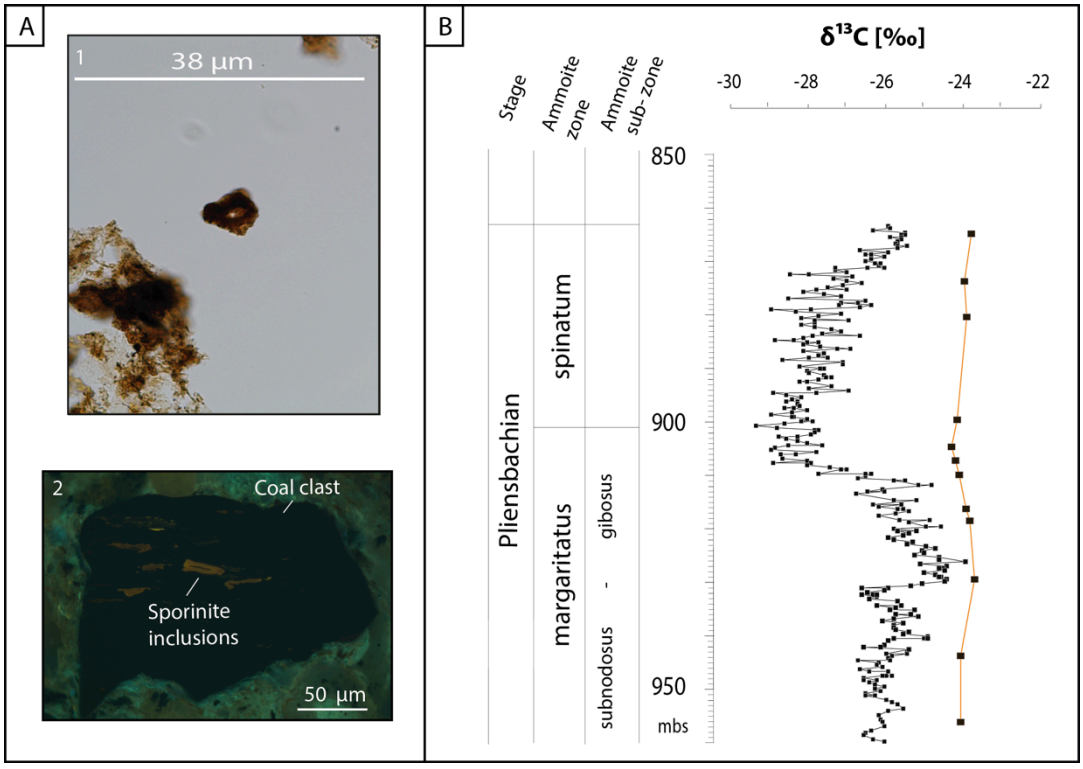

Figure 5.5: **A:** photomicrographs of a Densospore (1, sample 902.4 mbs) and coal clast with well preserved sporinite inclusions (2, sample 906.2 mbs). **B:** $\delta^{13}C_{TOC}$ and $\delta^{13}C_{coal}$ record of the Upper Pliensbachian

5.4. Effect of compositional changes of the organic matter on the $\delta^{13}C_{TOC}$ signature

A negative linear relationship between Hydrogen indices indicative of the approximate source and source mixture of organic matter and component-specific isotope values can be used to determine the influence of organic matter changes on the $\delta^{13}C_{TOC}$ record (e.g.Tyson 1995, Sælen *et al.* 2000, Sluijs and Dickens 2012, Schootbrugge *et al.* 2013, Suan *et al.* 2015). Isotopic variations corresponding to

compositional changes of bulk organic matter will plot on, or close to a mixing line defined by the $\delta^{13}C_{TOC}$ and HI values for the marine and terrestrial end-members.

HI values are well constrained for sediments dominated by either terrestrial or marine organic matter (see section 5.3.3). Because isotope values of marine or terrestrial organic matter show change over geological time the isotope signatures of marine and terrestrial end-members need to be individually determined for the studied intervals. Toarcian sediments outside of the isotopically disturbed interval corresponding to the T-OAE indicate an offset of 3 to 4 ‰ between marine and terrestrial organic matter, with absolute values between −22 and −26 ‰ corresponding to fossil wood and phytoclasts, and between −29 to −30 ‰ for marine organic matter components (Hesselbo *et al.* 2000, Hesselbo *et al.* 2007, Al-Suwaidi *et al.* 2010, Hesselbo and Pieńkowski 2011, Suan *et al.* 2015). The slope of the negative linear HI–$\delta^{13}C_{TOC}$ correlation comprises –0.001 to –0.1 for Toarcian data compilations from the European Epicontinental Seaway (Yorkshire, Denkingen, Dotternhausen), Argentina and Siberia (Sælen *et al.* 2000, Frimmel *et al.* 2004, Al-Suwaidi *et al.* 2010, Suan *et al.* 2011, Suan *et al.* 2015), and –0.005 to –0.1 for the data compilation of Jurassic and Cretaceous isotope values and corresponding kerogen type (grey bar in Figure 5.6 A–D, Tyson *et al*. 1995, p. 413).

In order to calibrate the HI–$\delta^{13}C_{TOC}$ background linear relationship for Lower Jurassic organic matter, it is important to identify an environmentally undisturbed interval, since changes in e.g. the aforementioned water column oxygenation, but also atmospheric pCO_2 and possibly water availability might lead to non-linear changes in the isotope-fractionation of marine and terrestrial organic matter as seen at present-day (Feng and Epstein 1995, Kürschner *et al.* 1996, Popp *et al.* 1998, Kohn 2010, Schubert and Jahren 2012, Kohn 2016). In the Hettangian to Pliensbachian strata of the Mochras core, the determination of a background signal is complicated by isotope excursions occurring throughout the record. However, the lower *ibex*, *davoei* and lower *margaritatus* ammonite zones most likely represents an interval not being affected by a large perturbation in $\delta^{13}C_{TOC}$. The small-scale isotope excursions recorded in this interval in the Mochras core, and other locations (see Chapter 3), appear to be largely driven by orbital eccentricity pacing (see Chapter 4).

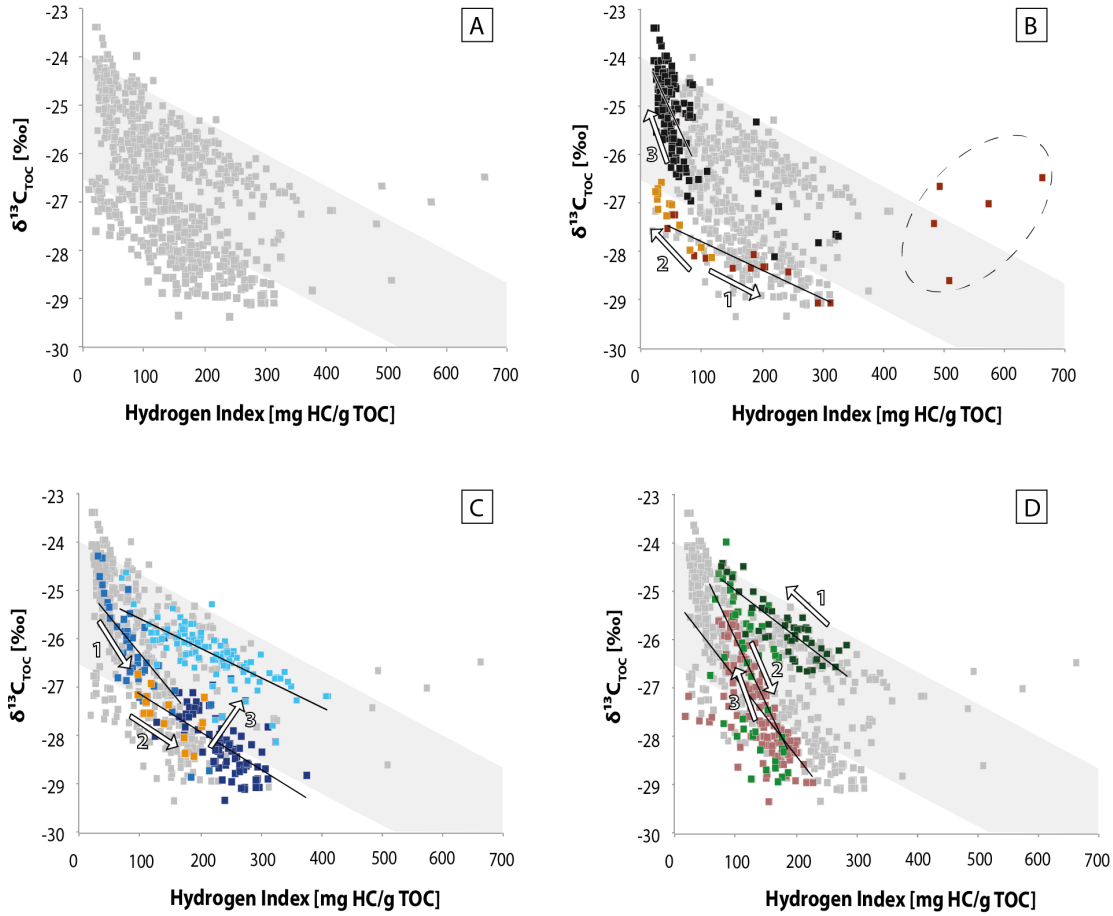

Figure 5.6: HI–$\delta^{13}C_{TOC}$ plots. The grey band shows the relationship between $\delta^{13}C_{TOC}$ and Hydrogen Index recorded in Jurassic and Cretaceous sediments (after Tyson, 1995). The stratigraphic positions of paired HI–$\delta^{13}C_{TOC}$ data plotted here are shown in Figure 5.1. and Figure 5.11. **A:** composite dataset of the Hettangian to Pliensbachian **B:** red squares: lowermost Hettangian negative CIE (pre-*planorbis* beds to lower *liasicus* Zone, 1906.5 to 1886.3 mbs, y = −0.0059×−27.19, R^2 = 0.84, excluding outliers); orange squares: Lower Hettangian positive CIE (lower *liasicus* to lower *angulata* zones, 1180.5 to 1794.2 mbs); black squares: mid-Hettangian to upper Sinemurian gradual positive $\delta^{13}C_{TOC}$ shift (lower *angulata* to mid-*oxynotum* zones, 1760.3 to 1350.5 mbs, −0.26×−23.73, R^2 = 0.32 (excluding outlier of HI>200)); grey squares: composite dataset **C:** blue squares: onset of the upper Sinemurian to lower Pliensbachian negative CIE (upper *oxynotum* to uppermost *raricostatum* zones, 1350.5 to 1235.2, y = −0.015 × −24.77, R^2 = 0.57); orange squares: peak negative CIE (uppermost *raricostatum* to lower *jamesoni* zones, 1235.2 to 1206.9 mbs); dark blue: gradual recovery (lower *jamesoni* to lowermost *ibex* zones, 1206.9 to 1100 mbs, y = −0.0077 x −26.36, R^2 = 0.51 (trendline includes peak negative excursion); light blue: lower Pliensbachian (lowermost *ibex* Zone to mid-*margaritatus* Zone, 1106.9 to 960.4 mbs, y = −0.0063 × −24.91, R^2 = 0.58) **D:** dark green squares: upper Pliensbachian positive CIE (mid- to upper *margaritatus Zone* positive CIE, 960,4 to 927.5 mbs, y = −0.0097 × −23.99, R^2 = 0.68), upper Pliensbachian (uppermost *margaritatus* Zone negative CIE, 927.5 to 900.7 mbs) (light green, y = −0.026 × −23.27, R^2 = 0.0.39), upper Pliensbachian (*spinatum* Zone, 900.7 to 863.6 mbs) gradual recovery (red, y = −0.016 × −25.14, R^2 = 0.44).

These cyclic changes of the carbon-isotope record can be considered as background fluctuations, as they evidently occur throughout the entire record. The interval is therefore considered to represent undisturbed background values. The *ibex* Zone and *davoei* Zone paired HI–$\delta^{13}C_{TOC}$ data plot along a trend line comprising a slope of −0.006 (see light blue squares, Figure 5.6 C), and fall within the background range suggested by previous studies.

The HI–$\delta^{13}C_{TOC}$ plot of the composite Mochras dataset (Figure 5.6 A) indicates two main trends, one of which comprises paired HI–$\delta^{13}C_{TOC}$ data plotting along the suggested background values, and the second group plotting on a steeper slope. The latter might representing changes in the isotopic composition, either unrelated or little related to relative changes in type of organic matter, or representing a gradual change to a different type of (terrestrial) organic matter with different fractionation properties. The following text discusses the development of paired HI–$\delta^{13}C_{TOC}$ data within individual long-term isotope trends to assess the impact of organic-matter changes.

5.4.1. Long-term and large-magnitude $\delta^{13}C_{TOC}$ trends

The paired HI–$\delta^{13}C_{TOC}$ data corresponding to the lower Hettangian negative CIE in the pre-*planorbis* beds to lower *liasicus* Zone (red squares, Figure 5.6 B, trend marked by white arrow 1) and lower *liasicus* to lower *angulata* Zone positive $\delta^{13}C_{TOC}$ excursion (orange squares, Figure 5.6 B, trend marked by white arrow 2) plot along a trend-line with a similar slope as suggested for terrestrial-marine end-member values, albeit with overall ~2‰ lighter isotope background values. Both isotope excursions might therefore be a function of changes in the relative amount of marine and terrestrial organic matter. The HI outliers in the pre-*planorbis* beds, corresponding to values of 482 mg HC/g TOC and above (circled red squares, Figure 5.6 B), comprise isotope values higher than suggested for marine organic matter of such HI composition, and are not included in the trend-line calculation.

The Hettangian (lower *liasicus* Zone) to upper Sinemurian (mid-*oxynotum* Zone) long-term positive carbon-isotope shift is associated with very low HI values (~80 mg HC/g TOC) and the paired HI–$\delta^{13}C_{TOC}$ data that follow a steep slope (black squares,

Figure 5.6 B, trend marked by white arrow 3).

The paired HI–$\delta^{13}C_{TOC}$ data at the onset of the Sinemurian-Pliensbachian boundary negative excursion (*raricostatum* Zone, ~1340 to ca. 1255 mbs) follow a similar path to the preceding interval, plotting on a steep line (medium blue squares, Figure 5.6 C trend marked by white arrow 1). As in the preceding long-term positive trend, organic-matter changes appear to be of subordinate importance in the negative excursion interval. However, paired HI–$\delta^{13}C_{TOC}$ data corresponding to the sharp drop in isotope values in the lowermost *jamesoni* Zone (orange squares, Figure 5.6 C, trend marked by white arrow 2) correspond to a concomitant increase in HI and plot along a less steep slope, similar to the suggested background trend, with isotopic signatures about 1.5‰ lower for each end-member compared to suggested background values for the Early Toarcian. The lowermost *jamesoni* Zone negative shift is therefore possibly a function of an abrupt increase in the relative proportion of marine organic matter. The paired HI–$\delta^{13}C_{TOC}$ data corresponding to the recovery towards more positive values suggest a similar trend-line and the positive shift appear as a function of increased abundance of terrestrial organic matter. However, the paired HI–$\delta^{13}C_{TOC}$ data actually consecutively follow a pathway perpendicular to the trend-line on which they plot (trend marked by white arrow 3 in in Figure 5.6 C), as expected for the gradual removal of isotopically light carbon from the ocean–atmosphere system. The *ibex* Zone to mid-*margaritatus* Zone (1106 to 927 mbs) paired HI–$\delta^{13}C_{TOC}$ data is assumed to represent the isotopically undisturbed background values, as discussed above (light blue spares, Figure 5.6 C).

TOC values of samples corresponding stratigraphically to both the gradual and sharp positive carbon-isotope shift between 930 and 927 mbs in the upper *margaritatus* Zone are very low, limiting the amount of reliable HI data (TOC>0.5 wt%). The available data indicate a similar, though slightly steeper path for the gradual positive isotope shift (dark green squares, Figure 5.6 D, trend marked by white arrow 1) than seen in the subjacent stratigraphic record.

The subsequent gradual and sharp negative $\delta^{13}C_{TOC}$ shift (medium green, Figure 5.6 D, trend marked by white arrow 2) follows a steep trend, similar to the negative excursion in the *raricostatum* Zone, indicating a clear superimposed driving

mechanism and suggesting a marginal causal relationship between isotopic changes and the nature of the organic matter in this interval. The longer-term recovery towards more positive isotope values follows a similar steep trend towards background values (red squares, Figure 5.6 D, trend marked by white arrow 3).

5.4.2. Eccentricity-paced small-amplitude $\delta^{13}C_{TOC}$ excursions

Some individual eccentricity-paced negative carbon isotopic excursions in the Mochras record correspond stratigraphically to samples that exhibit elevated TOC and HI values as e.g. in the *davoei* and mid-*margaritatus* zones (Figures 5.1 and 5.7). It is likely that the higher amount of marine organic matter contributes to the isotopic signature of these particular eccentricity-paced CIEs. The increase in the relative amount of marine organic matter appears, however, to be inconsistently paced by orbital parameters, and is not associated with every eccentricity-paced negative shift (e.g. lower *semicostatum* Zone, *obtusum* to *oxynotum* zones), or are only associated with individual samples with elevated TOC and HI (e.g. the transition between the *bucklandi* and *semicostatum* zones, see Figures 5.1 and 5.7).

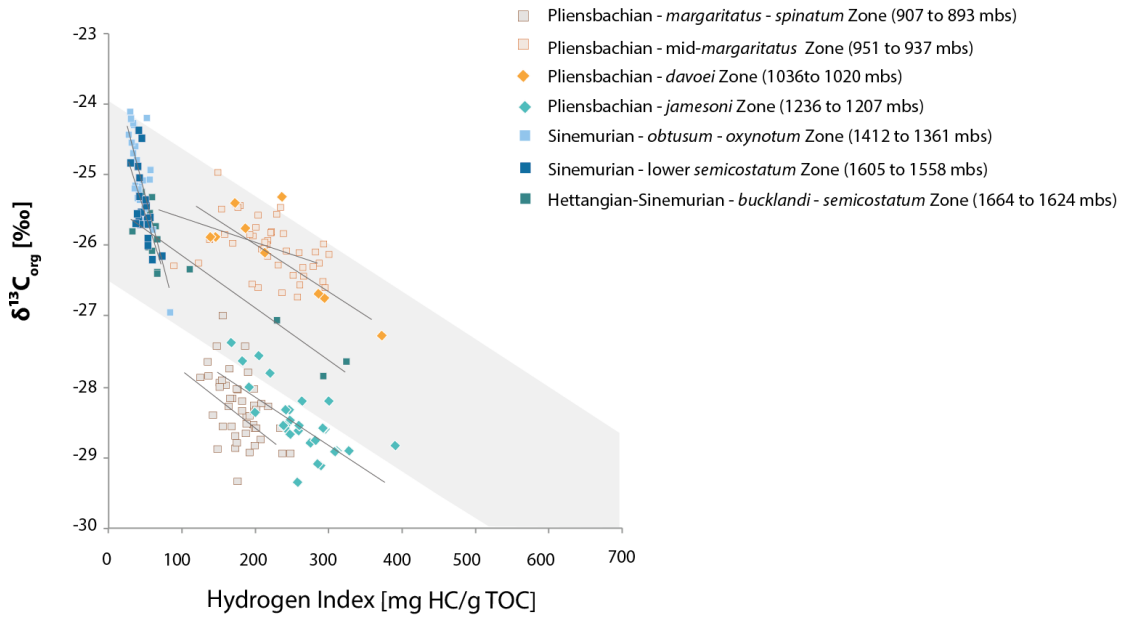

Figure 5.7: $\delta^{13}C_{TOC}$-HI plots of some small-amplitude CIEs, exemplifying varying HI changes concomitant with orbitally paced small-scale isotopic excursions.

5.5. Inorganic geochemical characterization

Elemental concentrations of non-biogenic components in the sediment obtained by hand-held XRF analysis can give information about siliciclastic sediment supply and mineral grain size, indicative for changing climatic and environmental conditions. Here, the ratios between elemental titanium and aluminium (Ti/Al), zirconium and rubidium (Zr/Rb) and silica and aluminium (Si/Al) have been determined to detect changes in the sediment grain size and relative abundance of quartz and clay minerals (see Figure 5.8). Elemental Ti can be sourced from silicate mineral phases where it occurs as Ti-oxides, but also from aluminosilicates. Elemental aluminum is commonly sourced from aluminosilicates. The Ti/Al ratio is therefore indicative for the grain-size of a sediment, distinguishing between the coarser fraction in which silicate minerals occur, and the clay fraction of aluminosilicates (Calvert and Pedersen 2007). Zr/Rb ratios similarly indicate the grain size of sediment. Zirconium occurs in zircon minerals ($ZrSiO_4$), commonly in the fine sand and silt fractions, whereas rubidium is generally sourced from fine-grained aluminosilicate minerals, where it readily substitutes for potassium (Calvert and Pederson 2007). Changes in the ratio between quartz and alominosilicate phases can be determined with Al normalized Si concentrations, as elemental (non-biogenic) silicon (Si) is commonly sourced from coarser grained quartz, or finer grained aluminosilicates (Calvert and Pedersen 2007). Biogenic silica was not observed in the Toarcian strata (Xu *et al.* 2018), and is assumed to be absent in the here studied stratigraphic levels. Under this assumption, the ratio between quartz and aluminosilicate phases can therefore be indicated by Si concentrations normalized to Al (generally derived from aluminosilicates).

Elemental ratios calculated from hand-held XRF measurements (Figure 5.8) indicate episodic changes in the amount of quartz-derived silicon relative to that in aluminosilicates, and coeval increases in the grain size of the detrital mineral phase, as shown by episodic increase in Si/Al, Ti/Al and Zr/Rb in the Hettangian (*angulata* and *bucklandi* zones) and Sinemurian (*semicostatum*, *turneri*, *obtusum* and *oxynotum* zones, see Figure 5.8). The elemental ratios of Si/Al, Ti/Al and Zr/Rb increase gradually through the *jamesoni* Zone, concomitantly with the Sinemurian–Pliensbachian boundary negative CIE and recovery phase, implying a slight gradual

increase in detrital Si input and concomitant increase in grain size.

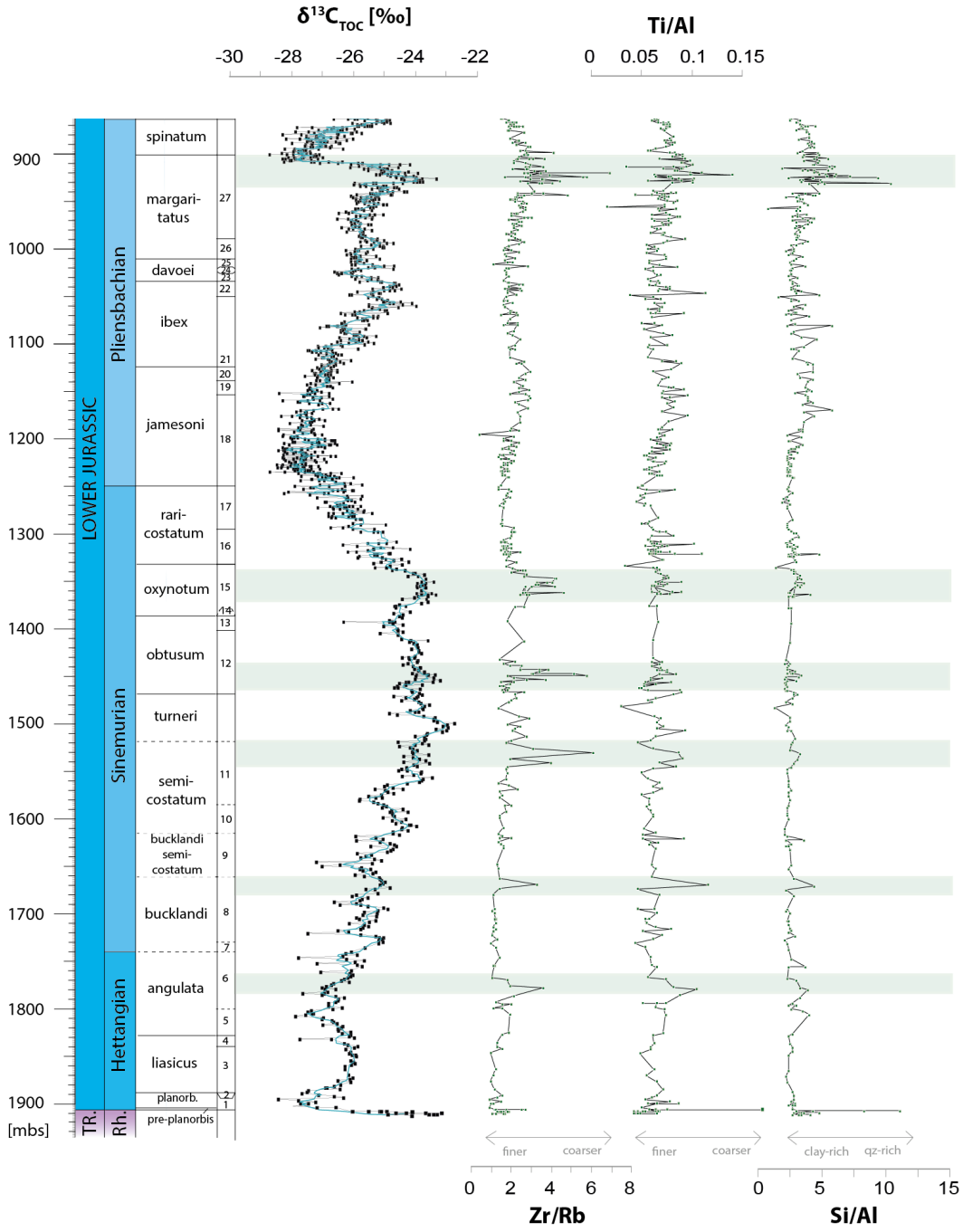

Figure 5.8: $\delta^{13}C_{TOC}$ record and elemental ratios of Si/Al, Ti/Al and Zr/Rb obtained by hand-held XRF analysis. Qz=Quartz. Key for ammonite subzone numbers given in Chapter 3, Figure 3.1.

The upper Pliensbachian *margaritatus* Zone is marked by a further gradual increase in quartzose siliciclastic content, followed by a sharp increase in Si/Al. Ti/Al and Zr/Rb indicate an increase in the grain size of the detrital mineral phase that is coeval with the increased content of detrital quartz. The increased coarse-grained siliciclastic content appears in parallel with the upper part of the mid-*margaritatus* Zone positive CIE, and reaches a maximum concomitantly with the abrupt shift towards peak positive carbon-isotope values, before isotope and elemental ratios values decrease gradually as part of the uppermost *margaritatus* Zone and *spinatum* Zone negative CIE.

Inorganic components (carbonate and mineral facies) were also determined on the sample set analyzed for maceral determinations (see Figure 5.1) and are based on 1000 counts per sample. The results refer to the vol.% of the analyzed field. The carbonate facies in Hettangian and Sinemurian samples is dominated by calcareous groundmass with a subordinate amount of zooclasts and dolomite (see Figure 5.9 and 5.10 A,B). Pyrite appears in small (up to 4 vol. %) and is associated with pyritised organic matter in and around zooclasts, and also appears finely dispersed in the carbonate matrix (see 5.10). The relative abundance of detrital sedimentary grains (quartz, mica, Figure 5.8) is generally low (0.2 to 1.8 vol. %).

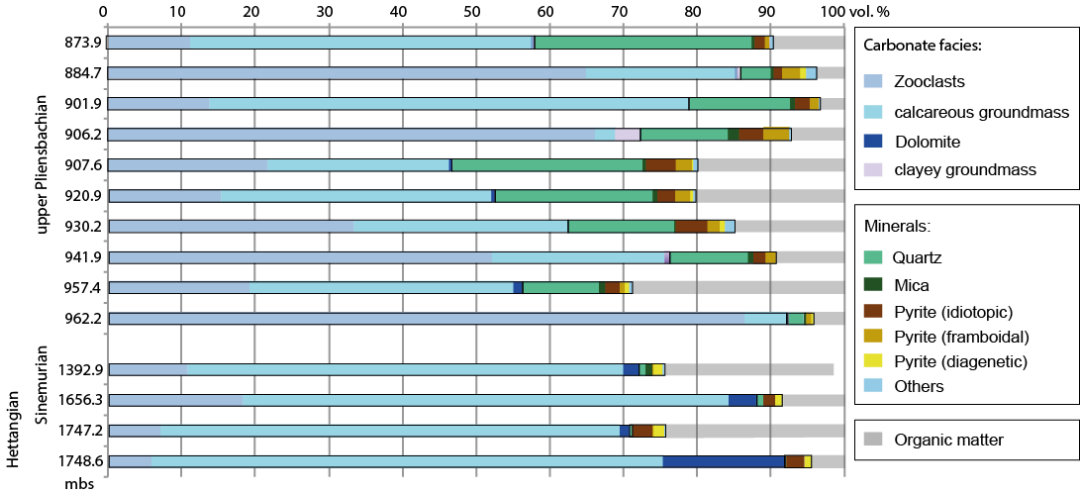

Figure 5.9: Petrographic results of carbonate and other mineral facies

The Pliensbachian samples comprise a varying amount of carbonate with different relative amount of zooclasts and calcareous groundmass in the carbonate facies (11.1 to 86 and 5.5 to 46 vol. % of the bulk rock, respectively, see Figure 5.10 C, D). The amount of zooclasts is generally higher compared with that present in Hettangian and Sinemurian strata. Pyrite is predominantly associated with sedimentary organic matter (Figure 5.10 E, F) and occurs in amounts of 1.4 to 6.8 vol.%. The quantity of detrital minerals (predominantly quartz) is considerably higher in the Pliensbachian upper *margaritatus* Zone (samples 930.2, 920.9 and 907.6, 15 to 25 vol.%), corresponding to the upper part of the positive CIE.

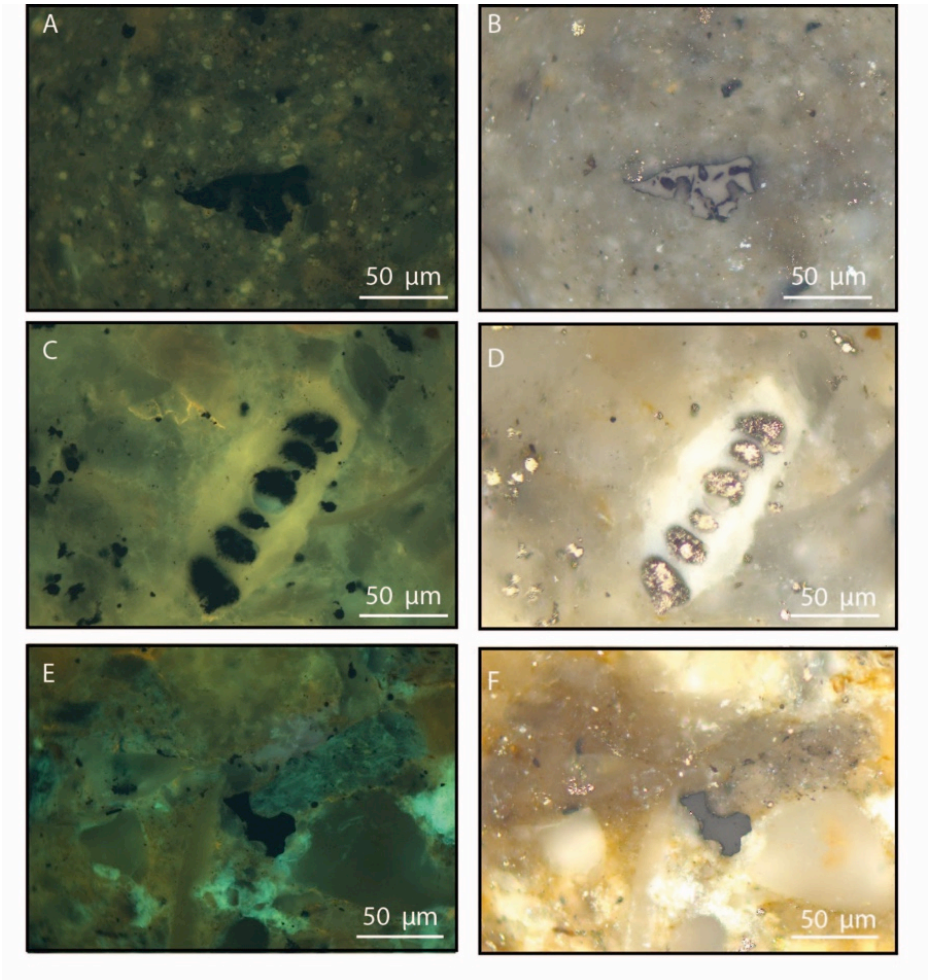

Figure 5.10: Photomicrographs showing the organo-mineral facies of petrographically analyzed samples. **A:** microfacies of sample 1329 mbs representing the typical carbonate mud dominated microfacies of the Hettangian and Sinemurian studied samples. (fluorescence mode, oil immersion) **B:** same view in reflected white light, with finely dispersed pyrite visible in the carbonaceous matrix. **C:**

Foraminifera with pyritized organic matter, zooclasts and carbonate matrix (sample 873.9 mbs) **C:** same view in reflected white light, showing the framboidal pyrite associated with the organic matter in the Foraminifera and dispersed in the carbonate matrix. **D:** same view in reflected white light. **E:** microfacies of sample 884.7mbs, representing the typical facies for the studied Pliensbachian samples, comprising coal fragments, quartz grains. carbonate grains, zooclasts and carbonate matrix. **F:** microfacies of sample 920.9 mbs, representing the typical facies for the studied Pliensbachian samples, comprising zooclasts (foraminifera), finely dispersed amorphous organic matter, alginite and carbonate matrix.

5.6. Discussion

5.6.1. Depositional environment

Based on the general dominance of acritarchs and lack of dinoflagellates in the microfossil assemblages, previous work suggested stable, stratified water conditions with low-nutrient surface waters during deposition of the Hettangian to upper Sinemurian strata of the Mochras core (van de Schootbrugge *et al.* 2005). Persistent low TOC values and relatively low amounts of zooclasts in the organo-mineral facies (Figure 5.9) of the Hettangian and Sinemurian samples analyzed here suggest a low bioproductivity environment. However, the presence of Liptodetrinite and absence of Bituminite suggests rather well-oxygenated surface waters and bottom waters/sediments, as low-oxygen conditions would have promoted the generation of bituminite (Gorbanenko and Luigouis 2015).

The increase in TOC and AOM in upper Sinemurian and Pliensbachian strata was also recognized by van de Schootbrugge *et al*. (2005), and linked to the Late Sinemurian to Pliensbachian transgression, supporting the preservation and bacterial degradation of organic matter through the development of low-oxygen bottom waters (van de Schootbrugge *et al.* 2005). Due to the higher amount of zooclasts and bioturbation, the increased TOC values are likely a function of both, increased marine bioproductivity and increased preservation. The presence of bituminite in the Pliensbachian samples support the presence of prevailing low-oxygen bottom waters during deposition of these sediments. Strongly bioturbated intervals in the Pliensbachian strata, however, imply distinct episodic oxygenation of the bottom

waters (Ruhl *et al.* 2016). The presence of large amounts of liptodetrinite in all analyzed samples likely relates to turbulent water conditions (Gorbanenko and Ligouis 2015), suggesting strong wave action in the surface waters throughout the studied interval.

The relative amount of detrital siliciclastic sediment coarser than clay grade (quartz, mica, Figure 5.9) is very low in the Hettangian and Sinemurian samples, supporting either a distal palaeogeographic location of the depositional site, or generally low detrital input as a function of low rates of run-off and erosion. The episodic increase in detrital quartz and coarser grain-size of detrital minerals inferred form XRF data occurring in stratigraphically short intervals (upper *angulata*, upper *bucklandi*, upper *semicostatum*, lower *obtusum* and upper *oxynotum* zones) possibly indicates intervals of movement along the Mochras Fault, or brief sea-level changes (regression events).

Increased continental run-off, perhaps linked to warmer and more humid climates as suggested by van de Schootbrugge *et al*. (2005) might account for the gradual increase in coarse-grained siliciclastic input in the Lower Pliensbachian sediments. The change in palaeoenvironmental conditions were also suggested to have led to increased stratification as well as nutrient input, resulting in higher marine productivity and organic matter preservation. The prevailing productivity and preservation were, however, likely not persistent but of cyclic nature (see above).

The sharp increase in detrital quartz content in the upper *margaritatus* Zone sediments, coeval with a noticeable increase in the amount of macroscopic coal fragments, however, is likely witnessing reworking and erosion of the basement rock. This might be related to a late Pliensbachian regression event, also reported from several NW European localities, inferred from the observation of erosion, decreased sedimentation rates, ironstone and authigenic seep carbonate formation, and carbonate production crisis (e.g. Curtis and Spears 1968, Sellwood 1971, Blomeier and Reijmer 1999, Cobianchi and Picotti 2001, Léonide *et al.* 2007, van de Schootbrugge *et al.* 2010).

5.6.2. Origin of the spores, pollen and coal fragments

In order to determine if the $\delta^{13}C_{coal}$ record comprises the contemporaneous Early Jurassic atmospheric isotope signal, it is crucial to determine the origin and age of the coal fragments. The increase in the relative abundance of coal clasts coincides with the increase in detrital quartz, and is likely linked to the increased detrital input during lowering of sea level (see above).

The macroscopic coal fragments could potentially be sourced from contemporaneous Jurassic wood, here preserved as coal. The presence of Densospores (spores of lycopods, common in coal seams of Devonian to Permian age; Traverse 2007) in the bulk-sediment palynological assemblage, however, supports Paleozoic reworking. With the available palynological data, it is not evident if these Paleozoic spores were liberated from the coal fragments during sample preparation, or if they are sourced from the bulk sediment. Further palynological work on the spore inclusions within the coal fragments is needed to verify the age and therefore the sedimentary origin of the coal fragments.

5.6.3. Validity and limitations of the interpretation of HI–$\delta^{13}C_{TOC}$ plots

In addition to the effect of aerobic bacterial degradation organic matter in the water column, lowering the Hydrogen Index of the residual organic matter independently form the changes towards a higher relative contribution of terrestrial organic matter to the sediment, other factors can have an effect on the linear relationship between HI and $\delta^{13}C_{TOC}$ values. Complicating factors in the interpretation of HI–$\delta^{13}C_{TOC}$ plots are for example changes in the isotope fractionation as a response to ecological changes. The isotope fractionation of C3 plant tissues is affected by changes in pCO_2, independently of $\delta^{13}C_{CO_2}$ (Feng and Epstein 1995, Kürschner *et al.* 1996, Schubert and Jahren 2012), but possibly also by water availability (inferred from modern plants; Kohn 2010, Kohn 2016). Furthermore, differences in isotope fractionation have been observed between angiosperms and conifers, likely as a response to physiological changes (i.e. temperature, humidity, pCO2; Schouten *et al.* 2007). Previous work also showed that the magnitude of pCO_2-dependent isotope

fractionation in marine organic matter is highly variable with species and taxa (Laws *et al.* 1995). The non-linear fractionation response to palaeoenvironmental changes, such as pCO_2 may results in an offset in the linear background trend, which in HI–$\delta^{13}C_{TOC}$ plots can be interpreted as a superimposed isotope event. The lack of pCO_2-related isotopic fractionation in cyanobacteria such as *Synechococcus* (Popp *et al.* 1998) might, for example, explain the non-linear changes in isotope fractionation between fossil wood and the marine organic matter during the T-OAE, which is in many sediments marked by an elevated contribution of cyanobacteria (Suan *et al.* 2015).

The Early Jurassic was a time of constant palaeoenvironmental, palaeoceanographic and biotic change, accompanied by CO_2 emission and sequestration, and subsequent climatic changes (van de Schootbrugge *et al.* 2005). It is therefore expected that non-linear changes in the fractionation of individual organic compounds also occurred during the Early Jurassic. Attention must also be given to the potential increase in the relative abundance of terrestrial spores, which are marked by high HI values, similar to marine organic matter, but correspond to isotope values typical for terrestrial organic matter. Furthermore, the HI–$\delta^{13}C_{TOC}$ plots do not take into account the extent of potentially reworked terrestrial material contributing to the total organic matter admixture, inevitably supplying a non-contemporaneous isotope signal, as e.g. potentially in the upper *margaritatus* Zone carbon-isotope record of the Mochras core. However, with careful consideration of the possible effects of changes in atmospheric CO_2, climatic conditions, reworked organic matter, microfossil assemblage and analytical sample bias (artificially low HI values), the HI–$\delta^{13}C_{TOC}$ plots are an approximation to indicate organic matter related biases in the $\delta^{13}C_{TOC}$ record, which should be further supported by compound-specific isotope analysis.

5.6.4. Implications of changes in organic matter on the long-term carbon-isotope record

The paired HI–$\delta^{13}C_{TOC}$ data indicates several isotope excursions that are accompanied by changes in the relative composition of organic matter (see Figure 5.6, 5.11). The following discusses the individual long- and short-scale isotope excursions in the

Hettangian to Pliensbachian strata of the Mochras core and associated changes in HI in consideration of the depositional environment and possible factors limiting the interpretation of the paired HI–$\delta^{13}C_{TOC}$ data.

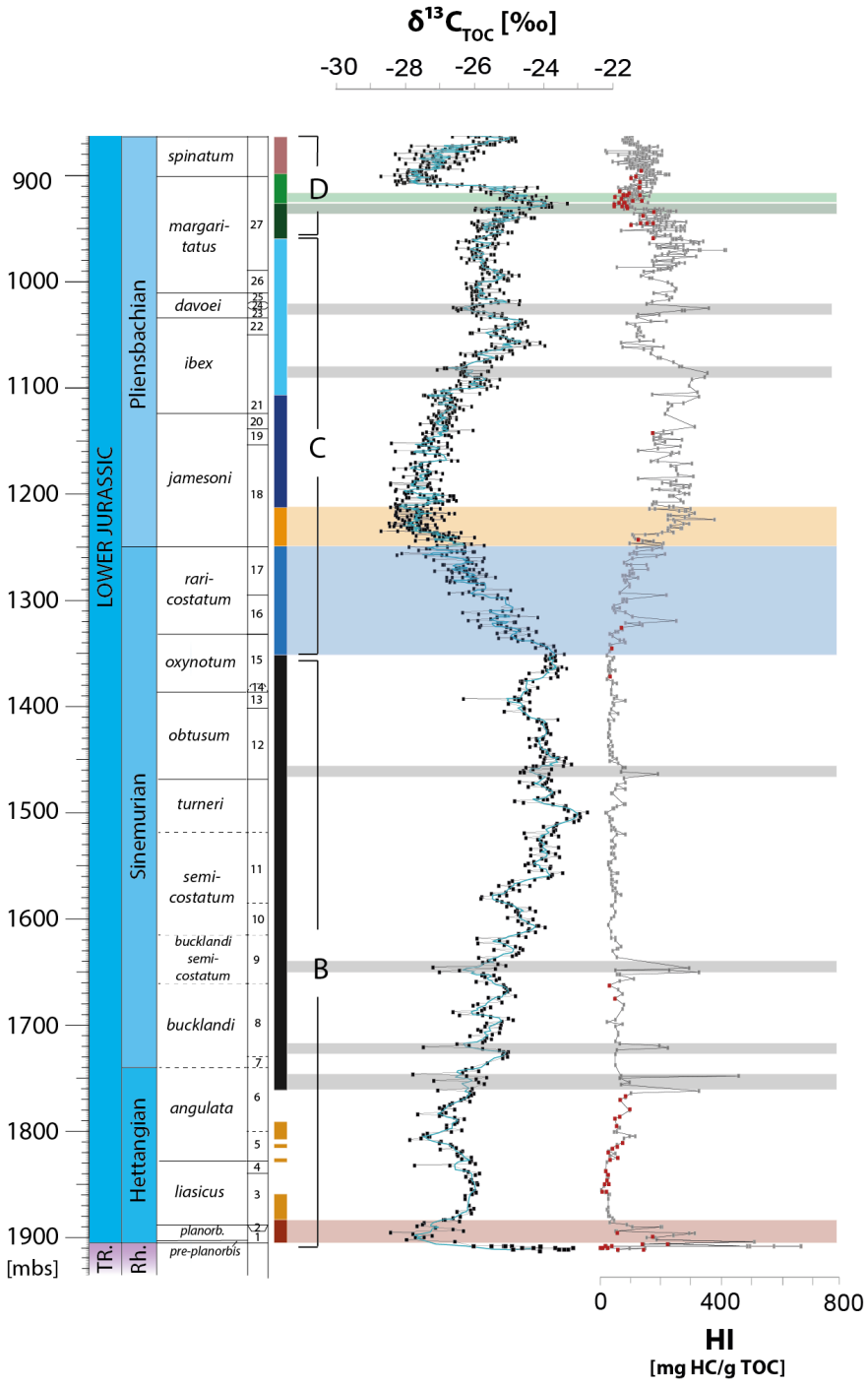

Figure 5.11: $\delta^{13}C_{TOC}$ and Hydrogen Index (HI) record of the Hettangain to Pliensbachian strata of the Mochras core. Isotope excursions with accompanied changes in HI discussed in the text are marked in the figure. Colors refer to paired HI–$\delta^{13}C_{TOC}$ plots in Figure 5.6.

Lowermost Hettangian

The paired HI–$\delta^{13}C_{TOC}$ data from the pre-*planorbis* beds and lowermost *planorbis* Zone indicate a different nature of the organic matter. The exceptionally high HI values correspond to $\delta^{13}C_{TOC}$ values higher than expected for marine organic matter. A possible organic source for these outliers is a relatively large amount of conifer spores that, although of terrigenous origin, are characterized by high HI values (Taylor, 1995). Increased abundance of conifer pollen has been reported from the uppermost Triassic in the Eiberg Basin and the Bristol Channel Basin, occurring at the onset of the initial $\delta^{13}C_{TOC}$ negative CIE associated with the Triassic–Jurassic mass extinction (Ruhl *et al.* 2009, Bonis *et al.* 2010). A further peak in spore abundance, albeit smaller in magnitude, is recorded at St Audries Bay (Bristol Channel Basin), located just above the Triassic–Jurassic boundary (Bonis *et al.* 2010). However, further palynological investigations are needed to elucidate the relationship between spores and elevated HI in the Mochras record, and a possible correlation with the spore peak at the Triassic–Jurassic boundary in St Audries Bay.

Although the pulsed volcanic and/or thermogenic and/or biogenic release of isotopically light carbon has been suggested for the Early Hettangian (e.g. Hesselbo *et al.* 2002, Schoene *et al.* 2010, Whiteside *et al.* 2010), and thought to drive the carbon-isotope record, the lowermost Hettangian negative and subsequent positive CIE in the lower *liasicus* to *angulata* Zone in the Mochras record appear to be, at least partly, accompanied and, potentially, driven by an increase in the relative amount of marine organic matter.

Hettangian to upper Sinemurian long-term positive CIE:

The Hettangian (lower *liasicus* Zone) to upper Sinemurian (mid-*oxynotum* Zone) gradual long-term positive carbon-isotope shift is associated with consistently low HI values (~80 mg HC/g TOC) and the paired HI–$\delta^{13}C_{TOC}$ data follow a steep slope (black squares, Figure 5.6 B, trend marked by white arrow 3). Due to the likely well-oxidized water conditions in the Hettangian and Sinemurian strata (as indicated by the large amount of liptodetrinite macerals and absence of bituminite in the organic matter composition), the low HI values in the Hettangian strata might be the result of

bacterial degradation in the water column leading to lower preservation of hydrogen-rich lipids and therefore lower HI values. Possible changes in the source of organic matter concomitant with the broad positive excursion in $\delta^{13}C_{TOC}$ might not be preserved due to the high rates of oxidation, wherefore no interpretation of the paired HI–$\delta^{13}C_{TOC}$ data trends can be made.

Sinemurian–Pliensbachian boundary CIE:

From interpretation of the paired HI–$\delta^{13}C_{TOC}$ data it is evident that the gradual turnover in the biotic assemblages towards a higher relative amount of isotopically light, hydrogen-rich marine organic matter in the uppermost *raricostatum* Zone has acted in a subordinate role in driving the onset of the negative CIE at the Sinemurian-Pliensbachian boundary. This interpretation is in agreement with the coeval appearance of the negative excursion in $\delta^{13}C_{carb}$ and $\delta^{13}C_{wood}$ at the Yorkshire coast (Korte and Hesselbo 2011), indicating a superimposed release of isotopically light carbon affecting both the marine and terrestrial realms. A late phase of CAMP volcanism at the Sinemurian–Pliensbachian boundary has been suggested as a source for the isotopically light carbon, as the negative excursion correlates with increased volcanic activity (Ruhl *et al*. 2016, see Chapter 4). Although the isotopic changes are either not, or only insignificantly, driven by a change in bulk organic constituents, rising HI values indicate a gradual trend towards a higher contribution from marine organic matter, or a gradual change towards lower-oxygen conditions in the water column and the sediment, promoting the preservation of lipid-rich organic matter. The extensive changes in palaeoenvironmental conditions, possibly as a response to the release of greenhouse gases, and/or the opening of the Hispanic corridor in the latest Sinemurian (Damborenea 1996, Aberhan 2001, 2002), might have changed the nutrient supply and favored conditions for higher bioproductivity in the upper water column, accompanied by greater preservation of organic matter supported by the development of low-oxygen bottom waters. The ~1.5 ‰ negative shift in isotopic values in the lower *jamesoni* Zone, however, appears to some degree controlled by an abrupt increase in the relative amount of marine organic matter.

Interestingly, the lower *jamesoni* Zone negative shift is recorded in the $\delta^{13}C_{carb}$ record of the Mochras core, and the fossil calcite $\delta^{13}C$ record of the e.g. the Cleveland Basin (Robin Hood's Bay; Korte and Hesselbo 2011). The coeval appearance of the CIE in the organic and inorganic carbon reservoir might imply that the abrupt change towards an increased amount of marine organic matter appeared concomitantly with atmospheric signal.

The gradual trend of the organic matter carbon isotopic record towards more positive values following the lower *jamesoni* Zone negative shift appears to be unrelated to compositional organic matter changes. The gradual fixation of increased quantities of isotopically light carbon in sediments in a spatially extended (global) context might have increased the carbon-isotope ratio in the ocean-atmosphere system, as postulated for the Hettangian-Sinemurian gradual positive $\delta^{13}C$ shift, albeit with a higher relative amount of marine organic matter in the bulk organic matter in the Mochras core.

The Pliensbachian upper ibex, davoei and lower margaritatus zones

The upper *ibex*, *davoei* and lower *margaritatus* zones are characterized by clearly expressed eccentricity-paced carbon-isotope excursions, some of which are accompanied by concomitant changes in the source of organic matter (see figure 5.11). The fluctuating relative amount of marine versus terrestrial organic matter likely contributes to the very pronounced expression of the cyclic isotopic shifts in the $\delta^{13}C_{carb}$ record. However, changes in organic-matter sourcing was probably not the driving mechanism behind the isotopic shifts, but rather a consequence of superimposed environmental changes, as some of the cyclic 0.5–2 ‰ isotope excursions also appear in the $\delta^{13}C_{carb}$ record of the Mochras core (van de Schootbrugge *et al.* 2005), e.g. in the negative shift in the *davoei* and the upper lower *margaritatus* Zone, and are also expressed in the carbonate carbon-isotope reservoir of other NE European basins (e.g. Lusitanian Basin; Silva *et al.* 2011). It is therefore evident, that these shifts recorded in the $\delta^{13}C_{TOC}$ record of the Mochras core are not solely driven by the change of the organic matter composition.

The Upper Pliensbachian margaritatus *Zone positive CIE*

The positive excursion in the upper Pliensbachian *margaritatus* Zone likely corresponds to the excursion recorded in different carbon-reservoirs in numerous European localities (e.g. Jenkyns and Clayton 1986, Korte and Hesselbo 2011, Silva *et al.* 2011). As the positive CIE coincides with widespread enhanced preservation of organic-rich marine strata (Silva *et al.* 2011 and references therein) the signal can be readily linked to enhanced burial of organic carbon in the absence of counterbalancing atmospheric injection of isotopically light carbon (Suan *et al.* 2010, Korte and Hesselbo 2011, Silva *et al.* 2011).

The positive excursion expressed in the Mochras core is, however, largely coincident with an increase in the relative amount of oxidized terrestrial organic matter indicated by the organo-facies (Figure 5.3, slightly higher Oxygen Index values (Figure 5.1), and elemental ratios of Si/Al and Rb/Zr (see Figure 5.9) associated with coarser siliciclastic sediment content.

If the preceding interval between the *ibex* to lower *margaritatus* zones represents the Late Pliensbachian background values defining the HI–$\delta^{13}C_{TOC}$ end-members of a undisturbed environment, the positive CIE in the upper *margaritatus* Zone (960.4 to 927.5 mbs) appears slightly off-set to this trend, and possibly contains a component of increasing $\delta^{13}C_{TOC}$ values superimposed on the changes in organic matter. Increased input of reworked Palaeozoic coals, comprising up to 15 vol.% of the total organic-matter content, could bias to the contemporaneous bulk organic carbon-isotope record. It is therefore crucial to determine the origin and age of the coal fragments by palynological analysis of the spore inclusions.

Uppermost *margaritatus* and *spinatum* negative CIE

The paired HI–$\delta^{13}C_{TOC}$ data for the *margaritatus* and *spinatum* Zone negative excursion do not imply a change in the composition of the sedimentary organic matter as a trigger or amplifying mechanism. The larger magnitude of the negative excursion in the Mochras core compared to the coeval excursion recorded in $\delta^{13}C_{TOC}$ and the $\delta^{13}C_{carb}$ of other European sections (Paris Basin and Grandes Causses Basin; Harazim

et al. 2013, Peti *et al.* 2017; see Chapter 4, Figure 4.7), can therefore not be explained by local changes in the organic-matter composition as a response to the drastic changes in palaeoenvironmental conditions during the late Pliensbachian cooling and regression event. However, there is no comprehensive understanding concerning changes in taxa and isotope fractionation in response to the climatic changes. Notably, the negative excursion occurs concomitant with a biotic turnover in the marine microfossil assemblage, from an acritarch dominated environment to the abundant occurrence of dinoflagellates (van de Schootbrugge *et al*. 2005).

Eccentricity-paced small-scale isotope excursions

Compositional changes of the bulk organic matter do appear sporadic and not concomitant with every small-scale isotope excursion, and the magnitude of change in HI does not consistently correlate with the magnitude of the corresponding isotopic change (see Figure 5.6, 5.11). The organo-facies changes are therefore likely not the primary driving mechanism of these small-scale CIEs. However, a general change in the climatic conditions, such as a mega-monsoonal climate regime as suggested by Röhl *et al.* (2001), and van de Schootbrugge *et al.* (2005), might have amplified the expression of orbitally paced isotope excursions in the bulk organic carbon-isotope record in the lower to mid Pliensbachian, by e.g. cyclic changes in the nutrient supply or preservation.

5.7. Conclusion

The organic matter preserved in the Hettangian to Pliensbachian strata of the Mochras core is of immature to early mature nature. The sediments are organic-lean and dominated by terrestrial organic matter and/or oxidized marine organic matter residues. Detailed organo-facies, TOC and HI data suggest a relatively higher bioproductivity, and slightly increased abundance of marine organic matter in the Pliensbachian compared to the Hettangian and Sinemurian strata, which is likely a function of bottom water oxygenation affecting preservation and productivity, induced

by increased continental run-off leading to nutrient input and episodic development of low-oxygen environments.

Changes in the relative abundance of isotopically light organic constituents appear to play a subordinate role as a driving mechanism of long- and short-term bulk $\delta^{13}C_{TOC}$ carbon-isotope excursions. Changes in the composition of organic matter likely contributing to shifts in the $\delta^{13}C_{TOC}$ record appear in sediments of the lower Hettangian (lower *liasicus* to lower *angulata* Zone). The Hettangian to lower Sinemurian gradual positive carbon-isotope shift appears not to be accompanied by changes in the relative composition of organic matter. The organic matter preserved in this interval is likely degraded through aerobic bacterial processes, wherefore no certain interpretation of organic matter changes can be made. The Upper Sinemurian to Lower Pliensbachian negative carbon-isotope excursion could potentially be a function of atmospheric release of isotopically light carbon as suggested by Ruhl *et al*. (2016). Increase in the relative amount of marine organic matter in the upper Sinemurian and lower Pliensbachian part of the core appears to be a subordinate driving mechanism of the carbon-isotope record. The organic matter changes are likely a consequence of ecological, climatic and/or palaeoenvironmental changes triggered by CO_2 emission and the palaeoceanographic changes induced by the opening of the Hispanic Corridor.

The Upper Pliensbachian positive carbon-isotope excursion appears concomitantly with increased detrital content, associated with increased terrestrial organic matter input. Further investigations are needed to determine the source and age of detrital coal fragments, to examine the possible non-contemporaneous isotope signature contributing the $\delta^{13}C_{TOC}$ signature in that particular interval.

The upper Pliensbachian upper *margaritatus* Zone and *spinatum* Zone negative carbon-isotope excursion appears not to be associated with major changes in the source of organic matter. The large magnitude of the upper Pliensbachian negative excursion compared to the expression of the same event in other localities (Paris Basin and Grandes Causses Basin; Harazim *et al.* 2013, Peti *et al.* 2017) is therefore evidently linked to a concomitant change of the relative abundance of marine organic matter in the bulk sediment.

Eccentricity-paced small-amplitude negative carbon-isotope excursions appear to some extent to be accompanied by changes in organic matter. However, fluctuations in the relative amount of marine *versus* terrestrial organic matter cannot have been the main driving mechanism changing the isotopic composition of the bulk organic matter, as such changes do not appear with and correspond to each of the eccentricity-paced $\delta^{13}C_{TOC}$ excursions.

Chapter 6 : Stratigraphic framework of the Lower Jurassic of the northern Neuquén Basin, Mendoza Region, Argentina

6. Abstract

Marine Lower Jurassic sections crop out about 30 km West of Malargüe in the northern Neuquén Basin, Argentina. The sedimentological examination of sections along the Arroyo Serrucho creek and the newly discovered Las Overas and Las Overas-C sections allocate the strata to the Puesto Arraya and Tres Esquinas Formations, which recorded gradual deepening of the northern Neuquén Basin from shore-face to inner-basin deposits. The sections examined herein expand the sedimentological record of previously studied sections in the Arroyo Serrucho creek, both down- and up-section. Biostratigraphic correlation confirms a Late Pliensbachian to Toarcian age of the successions studied here, and allows refinement of the stratigraphic position of the *D. tenuicostatum–D. hoelderi* ammonite Zone boundary.

6.1. Palaeogeography and Tectonic Setting of the Neuquén Basin, Argentina

The Neuquén Basin is a north-south-oriented, broadly triangular-shaped Mesozoic back-arc basin, located in west-central Argentina on the eastern side of the Andes (Howell *et al.* 2005, Figure 6.1). The basin covers an area of ~120,000 km^2, comprising up to ~6 km of Upper Triassic to Eocene sedimentary infill (Legarreta and Uliana 1996). In the Early Jurassic, the basin was approximately located between 35° and 45°S (Franzese *et al.* 2003). The complex tectonic history of the basin was largely controlled by the break-up of Gondwana, subduction of the proto-Pacific plate, and subsequent development of the Andean magmatic arc on the western margin (Franzese *et al.* 2003, Howell *et al.* 2005, Franzese *et al.* 2006).

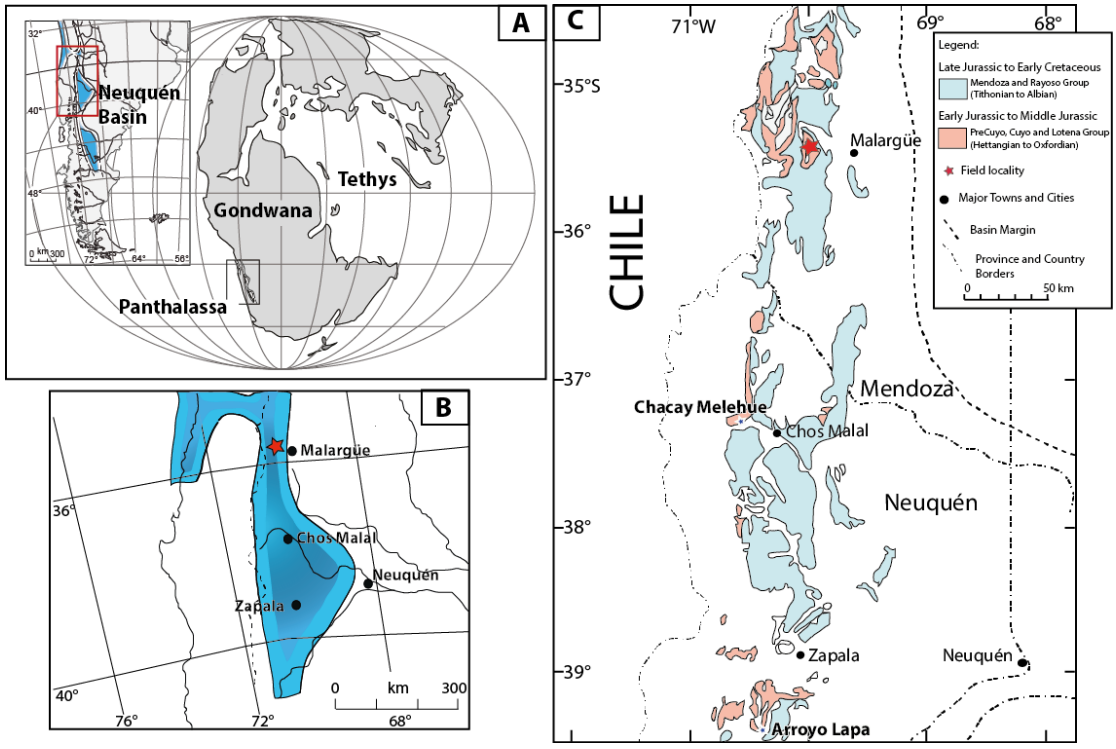

Figure 6.1: Toarcian paleogeography (after Blakey 2007) and Argentinian paleogeography (after Vicente 2005) with interior seaway including the location of the Neuquén Basin (indicated by the red square). **B:** Neuquén Basin during the Early Jurassic, after Vicente (2005). Relative water depth indicated by color **C:** Geological map indicating Jurassic and Cretaceous strata cropping out in the Neuquén Basin. Study area is marked with a red star. Modified from Gulisano and Pleimling (1995). Present-day coordinates are given on the map of Argentina whereas the palaeogeographic map shows paleolatitudes.

The Neuquén Basin originated in the Late Triassic, when the area was subject to continental extension related to the collapse of the Gondwana orogen (Franzese and Spalletti 2001). The rifting generated a series of unconnected N–S-trending half-grabens, acting as individual depocentres (Riccardi 1983, Vergani *et al.* 1995, Franzese and Spalletti 2001, see Figure 6.2A).The pre-Andean volcanic arc (Chilean Coastal Cordillera) on the western margin of the young basin functioned as a barrier to the Panthalassa Ocean (proto-Pacific), wherefore sedimentation during the pre-rift phase was dominated by continental siliciclastic-, volcaniclastic and pyroclastic deposition (Lapa Formation, Vicente 2005, Franzese *et al.* 2006).

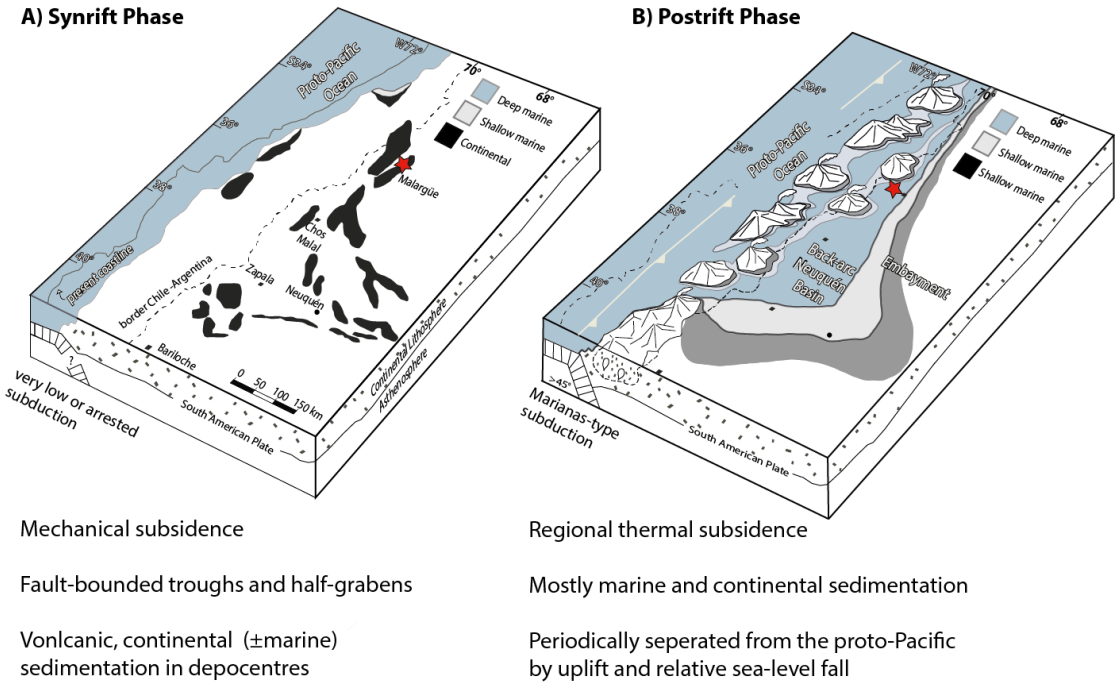

Figure 6.2: Schematic evolution of the Neuquén Basin from the Late Triassic to the Early Cretaceous. **A:** Late Triassic to earliest Jurassic (240–195 Myr) characterized by pre-subduction rifting in a series of narrow grabens, with predominantly volcanic and continental sedimentation with some marine sedimentation along the western margin and **B:** Early Jurassic to Cretaceous (180–135Ma) onset of subduction along the western margin of Gondwana and the early development of the Andean chain. Figure was modified from (Howell *et al.* 2005), based on Ramos *et al.* (1982), Vergani *et al.* (1995), Franzese and Spalletti (2001), Franzese *et al.* (2003). Location of study area marked with a red star.

The development of an active subduction zone on the western margin of Gondwana in the Early Jurassic to Early Cretaceous was associated with the evolution of the magmatic arc and back-arc subsidence within the Neuquén Basin area (syn- and post-rift phase), interrupted by episodic basin inversion (Vergani *et al.* 1995, Franzese and Spalletti 2001). Marine sedimentation started in the Late Triassic/Early Jurassic in the northern basin, when a narrow marine corridor developed and connected the basin to the Panthalassa Ocean (Figure 6.2B, Legarreta and Uliana 1996, Vicente 2005). In the Late Pliensbachian and Toarcian, the seaway expanded southward and the dispersed depocentres, developed during the pre-rift phase, were integrated in the Neuquén Basin (Vicente 2005). The sediments deposited in the marine phase were sourced from the eastern and western margins of the basin. Siliciclastic sediments were supplied

from the cratonic eastern margin, forming a transgressive siliciclastic platform, whereas volcaniclastics, sourced from the Chilean Coastal Cordillera, entered the basin on the western margin (Vicente 2005). Thermal subsidence and regional back-arc extension led to marine transgression and general deepening during the Late Pliensbachian and Early Toarcian, recorded in deep-marine turbiditic facies (Legarreta and Uliana 1996, Vicente 2005). Transgressive–regressive cycles were driven by changes in the subsidence rate, localized and episodic uplift, and eustatic sea-level oscillations (Howell *et al.* 2005). During the Late Cretaceous to Cenozoic, the transition to a shallow-dipping subduction Zone resulted in extensive crustal shortening and uplift of the foreland thrust belt (Ramos *et al.* 1982, Howell *et al.* 2005).

At the present day, Lower Jurassic strata crop out in scattered and isolated patches across the Neuquén Basin (see Figure 6.1, 6.2). The field area of this study is located in the northern Neuquén Basin (see Figure 6.1, 6.2 and 6.3). All sections studied are located in Mendoza Province, about 30 km west of Malargüe (see Figure 6.3). Fieldwork was performed along, and east of the Arroyo Serrrucho creek, where Jurassic strata crop out on the eastern side of the N–S-striking Cerro Pucheanqu anticline (Gulisano and Pleimling 1995). The Lower Jurassic succession is represented by the Upper Puesto Arraya, and Tres Esquinas Formation (see Figure 6.4), which are the local equivalent to the Los Molles Formation in the southern part of the Basin. The Puesto Arraya Formation and Tres Esquinas Formation were deposited during the Hettangian to Late Pliensbachian, and Early Toarcian to Aalenian, respectively (Gulisano and Pleimling 1995). The formations are part of the lower Cuyo Group, which represents the initial marine sedimentation in the Neuquén Basin (Weaver 1931).

The lower Puesto Arraya Formation (mid-Hettangian to Late Pliensbachian) is dominated by well-sorted sandstones, and changes up-sequence to a more carbonate-rich facies, including a rich fauna of gastropods and bivalves in life position, intercalated with storm-generated beds and thin mudstone beds. Up section, the succession successively change into finer grained, muddier facies with increasing organic-carbon content in the upper Puesto Arraya Formation (Gulisano and Pleimling 1995). The lower Puesto Arraya Formation is interpreted to represent fan deltaic

sediments, progressively changing into shallow-water shelf deposits of a storm-dominated platform. Marine transgression and basin deepening during the initial phase of basin subsidence gradually deepened the depositional environment from near-shore to an inner-shelf environment recorded in the upper Puesto Arraya Formation (Lanes 2005, Valencio *et al.* 2005).

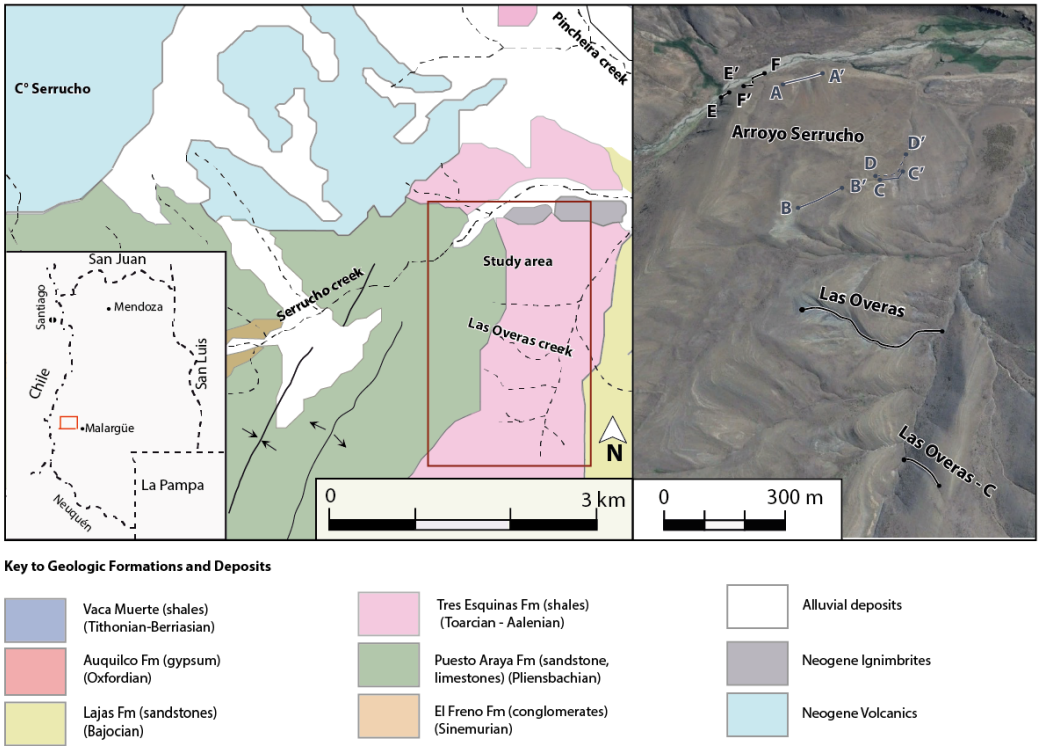

Figure 6.3: Location of the study area marked on a geographical and geological map (left), and satellite image showing the location of sections examined in this study (Las Overas, Las Overas-C, Arroyo Serrucho E–E' and F–F') in relation to previous studies in the field area (Arroyo Serrucho A'A', B–B', C'C': Al-Suwaidi *et al*. 2010, Al-Suwaidi *et al*. 2016, and Arroyo Serrucho D-D': Mazzini *et al*. 2010). Geological sketch of study area after Gulisano and Pleimling (1995). Satellite image courtesy of Google Earth (2017).

The Tres Esquinas Formation (Toarcian) comprises dark calcareous silt- and claystones, partly laminated, with successively increasing amounts of intercalated sandstones (Gulisano and Pleimling 1995). Progressive subsidence during the Late Pliensbachian–Toarcian resulted in further deepening, expressed by a decrease in

grain size, fewer storm-induced deposits and, increased organic-matter content in the Tres Esquinas Formation, (Lanes 2005, Valencio *et al.* 2005).

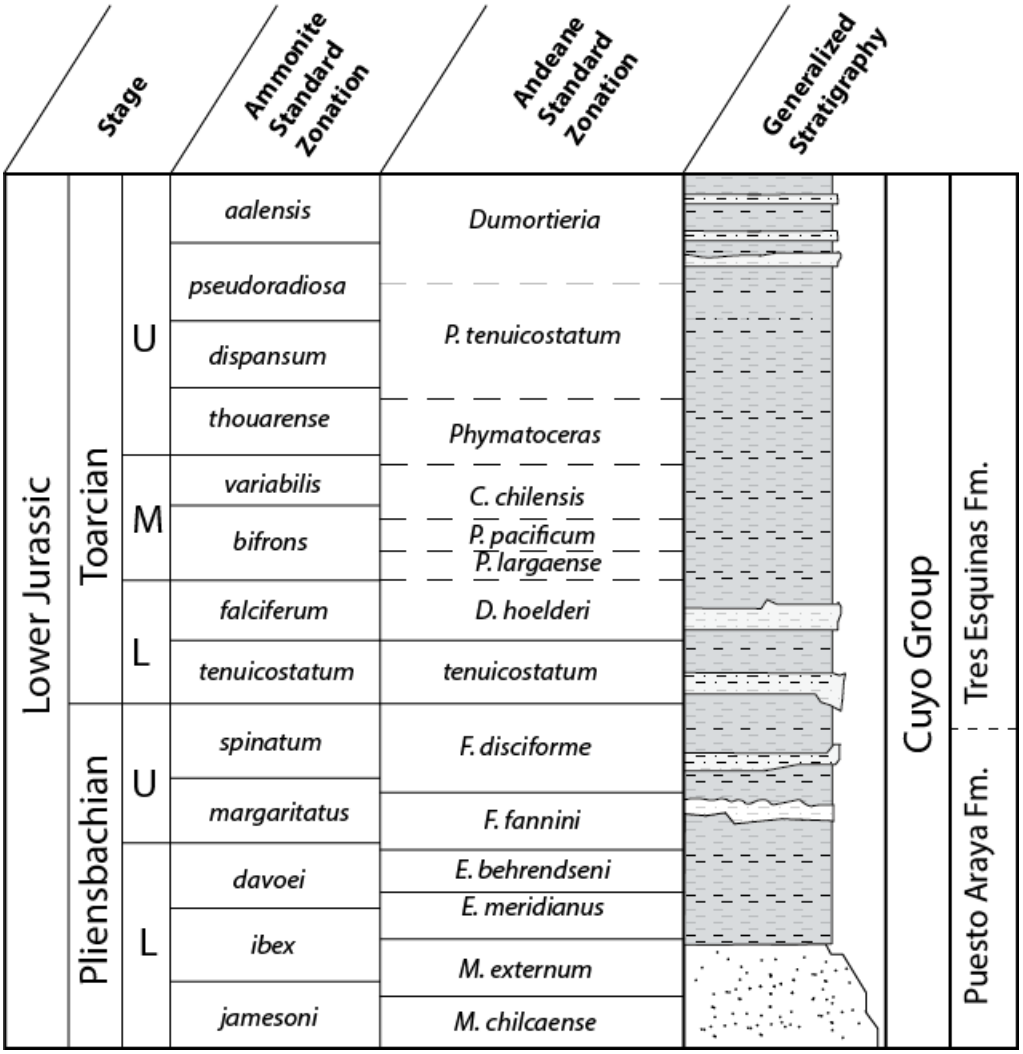

Figure 6.4: Table showing the epoch/age, standard northwestern European biozones, Andean ammonite zonation and biostratigraphy and correlation to the European zonation (adapted from Riccardi (2008b), generalized stratigraphic log of the Puesto Arraya Formation and the Tres Esquinas Formation of the Cuyo Group (adapted from Gulisano and Pleimling-Gutiérrez (1995). U = upper; M = middle; L = lower; *P. tenuicostatum* = ?*Phlyseogrammoceras tenuicostatum*; C. *chilensis* = *Collina chilensis*; *P. pacificum* = *Peronoceras pacificum*; *P. largaense* = *Peronoceras largaense*; *D. hoelderi* = *Dactylioceras hoelderi*; *F. disciforme* = *Fanninoceras disciforme*; *F.* fannini = *Fanninoceras fannini*; *A. behrendseni* = *Austromorphites behrendseni*; *E. meridianus* = *Eoamaltheus meridianus*; *M. externum* = *Meridiceras externum*; *M. chilcaense* = *Miltoceras chilcaense*. Fm. = Formation.

6.2. Lithofacies of the study area

Four stratigraphic sections (Arroyo Serrucho (E–E', F–F'), Las Overas and Las Overas C, Figure 6.3) have been logged and sampled within two field seasons in spring 2014 and 2016, by the science party including Hugh Jenkyns and Micha Ruhl (University of Oxford, UK), Stephen Hesselbo (University of Exeter, UK), Aisha Al-Suwaidi (Peroleoum Institute, UAE), Susana Damborenea and Miguel Manceñido (University de la Plata, Argentina) and myself. Detailed lithological descriptions and lithologs of all studied sections can be found in the appendix A-8 to A-11 and Figure A-8 to A-11, respectively. Digital lithologs can be found in D-A-3.

The section Arroyo Serrucho E–E' is the lowest stratigraphic section examined in this study, located along the Serrucho riverbed (Figure 6.3, 6.5 and 6.6A). The section covers 15.7 m and comprises calcareous and fossiliferous, red-weathering mud-, silt- and sandstones, and some intercalated volcanic ash beds. The individual beds are between 10 to 60 cm thick and show fining- and thickening upwards trends. The rich fauna includes bivalves in life position, crinoids and trace fossils (*Thalassinoides* and *Lapispira bispiralis*). Shell debris is more common in the upper 10 cm of the individual beds. Abundant gastropods were observed stratigraphically just below the section.

Arroyo Serrucho F–F' is also located along the riverbed and covers 30.2 m (Figure 6.3, 6.5, and 6.6). The base of the section lies approximately 50 m higher in stratigraphy compared to the top of the section Arroyo Serrucho E–E' (see Figure 6.5A). The lithology is similar to that of Serrucho E–E', comprising red-weathering calcareous and fossiliferous mud- silt- and sandstones as e.g. in Figure 6.6.B, with some intercalated volcaniclastic beds. Fossils in life position, however, occur only at the base of the sections. Towards the top of the section the lithology contains an increasing amount of finer grained mudstones and some siderite-cemented beds occur.

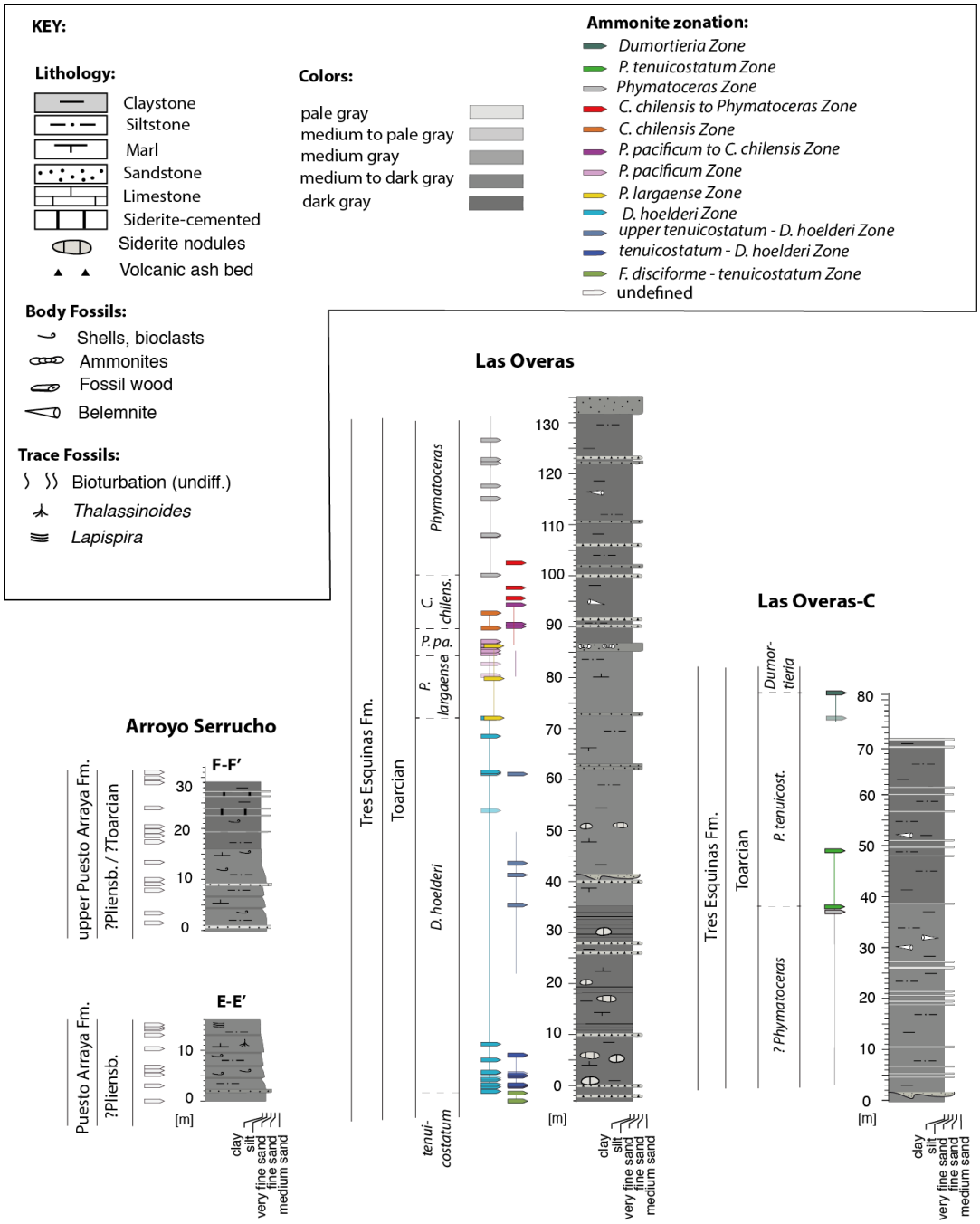

Figure 6.5: Simplified lithological logs of the Sections Arroyo Serrucho E-E' and Arroyo Serrucho F-F', Las Overas and Las Overas-C, including Ammonite zonal assignements. Detailed lithological logs can be found in the appendix (Figure A-8 to A-11), and digital versions including sample positions can be found in the digital appendix D-A-3.

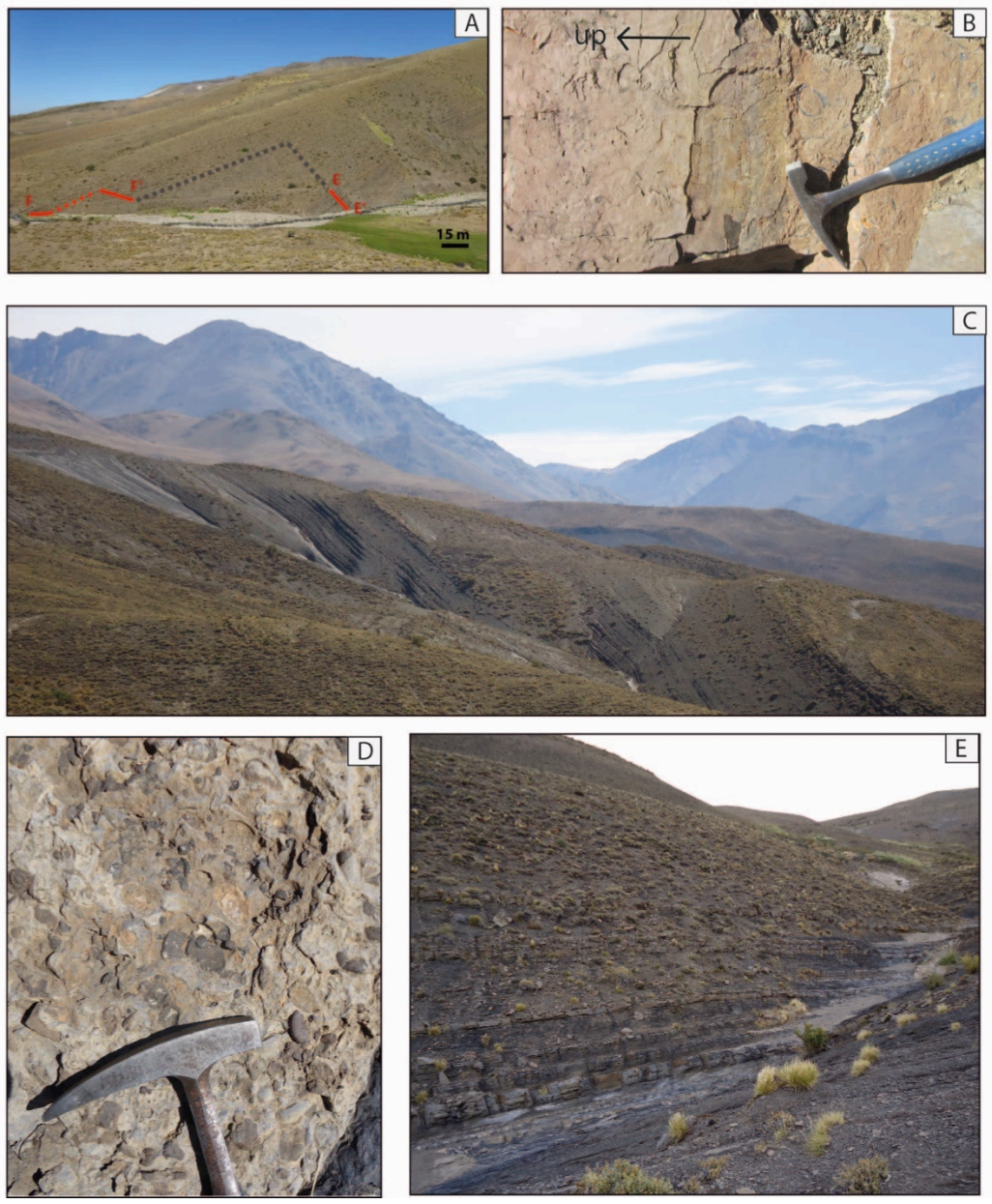

Figure 6.6: **A:** Photograph showing the relative locations of Arroyo Serrucho E–E' and F–F'. **B:** Lithology of a fining-upward bed as characteristic of the lithology of Arroyo Serrucho F–F'. **C:** View on the lower Las Overas section. **D:** ammonite-rich phosphate bed at ~85m in the Las Overas section. **E:** View on the upper Las Overas section.

The Las Overas section is located in the Overas creek, about 600 m NNE of Arroyo Serrucho F–F', and covers 133.4 m of stratigraphy (Figure 6.3). The section lies stratigraphically above the Arroyo Serrucho section; however, the stratigraphic gap between the sections could not be determined in the field. The sediments are generally

finer grained compared to those of the Arroyo Serrucho sections. Ammonites are common, but no bivalves are present in life position. Laminated shales beds appear within the lower ~35 m. Red to pink weathering siderite nodules and siderite cemented beds appear within the lower ~52 m of the section. From 35 m upwards, cross-bedded, erosional storm deposits occur commonly and the fine-grained calcareous mudstones appear lighter in colour. A distinct condensed and phosphate-rich bed with abundant ammonites and fossil wood fragments appears between ~85–86.5 m (Figure 6.5). From ~86.5 m upwards, the lithology changes to very homogenous, dark grey and silt-rich mudstone facies (see Figure 6.5) with commonly intercalated cross-bedded arenaceous deposits and with the local occurrence of belemnites in distinct horizons.

The base of the Las Overas-C section is located approximately 400 m NNE of the top of the Las Overas section (Figure 6.3). The Las Overas-C section continues stratigraphically above the Las Overas section. The exact relative stratigraphic position of the top of Las Overas and the base of Las Overas-C could not be determined in the field. The lithology comprises a very homogenous succession of silt-rich mudstones and intercalated beds of sandstone with internal structures (cross-bedding) and hard-cemented mudstone beds.

6.3. Biostratigraphic framework of the study area

Within the course of two field seasons, 10 ammonites were collected from the Arroyo Serrucho E–E' section, 17 ammonites from the Arroyo Serrucho F–F' section, 57 ammonites from the Las Overas Section and 5 from the Las-Overas C Section. The determinations of collected ammonite specimens were performed by Dr Alberto Riccardi at the National University La Plata, Argentina. The preservation of the collected fossils is generally poor. Specimens collected within the stratigraphy corresponding to Las Overas and Las Overas-C section could be assigned to ammonite zones. The species determination of each sample has not yet been provided. The ammonite biostratigraphy used in the following chapter is based on the first occurrence of ammonites identified for a specific ammonite zone (see Figure 6.4). A

list of ammonite samples, corresponding stratigraphical position and zonal interpretation can be found in the digital appendix D-A-4.

The lowermost Las Overas section comprises ammonites allocated to the upper *Fanninoceras disciforme* to *D. tenuicostatum* Andean ammonite zones (see Figure 6.5). Ammonites identified as indicative for the *Dactylioceras hoelderi* Zone appear between -1.15 to 72.1 m, suggesting a stratigraphically expanded expression of the Zone. The *Peronoceras largaense* Zone (72.1 to 84.7 m), *Peronoceras pacificum* Zone (86.2 to 87 m) and *Collina chilensis* Zone (89.7 to 100.13 m) appear to be stratigraphically condensed. Uncertainties in the biostratigraphic interpretation occur at the upper *P. largaense* and lower *P. pacificum* Zone, where ammonites of both zones appear in the same stratigraphic horizon.

The Las Overas-C section comprises a single ammonite indicative for the *Phymatoceras* Zone (37 m), overlain by beds containng ammonites indicating the *Phlyseogrammoceras tenuicostatum* Zone between 38 and 49 m. A single *in situ* ammonite identified as evidence for the *Dumortieia* Zone ammonite Zone has been found at ~79.5 m, above the top of the studied interval of the Las Overas-C section, and a further ammonite, *ex situ*, slightly below (74 m), indicating the *Dumortieia* ammonite Zone boundary to be present at least at the 79.5 m level.

6.4. Discussion

Depositional setting

The lithological observations of the Arroyo Serrucho sections (E–E' and F–F') correspond well with the previous descriptions of the near-shore to inner-shelf deposits of the Pliensbachian Upper Puesto Aarraya Formation by (Gulisano and Pleimling 1995). The carbonate-rich deposits in the Arroyo Serrucho E–E' and the lower Arroyo Serrucho F–F' sections, comprising a rich fauna including bivalves in life position and common burrows, indicate well-oxygenated conditions. Abundant gastropods were observed stratigraphically below the Arroyo Serrucho E–E' section, which indicate the inner-shelf environment. Furthermore, the occurrence of *Lapispira*

bispirales from the Neuquén Basin is restricted to deposits of the shore-face and the offshore–shoreface transition Zone (Lanes *et al.* 2006). The increase of fine-grained sediments (mudstones) in the Arroyo Serrucho F–F' section likely indicates the gradual deepening during basin subsidence and sea-level rise. The observed lithology in the Las Overas and Las Overas-C sections corresponds to the descriptions of the lower Tres Esquinas Formation, representing gradual deepening from inner-shelf to less well-oxygenated outer shelf deposits, as described by Gulisano and Pleimling (1995). As the study area is located close to the seaway that fed water from the Panthalassa Ocean into the Neuquén Basin (see Figure 6.1 and 6.2), the gradual deepening of the depositional environment was likely influenced by sea-level changes induced by both global sea-level fluctuations and basin subsidence.

Stratigraphy

Although no ammonite biostratigraphy is available for the Arroyo Serrucho sections, the occurrence of the trace fossil *Lapispira bispiralis* in the upper Arroyo Serrucho E–E' section suggests that the strata correspond to sediments older than Toarcian, as the occurrence of *Lapispira* in the Neuquén Basin is only known from the Hettangian to Late Pliensbachian strata (Lanes *et al.* 2006). The stratigraphically higher section Arroyo Serrucho F–F' cannot be allocated to a zone or stage level, but likely represents the uppermost Puesto Arroyo Formation, and therefore Uppermost Pliensbachian strata.

The biostratigraphic framework of the Las Overas and Las Overas-C sections, based on the Andean ammonite zonation, indicates Lower Toarcian to lower Upper Toarcian (*tenuicostum* to *Phymatoceas* Zone), and lower Upper to uppermost Toarcian (*Phymatoceras* to lower *Dumortieria* Zone), respectively. This stratigraphic interval is approximately equivalent to the *tenuicostatum* to upper Toarcian *aalensis* Zone of the NW European ammonite zonation scheme (based on Riccardi 2008a, Riccardi 2008b, see Figure 6.7).

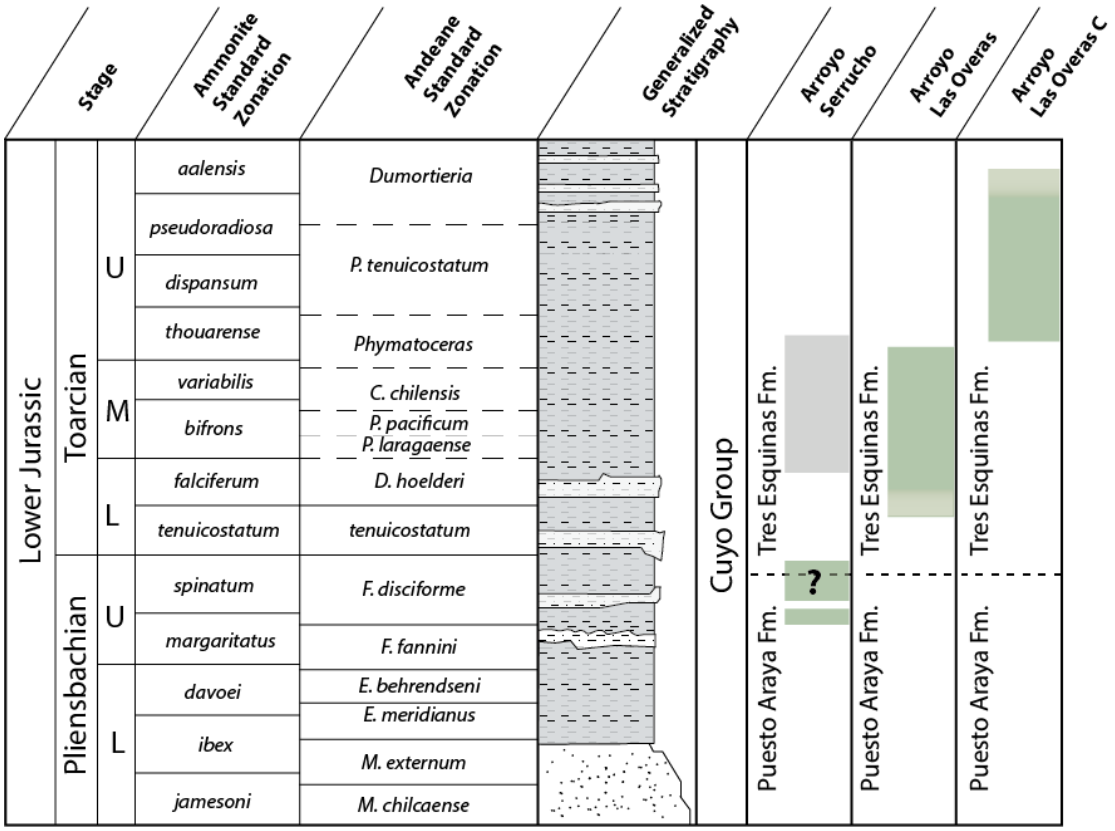

Figure 6.7: Table showing the epoch/age, standard northwestern European biozones (Page 2004), Andean ammonite zonation and biostratigraphy and correlation to the European zonation adapted from Riccardi (2008a, 2008b). Generalized stratigraphic log of the Puesto Arraya and Tres Esquinas Formation of the Cuyo Group, stratigraphic and biostratigraphic intervals present within the herein studied sections (green) and previously studied sections (grey, Al-Suwaidi *et al*. 2016 adapted to the newly defined *D. tenuicostatum–D. hoelderi* boundary). Ammonite biostratigraphy is adapted from Riccardi (2008a, 2008b), chronozones, and epoch/age are adapted from Gradstein *et al*. (2012). Stratigraphic log adapted from Gulisano & Pleimling 1995. Key for abbreviations given in Figure 6.4.

The *P*. *largaense*, *P*. *pacificum* and *C*. *chilensis* Zones (approximately equivalent to *bifrons* and *variabilis* zones) appear stratigraphically less expanded compared to the under- and overlying *D*. *hoelderi* und *Phymatoceras* Zone, probably related to differences in the sedimentation rate. The ammonite-rich phosphate bed in the *P. pacificum* Zone (Las Overas section, ~85 to 86.5 m, see Figure 6.5) suggests a condensed nature of the lithology and supports a low sedimentation rate in this interval.

The biostratigraphic framework of the Las Overas section suggests a stratigraphic overlap with the previously studied, biostratigraphically well-calibrated sections in the Arroyo Serrucho creek. As shown in Figure 6.3, the Arroyo Serrucho sections A to D are located in close proximity to the sections studied herein (300 to 600 m NW). The area between those sections appears tectonically undisturbed and the stratigraphic appearance of ammonite zones should be comparable, aiding a calibration of the ammonite biostratigraphy established herein.

The ammonite biostratigraphy of the Arroyo Serrucho Sections A to D (Al-Suwaidi *et al*. 2016) suggests a comparably condensed stratigraphic expression of the *P. pacificum* and *C. chiliensis* zones (see Figure 6.8). The *D. tenuicostatum–D. hoelderi* zone boundary, however, lies approximately 45 m lower in the Las Overas section compared to the Arroyo Serrucho section. Al-Suwaidi *et al*. (2016) defined this boundary based on the first occurrence of *Harpoceras* cf. *serpentinum* (Schlotheim), classified as indicative genera for the *Dactylioceras hoelderi* Assemblage Zone (Riccardi 2008a, 2008b). In the Serrucho section, no ammonites were found below the horizon containing this specimen, which indicates the presence of the *D. tenuicostatum* standard Zone. Therefore, the *D. tenuicostatum–D. hoelderi* boundary can readily be adapted to the lower stratigraphic position indicated by the Las Overas ammonite assemblage (red line, Figure 6.8). However, the newly defined boundary should be verified by actual ammonite determinations once available.

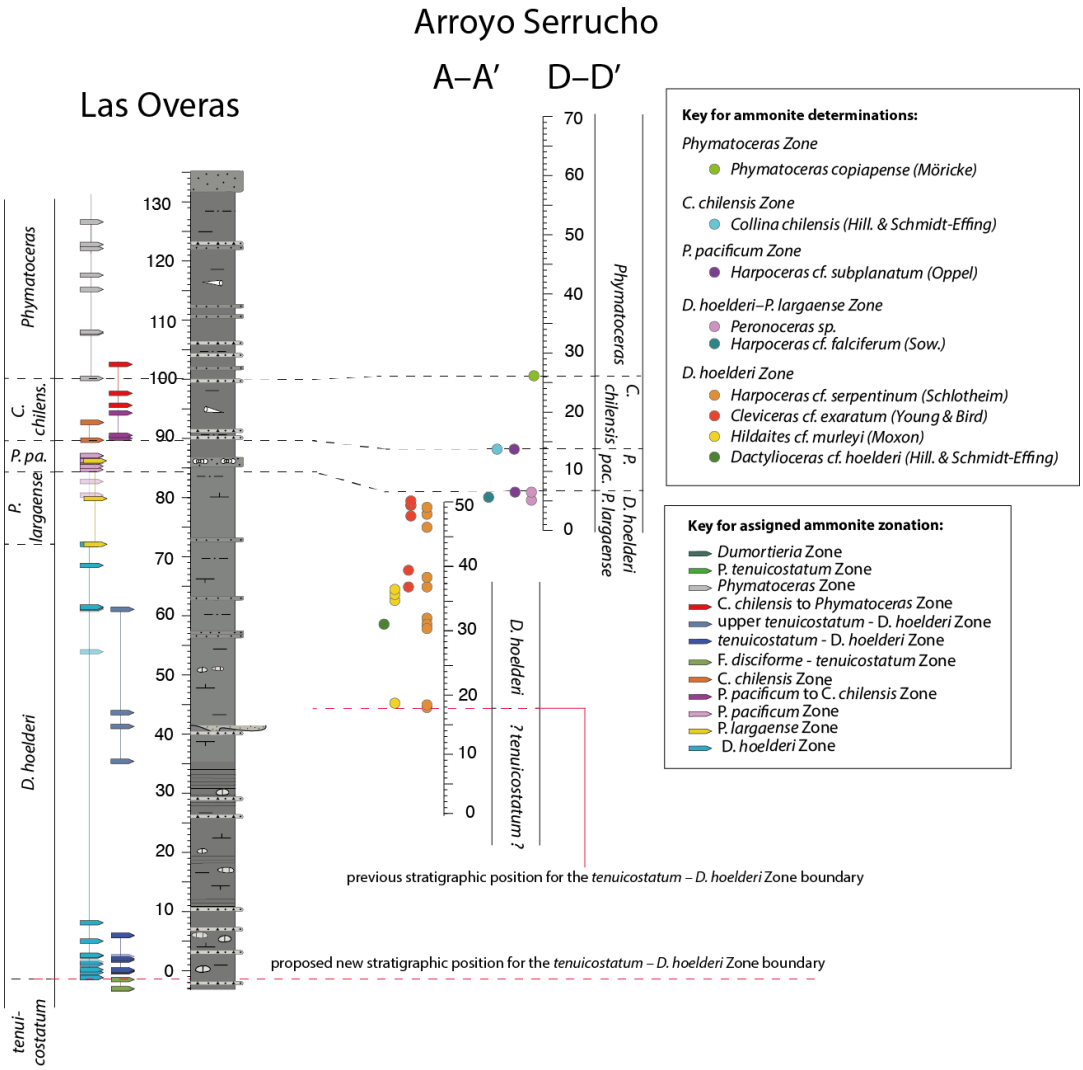

Figure 6.8: Correlation of the provisional biostratigraphy of the Las Overas section (this study) and the nearby biostratigraphically calibrated sections Arroyo Serrucho A–A' and D–D'. Ammonite biostratigraphy for Arroyo Serrucho sections adapted from Al-Suwaidi *et al*. (2016). The proposed new boundary for the *D. tenuicostatum* - D. *hoelderi* Zone boundary is marked as dashed red line.

6.5. Conclusion

The four studied sections (Arroyo Serrucho E–E', F–F'), Las Overas and Las Overas-C, located in the Mondoza Province of the northern Neuquén Basin, correspond to the Upper Puesto Arraya and Lower Tres Esquinas Formation and record Late Pliensbachian to Late Toarcian marine sedimentation during gradual deepening of the basin. The partial stratigraphic overlap of the Las Overas section with the well-studied

Arroyo Serrucho sections of previous studies (Mazzini *et al*. 2010, Al-Suwaidi *et al*. 2016) allows validation of the biostratigraphical framework, and suggests the *D. tenuicostatum–D. hoelderi* boundary to be stratigraphically below the previously defined stratigraphic level. The new boundary supports a stratigraphically expanded expression of the D. *hoelderi* Zone, compared to the comparably condensed *P. largaense*, *P. pacificum* and *C. chilensis* zones.

Chapter 7 : Chemostratigraphic constraints of the Early Jurassic Toarcian stage in the Neuquén Basin, Argentina

7. Abstract

The Toarcian oceanic anoxic event (T-OAE), recognized by the widespread coeval appearance of organic-rich marine and lacustrine black shales, is associated with a negative carbon-isotope excursion, which has previously also been documented in the Neuquén Basin, Argentina. A new biostratigraphically calibrated chemostratigraphic record from stratigraphically expanded sections located in the N Neuquén Basin expands previous records from the nearby Arroyo Serrucho section to stratigraphically lower and higher strata, covering the uppermost *D. tenuicostatum* to *Dumortieria* Andean ammonite zones of the Toarcian Stage. The new record likely illustrates the complete negative carbon-isotope excursion event associated with the T-OAE and provides the stratigraphical framework for future work on the accurate numerical dating of volcanic ash beds intercalated in the studied sections. Characterization of the organic matter suggests differences between the depositional setting and burial history in comparison to the chemostratigraphic record from the S Neuquén Basin. Correlation of the $\delta^{13}C_{TOC}$ record of the studied section to a coeval European record illustrates the global nature of the Early Toarcian isotope record and corresponding disturbance of the global sulfur cycle, suggested by the coeval occurrence of siderite-bearing strata in both sections.

7.1. Introduction

The Early Toarcian Oceanic Anoxic event (T-OAE, ~183 Myr) is marked by severe global environmental and oceanographic change. The event was initially recognized by the apparent coeval appearance of organic-rich laminated black shales from globally distributed marine sedimentary records of the Early Toarcian *tenuicostatum* and *falciferum* Boreal ammonite zones (Jenkyns 1988). It is thought that the emission of large amounts of greenhouse gases into the ocean-atmosphere system led to a cascade of environmental changes, such as the development of widespread anoxic/euxinic oceanic conditions, favouring the deposition of organic-rich sediments

(Jenkyns 2010). Increased atmospheric CO_2 levels (Hesselbo *et al.* 2000, McElwain *et al.* 2005) may have supported a rise in global temperatures (Dera *et al.* 2009a, Gradstein 2012, Korte *et al.* 2015) and accelerated the hydrological cycle and weathering rates, subsequently leading to enhanced riverine input of nutrients to the ocean and lakes (Jenkyns *et al.* 2002, Cohen *et al.* 2004, Dera *et al.* 2009a, Kemp *et al.* 2011, Percival *et al.* 2016, Them *et al.* 2017b, Xu *et al.* 2017b). Increased delivery of nutrients and freshwater into the oceans likely resulted in productivity- and stratification-driven shallow-water low-oxygen environments, supporting the burial of large amounts of organic matter (e.g. Jenkyns 2010). Furthermore, the event is associated with an abrupt and a major extinction of marine organisms (Little and Benton 1995, Harries and Little 1999, Caruthers *et al.* 2014), exemplifying the magnitude of the environmental impact associated with the T-OAE.

The geochemical record of the T-OAE is characterized by the appearance of a broad positive carbon-isotope excursion, punctuated by an abrupt negative shift of approximately −3 to −9‰, depending on the analyzed material (Jenkyns and Clayton 1986, 1997, Hesselbo *et al.* 2000, Hesselbo *et al.* 2007, Hermoso *et al.* 2009a). The positive excursion is attributed to large-scale organic-carbon burial in various settings (shelf-sea, deep marine, continental lakes; Jenkyns and Clayton 1986, Jenkyns 1988, Xu *et al.* 2017b), which removed a large amount of isotopically light carbon from the ocean-atmosphere system, and is manifested by the globally widespread organic-rich deposits. The negative excursion has been recorded in various carbon-isotope reservoirs (wood, carbonate, bulk marine organic matter and compound specific marine organic matter), at a number of locations in Europe, as well as being globally registered in Japan, China, Siberia, Canada, and even in the southern Hemisphere, in the Neuquén Basin, Argentina (Sælen *et al.* 2000, Schouten *et al.* 2000, Al-Suwaidi *et al.* 2010, Caruthers *et al.* 2011, Gröcke *et al.* 2011, Suan *et al.* 2011, Xu *et al.* 2017b). The coeval appearance of the signal in both the marine and terrestrial realm is thought to indicate a global perturbation of the carbon cycle (e.g. Schouten *et al.* 2000, Al-Suwaidi *et al.* 2010, French *et al.* 2014). The negative excursion is commonly attributed to the release of large amounts of isotopically light carbon into the ocean–atmosphere system (Hesselbo *et al.* 2000, McElwain *et al.* 2005, Svensen *et al.* 2007).

The ultimate trigger mechanisms that sourced the increased levels of atmospheric

CO_2 leading to the development of cascading environmental perturbations associated with the T-OAE is subject to ongoing debate. The apparent synchrony (within dating errors) between the environmental perturbations associated with the T-OAE, and the emplacement of the Karoo-Ferrar Large Igneous Province (LIP), points to the increased release of volcanically sourced greenhouse gases (Pálfy and Smith 2000, Wignall 2001, Pálfy 2002, Caruthers *et al.* 2014, Sell *et al.* 2014, Burgess *et al.* 2015). However, quantitative estimates of LIP volatiles are not thought to have been high enough to have significantly perturbed the carbon cycle (Dickens *et al.* 1995, Wignall 2001, Self *et al.* 2005, Self *et al.* 2006, Beerling and Brentnall 2007, Svensen *et al.* 2007, Sell *et al.* 2014). The duration of the main phase of magmatism (~6 Myrs; e.g. Jourdan *et al*. 2005) further compromises the idea of a simple casal link to such a short-lived event as the T-OAE (> 1Myr; e.g. Kemp *et al.* 2011, Boulila *et al.* 2014, Huang and Hesselbo 2014).

Further hypotheses suggest that initial volcanic emission and subsequent warming triggered the dissociation of large amounts of gas hydrates, which injected biogenic and therefore isotopically light carbon into the ocean–atmosphere system (e.g. Hesselbo *et al.* 2000, McElwain *et al.* 2005). However, the pattern and magnitude of change in carbon dioxide levels are difficult to reconcile with the input of hydrate-derived methane due to the uncertainty of the size of ancient hydrate reservoirs (Milkov 2004, McElwain *et al.* 2005). Alternatively, the degassing of organic-rich strata (Gondwana coals and shales), caused by thermogenic alteration triggered by sill intrusion during the onset of the Karoo-Ferrar large LIP emplacement has been considered as source for the increased atmospheric CO_2 levels (McElwain *et al.* 2005, Svensen *et al.* 2007, Svensen *et al.* 2012).

In any case, the onset of the Karoo-Ferrar LIP plausibly appears to have been the initial driving force. Key to this hypothesis is the synchrony of the LIP volcanism and sill emplacement and the deposition of organic-rich sediments defining the OAE. The sill intrusions emplaced in the Karoo and Ferrar provinces are well dated (e.g. Svensen *et al.* 2007, Svensen *et al.* 2012, Burgess *et al.* 2015); however, the accurate dating of the onset of the T-OAE is challenging due to the lack of datable strata within the well-studied Toarcian sections in NW Europe. Several sedimentary sections of

Toarcian age in North and South America contain intercalated volcanic ash beds suitable for radioisotopic dating. Previous studies on suitable sections, however, generally lack enough of a well-defined geochemical and biostratigraphical framework to define unambiguously the T-OAE, and allow a temporal correlation to the intrusive (and extrusive) phase of the Karoo-Ferrar LIP. Other sections may be well constrained regarding the temporal framework (bio- and chemostratigraphy), but radiometric ages were taken from layers stratigraphically decoupled from the negative excursion, requiring interpolation, or only providing dates with large error margins (see Figure 7.1 and references therein).

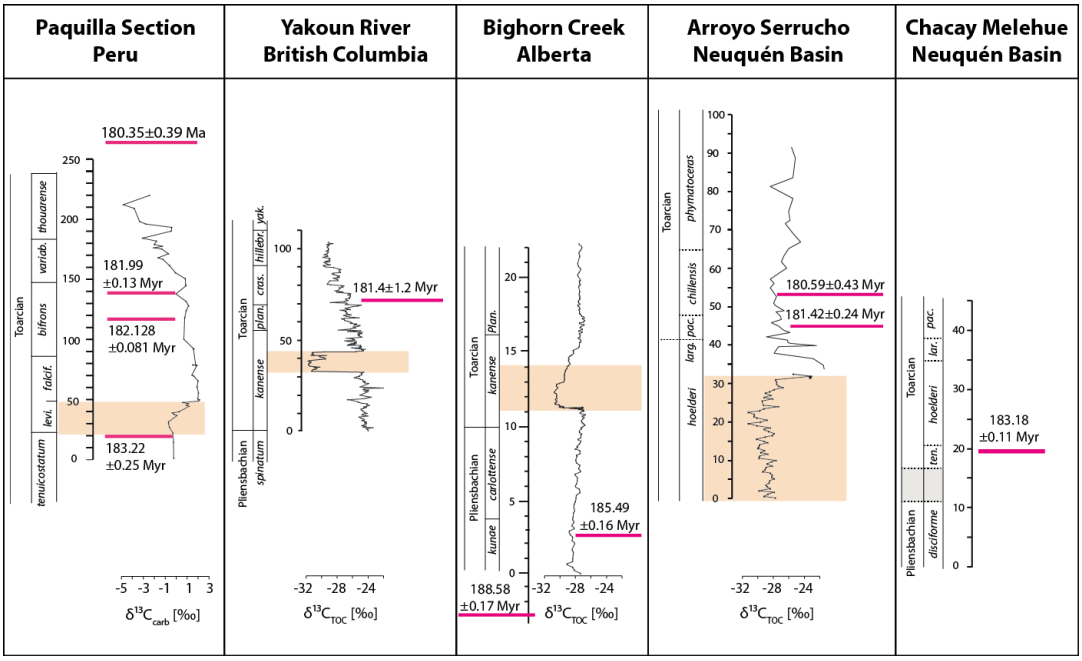

Figure 7.1: Comparison of Upper Pliensbachian and Lower Toarcian sections. Mochras core: $\delta^{13}C_{TOC}$ data from (Xu *et al*. 2018). Peru: $\delta^{13}C_{carb}$ data from Guex *et al*. 2012a, with ammonite biostratigraphy using European zonation, radiometric dates from Sell *et al.* (2014). British Columbia: $\delta^{13}C_{TOC}$ and N American ammonite zonation adapted from Caruthers *et al*. 2011, 2012, radio-isotopic age from Pálfy *et al.* (1997). Bighorn Creek, Alberta: $\delta^{13}C_{TOC}$ and radio-isotopic data from Them *et al.* (2017a), Them *et al.* (2017b). Arroyo Serrucho, Argentina: $\delta^{13}C_{TOC}$ from Mazzini *et al.* (2010) and Al-Suwaidi *et al.* (2016), Andean ammonite zonation modified from Al-Suwaidi *et al.* (2016), base of D. *hoelderi* Zone adapted to new biostratigraphical framework (see Chapter 6), radioisotopic ages from Mazzini *et al.* (2010). Chacay Melehue, Argentina: Andean ammonite zonation and radioisotopic age after Riccardi and Kamo (2014). Intervals marked in orange indicate the stratigraphic position of the T-OAE.

The Neuquén Basin in Argentina offers a suitable framework for further integrated studies on the chemo-, bio- and chronostratigraphy of the Toarcian stage. Recent studies on the geochemical record of the Upper Pliensbachian and Toarcian stages of this area (Al-Suwaidi *et al.* 2010, Al-Suwaidi *et al.* 2016) have proven the expression of the T-OAE in the marine sedimentary record in this basin, and the correlation between the European and Andean ammonite zonation (Riccardi 2008a, 2008b) allows comparison to the well-studied chemostratigraphic records from NW Europe. Numerous volcanic ash beds intercalated in the Lower Jurassic marine sedimentary succession of the back-arc setting provide material for absolute dating methods.

This chapter aims to provide a biostratigraphically calibrated chemostratigraphic record of the sedimentary record of the Toarcian stage in the N Neuquén Basin, Argentina, as a framework for further chronological constraints on the Toarcian Oceanic Anoxic Event and the temporal correlation to the Karoo-Ferrar LIP. The characterization of organic and inorganic matter throughout the studied interval provides further information about the depositional environment and the nature of the carbon-isotope signal.

7.2. Materials and Methods

- All materials were collected within two field seasons in spring 2014 and 2016, with the help of Hugh Jenkyns and Micha Ruhl (University of Oxford, UK), Stephen Hesselbo (University of Exeter, UK), Aisha Al-Suwaidi (Petroleoum Institute, UAE), Susana Damborenea and Miguel Manceñido (University de la Plata, Argentina).
- Bulk organic carbon-isotope analysis ($\delta^{13}C_{TOC}$) was performed at the Stable Isotope laboratory of the Open University (Milton Keynes) on a total of 553 samples from the 4 studies sections: Arroyo Serrucho E-E' (20 samples, 0.8 m average sample spacing), Arroyo Serrucho F–F' (62 samples, 0.4 m average sample spacing), Las Overas (408 samples, 0.4 m average sample spacing). For details on analytical method see Chapter 1.4.1

- Rock Eval analysis was performed on 351 samples at the Department of Earth Sciences, Oxford). For details on analytical method see Chapter 1.4.3
- Palynological work was performed by Malcolm Jones (sample preparation, Palynological Laboratory Services Ltd) and by Paul Dodsworth (sample analysis and interpretation, StrataSolve Ltd) on 5 samples. For details on analytical method see Chapter 1.4.8
- For detailed litho- and biostratigraphical framework of the here studied sections see Chapter 6.
- Data tables can be found in appendix D-A-5

7.3. $\delta^{13}C_{TOC}$ record of the Toarcian stage in the Northern Neuquén Basin

The lithostratigraphic framework of the stratigraphic sections Arroyo Serrucho F–F' and E–E' suggests that the corresponding strata belong to the upper Puesto Arraya Formation, representing Upper Pliensbachian deposit (see Chapter 6), although the sections are not biostratigraphically calibrated. The Arroyo Serrucho F–F' and E–E' sections show carbon-isotope values ranging between −22.4 and −25.1‰, and −22.4 to −24.8‰, respectively (see Figure 7.2).

The $\delta^{13}C_{TOC}$ values recorded in the Las Overas section (see Figure 7.2) range between −21 and −31‰. The lowermost Las Overas section illustrates a sharp positive shift, from values as low as −27.1‰ at the bottom of the section (*D. tenuicostatum* Zone) to −21.3‰ in the lowermost *D. hoelderi* zone (−0.3 m).

The positive shift is followed by a stratigraphically expanded negative excursion throughout most of the *D. hoelderi* Zone. The excursion comprises a gradual, stepwise onset, interrupted by short positive shifts up to 16.8 m above the base of the section, where carbon-isotope values are as low as −30.4‰ at (see Figure 7.2). From this point, isotope values stay relatively low up to 46.1 m with an average of ~ −29 ‰, albeit fluctuating by 1-2‰ on a 0.4 to 2 m scale. The upper part of the negative

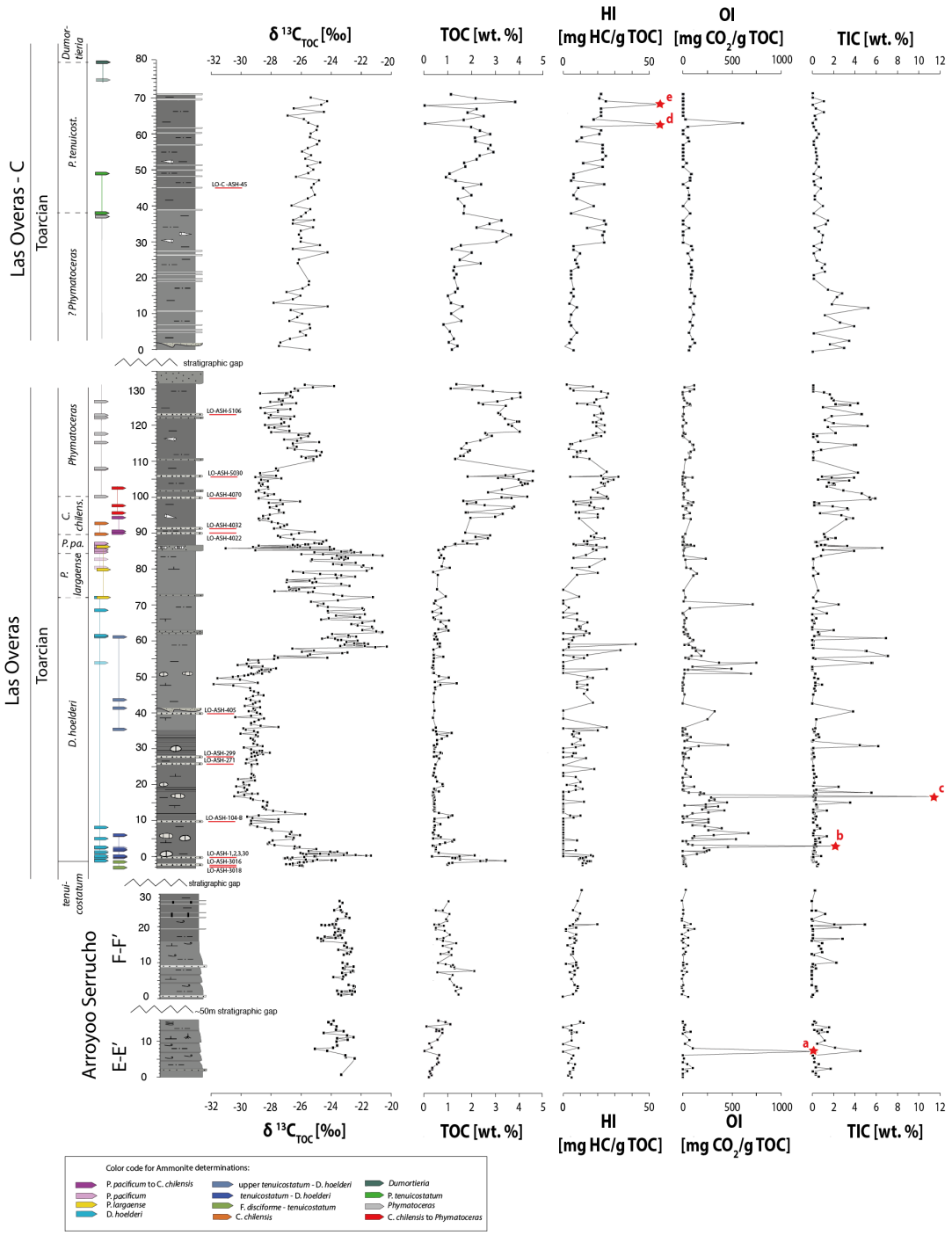

Figure 7.2: $\delta^{13}C_{TOC}$ record and Rock Eval data (TOC, HI, OI, TIC) of the four studied sections, stratigraphic position of samples volcanic ash beds marked in red. Rock Eval outlier values marked with red stars. Oxygen Index [mg CO_2/g TOC]: **a)** 1350 **b)** 1567 **c)** 2567. Hydrogen Index [mg HC/g TOC] (values not plotted not in scale): **d)** 729 mg HC/g TOC, **e)** 760 mg HC/g TOC.

excursion in the lower upper *D. hoelderi* zone is marked by two distinct negative $\delta^{13}C_{TOC}$ shifts to −31.8 and −31.5‰, appearing between ~46.5 and 51 m, and a third shift at 53.4 m reaching down to −31.4‰, followed by a sharp turn towards more positive isotope values, reaching a maximum of −20.3 ‰ at 58 m. The isotope record of the subjacent strata is highly fluctuating (~2‰), but characterized by an overarching gradual ~6 ‰ negative trend throughout the upper *D. hoeldri* to upper *P. largense* zone, reaching down to ~ −27 ‰, before increasing again up to −20.5‰ within the uppermost *P. largense* Zone. The lower *P. pacifcum* zone, which corresponds to a condensed and ammonite-rich phosphate nodule bed, is marked by a negative shift from −22.5‰ to ~ −28.5 ‰.

Values increase again to ~ −24 ‰ just above the phosphate bed. The *C. chilensis* and lower *Phymatoceras* zone are marked by a gradual ~4‰ negative shift and a subsequent sharp (~3‰) positive shift (ca. between 106–111 m), followed by a similar sequence in the subjacent strata of the *Phymatoceras* zone. The Las Overas-C section is characterized by a ~3‰ positive isotope shift, from ~ −27 to ~ −24‰ between the base of the section and the upper *P. tenuicostatum* zone (see Figure 7.2).

7.4. Geochemical organic-matter characterization

Rock Eval Parameters

The Total Organic Carbon content (TOC) of the lowermost studied section (Arroyo Serrucho E–E') is marked by low TOC values of 0.4 wt% on average, showing a gradual increase from 0.2 wt% at the bottom to ca. 1 wt% at the top of the section (see Figure 7.2). Arroyo Serrucho F–F' is characterized by slightly higher TOC values (0.9 wt% in average), and a gradual decrease from ca. 1.4 wt% to 0.7 wt% throughout the section.

The Las Overas section is marked by TOC values between 0.6 and 3% in the uppermost *D. tenuicostatum* Zone. The values drop in the lowermost *D. hoelderi* Zone and stay as low as 0.4 wt% on average throughout the *D. hoelderi* and *P. largense* Zone. The low TOC values correspond to the stratigraphically expanded negative carbon-isotope excursion and the subsequent positive isotope shift. Individual maxima

in TOC, reaching up to 1 wt%, corresponding to small-scale positive isotope shifts in the lower *D. hoelderi* Zone, and to negative isotope shifts in the upper *D. hoelderi* Zone. The TOC values in the Las Overas section increase gradually from the base of the *P. pacificum* Zone onward, reaching ~4 wt% in the lower *Phymatoceras* Zone, concomitantly with the minima in $\delta^{13}C_{TOC}$, decrease to ca. 1 wt% concomitantly with the positive isotope shift, and increase again to values up to 3.7 wt% in the upper part of the section. A sharp drop in TOC appears in the uppermost metre, with TOC values falling to 0.7 wt%.

The average T_{max} of the analyzed samples from all four studied sections (T_{max}=520ºC) indicates a high thermal maturity of the sediments. Hydrogen Indices (HI, mg HC/g TOC) are generally low throughout all studied sections (<100 mg HC/g TOC), likely as a result of the thermal maturation. HI values recorded in the lower Las Overas section are considered as unreliable due to the low TOC (Tyson 1995). Oxygen Indices are also low (<100 mg CO_2/g TOC), although slightly elevated (~290 mg CO_2/g TOC in average) within the lowermost *hoelderi* Zone (-1.15 to 20 m). The Total Inorganic Carbon content (TIC) is low in the Arroyo Serrucho Sections (~0.8 wt%). The lower Las Overas section is marked by low (~0. 3 wt%) TIC values, with individual peaks reaching up to 7 wt%. The *chilensis* and *Phymatoceras* zones show slightly higher, albeit highly fluctuating TIC values (~1 wt% in average).

Palynofacies

Kerogen and oxidized slides of five samples from the Arroyo Serrucho F-F' (AS-520, 21.65 m) and Las Overas Section (LO-3019, -1.9 m; LO-146, 14.5 m; LO-484, 48.1 m; LO-5004, 101.3 m) have been analyzed for palynological organic matter content. Detailed description of the organic recovery can be found in the appendix (A-12).

The palynofacies of all studied samples is dominated by black phytoclast debris with subordinate dark brown fossil wood/coal fragments (Palynomaceral 4 and 1, respectively; Van der Zwan 1990, see Figure 7.3) and probably sapropelic amorphous organic matter (AOM). The Arroyo Serrucho F–F' sample (LO-520) contains the

largest relative amount of phytoclasts, which appear larger in size compared to those in stratigraphically higher strata. The relative amount of AOM increases up-sequence with increasing TOC content (see Table 7.1).

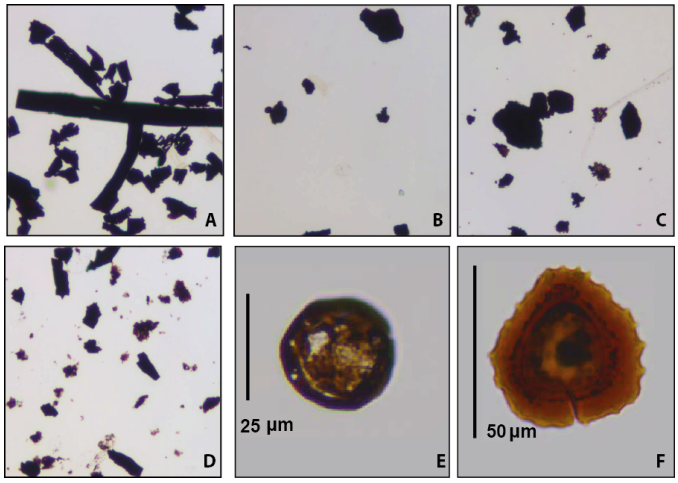

Figure 7.3: Phytoclast assemblages in kerogen slides (>15µm), 400 x 400 µm fields of view and Palynomorphs from the Arroyo Serrucho F–F' and Las Overas sections. A) Arroyo Serrucho AS-520, B) Las Overas LO-3019, C) Las Overas LO-484, D) Las Overas LO-500. E) *Corollina meyeriana* (Klaus 1960) Venkatachala & Goczán 1964, LO-3019 (kerogen), F) *Densosporites dentatus* (Waltz) Potonie & Kremp 1956, LO-146.

Table 7.1: Palynological distribution

Sample	Height [m]	AOM [absolute abundance 15mm=100 counts]	Phytoclasts	TOC [wt.%]	Diversity of Spores and Pollen in Kerogen/Oxidized slide
LO-5004	101.3	45	55	2.3	0/2
LO-484	48.1	18	2	1	2/4
LO-146	14.5	9	91	0.1	2/8
LO-3019	-1.9	1	99	0.9	0.9
AS-520	21.6	0	100	1	1

The recovery of pollen and spores from all samples was generally low (see Table 7.1), likely due to the relatively high thermal maturity of the Lower Jurassic strata in the study area. *In situ* Jurassic circumpolloid pollen (*Corollina meyeriana*) appear in kerogen samples, but are absent from preparations that have received extended

laboratory oxidation. Reworked Carboniferous spores are more numerous in the oxidized preparations (i.e. *Densosporites* spp., see Figure 7.3 and appendix A-12). The reworked spores have probably been liberated from coal fragments by the oxidative treatment, and/or have been derived from other organic matter in the rock matrix encasing the coals.

7.5. Mercury as a tracer for distal volcanism

Sedimentary mercury (Hg) concentrations can be used as a proxy for ancient distal volcanism (Percival *et al.* 2015). Subaerially emitted gaseous mercury, sourced directly from volcanic emissions, has an atmospheric residence time sufficient for global distribution (~0.5 to 2 years; Pyle and Mather 2003, Blum *et al.* 2014). Distal large-scale volcanism is therefore thought to overprint the mercury signal from local volcanism, such as the arc volcanism to the West of the Neuquén Basin (Percival *et al.* 2015). To emphasize the increase in sedimentary mercury concentrations due to increased environmental Hg levels, rather than the increase of organic matter to which mercury is typically absorbed, Hg concentrations are typically normalized against the sedimentary total organic matter content. The Total Organic Carbon content of the lower Las Overas section is generally low (see above). As expected, such low sedimentary organic carbon contents are matched by low mercury concentrations. Sample selection for the analysis of Hg concentrations was therefore based on samples with TOC>0.2 wt%.

The TOC-normalized mercury levels of samples from the Arroyo Serrucho F–F' section, give very low values (< 20 ppb/wt%, see Figure 7.4), likely representing undisturbed background values of the upper Pliensbachian sediments. Hg/TOC ratios are also low in the lowermost 3 m of the Las Overas section (<50 ppb/wt%), where TOC and $\delta^{13}C_{TOC}$ levels are relatively high. In the interval characterized by the negative CIE, Hg and Hg/TOC values are both increased. Hg/TOC values rise gradually up to 50 ppb/wt% at 20 m, decrease slightly at ~30 m, and increase sharply to 85 ppb/wt% at 34 m. The highest Hg/TOC concentrations appear in parallel with the most negative values in $\delta^{13}C_{TOC}$, comprising ~130 ppb/wt% between 50 to 55 m.

The subsequent sharp increase in $\delta^{13}C_{TOC}$ and TOC is associated with a decrease in Hg and Hg/TOC concentrations, and mercury levels stay low (<50 ppb/wt%) in the superjacent strata of the Las Overas section, and are even lower in the Las Overas-C section (<20 ppb/wt.%).

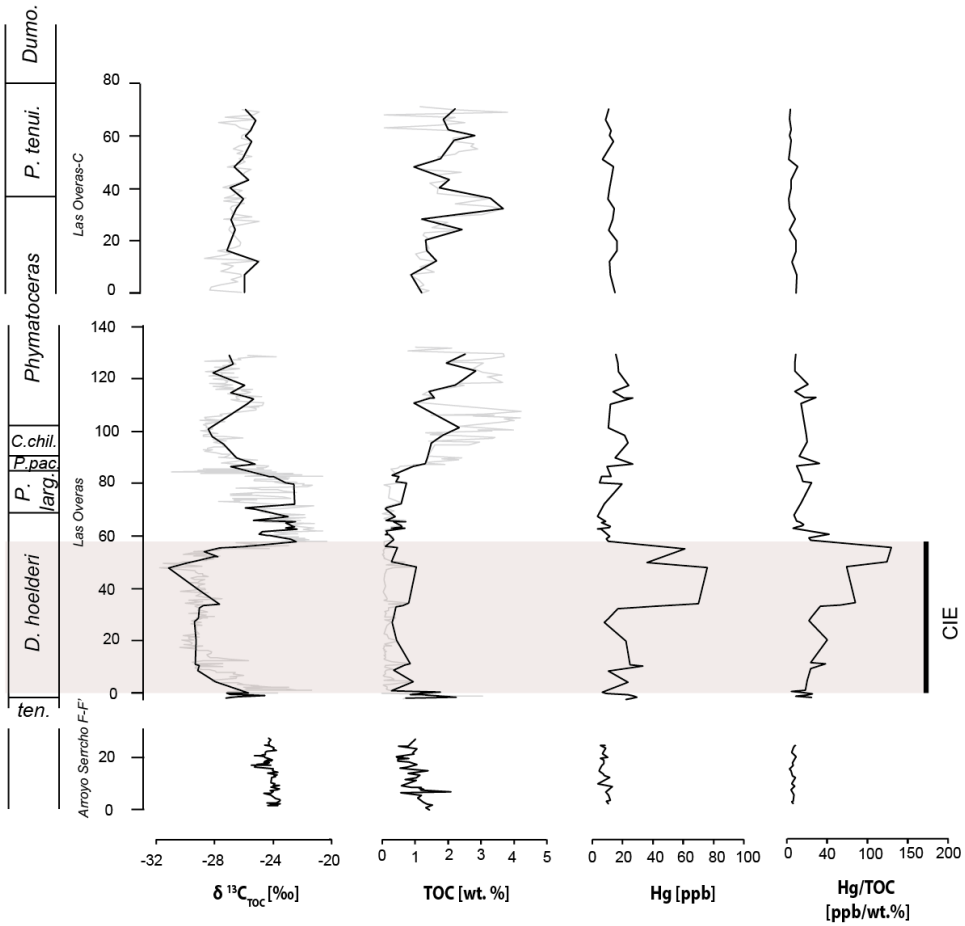

Figure 7.4: Bulk rock sedimentary mercury levels (Hg) and TOC normalized mercury levels (Hg/TOC) of the Las Overas F–F', Las Overas and Las Overas-C sections. $\delta^{13}C_{TOC}$ and TOC in high resolution (grey) and lower resolution corresponding to Hg analysis (black) are also shown.

7.6. Discussion

The new chemostratigraphic records from the Las Overas and Las Overar-C sections expand the Toarcian record of the previous studies on the Arroyo Serrucho creek to stratigraphically lower and higher strata. The chemostratigraphic records now covers

the uppermost *D. tenuicostatum* Zone (according to the newly defined base of the *D. hoelderi* Zone, see Chapter 6), to the lower *Dumorteria* Zone, interrupted by a stratigraphical gap between in the *Phymatoceras* Zone in between the top of the Las Oveas and the bass of Las Overas-C section (see Figure 7.2). The interval is equivalent to the Toarcian uppermost *D. tenuicostatum* to upper *pseudoradiosa* boreal ammonite zones (Riccardi 2008 a,b). The correlation of the $\delta^{13}C_{TOC}$ and TOC records of the Las Overas and previously studied nearby Arroyo Serrucho sections supports the accuracy of the biostratigraphic calibration of the *D. hoelderi* to lower *Phymatoceras* zones in the study area (see Figure 7.5).

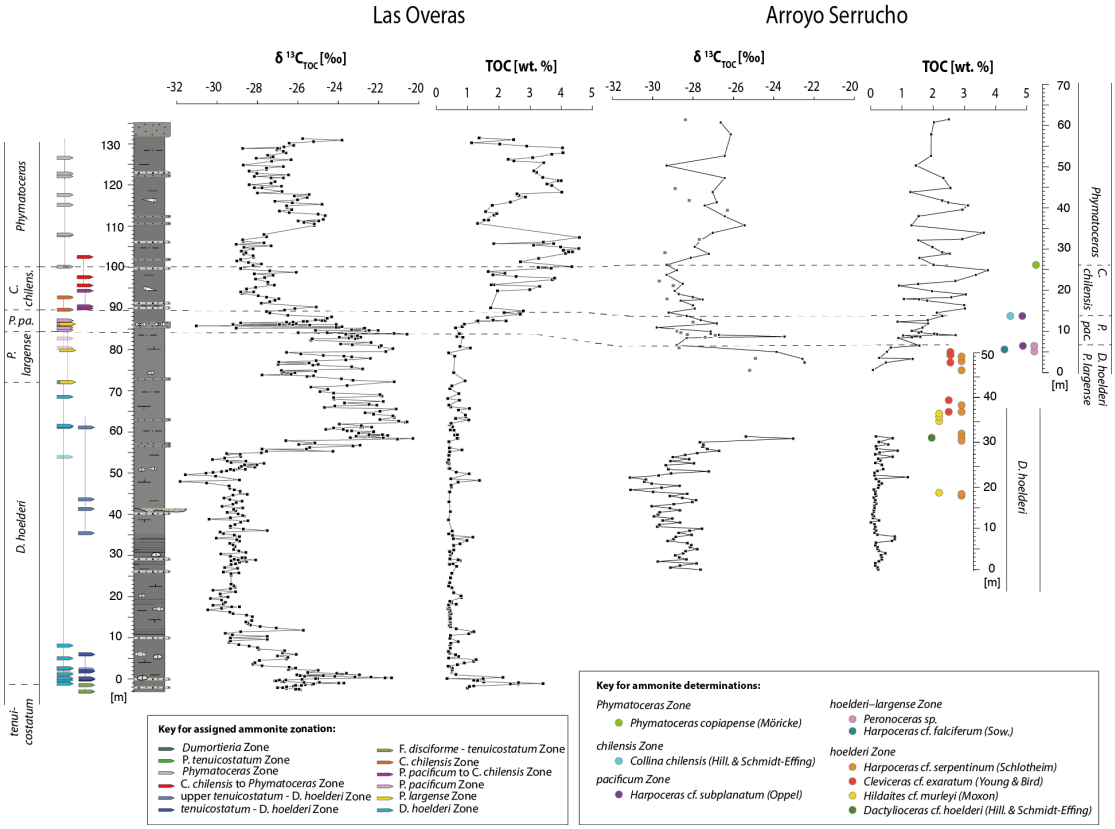

Figure 7.5: Correlation of the $\delta^{13}C_{TOC}$ and TOC records of the biostratigraphically calibrated Las Overas section (this study) and Arroyo Serrucho sections ($\delta^{13}C_{TOC}$ and TOC data from Mazzini *et al.* (2010), Al-Suwaidi *et al.* (2016), biostratigraphical framework modified from Al-Suwaidi *et al.* (2016) to show the proposed new position for the base of the *D. hoelderi* Zone (see Chapter 6). For map indicating the relative position of the sections see Figure 6.3 in Chapter 6.

The increase in sedimentary mercury concentrations, supporting increased volcanic activity of the Karoo-Ferrar LIP, has previously been detected in widely distributed Lower Toarcian sections, appearing concomitantly with the negative carbon-isotope excursion in the upper *D. tenuicostatum* and *falciferum* ammonite zones and corresponding local equivalents (see Percival *et al.* 2015). The observed peaks in sedimentary Hg and Hg/TOC in the Las Overas section, also present in parallel with the negative CIE strongly supports a perturbation to the global Hg cycle, and can be used as an additional stratigraphic marker.

Correlation of the new chemostratigraphic record ($\delta^{13}C_{TOC}$, TOC and Hg) to the Arroyo Lapa section (southern Neuquén Basin; Al-Suwaidi *et al.* 2010, Al-Suwaidi *et al.* 2016) can be made on the basis of ammonite biostratigraphy (see Figure 7.6). Uncertainties in the biostratigraphic constraints in the Arroyo Lapa section occur at the *D. tenuicostatum*–D. *hoelderi* boundary, wherefore the boundary is not clearly defined (marked as grey area between those ammonite zones in Figure 7.6). However, both records illustrate a similar and comparable negative $\delta^{13}C_{TOC}$ in the (upper *tenuicostatum*) and lower *D. hoelderi* Zone, comprising values between −28 and −31‰, representing the geochemical record of the T-OAE. Although the Arroyo Lapa section is marked by an erosion surface at a level recording the top of the negative CIE, the likely undisturbed Las Overas and Arroyo Serrucho isotopic signatures shows a similarly abrupt positive shift ending the negative excursion. Furthermore, the $\delta^{13}C_{TOC}$ records of the upper *D. hoelderi* Zone show a comparable trend to more negative values, suggesting that the scour infill in Arroyo Lapa does indeed record the contemporaneous signal.

Remarkably high TOC values (~10 wt%) appearing in the interval of stratigraphic uncertainty between the *tennuicostatum* and D. *hoelderi* Zone in the Arroyo Lapa section likely correspond to the elevated TOC in the lowermost *D. hoelderi* Zone of the Las Overas section (up to 3 wt%). The correlation of increased TOC concomitant with the positive shift in $\delta^{13}C_{TOC}$ in the uppermost *D. tenuicostatum* Zone/lowermost *hoelderi* Zone recorded in both locations suggests that the lower Las Overas strata (lowermost ~3 m) likely marks the onset of the T-OAE. However, without

chemostratigraphic records from lower in the *D. tenuicostatum* Zone in the Las Overas section, this interpretation cannot be confirmed.

Although increased TOC levels occur in both sections at the onset of the T-OAE, distinct differences between the Las Overas and the Arroyo Lapa sections appear in sedimentary organic-matter content and assemblage, and the stratigraphic thickness throughout the stratigraphically higher intervals. In the Arroyo Lapa section, the high TOC values appear concomitantly with elevated HI values (up to 450 mg HC/g TOC) interpreted to result from the increased preservation of marine organic matter and/or its ratio to terrestrial organic matter over this interval (see Al-Suwaidi *et al*. 2010). In the Las Overas section, such an increase in HI values has not been recorded.

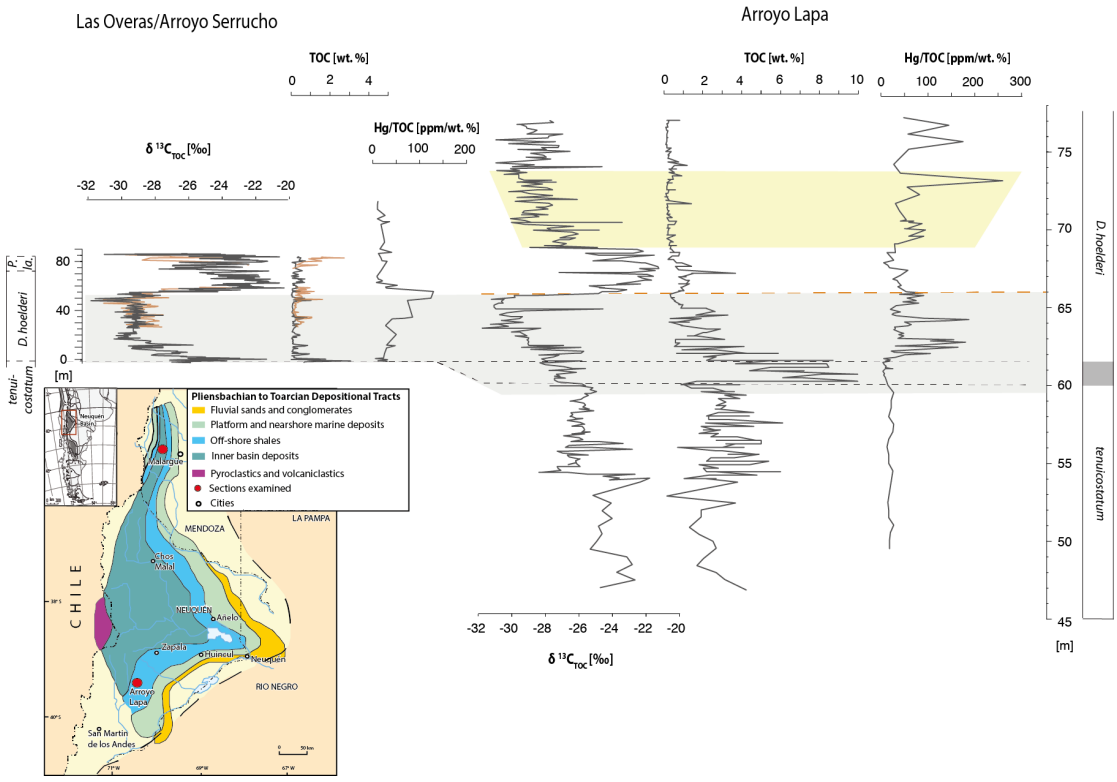

Figure 7.6: Correlation of the $\delta^{13}C_{TOC}$ and TOC records of the Northern and Southern Neuquén Basin, at the Las Overas (black) & Arroro Serrucho (orange) section and Arroyo Lapa section, respectively. Erosion surface in Arroyo Lapa marked as orange dashed line, channel scour marked in yellow. Data from Al-Suwaidi *et al.* (2010), Mazzini *et al.* (2010), Al-Suwaidi *et al.* (2016) and this study. Map of the Neuquén Basin, showing Pliensbachian to Toarcian depositional tracts within the basin. Red circles indicate field localities examined in this study. Las Overas and Arroyo Serrucho sections in the North,

Arroyo Lapa section. Map adapted from Riccardi *et al.* (2011), modified from Legarreta and Uliana (1996).

Following the stratigraphically short interval of increased TOC levels, the Arroyo Lapa section contains a distinctly higher organic-matter content throughout the *D. hoelderi* Zone (fluctuating between 0.3 and 5 wt%), compared to the Las Overas section (0.4 wt% in average). Interestingly, both sections show a similar lithology in the lower *D. hoelderi* Zone, characterized by dark-coloured and laminated shales, indicating low-oxygen depositional environments prone to organic-matter deposition and preservation. Pyrite framboid diameter distribution, Pristane/Phytane ratios, and $\delta^{98/95}$Mo data from the southern Neuquén Basin also suggest short anoxic intervals during the T-OAE (Al-Suwaidi 2011). The measured low TOC values in the Las Overas section might result from a higher grade of thermal maturation, as suggested by high T_{max} values (~T_{max}=520ºC). However, as a significantly higher amount of TOC is retained in the sediments in the upper Las Overas section (up to 4 wt% in the *C. chilensis* and *Phymatoceras* zones, see Figure 7.6), additional mechanisms may have led to distinctively lower TOC values in the *D. hoelderi* Zone. Globally increased continental weathering rates concomitant with the T-OAE were inferred from relatively radiogenic $^{187}Os/^{188}Os_i$ values recorded at various locations on the Northern Hemisphere (Cleveland Basin and Cardigan Bay Basin, UK, and Bighorn Creek, Alberta; Cohen *et al.* 2004, Percival *et al.* 2016, Them *et al.* 2017a, Them *et al.* 2017b). It is therefore likely that weathering- and sedimentation rates were similarly increased in the Neuquén Basin. During the Late Pliensbachian/Early Toarcian, the northern Neuquén Basin was located within an inner-basin depositional setting, close to the connection to the Panthalassa Ocean (see Figure 7.6). The Late Pliensbachian and Early Toarcian transgression, induced by thermal subsidence and regional back-arc extension (Legarreta and Uliana 1996, Vicente 2005) likely provided accommodation space, and highly elevated weathering rates during the Early Toarcian, similar to the European and N American realm, might have led to high sedimentation rates. The low TOC values in the lower *D. hoelderi* Zone may therefore be largely a function of sediment dilution.

The input of eroded and reworked sediment, predominantly during the early *D. hoelderi* Zone, is further supported by the stratigraphically expanded appearance of the *D. hoelderi* Zone, as well as palynological data, and relative increase in oxidized organic matter, based on elevated Oxygen Indices within the lower 20 m of the *D. hoelderi* Zone. The organic-matter assemblage in the Las Overas section comprises Densospores (spores of *lycopods*), which are common in coal seams of Devonian to Permian age (Traverse 2007). The relatively simple recovered in the Arroyo Serrucho and Las Overas sediments (after oxidation) are not found in the younger Carboniferous in Gondwana, suggesting a probably Mississippian to Early Pennsylvanian (mid Viséan to early Bashkirian) age of the spore. The palynological data therefore indicates a reworked provenance of the coal fragments from regional Carboniferous terrestrial deposits rather than from other Lower Jurassic strata. The increase in the relative amount of amorphous organic matter up-section, concomitantly with the increase in TOC, indicates a possible shift in depositional setting from proximal to distal. This inference is further supported by lithological constraints suggesting a gradual deepening of the despositional environment (see Chapter 6).

The contribution of reworked Carboniferous terrestrial organic matter to the bulk organic matter assemblage possibly also had an impact on the $\delta^{13}C_{TOC}$ signature of the analyzed sediments. However, as the $\delta^{13}C_{TOC}$ record of the interval of high allochthonous input appears to correlate well with the Arroyo Lapa section record from the southern Neuquén Basin, the contribution of the Carboniferous isotope signal appears insignificant. This supposition is further supported by the correlation of the Las Overas and Las Overas-C carbon-isotope records with the coeval chemostratigraphic record of the Mochras core, Cardigan Bay Basin, UK (Xu *et al*. 2018), which allows comparison between the Southern and Northern Hemisphere isotope signals (Figure 7.7).

The Las Overas $\delta^{13}C_{TOC}$ record of the lower Toarcian correlates well with the Mochras core record. The carbon-isotope record of the *D. hoelderi* Zone (=*serpentinum* Zone) appears comparable in magnitude to the equivalent *serpentinum* Zone in Mochras, although the negative excursion associated with the T-OAE appears

stratigraphically more expanded in the Las Overas section. The comparison of the carbon-isotope records following the *serpentinum*/*hoelderi* Zone is complicated due to the distinct differences in stratigraphic thickness of the individual ammonite zones in the Argentinian sections. The *P. largense* to lower *C. chilensis* Zone and equivalent *bifrons* Zone both show a comparable overarching 2–4‰ negative shift. The upper *C. chilensis* Zone in the Las Overas section, equivalent to the European *variabilis* Zone, appears too condensed to allow a comparison of the isotope record. The *Phymatoceras*/*thouarense* Zone $\delta^{13}C_{TOC}$ record appears distinctly different. The correlation is uncertain due to the very expanded appearance of the Argentinian section, and the stratigraphic gap of between the Las Overas and Las Overas-C section. The *P. tenuicostatum* Zone record is incomplete in the Northern Neuquén sections, but suggests a similar gradual positive trend in carbon-isotope values compared to the corresponding *dispansum* and *pseudoradiosa* Zone isotope record from the Mochras core.

In the Mochras core, the stratigraphic interval between the Pliensbachian-Toarcian boundary to *exaratum* Subzone of the *serpentinum* Zone is characterized by the increased occurrence of siderite nodules (Xu *et al*. 2018). Siderite nodules and siderite-cemented beds also occur in the equivalent *D. hoelderi* Zone of the Las Overas section (see Figure 7.7, appendix A-10 and digital appendix D-A-3). The exact stratigraphic correlation of the siderite-bearing intervals between both sections is hampered by the limited stratigraphic extent of the Las Overas section, and the lower resolution of the ammonite biostratigraphy in the Las Overas section, compared to the Mochras core, which has been calibrated to ammonite subzone level. However, in both sections siderite-bearing beds and nodules appear concomitant with the T-OAE negative CIE and subsequent recovery to more positive carbon-isotope values, but are absent in the above strata.

Siderite ($FeCO_3$) is an iron bearing carbonate mineral. With abundant iron (Fe) and carbonate (CO_3^{2-}) available, siderite forms during early diagenesis in reducing low-sulfate (SO_4) environments (Curtis and Spears 1968, Huggett *et al.* 2000). The Early Jurassic oceans were likely pre-conditioned with a low-sulfate signature due to the widespread deposition of evaporites during the onset of rifting between North America and Europe/North Africa (Austin *et al.* 1989, Davison 2005) and along the

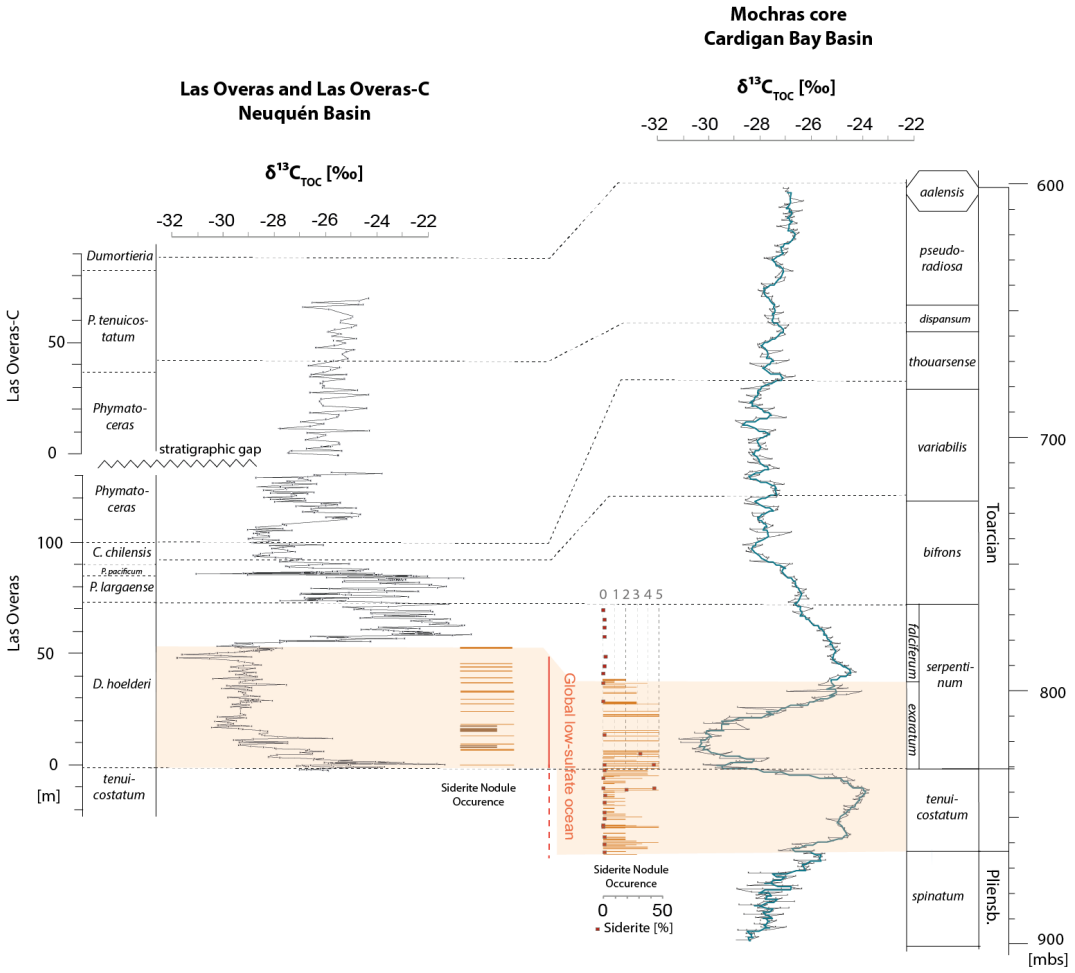

Figure 7.7: Correlation of the $\delta^{13}C_{TOC}$ record and siderite nodule occurrence of the Toarcian stage of the Neuquén Basin (Las Overas and Las Overas-C section,) and the Cardigan Bay Basin (Mochras core, data from Xu *et al*. 2018). Occurrence of siderite nodules in the Las Overas section is based on lithological field descriptions (see appendix A-10). Orange lines indicate siderite nodules >2 cm and siderite cemented beds. Brown lines indicate intervals where finely dispersed siderite nodules of <2 cm diameter occur. Occurrence of siderite nodules in the Mochras core strata is based on the visual estimation of the degree of red colouring on the core-slab: colour intensity is shown by red lines on a scale of 0 to 5, The percentage of siderite (measured by XRD) are indicated by red squares, data from Xu *et al*. (2018).

south- western passive margin of the Tethys Ocean (Chandler *et al.* 1992). Further drawdown of sulfur might have resulted from large-scale early digenetic formation of pyrite (FeS_2) in response to oxidation of organic matter. Pyrite formation and concomitant reduction of iron and sulfate (Wilkin and Barnes 1996) leads to a

depletion of sulfate in the pore-waters. Further available Fe^{2+}, together with CO_3^{2-}, may subsequently form siderite. The apparent coeval appearance of organic-rich strata during the Early Toarcian (*tenuicostatum* and *falciferum* Boreal ammonite zones) is well documented from globally distributed marine sedimentary records (see Jenkyns 1988), and concomitant elevated pyrite concentrations have been recognized in the Tethyan realm (Wignall *et al.* 2010, Kemp *et al.* 2011, Xu *et al.* 2018). The drawdown of sulfur from the global ocean reservoir by pyrite formation and burial is further supported by a major perturbation of the sulfur cycle, recorded by increasing sulfur-isotope compositions occurring along the interval between the Pliensbachian-Toarcian boundary and the overarching positive carbon-isotope excursion, suggesting low-sulfur oceans (Gill *et al.* 2011, Newton *et al.* 2011). Globally enhanced weathering rates, as witnessed by osmium-isotope studies (see above) likely supplied increased amounts of iron, facilitating the siderite formation (Xu *et al*. 2018).

The occurrence of siderite nodules and siderite-bearing beds in the Las Overas section also supports the prevailing enhanced weathering rates during the *D. hoelderi* Zone, as indicated by increased sedimentation rates (see above). The apparent coeval occurrence of siderite-bearing beds in the Mochras core and the Neuquén Basin supports the global nature of the transient perturbations to the biogeochemical cycle during the T-OAE. However, further work on the stratigraphic interval below the Las Overas section is needed to confirm the overall concomitance of the phenomena.

7.7. Conclusion

The new biostraigraphically calibrated $\delta^{13}C_{TOC}$ data from the Las Overas and Las Overas-C section located in the N Neuquén Basin expands previous records from the nearby Arroro Serrucho sections, and provides a stratigraphically expanded record from the uppermost *D. tenuicostatum* Zone in the Lower Toarcian to the upper Toarcian lower *Dumortieria* Zone, interrupted by a stratigraphic gap in the *Phymatoceras* Zone. The studied interval is equivalent to the *D. tenuicostatum* to upper *pseaudoradiosa* European ammonite zones.

The stratigraphically expanded ~6‰ negative excursion exemplifies the local expression of the T-OAE. The correlation of the $\delta^{13}C_{TOC}$, TOC and Hg/TOC records to the same age strata in the Southern Neuquén Basin (Arroyo Lapa section) supports the likely complete nature of the negative excursion recorded in the lower *D. hoelderi* Zone of the Las Overas section, although strata lower in the *D. tenuicostatum* Zone should be examined to confirm this interpretation. The new data offer a solid bio- and chemostratigraphical framework for the integration of radio-isotopic ages from the various volcanic ash beds collected throughout the sections

The geochemical characterization of the section reveals the organic-lean character of the sediments, likely due to thermal maturation of the section. The extremely low TOC values corresponding to the negative CIE can be ascribed to relatively high sediment input and dilution due to increased weathering rates induced by the warmer and wetter climate during the T-OAE. The contribution of reworked Carboniferous organic matter, indicated by palynology, appear not to have biased the bulk organic carbon-isotope signal.

The correlation of the Argentinian sections to the stratigraphically expanded and continuous $\delta^{13}C_{TOC}$ signatures of the Mochras core, Cardigan Bay Basin, UK, suggests that both records indicate the signal of the global carbon cycle of the Early Toarcian. The Upper Toarcian correlation is complicated by very different stratigraphic characteristics of the sections, and the stratigraphic gap in the Neuquén Basin record. The apparent coeval occurrence of siderite nodules and siderite-cemented beds in sections from the Northern and Southern Hemisphere exemplify transient global low sulfate concentrations in the seawater during the T-OAE as a response to large-scale deposition of organic matter and pyrite, and increased continental weathering rates.

Chapter 8 : Conclusions and future work

8. Conclusions

The first aim of this thesis was to improve the overall understanding of the evolution of the Early Jurassic $\delta^{13}C_{TOC}$ record prior to the T-OAE. On this matter, Chapters 3 to 5 provided a continuous $\delta^{13}C_{TOC}$ record of the Hettangian to Pliensbachian stages and investigated the timing, pacing, and geochemical nature of excursion intervals. The $\delta^{13}C_{TOC}$ record aggregates several carbon-isotope excursions of different stratigraphic extent and magnitude (see Figure 8.1). On a large scale, the $\delta^{13}C_{TOC}$ record comprises several large-amplitude (2–6‰) excursions: the Triassic–Jurassic boundary negative excursion, a broad positive excursion in the Hettangian and upper Sinemurian strata, the Sinemurian–Pliensbachian boundary negative excursion, the upper Pliensbachian *margaritatus* Zone positive excursion and *margaritatus–spinatum zone* negative excursion, and the Pliensbachian-Toarcian boundary negative excursion (see Figure 8.1). Changes in the relative abundance of marine vs terrestrial constituents in the bulk organic matter appears to be a subordinate mechanism driving the carbon-isotope excursions, although minor changes occur concomitantly with the Triassic–Jurassic boundary negative excursion, the Sinemurian–Pliensbachian boundary negative excursion and the upper Pliensbachian *margaritatus* Zone positive excursion (see Figure 8.1). With the exception of the Hettangian to upper Sinemurian broad positive shift, all large-scale excursions recorded in the Mochras strata have been found in other NW European sections, but only the Triassic–Jurassic boundary negative excursion has been recognized globally so far. As the upper Pliensbachian *margaritatus* Zone positive excursion and the Pliensbachian–Toarcian boundary negative excursion were associated with the burial and release of isotopically light carbon, respectively, the isotope events likely represent changes in the global carbon cycle and could potentially, although with care, be used as chemostratigraphic markers. Causal mechanisms and the spatial occurrence of the Sinemurian–Pliensbachian boundary excursion and the upper Pliensbachian *margaritatus–spinatum zone* negative excursions are so far little understood and their global extent is ambiguous.

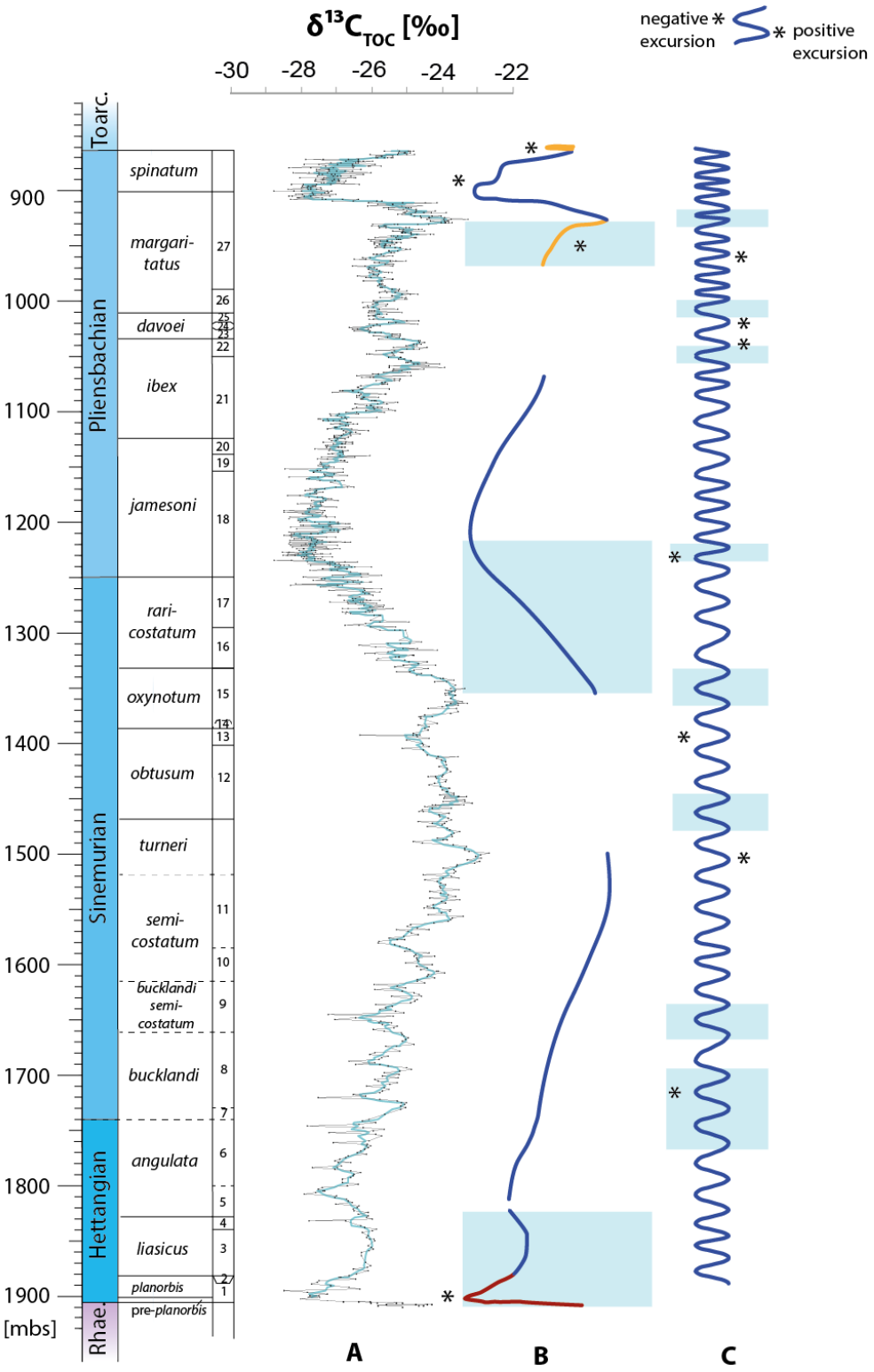

Figure 8.1 Schematic illustrations of large- and small amplitude $\delta^{13}C_{TOC}$ trends recorded in the Mochras core. **A:** $\delta^{13}C_{TOC}$ record. Blue line represents a 9-point moving average for data from the Hettangian to Upper Sinemurian, and 7-point moving average for the Upper Sinemurian to Toarcian. **B:** Schematic illustration of the large-scale $\delta^{13}C_{TOC}$ excursions. Red: excursion recognized globally, orange: excursions likely to represent a global signal, dark blue: spatial extent of excursions ambiguous. *:

Excursion event also recognized in other locations - regional to potentially global significance **C:** Schematic illustration of orbitally paced small-amplitude fluctuation recorded in the $\delta^{13}C_{TOC}$. Light blue shading marks excursion events associated with minor changes in relative composition of the bulk organic matter.

On a smaller scale, the $\delta^{13}C_{TOC}$ record of the Mochras drill-core is characterized by the frequent fluctuation of isotope values between 0.5 and 2‰ magnitude, occurring continuously and superimposed on the long-term carbon-isotope trends (see Figure 8.1). Several individual isotope shifts were previously identified and characterized in datasets from NW European sections, where they also occur in multiple carbon-isotope reservoirs, and some were recognized in a wider regional extent. The excursions previously recorded elsewhere appear less singular in the collective context of the continuous and stratigraphically expanded Mochras record, which also comprises $\delta^{13}C_{TOC}$ excursions not previously identified elsewhere. Spectral and time series analysis of the $\delta^{13}C_{TOC}$ record from Mochras suggests that these isotope fluctuations correspond to long eccentricity (405-kyrs) orbital cycles, possibly modulated by longer frequencies (Myrs-scale). Changes in in the relative amount of marine/terrestrial organic matter do appear with some, but not all, eccentricity-paced $\delta^{13}C_{TOC}$ excursions, implying such changes to be subordinate in driving the isotope excursions. It is not yet conclusive whether the eccentricity-paced fluctuations in the $\delta^{13}C_{TOC}$ record indicate changes in the global carbon cycle or represent local to regional sensitivity to orbitally paced climatic changes. However, the discovery of an orbital signal leads away from the interpretation of small-amplitude excursions as stand-alone events and stresses the importance of orbital forcing as a driving mechanism behind small-amplitude carbon-isotope excursions. Due to the continuous occurrence of small-amplitude excursions of, as yet, ambiguous spatial expression, these excursions are impractical in the use as chemostratigraphic markers, unless in the context of a well defined biostratigraphic framework. However, orbital tuning of the isotope record provides an astronomical timescale, providing a temporal framework for the Hettangian, Sinemurian and Pliensbachian stages, individual ammonite zones, as well as for the recorded isotope events.

This thesis also aimed to investigate further the expression of the T-OAE on the Southern Hemisphere, and to generate a robust stratigraphical framework for future work on the numerical dating of the onset of the T-OAE (Chapter 6 and 7). Oceanic anoxic events are, by definition, time intervals in the Mesozoic that are characterized by global and coeval deposition of marine organic-rich sediments, which were not strictly controlled by the local basin geometry (Schlanger and Jenkyns 1976). The organic-lean character sedimentary record of the T-OAE in the northern Neuquén Basin, however, exemplifies the importance of multi-proxy analysis when identifying such events. Although low-oxygen environments are indicated in the lithological record of the Las Overas section, here, the local interplay between changes in the basinal setting and palaeoenvironment during the T-OAE likely led to a localized overprint that depressed the organic-rich sedimentary character seen elsewhere. Such local differences stress the need for an integrated bio- and multi-proxy geochemical approach in order to unambiguously define palaeoenvironmental events such as the T-OAE. At the same time, bearing the aforementioned local differences in the geochemical expression of the T-OAE in mind, the Southern Hemisphere geochemical records of $\delta^{13}C_{TOC}$ and Hg, and lithostratigraphical record comprising siderite-bearing strata, illustrates the global and coeval nature of the T-OAE and associated disturbance of biogeochemical cycles.

8.1. Future work

In order to further refine the Early Jurassic timescale, the biostratigraphic framework of the Hettangian and Sinemurian of the Mochras core must be improved where ammonite zone boundaries are not clearly defined yet, and a higher-resolution dataset similar to the existing elemental calcium carbonate record for the Pliensbachian is needed for further and more accurate time series analysis. The re-drilling of the Mochras core (‘Mochras B’) will provide better-preserved materials suitable for such high-resolution studies. The integration of numerical ages from the Toarcian stage of the stratigraphically well-defined Las Overas and Las Overas-C section will provide numerical anchor points. The stratigraphic position of sampled volcanic ash beds intercalated in the Las Overas and Las Overas-C sections, potentially providing new

numerical ages for the Early Jurassic time scale is shown in Figure 7.2. Preliminary results of the U-Pb dating of zircon crystals derived these volcanic ash beds indicate a reworked nature of some of the samples (see Figure 8.2). Other, likely not reworked ash beds contain large, euhedral and prismatic zircon populations, suitable for U-Pb dating, although inclusions are common. Initial results of the isotopic signature indicate a large number of inherited zircons, revealing considerably older U-Pb ages. The final dataset will therefore require careful data selection of the ages and re-assessment of previous age constraints from the nearby Arroyo Serrucho sections (U-Pb ages given in Mazzini *et al*. 2016).

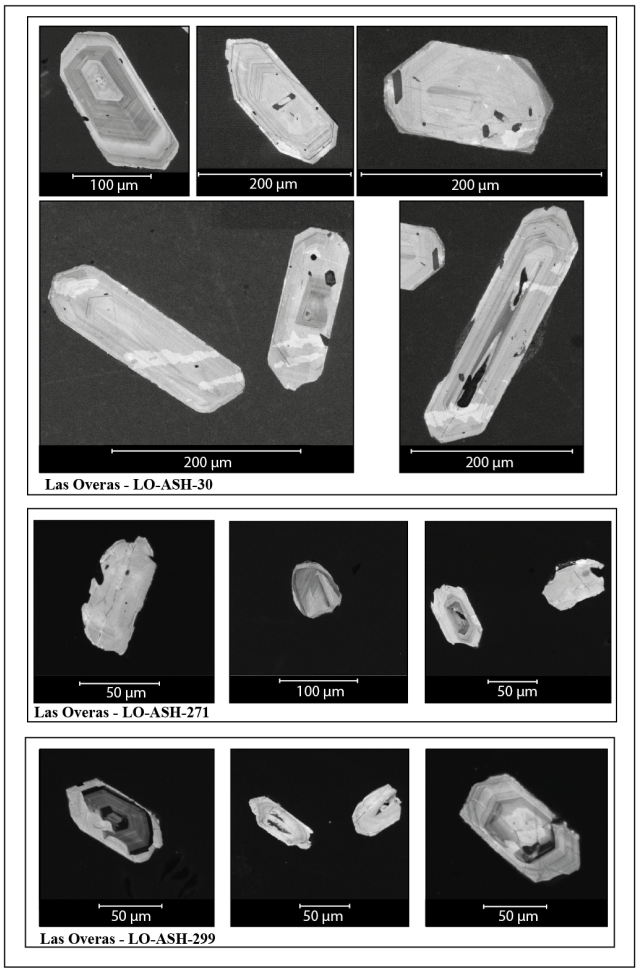

Figure 8.2 Cathodoluminescence images of the equatorial section of epoxy-mounted and polished zircon grains from the samples LO-ASH-30, LO-ASH-271 and LO-AHS 299, showing different zircon populations. ASH-271 and LO-ASH-299 comprise small crystals of likely eroded and detrital nature, unsuitable for numerical dating. LO-ASH-30 comprises large prismatic grains, inclusions are common.

For the temporal correlation between the onset of the T-OAE and the Karroo-Ferrar LIP further work expanding the Las Overas stratigraphic record towards the *tenuicostatum* Zone is needed to unambiguously define the onset of the negative excursion associated with the T-OAE.

More work is needed in order to elucidate the local to global expression of the large-amplitude excursions and orbitally-paced small-amplitude CIEs in the Early Jurassic Mochras core carbon-isotope record in order to disentangle the global carbon-cycle signal, but also define causal mechanisms driving the isotopic shifts. To investigate the spatial extent of the isotope sifts, a $\delta^{13}C_{carb}$ record of comparable resolution to the Mochras core record, and compound specific carbon-isotope records of the same stratigraphic interval are required. Furthermore, $\delta^{13}C$ records from distant basins appear as a useful approach. Furthermore, the herein used method to determine changes in the source of organic matter, based on the linear relation of HI and $\delta^{13}C_{TOC}$ values, only offers an approximation on the matter, and should be validated by compound-specific $\delta^{13}C$ analysis, especially to define the true magnitude of the Sinemurian–Pliensbachian event and the Upper Pliensbachian *margaritatus–spinatum* zone negative excursions.

Comparing carbon-isotope excursion events recorded in the Mochras core to other events recognized in the geological record and occurring under comparable environmental conditions will help to improve the general understanding of mechanisms driving the regional to global carbon-isotope record. Individual large-magnitude excursions, the sequence of events, and the orbitally paced baseline variability should therefore be compared to records from other time intervals. The Upper Cretaceous Campanian to Maastrictian stages, for example, comprise a sequence of positive and negative carbon-isotope excursions, which are recognized in both the Tethyan and Boreal realm to even global extent (see Jarvis *et al*. 2002, Linner 2017). Comparable to the Mochras record, orbitally paced smaller-amplitude excursions also occur superimposed on the Campanian and Maastrichtian isotope events (Voigt *et al*. 2012). Most interesting for a closer comparison to the Upper Pliensbachian *margaritatus–spinatum* event in the Mochras record are the Late Campanian event and the Campanian–Maastrichtian boundary event, which are both

associated with negative carbon-isotope excursions occurring during global cooling and low sea-level. Similar to the Late Pliensbachian event, persistent cool temperatures during the excursion events require a causal mechanism not affecting the global atmospheric carbon reservoir. Proposed causal mechanisms for the Late Cretaceous events can potentially be projected to the Early Jurassic world, giving new insights into the interpretation and genesis of isotope excursion.

Carbon-cycle and earth system modeling is required to test previously proposed causal mechanisms for both long- and short-term isotope shifts recorded in the Mochras core. Model simulations, such as carbon cycle box models (e.g. Long-term Ocean-atmosphere-Sediment CArbon cycle Reservoir Model (LOSCAR), Zeebe 2012), have been used in previous studies, i.e. on the Paleocene–Eocene Thermal Maximum, to constrain if proposed mechanisms can act within the time frame of which they were recorded, produce excursions in the magnitude as they occur, and test carbon release rates against climate sensitivities (see e.g. Zeebe *et al*. 2009, Frieling *et al*. 2016). Regarding the Mochras record, model simulations could be used to test the the carbon-cycle response to mechanisms such as gas hydrate release, changes in the ocean circulation, deep-sea carbonate dissolution, release of mantle CO_2, release of methane hydrates or thermogenic methane release, using the herein presented carbon-isotope record and time scale, together with further data sets from previous studies on the Early Jurassic, such as temperature and oceanographic changes. This approach could, for example, test the likelihood of methane hydrate release contributing to the Upper Pliensbachian *margaritatus-spinatum* negative excursion. A potentially important factor to understand orbital forcing of the carbon cycle is the possible size and variations of continental wetlands under the Early Jurassic climate conditions, as well as local changes in the composition of organic matter and changes in the relative deposition of organic and inorganic carbon. Similar scenarios have been proposed as possible driving mechanism for orbitally forced fluctuations in other time intervals of Earth history (e.g. Zachos *et al*. 2010, Ma *et al*. 2011).

Chapter 9 : Appendix

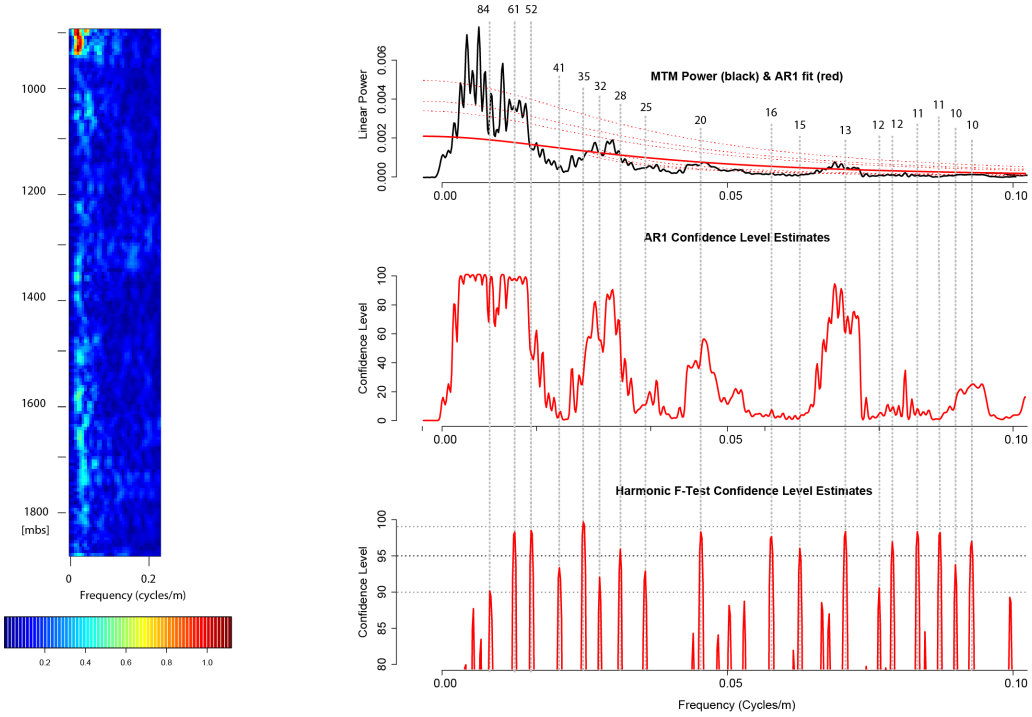

Figure A-1: Wavelet analysis (left) and MTM power spectrum (right) of the unsegmented $\delta^{13}C_{TOC}$ record from the Mochras core (dataset modified by linear interpolation, and periodicities >200 m removed). The linear interpolation of the unsegmented record manipulates the record dataset to an average sample spacing of 0.6 m, generating 383 artificial datapoints. Spectral peaks with a significance >90% are marked in the figure.

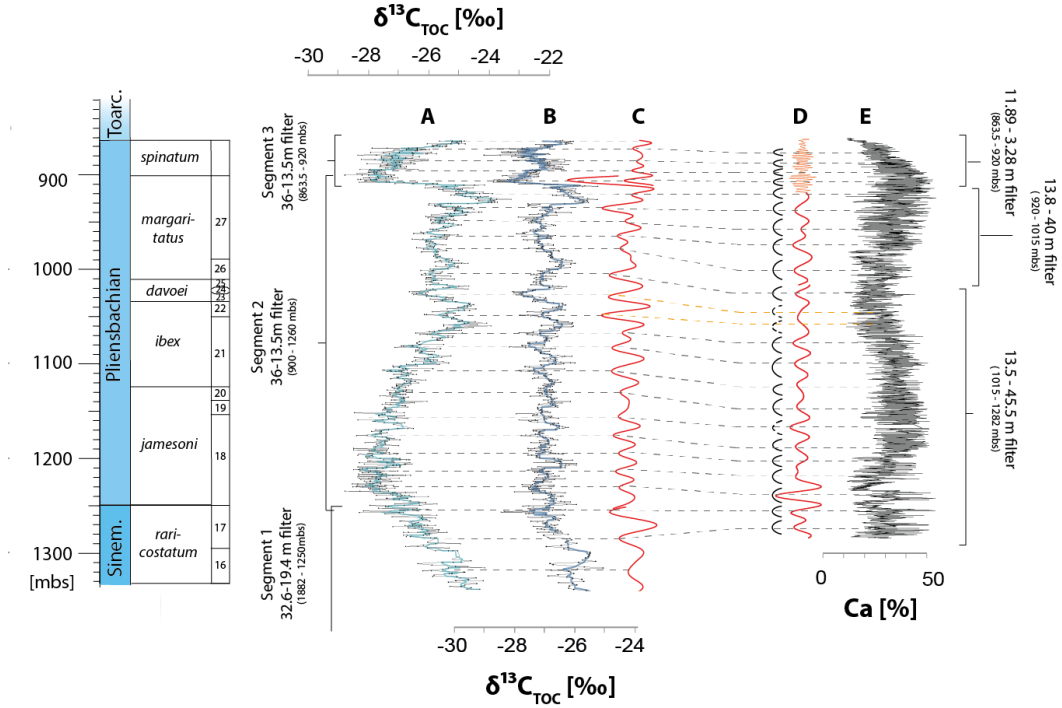

Figure A-2: Comparison of the $\delta^{13}C_{TOC}$ (this study) and elemental calcium concentrations (Ruhl *et al*. 2016) and filtered dominant spectral peaks occurring within the Pliensbachian strata of the Mochas core. **A)** $\delta^{13}C_{TOC}$ record, **B)** detrended, high band-pass filtered and interpolated $\delta^{13}C_{TOC}$ dataset, **C)** band-pass filter of dominant spectral peaks of the $\delta^{13}C_{TOC}$ record (filter given in figure), **D)** band-pass filter of dominant spectral peaks of elemental calcium concentrations (filter given in figure), **E)** elemental calcium concentrations (Ruhl *et al*. 2016). Grey dashed lines indicate stratigraphic intervals interpreted as eccentricity cycles in both studies. Orange dashed lines indicates uncertainties in the correlation of the cycle determination.

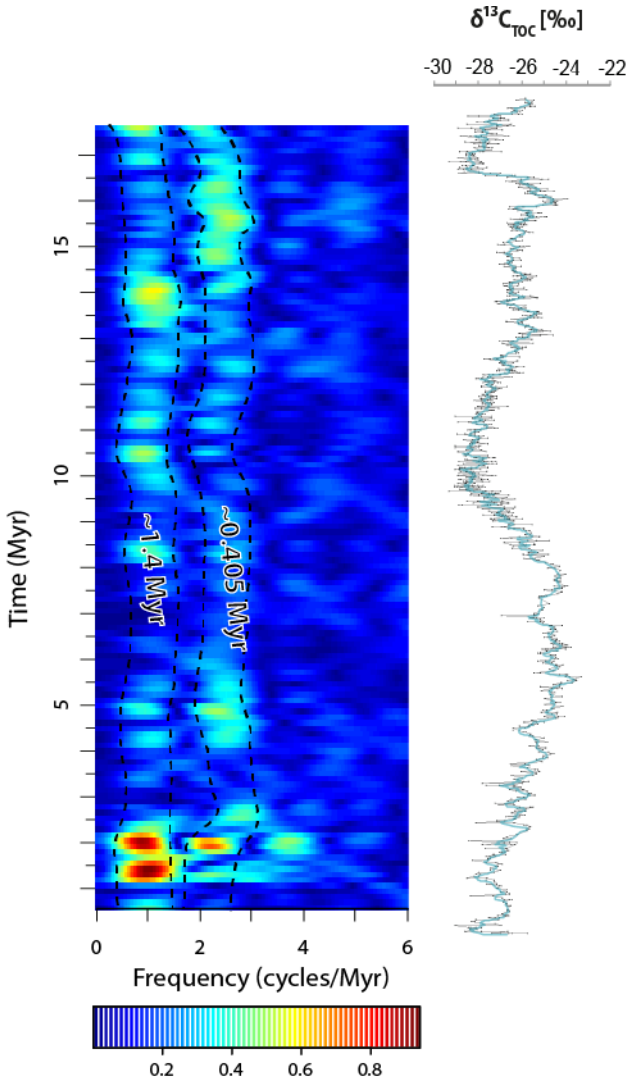

Figure A-3: Wavelet analysis ('eha' function) of the tuned C-isotope record obtained using the Astrochron toolkit (R (3.1.2) Package for astrochronology, version 0.3.1; Meyers, 2014), with robust red noise models (Mann and Lees, 1996), showing intervals of well-expressed cyclicity.

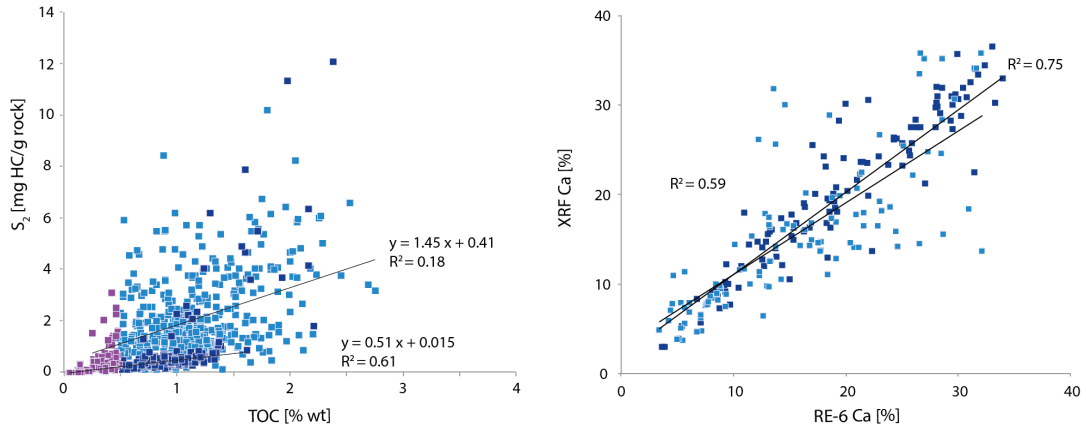

Figure A-4: **Left:** TOC-S_2 plot of the Hettangian to Upper Sinemurian dataset (dark blue, 1906.7 to 1350 mbs) and the upper Sinemurian to Pliensbachian samples (light blue, 1350 to 863.5 mbs). Purple squares indicate samples that were excluded from organo-facies interpretation due to low TOC values. Trendline of the Hettangian to upper Sinemurian dataset is calculated from outlier removed dataset, excluding data with S_2>1. **Right:** cross-plot of Calcium concentrations calculated from Rock Eval analysis (Re-6 Ca), assuming that all inorganic carbon was sourced from Calcium Carbonate, and Calcium measured by hand-held XRF analysis. Hettangian to Upper Sinemurian dataset (1906.7 to 1350 mbs) represented by dark blue squares, upper Sinemurian to Pliensbachian samples (1350 to 863.5 mbs) marked as light blue squares. The correlation indicates that likely not all inorganic carbon was sourced from Calcium carbonate, wherefore total inorganic carbon values obtained by Rock Eval analysis is not indicative for the calcium carbonate content.

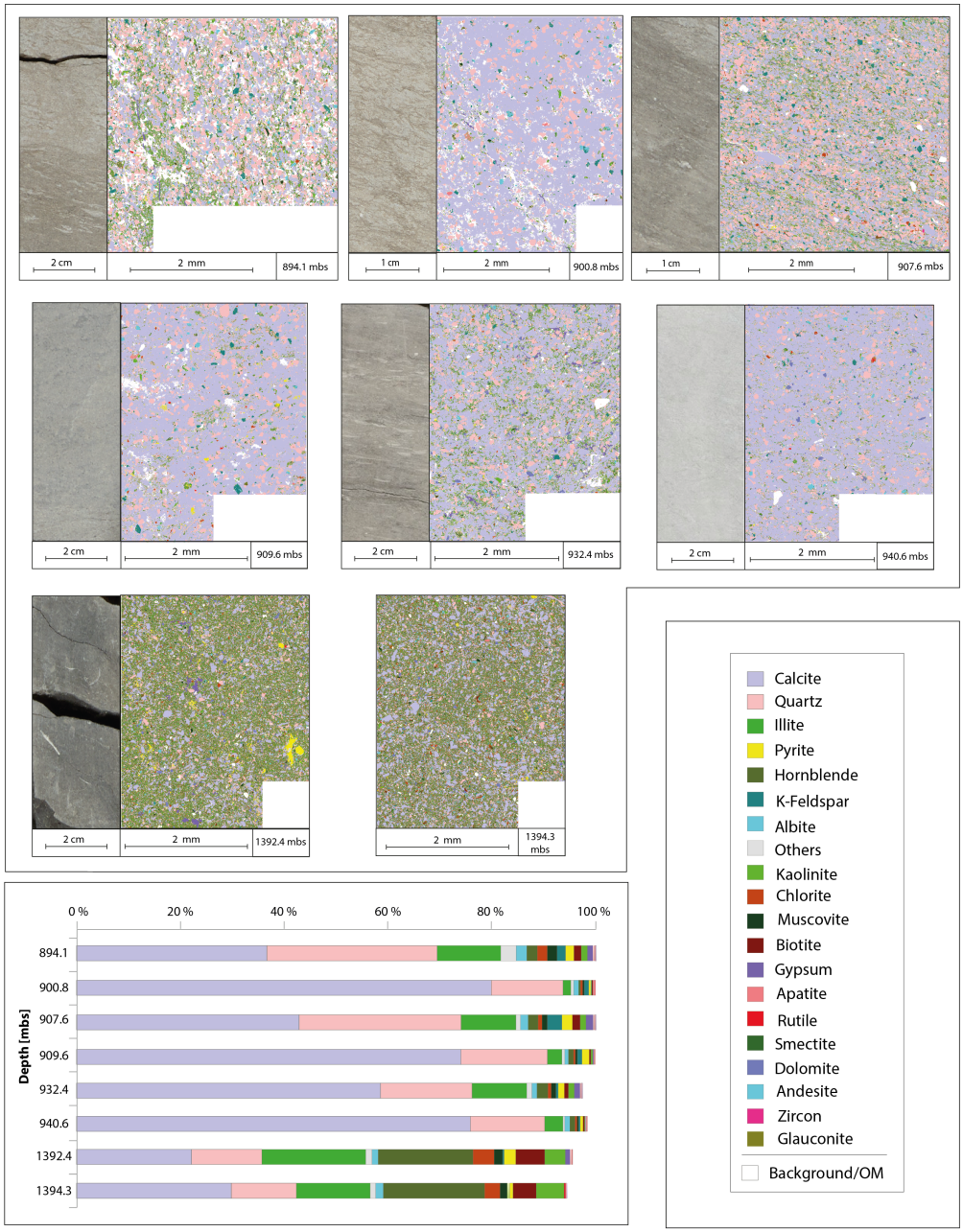

Figure A-5: The SEM-EDS and QUEMSCAN analyses showing differences in the lithology of the Mochras core sediments. Samples corresponding to the upper *obtusum* zone (G, H) are representative for the dark and soft mudstone lithology of the Hettangian to upper Sinemurian strata. Sediments comprise a majority of components in the clay and silt fraction and contain slightly higher amounts of clay minerals (15-20% Illite, 4-5% Kaolinite, 4–5% Chlorite) compared to the Pliensbachian samples (A–F, 1.5-12% Illite, 0.1–1.2% Kaolinite, 0.4–1.9% Chlorite). The Pliensbachian samples comprise Calcite (25-30%) and quartz (10-15%) as detrital grains (A,C,E) in the silt fraction and as calcite cement (B,D,F).

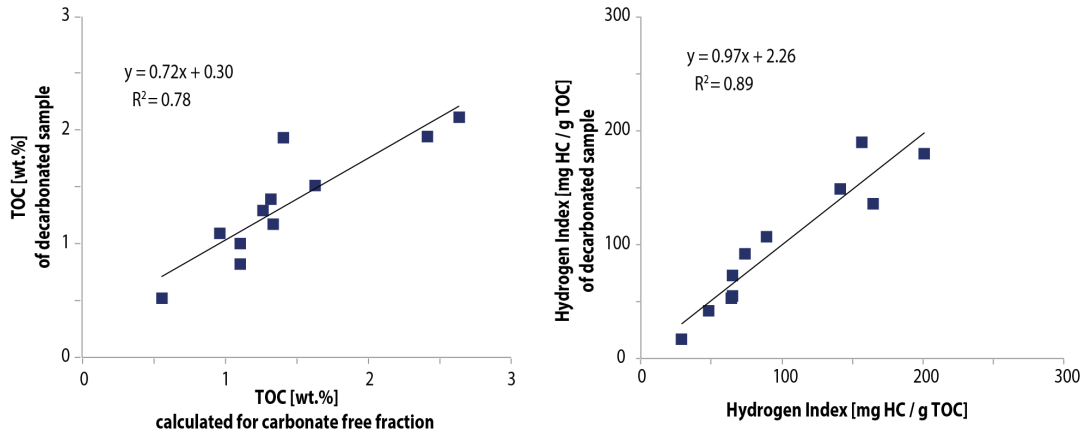

A-6: Correlation of Rock Eval parameter of bulk rock powders and decarbonated powders. Note that TOC for bulk rock powders was calculated for the carbonate free fraction

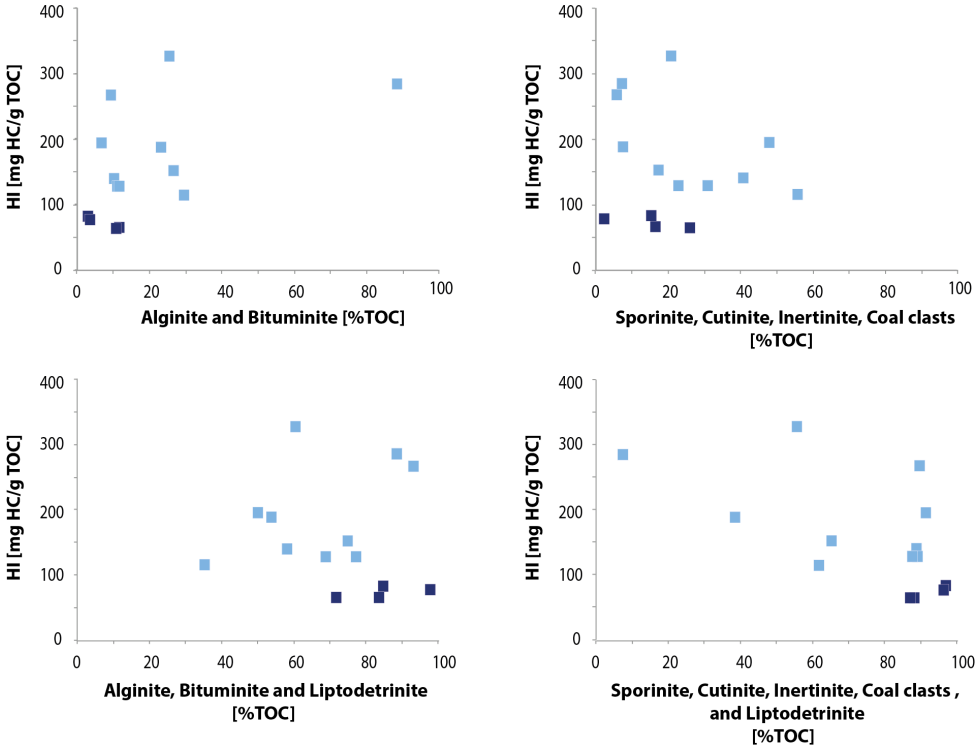

Figure A-7: Cross-plots between HI and marine and terrestrial organic matter excluding and including liptodetrinite. No correlation is evident to identify the precursor source of Liptodetrinite. Dark blue squares: Hettangain and Sinemurian samples, light blue squares: Pliensbachian samples.

A-8: Arroyo Serrucho – E–E'

Section Arroyo Serrucho E-E' is located along the Serrucho riverbed, and is the lowest stratigraphic section examined in this study (S 35º25'53.7", W 69º54'22"). The section was logged and sampled in 2016 and covers 15.7 m in stratigraphy.

The section comprises calcareous and fossiliferous, red-weathering mud-, silt- and sandstones, and some intercalated volcanic ash beds. The individual beds are between 10 to 60 cm thick and show fining- and coarsening-upwards trends. The rich fauna includes bivalves in life position, crinoids and trace fossils (*Thalassinoides* and *Lapispira bispiralis*). Shell debris is more common in the upper 10 cm of the individual beds. Abundant gastropods were observed stratigraphically just below the section.

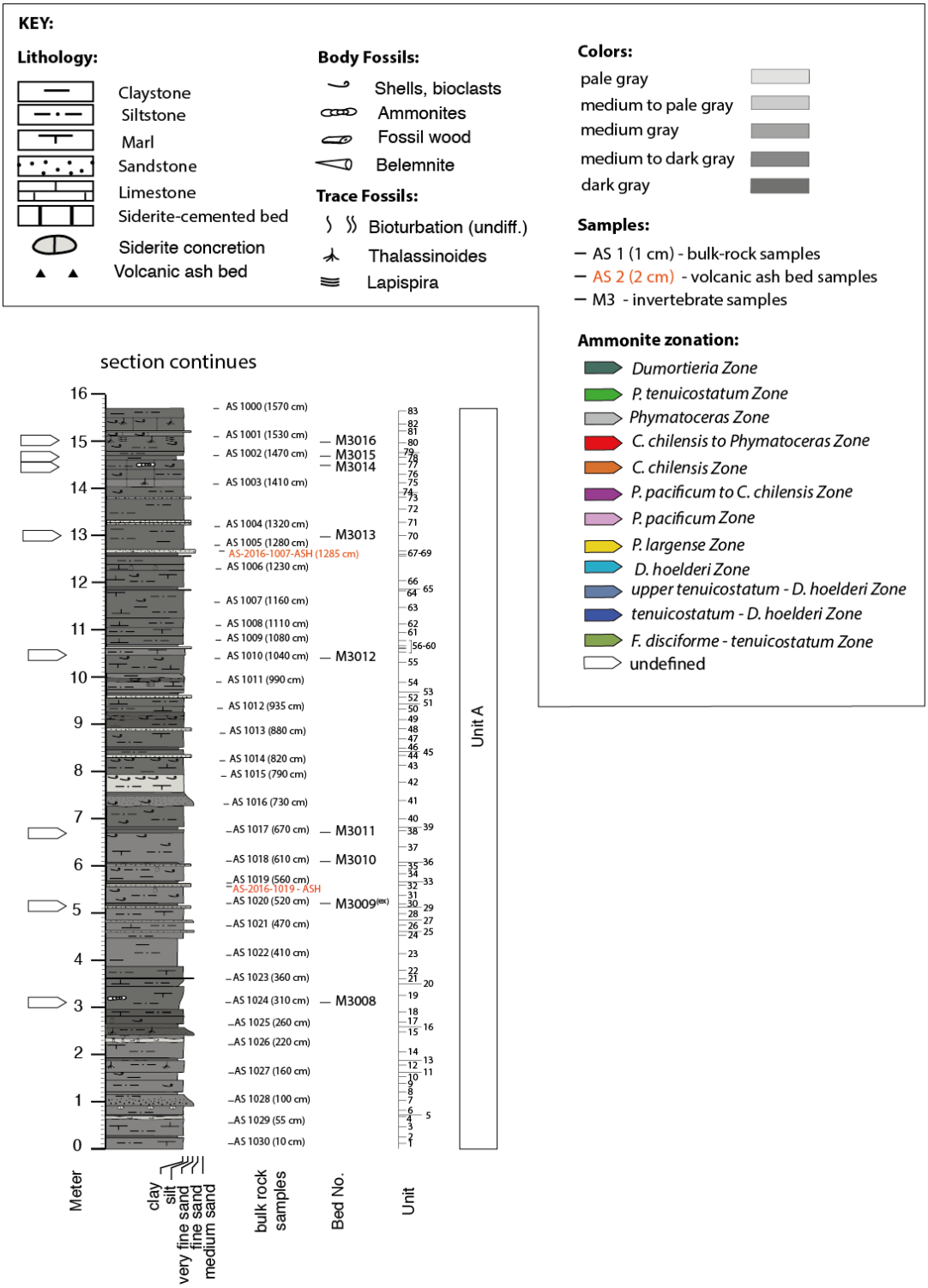

Figure A-8: stratigraphic log of section Arroyo Serrucho E–E'

A-9: Arroyo Serrucho 2016 – F–F'

Arroyo Serrucho F–F' (S 35°25'50.6" W 69°54'17.7", logged and sampled in 2016) is also located along the river bed, approximately 50 m higher in stratigraphy compared to Serrucho E–E'. The section covers 30.2 m of stratigraphy.

Unit A (0 m to 8.3 m) is bracketed by two sandstone packages (Beds no 2, 3, 7 and 35). Between the sandstones, the unit comprises medium grey to medium dark grey, hard-cemented silt-rich calcareous mudstones with increasing shell debris towards the top of the unit.

Unit B (8.3 m to 24.9 m) comprises beds of medium dark to dark grey calcareous mudstones. The thickness of the beds varies between 5 and 60 cm. The beds with a thickness of 40 to 60 cm are generally more fossiliferous towards the top (i.e. Beds no. 47, 48, 105) and some show trace fossils at the top (i.e. Beds no. 105, 107).

Unit C comprises light to dark grey fossiliferous calcareous mudstone beds with a high silt content. Shell debris and burrows at the top of individual beds are common. Two siderite-cemented sandstone beds appear (Beds no. 111, 125).

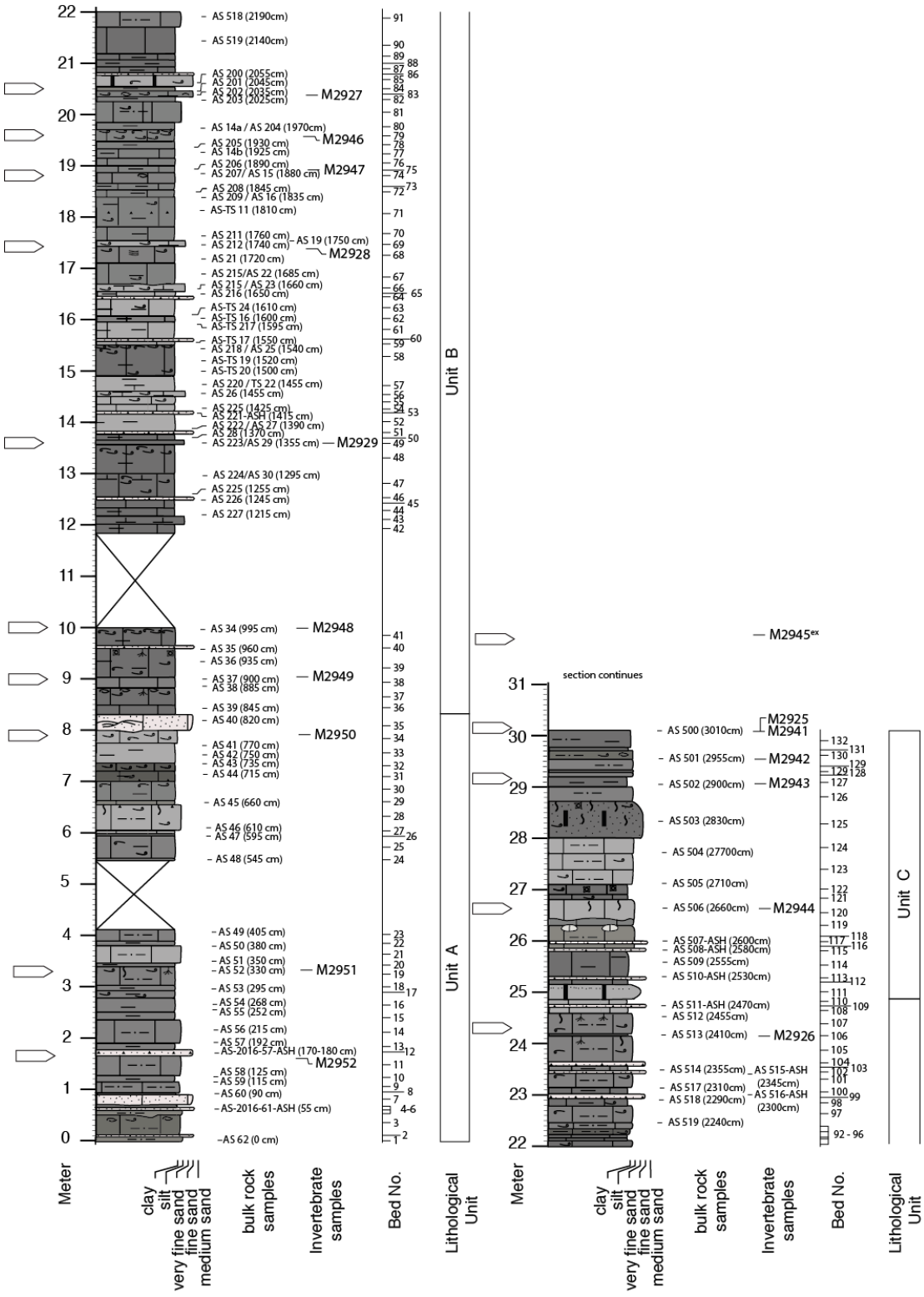

Figure A-9: stratigraphic log of section Arroyo Serrucho F–F'. See Figure A-8 for key and ammonite zonation color scheme.

A-10: Arroyo Las Overas

Arroyo Las Overas: base: S 36°26'38" W 69°53'48", 2220 m elevation

The section studied in the Las Overas creek section is 133.4 m thick. The section between 0 to 86 m was logged and sampled during the 2014 field season. The intervals beween -1.2m to 0 m, and 86 m to 140 m were studied during the field season in 2016. The section can be divided into 18 Units. The main lithology comprises mudstones with varying degrees of cementation, with dark laminated shales and intervals with fine sandstone beds and sandstone-filled scours intercalated in the mudstone succession.

Unit A (-2.6–3 m) comprises medium to dark grey silty mudtone beds with differential cementation. The beds appear lighter grey towards the top of the Unit. Well-cemented beds show prominent bedding planes (beds 15, 18). Bed 13 appears nodular. Bed No. 11 contains red-weathering siderite nodules up to 20 cm in diameter. The mudstones in this unit contain several volcanic ash layers. Bivalves and ammonites are common.

Unit B (3–8.2 m) comprises medium to dark mudstone with weakly differential cementation at the base of the unit. Bed 21 shows a weak lamination and small siderite nodules appear on top. The mudstones change in colour towards medium to pale grey and green-grey up-sequence. Bed No. 25 contains red- weathering siderite nodules up to 20 cm in diameter. Some ammonites can be found in the upper part of the bed. A prominent layer of bivalve shells appears on top of the nodule bed. Higher up, siderite nodules of ~2cm diameter and spherical shape are finely dispersed within bed 27. The top of the Unit is marked by another siderite nodule bed overlain by pale grey to yellow-grey soft mudstone, possibly a very weathered volcanic ash layer.

The base of Unit C (8.2–11.7 m) is marked by medium to dark grey, very weakly laminated mudstone with differential cementation and hard carbonate nodules with preserved internal lamination. Up-sequence the mudstone gradually changes to medium dark brown and dark grey paper shale, with ~10cm beds with differential cementation. A distinct bed with pale grey-weathering carbonate nodules appears within this sub-unit.

Limestones at the base Unit D (11.7 – 18 m) contain shell debris and locally show cross-bedding and undulating ripple marks. The top of the bed is an erosion surface. The succeeding beds of Unit D are medium grey mudstones, and medium to light grey mudstones towards the top. Small pink- and brown-weathering nodules are common.

The base of Unit E (18–28.8 m) is marked by medium and medium to pale grey mudstones with some intercalated silty mudstone beds with ripple marks and cross-bedding in the lower part of the unit, and scours filled with siderite-cemented very fine sand and thin volcanic ash beds in the uppermost part of the unit. The top bed of the unit is marked by a thin, very fine-grained sandstone (Bed 63) with an erosional base.

Hard-cemented silty shale with weak to thick lamination and medium to dark grey colour, and medium to medium pale grey mudstone with irregular cementation is present in Unit D (28.8–36 m). Locally, prominent irregular beds with large (>20cm diameter) siderite nodules occur. The mudstone appears lighter in colour towards the top. The unit is caped by a thin layer of laminated shale (Bed 78).

The lithology changes up-section to relatively uniform medium to pale and pale grey mudstone in Unit G (36 – 47.7 m). A siderite nodule bed with internal hummocky cross-stratification and some sand-filled siderite cemented scours appear within the unit. Soft-sediment deformation below the level of the scours can be seen. Some ammonites and fossilized wood fragments appear in association with the scours. At the top of the unit, erosional sand-filled scours appear more commonly.

Unit H (47.7–54.1 m) comprises relatively uniform mudstones, changing from dark to medium pale grey colour. Between 50.3 m and 51.1 m, large siderite nodules mark a distinctive horizon.

In Unit I (54.1–75 m), the silt content increases progressively, and contains up to 60-cm-thick sandstone beds rich in shell debris and some ammonites. Cross-bedding and hummocky cross-stratification can be seen in the sandstone beds in the lower part of the unit (Bed No. 99, 111). The sandstone beds in the upper part locally show some very weak lamination (bed no. 120).

Silty mudstone beds of pale to medium grey colour are present in Unit J (75–85.2 m). Some fossiliferous beds (Bed No. 124, 128) contain shell debris and ammonites.

Unit L (85.2–86.3 m) is composed of phosphate-rich, very fine-grained sandstone beds. The base of the unit records some burrows and borings. Fossilized wood appears finely dispersed in the lower half of the unit. Ammonites are very common in the upper part suggesting a condensed nature of the lithology.

Unit M (86.3 – 88 m) comprises homogenous medium grey mudstone and shale, topped by a 30-cm-thick very fine-grained sandstone bed without internal structures.

Silty shales of Unit N (88–99.7 m) progessively become darker in colour, changing from medium to dark grey, and individual beds become thicker towards the top, but comprise medium grey mudstone and shale at the vey top. Several thin (< 10 cm) limestone and sandstone beds occur, as well as volcanic ash layers. Ammonites appear locally in the lower part of the unit.

Unit O (99.7–115.7 m) comprises homogenous dark grey mudstone with some silt content. Thin beds (<10 cm) of very fine sandstone (Beds no. 204, 241), limestone (Beds no. 218, 230), beef calcite (Beds no. 210, 212) and volcanic ashes (Beds no. 208, 226) are intercalated, predominantly within the lower part of the unit. Belemnites occur between 107 m and 108 m. Due to poor exposure, there is missing section between 108 and 110 m. Fossil wood appears between 110 and 112.5 m.

Unit P (115.7–120.8 m) appears lighter in colour (medium to medium dark grey). The silty mudstone beds of the unit contain intercalated thin (<15 cm) very fine sandstone beds, some of which have an erosional top or base. Beds no. 249 and 259 are characterized by cross-bedding structures.

Unit Q (120.8–131.9 m) comprises dark grey, homogenous mudstones and shales. The succession contains intercalated volcanic ash beds. Ammonites appear locally between 124 and 128 m.

Unit R (131.9–133.4 m) is represented by very fine-grained sandstone beds, between 5 and 30 cm thick, separated by thin layers of medium grey mudstone. Some sandstone beds have erosional tops or bases. Bed no 291 shows faint low-angle cross-lamination.

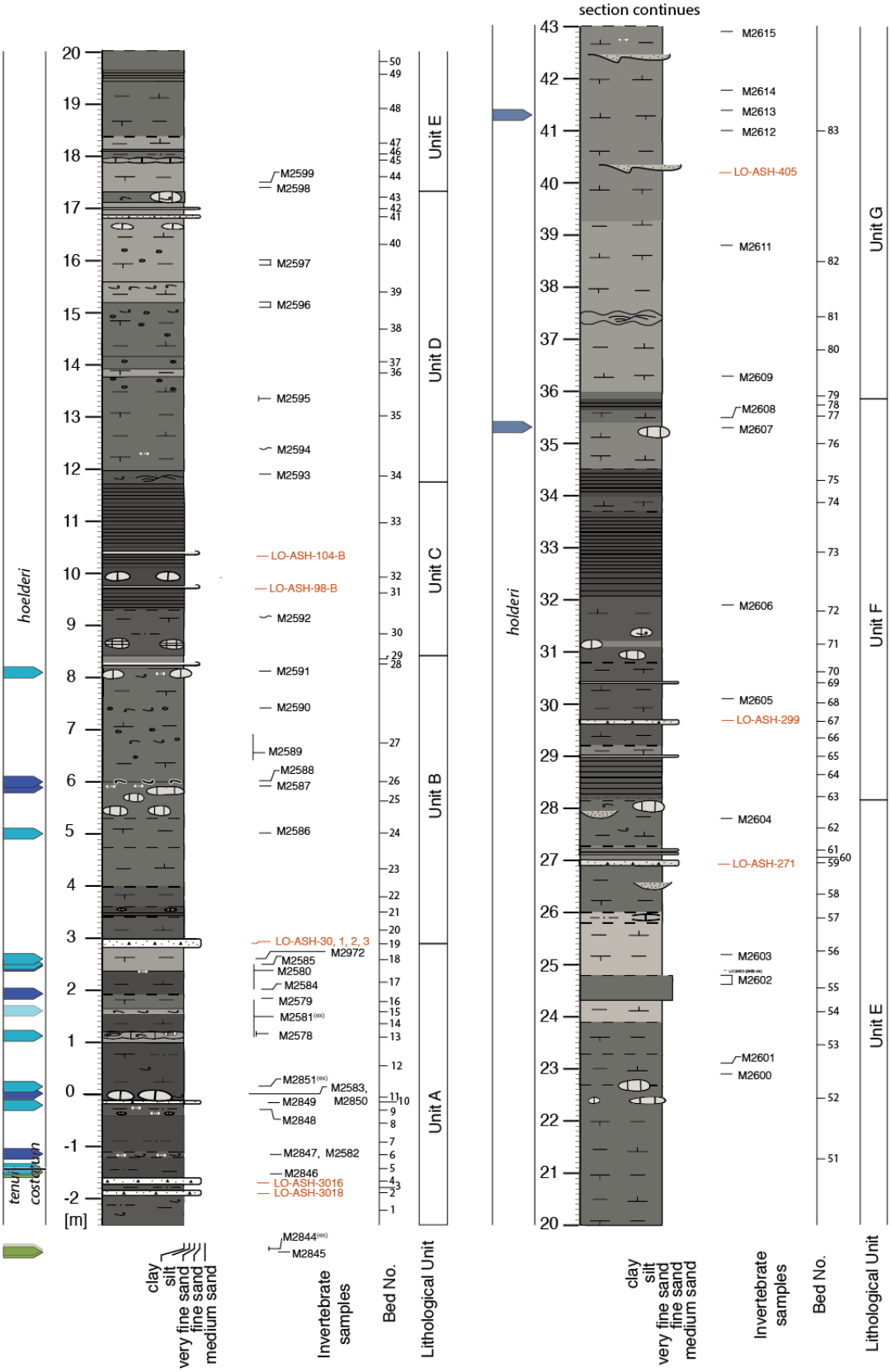

Figure A- 10: stratigraphic log of section Las Overas. See digital version (D-A-3) for sample position and labels. See Figure A-8 for key and ammonite zonation color scheme.

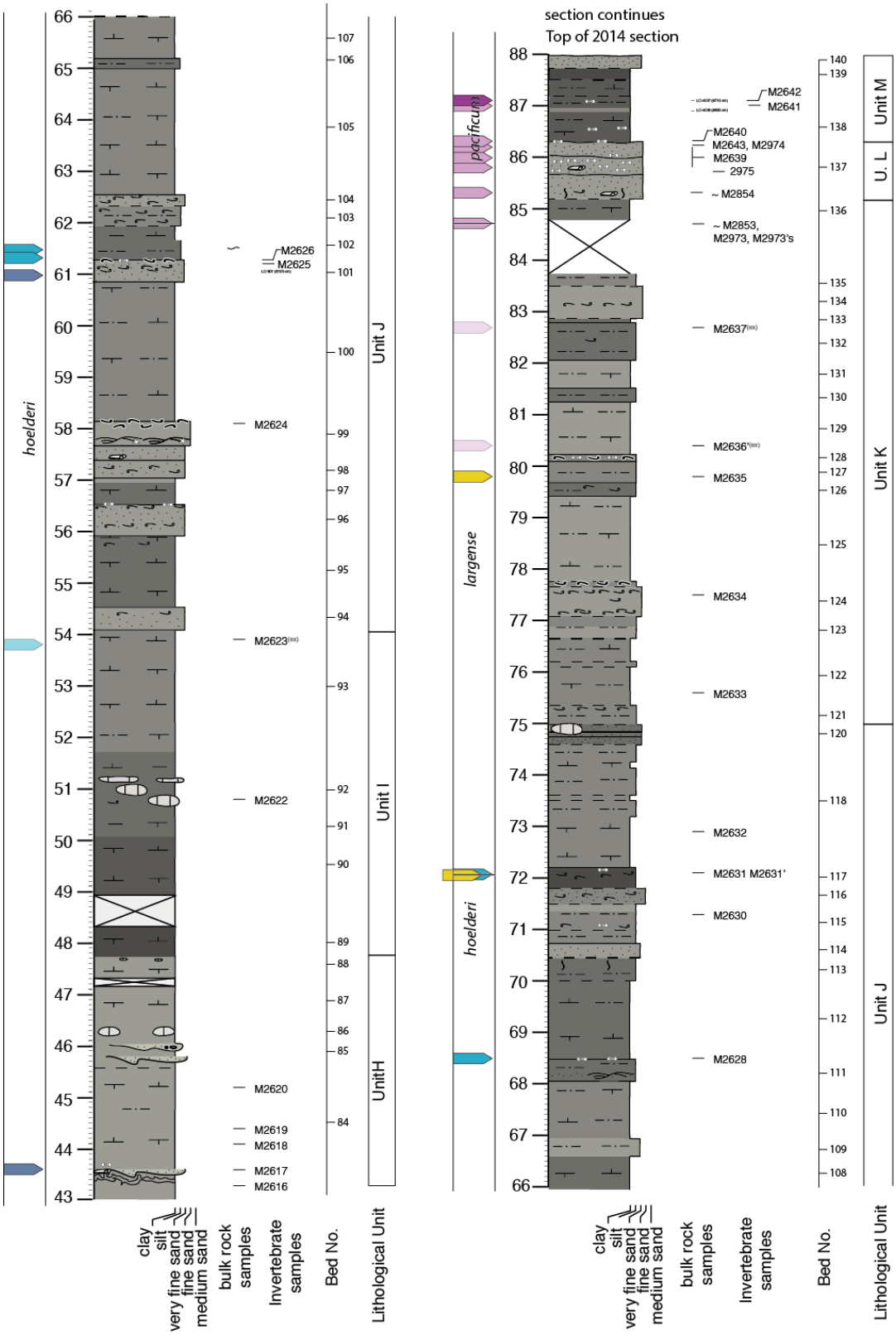

Figure A-10.b stratigraphic log of section Las Overas - continued

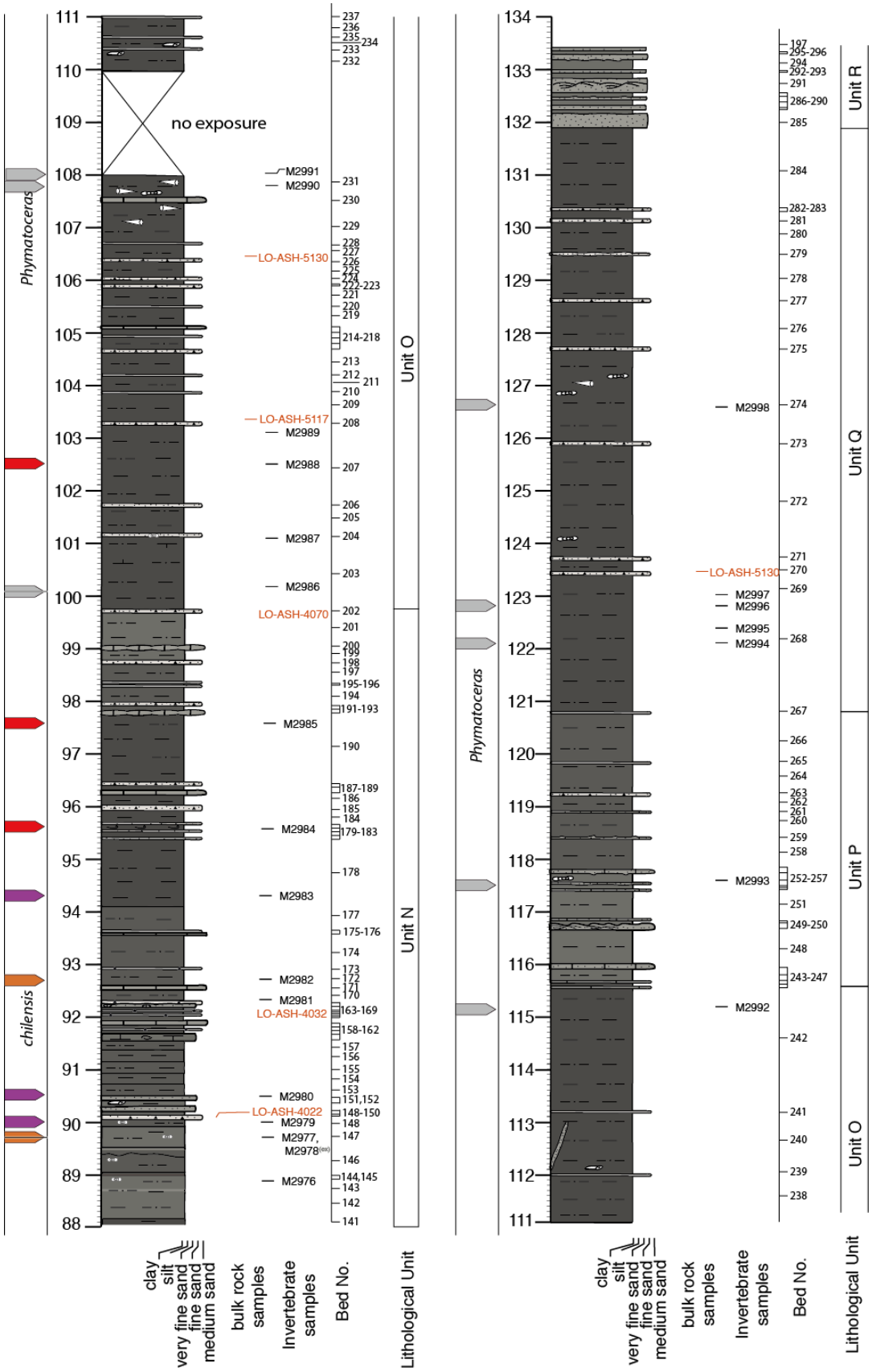

Figure A-10.c: stratigraphic log of section Las Overas - continued

A-11: Arroyo Las Overas - C:

The base of Arroyo Las Overas – C section is located at S 35°26'56", W 69°53'52", at 2340 m elevation and lies stratigraphically above the Arroyo Las Overas Section. The section comprises silty mudstone and intercalated beds of sandstone with internal structures (cross-bedding), volcanic ash layers and hard-cemented mudstone beds.

Unit A (0–4.4 m) comprises medium grey silty mudstone. Sandstone-filled scours appear in the upper part of the unit. The sand is fine-grained and slightly laminated.

Unit B (4.4–5.4 m) is characterized by silty mudstones interbedded with fine-grained lensoidal sandstone beds.

Silty, medium grey mudstones of Unit C (5.4–19.3 m) are interrupted by a sandstone-filled scour (Bed no. 18) and two ~10-cm-thick massive sandstone beds in the lower part (Beds No. 20, 24), and hard cemented, dark grey mudstone beds (Beds no. 26, 28, 31, 35, 41) and some volcanic ash layers.

In Unit D (9.3–21.5 m) silty mudstone is intercalated between fine-grained sandstone layers of varying thickness, with sharp scoured bases and low-angle cross-bedding.

Unit E consist of uniform, medium grey, silt-rich mudstones (21.4–25.2 m).

Similar to Unit B and D, fine-grained sandstone beds of varying thicknesses (5 to 40 cm) are intercalated between mudstone beds in Unit F (25.2 – 29 m). The sandstone beds have erosional bases and show low-angle cross-bedding.

Unit G (29–42.5 m) comprises a thick mudstone succession, locally interrupted by thin (~5cm) sandstone beds and dark grey, hard-cemented mudstone beds. The sandstone beds are more common in the lower part of the unit, whereas the dark mudstone beds appear more commonly towards the top. Two mudstone beds (Bedd no. 96 and 98) contain belemnites.

A dark grey mudstone and shale succession is present in Unit H (42.5–46.1 m), followed by a dark shales interrupted by several very fine grained sand beds, some with convolute top, in Unit I (46.1–47.1 m).

In Unit J (47.1–62.5 m), several volcanic ash layers (<5cm) are intercalated in a uniform succession of dark grey silty mudstones and shales. Hard-cemented, up to 10-cm-thick mudstone beds appear throughout the unit. Some appear nodular in shape. A belemnite bed is present at ~51 m, above bed no. 132. Two thin (<5 cm) fine-grained sandstone beds appear, one in the lower part of the Unit (Bed no. 124) and one in the upper part close to the top (Bed no. 143), containing belemnites.

In Unit K (62.5–64.3 m), dark grey silty mudstone and shales alternate with fine-grained sandstone beds, being similar to Unit B, D and F.

Unit L (64.3–69 m) is marked by a thick succession of shaly mudstones, dark grey in colour, with a ~40-cm-thick cemented mudstone layer (Bed no 158).

In Unit M, fine-grained sandstones appear in a shaly mudstone-dominated succession. The thickness of the sandstone beds increases towards the top of the Unit. Internal sedimentary structures (cross-bedding) can be seen.

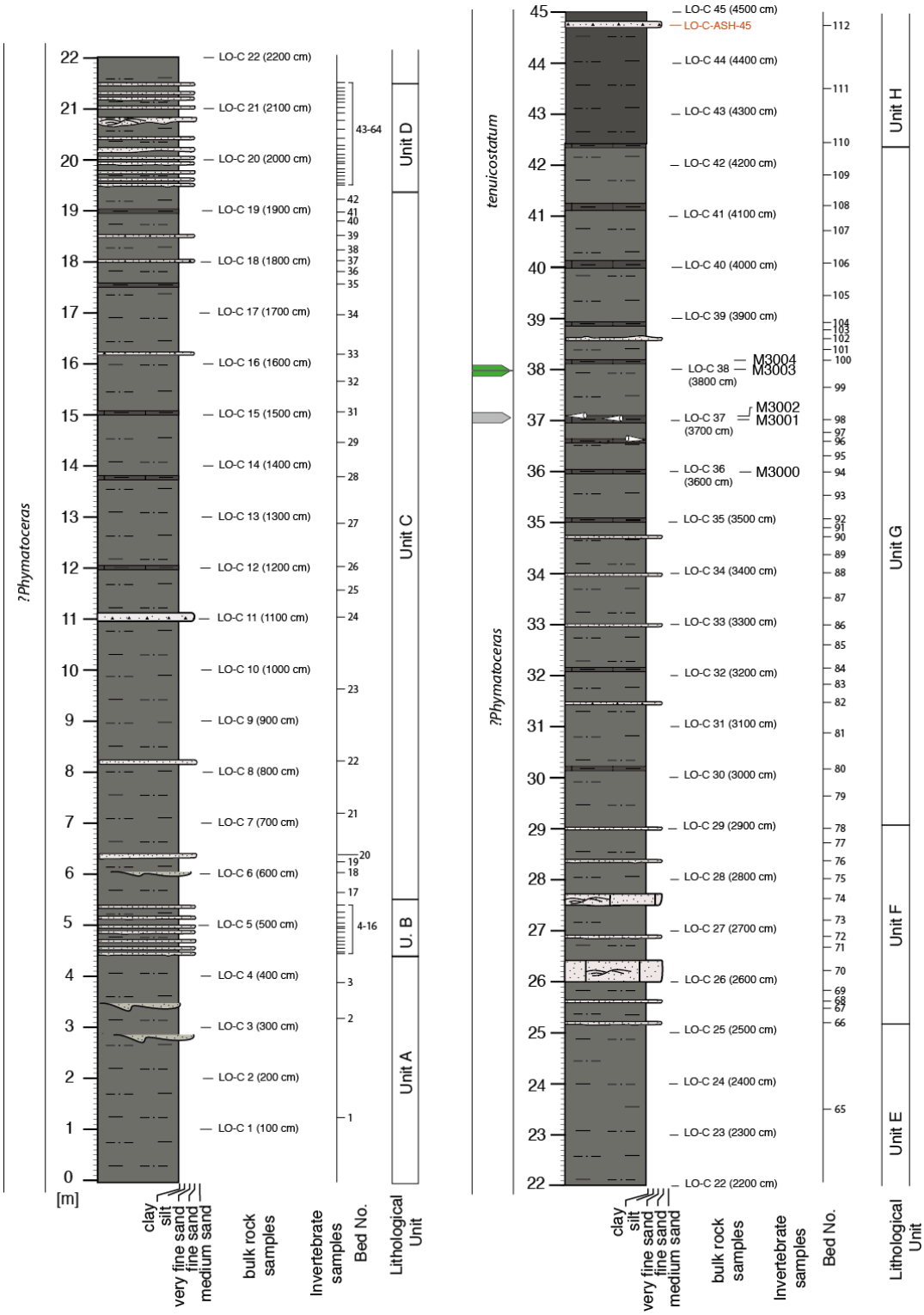

Figure A-11: stratigraphic log of section Las Overas-C. See Figure A-8 for key and ammonite zonation color scheme.

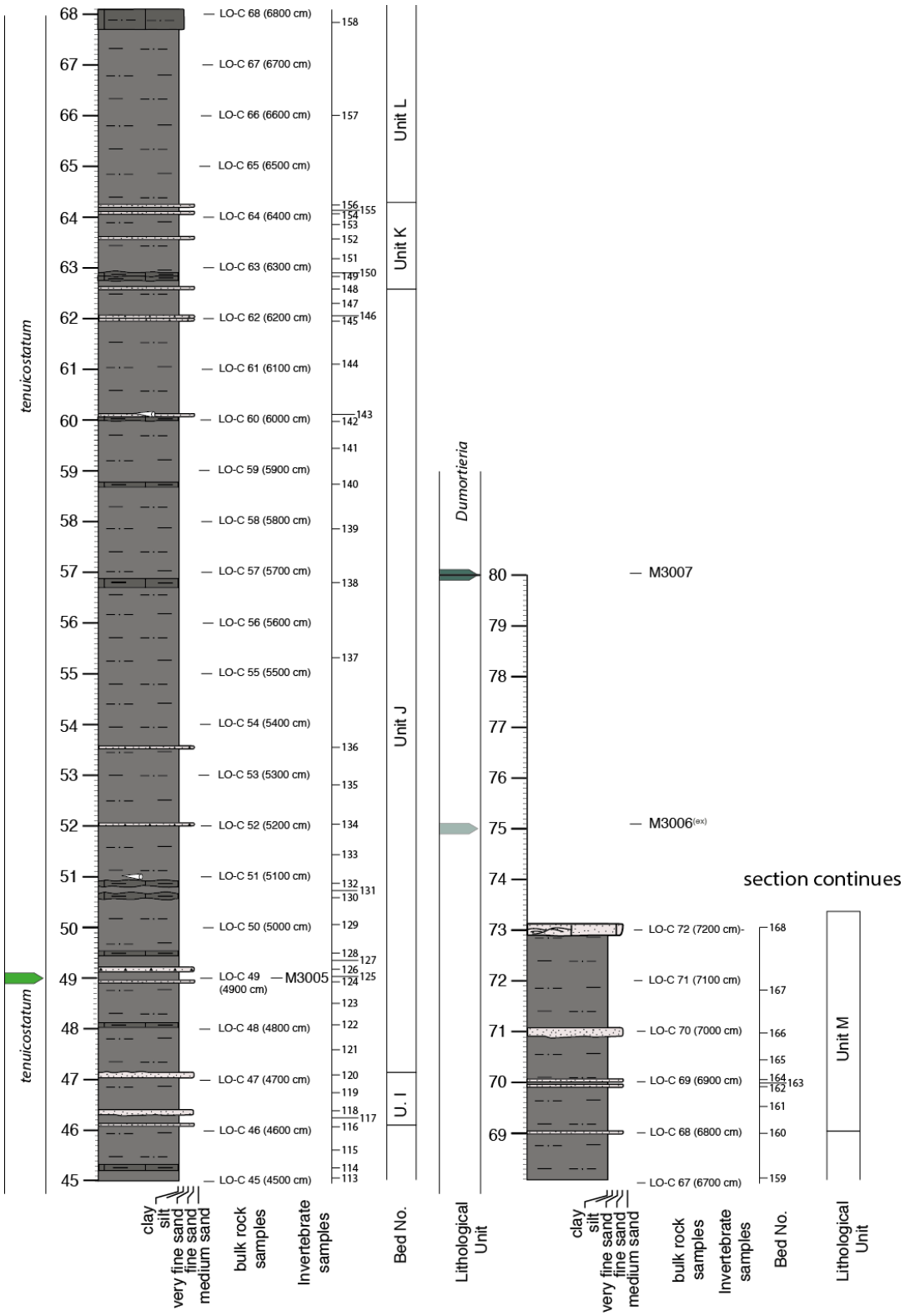

Figure A-11.b: stratigraphic log of section Las Overas-C - continued

A-12: Palynofacies

Sample preparation for palynofacies analysis was performed by Malcom Jones at the Palynological Laboratory Services Ltd, Isle of Anglesey in North Wales, UK. Quantitative and qualitative palynological analysis of the samples and was performed by Paul Dodsworth, StrataSolve Ltd, Warrington, UK. The results presented in the following are re-structured and reworded from the original report provided by Paul Dodsworth.

Sample AS-520 (0.97 wt.% TOC), located 21.65 m above the base of Section Arroyo Serrucho F–F', contains a single (questionable) pollen specimen (?*Corollina meyeriana*) in the kerogen slide. Black wood fragments are common, predominantly as elongated fragments and subordinate as equi-dimensional fragments (see figure A in plate 1), indicating a high-energy environment with high amounts of allochthonous input, e.g. upper / lower shoreface (Whitaker 1984).

Sample LO-3019 (0.85 wt.% TOC) is located in the pre$\delta^{13}C_{TOC}$ excursion interval of the lower Las Overas section (-1.9 m) and corresponds to the uppermost *D. tenuicostatum* Zone. Common Jurassic pollen (*Corollina meyeriana*, 4) are present in the kerogen slide (Plate 2, Fig. 1-3). The oxidized slide contains abundant spores (*Densosporites spp*., 3 (including D. *dentatus* 'group' (Plate 2, Figs. 23) and *D*. cf. *rarispinosus* (Plate 2, Fig. 24); *Raistrickia* cf. *clavata* (Plate 2, Fig. 15), and; questionable *Lycospora* spp. (Plate 2, Fig. 26). A proximochorate Jurassic dinoflagellate cyst is questionably assigned to *Sentusidinium* spp.). Black wood fragments are the dominant palynofacies (amorphous organic matter (AOM) *versus* phytoclast ratio = 1:99,), and appear in elongated and equi-dimensional shapes. The organic-matter composition suggests a high-energy environment, supporting alochthonous input and reworking.

Sample LO-146 is located in the lower *hoelderi* zone of the Las Overas section (14.5 m), and corresponds to the negative carbon-isotope excursion and contains a very low

total organic carbon content (0.1 wt % TOC). The kerogen slide contains a specimen of Jurassic pollen (Corollina *meyeriana*) and marine foraminiferal test linings. Similar to the subjacent sample, reworked Upper Palaeozoic (probably Carboniferous) spores (*Densosporites* spp., including D. *dentatus* 'group' (Plate 2, Figs. 20, 21, 25),

D. cf. *rarispinosus* (Plate 2, Fig. 19) and *D*. *triangularis* (Plate 2, Fig. 22); *Triquitrites* cf. *tricoranatus* (Plate 2, Fig. 17), and; questionable *Lycospora pusilla* are present. Spores of Upper Paleozoic to Jurassic origin, *Verrucosisporites* spp. (Plate 2, Fig. 12) were found. A single dinoflagellate cyst (*Chytroeisphaeridia*? spp. (Plate 2, Fig. 11)) was recovered. Equidimensional wood fragments are abundant (Plate 1, Fig. B). The ratio between amorphous organic matter and phytoclasts is 9:91.

Sample LO-484 is located in the lower upper *hoelderi* Zone of the Las Overas section (48.1 m), and corresponds to the most negative part of the $\delta^{13}C_{TOC}$ negative excursion, and with slightly elevated TOC (ca. 1wt.%). *Corollina meyeriana* occurs in the kerogen fraction. The oxidized slide comprises Jurassic dinoflagellate cycsts assigned to the proximochorate specimens questionably assigned to *Sentusidinium* spp. (Plate 2, Figs. 8, 9) and *Rhynchodiniopsis*? aff. *regalis* (less membranous paraplate ornament than type specimen of *R*? *regalis*) (Plate 2, Fig. 6, 7), although the stratigraphic range of *R*? *regalis* in Europe is younger (Bajocian–Bathonian, Middle Jurassic; e.g. Riding & Thomas 1992) than the Lower Jurassic strata studied here. Reworked spores (*Cingulizonates bialatus* and *Densosporites* spp.) are present. The ratio between amorphous organic matter and phytoclasts (18:72) in the palynofacies is higher compared to the subjacent strata (Plate 1, Fig.C), indicating a higher contribution of marine organic matter.

Sample LO-5004 (2.35 wt.% TOC), located 101.3 m above the base of the Las Overas section (lower *Phymatoceras* Zone). Two reworked Carboniferous Paleozoic spores (*Densosporites* spp. and *Triquitrites* cf. *tricoranatus* (Plate 2, Fig. 16) were found in the oxidized slide.

The palynofacies contains the highest amount of amorphous organic matter relative to

phytoclasts (45:55) of all analyzed samples (Plate 1, Fig. D) and might indicate the highest contribution of marine organic matter to the total organic-matter composition.

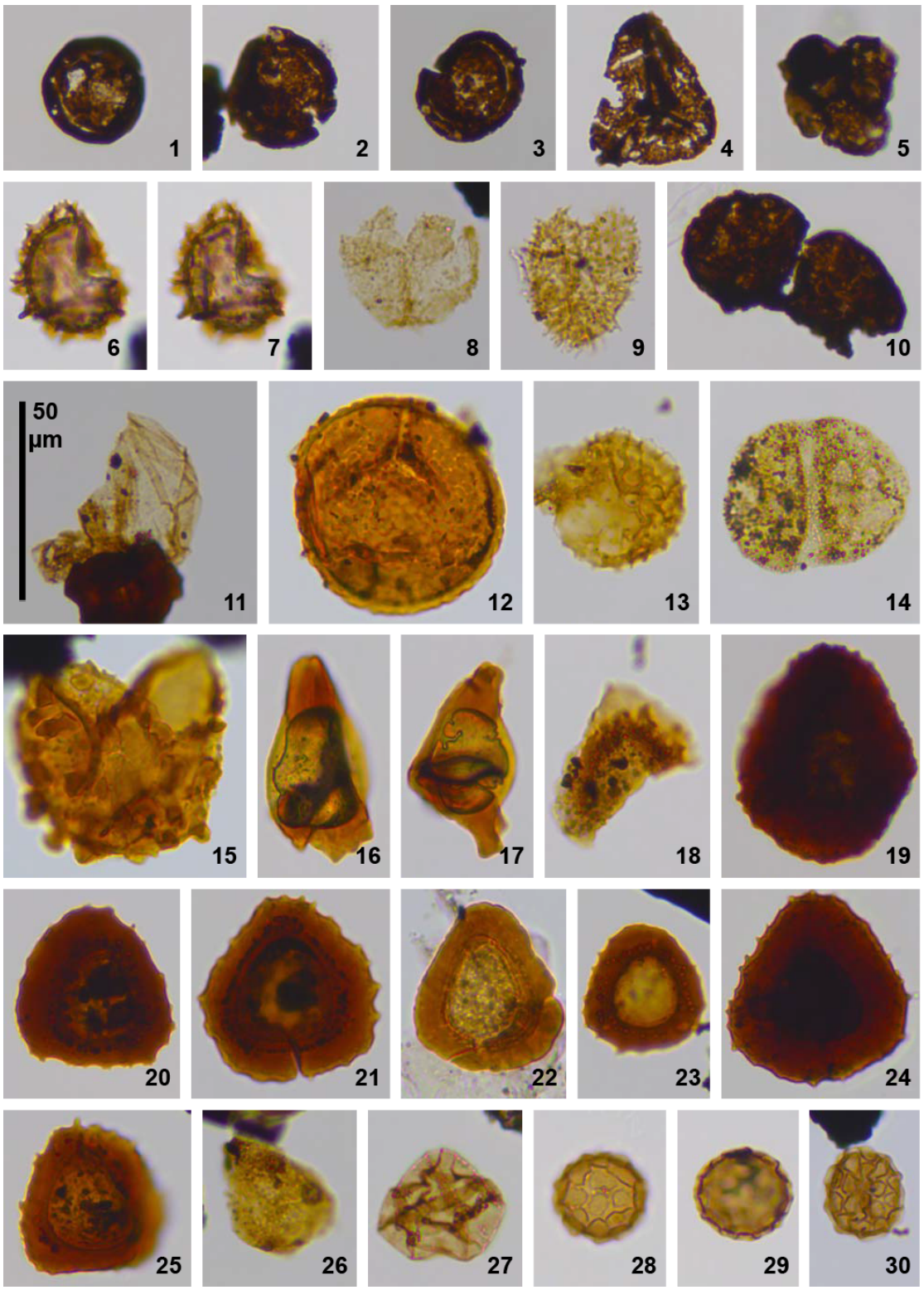

Figure A-12: Palynomorphs from Arroyo Serrucho and Las Overas samples. All pictures are to the same scale (see 50 μm in picture 11). **1.** *Corollina meyeriana* (Klaus 1960) Venkatachala & Goczán 1964, LO-3019 (kerogen) **2.** *Corollina meyeriana* (Klaus 1960) Venkatachala & Goczán 1964, LO-484 (kerogen), **3.** Corollina meyeriana (Klaus 1960) Venkatachala & Goczán 1964, LO-484 (kerogen) **4.** Trilete spore, ?*Dictyoplhyllidites* spp., LO-484 (kerogen) **5.** ?Foraminiferal test lining (spiral), LO-146 (kerogen) **6. & 7.** *Rynchodiniopsis*? aff. *regalis* (Gocht 1970) Jan du Chêne *et al*. 1985, Las Overas, LO-484, **8.** Proimochorate dinflagellate cyst, *Sentusidinium*? spp., LO-484, **9.** Proimochorate dinflagellate cyst, *Sentusidinium*? spp., LO-484 **10.** Foraminiferal test lining (two linked chambers), Las Overas, 14.5m (kerogen), **11.** *Chytroeisphaeridia*? spp., LO-146 **12.** *Verrucosisporites* spp., LO-146 **13.** ?*Retitriletes eminulus* (Dettmann 1963) Srivastava 1977, LO-2016 **14.** *Alisporites* spp., LO-484 **15.** *Raistrickia* aff. *saetosa* (Loose) Schopf, Wilson & Bentall 1944, Las Overas, -1.9m **16.** *Triquitrites* cf. *tricoranatus* Sullivan 1964 (similar high auriculae but lacking ornament on body), LO- 5004 **17.** *Triquitrites* cf. *tricoranatus* Sullivan 1964, LO-146 **18.** *Cingulizonates bialatus* (Walz) Smith & Butterworth 1967 fragment, LO-484 **19.** *Densosporites* cf. *rarispinosus* Playford 1963 (spinae slightly less-well developed), LO-146 **20.& 21.** *Densosporites dentatus* (Waltz) Potonie & Kremp 1956, LO-146 **22.** *Densosporites triangularis* Kosanke 1950 LO-146 **23.** *Densosporites dentatus* (Waltz) Potonie & Kremp 1956, LO-3019, N42/1; **24.** *Densosporites* cf. *rarispinosus* Playford 1963, LO-3019 (kerogen) **25.** *Densosporites dentatus* (Waltz) Potonie & Kremp 1956, LO-146 **26.** ?*Lycospora* spp., LO-3019 **27.** *Incertae sedis* type 1, possible dinoflagellate cyst or other alga, LO-146 **28.** *Incertae sedis* type 2, possible contaminant as not darkened in kerogen samples, possible Cymatiosphaera (prasinophyte alga) or reticulate-ornamented spore, LO-146 **29.** Incertae sedis type 2, LO-484 (kerogen), E46/3; **30.** *Incertae sedis* type 2, LO-484 (kerogen).

Chapter 10 : References

Aberhan, M. (2001). "Bivalve palaeobiogeography and the Hispanic Corridor: time of opening and effectiveness of a proto-Atlantic seaway." Palaeogeography, Palaeoclimatology, Palaeoecology **165**(3): 375-394.

Aberhan, M. (2002). "Opening of the Hispanic Corridor and Early Jurassic bivalve biodiversity." Geological Society, London, Special Publications **194**(1): 127-139.

Al-Suwaidi, A. H., G. N. Angelozzi, F. Baudin, S. E. Damborenea, S. P. Hesselbo, H. C. Jenkyns, M. O. Manceñido and A. C. Riccardi (2010). "First record of the Early Toarcian Oceanic Anoxic Event from the Southern Hemisphere, Neuquén Basin, Argentina." Journal of the Geological Society **167**(4): 633-636.

Al-Suwaidi, A. H. (2011). A Southern Hemisphere Record of the Toarcian Oceanic Anoxic Event from teh Neuquén Basin, Argentina. PhD, University of Oxford.

Al-Suwaidi, A. H., S. P. Hesselbo, S. E. Damborenea, M. O. Manceñido, H. C. Jenkyns, A. C. Riccardi, G. N. Angelozzi and F. Baudin (2016). "The Toarcian Oceanic Anoxic Event (Early Jurassic) in the Neuquén Basin, Argentina: a reassessment of age and carbon isotope stratigraphy." The Journal of Geology **124**(2): 171-193.

Arrhenius, S. (1896). "On the Influence of Carbonic Acid in the Air upon the Temperature of the Ground." Philosophical Magazine and Journal of Science **41**: 237-276.

Arrhenius, S. and J. W. Sandström (1903). Lehrbuch der kosmischen Physik, S. Hirzel.

Austin, J. A., B. E. Tucholke and E. Uchupi (1989). "Upper Triassic—Lower Jurassic salt basin southeast of the Grand Banks." Earth and Planetary Science Letters **92**(3-4): 357-370.

Bailey, T., Y. Rosenthal, J. McArthur, B. Van De Schootbrugge and M. Thirlwall (2003). "Paleoceanographic changes of the Late Pliensbachian–Early Toarcian interval: a possible link to the genesis of an Oceanic Anoxic Event." Earth and Planetary Science Letters **212**(3): 307-320.

Baksi, A. K. and D. Archibald (1997). "Mesozoic igneous activity in the Maranhão province, northern Brazil: $^{40}Ar/^{39}Ar$ evidence for separate episodes of basaltic magmatism." Earth and Planetary Science Letters 151(3-4): 139-153.

Bartolini, A., J. Guex, J. E. Spangenberg, B. Schoene, D. G. Taylor, U. Schaltegger and V. Atudorei (2012). "Disentangling the Hettangian carbon isotope record: Implications for the aftermath of the end-Triassic mass extinction." Geochemistry, Geophysics, Geosystems **13**(1), 1-11

Beerling, D. J. and S. J. Brentnall (2007). "Numerical evaluation of mechanisms driving Early Jurassic changes in global carbon cycling." Geology **35**(3): 247-250.

Berner, R. A. (1999). "A new look at the long-term carbon cycle." GSA Today **9**(11): 1-6.

Beutel, E., S. Nomade, A. Fronabarger and P. Renne (2005). "Pangea's complex breakup: A new rapidly changing stress field model." Earth and Planetary Science Letters **236**(1): 471-485.

Bin, C., W. Xiaoru and F. S. Lee (2001). "Pyrolysis coupled with atomic absorption spectrometry for the determination of mercury in Chinese medicinal materials." Analytica Chimica Acta **447**(1): 161-169.

Bjerrum, C. J., F. Surlyk, J. H. Callomon and R. L. Slingerland (2001). "Numerical paleoceanographic study of the Early Jurassic Transcontinental Laurasian Seaway." Paleoceanography **16**(4): 390-404.

Blackburn, T. J., P. E. Olsen, S. A. Bowring, N. M. McLean, D. V. Kent, J. Puffer, G. McHone, E. T. Rasbury and M. Et-Touhami (2013). "Zircon U-Pb Geochronology Links the End-Triassic Extinction with the Central Atlantic Magmatic Province." Science **340**(6135): 941-945.

Blakey, R. (2007). "Early Jurassic rectangular paleogeographic map in Mollweide." http://jan.ucc.nau.edu/,rcb7/200marect.jpg.

Blomeier, D. P. and J. J. Reijmer (1999). "Drowning of a Lower Jurassic carbonate platform: Jbel Bou Dahar, High Atlas, Morocco." Facies **41**(1): 81.

Blum, J. D., L. S. Sherman and M. W. Johnson (2014). "Mercury isotopes in earth and environmental sciences." Annual Review of Earth and Planetary Sciences **42**: 249-269.

Bond, D. P. and P. B. Wignall (2014). "Large igneous provinces and mass extinctions: an update." Geological Society of America Special Papers. **505**: SPE505-502.

Bonis, N. R., M. Ruhl and W. M. Kürschner (2010). "Climate change driven black shale deposition during the end-Triassic in the western Tethys." Palaeogeography, Palaeoclimatology, Palaeoecology **290**(1–4): 151-159.

Boulila, S., B. Galbrun, E. Huret, L. A. Hinnov, I. Rouget, S. Gardin and A. Bartolini (2014). "Astronomical calibration of the Toarcian Stage: implications for sequence stratigraphy and duration of the early Toarcian OAE." Earth and Planetary Science Letters **386**: 98-111.

Boulila, S., B. Galbrun, J. Laskar and H. Pälike (2012). "A~ 9myr cycle in Cenozoic $\delta^{13}C$ record and long-term orbital eccentricity modulation: Is there a link?" Earth and Planetary Science Letters **317**: 273-281.

Bradshaw, M. J., J. C. W. Cope, D. W. Cripps, D. T. Donovan, M. K. Howarth, P. F. Rawson, I. M. West and W. A. Wimbledon (1992). "Jurassic." Geological Society, London, Memoirs **13**(1): 107-129.

Brune, S., S. E. Williams and R. D. Müller (2017). "Potential links between continental rifting, CO_2 degassing and climate change through time." Nature Geoscience **10**(12): 941.

Burgess, S. D., S. A. Bowring, T. H. Fleming and D. H. Elliot (2015). "High-precision geochronology links the Ferrar large igneous province with early-Jurassic ocean anoxia and biotic crisis." Earth and Planetary Science Letters **415**: 90-99.

Callendar, G. S. (1938). "The artificial production of carbon dioxide and its influence on temperature." Quarterly Journal of the Royal Meteorological Society **64**(275): 223-240.

Calvert, S. and T. Pedersen (2007). "Elemental proxies for palaeoclimatic and palaeoceanographic variability in marine sediments: interpretation and application." Developments in Marine Geology **1**: 567-644.

Caruthers, A. H., D. R. Gröcke and P. L. Smith (2011). "The significance of an Early Jurassic (Toarcian) carbon-isotope excursion in Haida Gwaii (Queen Charlotte Islands), British Columbia, Canada." Earth and Planetary Science Letters **307**(1): 19-26.

Caruthers, A. H., P. L. Smith and D. R. Gröcke (2014). "The Pliensbachian–Toarcian (Early Jurassic) extinction: A North American perspective." Geological Society of America Special Papers **505**: 225-243.

Chandler, M. A., D. Rind and R. Ruedy (1992). "Pangaean climate during the Early Jurassic: GCM simulations and the sedimentary record of paleoclimate." Geological Society of America Bulletin **104**(5): 543-559.

Claypool, G. E. and I. Kaplan (1974). The origin and distribution of methane in marine sediments. Natural gases in marine sediments, Springer**:** 99-139.

Clemence, M.-E., A. Bartolini, S. Gardin, G. Paris, B. Valérie and K. Page (2010). "Early Hettangian benthic–planktonic coupling at Doniford (SW England): Palaeoenvironmental implications for the aftermath of the end-Triassic crisis." Palaeogeography Palaeoclimatology Palaeoecology **295**: 102-115.

Cobianchi, M. and V. Picotti (2001). "Sedimentary and biological response to sea-level and palaeoceanographic changes of a Lower–Middle Jurassic Tethyan platform margin (Southern Alps, Italy)." Palaeogeography, Palaeoclimatology, Palaeoecology **169** (3): 219-244.

Cohen, A. S., A. L. Coe, S. M. Harding and L. Schwark (2004). "Osmium isotope evidence for the regulation of atmospheric CO2 by continental weathering." Geology **32**(2): 157-160.

Copestake, P. and B. Johnson (2014). "Lower Jurassic foraminifera from the Llanbedr (Mochras Farm) Borehole, North Wales, UK." Paleontological Society (167): 1-403.

Courtillot, V. E. and P. R. Renne (2003). "On the ages of flood basalt events." Comptes Rendus Geoscience **335**(1): 113-140.

Coward, M. P. D., J.F.; Hempton, M.; Molroyd, J. (2003). Tectonic Evolution. London, The Geological Society.

Cramer, B. S., J. D. Wright, D. V. Kent and M. P. Aubry (2003). "Orbital climate forcing of δ13C excursions in the late Paleocene–early Eocene (chrons C24n–C25n)." Paleoceanography **18**(4).

Curtis, C. and D. Spears (1968). "The formation of sedimentary iron minerals." Economic Geology **63**(3): 257-270.

Dahl, B., J. Bojesen-Koefoed, A. Holm, H. Justwan, E. Rasmussen and E. Thomsen (2004). "A new approach to interpreting Rock-Eval S 2 and TOC data for kerogen quality assessment." Organic Geochemistry **35**(11): 1461-1477.

Damborenea, S. E. (1996). Palaeobiogeography of Early Jurassic bivalves along the southeastern Pacific margin. XIII Congreso Geológico Argentino and III Congreso de Exploración de Hidrocarburos, Acta (5), 151-167.

Davies, J. H. F. L., A. Marzoli, H. Bertrand, N. Youbi, M. Ernesto and U. Schaltegger (2017). "End-Triassic mass extinction started by intrusive CAMP activity." Nature Communications **8**: 15596.

Davison, I. (2005). "Central Atlantic margin basins of North West Africa: geology and hydrocarbon potential (Morocco to Guinea)." Journal of African Earth Sciences **43**(1): 254-274.

Dean, W. T., Donovan D. T. and Howarth M. K. (1961). The Liassic ammonite zones and subzones of the north-west European Province, British Museum (Natural History) 4 (10), 71p.

Deckart, K., G. Féraud and H. Bertrand (1997). "Age of Jurassic continental tholeiites of French Guyana, Surinam and Guinea: implications for the initial opening of the Central Atlantic Ocean." Earth and Planetary Science Letters **150**(3-4): 205-220.

Deenen, M. H. L., M. Ruhl, N. R. Bonis, W. Krijgsman, W. Kürschner, M. Reitsma and M. J. van Bergen (2010). "A new chronology for the end-Triassic mass extinction." Earth and Planetary Science Letters **291**: 113-125.

Demaison, G. J. and G. T. Moore (1980). "Anoxic environments and oil source bed genesis." Organic Geochemistry **2**(1): 9-31.

Dera, G., B. Brigaud, F. Monna, R. Laffont, E. Pucéat, J.-F. Deconinck, P. Pellenard, M. M. Joachimski and C. Durlet (2011). "Climatic ups and downs in a disturbed Jurassic world." Geology **39**(3): 215-218.

Dera, G. and Y. Donnadieu (2012). "Modeling evidences for global warming, Arctic seawater freshening, and sluggish oceanic circulation during the Early Toarcian anoxic event." Paleoceanography **27**(2).

Dera, G., P. Pellenard, P. Neige, J.-F. Deconinck, E. Pucéat and J.-L. Dommergues (2009b). "Distribution of clay minerals in Early Jurassic Peritethyan seas: palaeoclimatic significance inferred from multiproxy comparisons." Palaeogeography, Palaeoclimatology, Palaeoecology **271**(1): 39-51.

Dera, G., E. Pucéat, P. Pellenard, P. Neige, D. Delsate, M. M. Joachimski, L. Reisberg and M. Martinez (2009a). "Water mass exchange and variations in seawater temperature in the NW Tethys during the Early Jurassic: evidence from neodymium and oxygen isotopes of fish teeth and belemnites." Earth and Planetary Science Letters **286**(1): 198-207.

Dickens, G. R. (2003). "Rethinking the global carbon cycle with a large, dynamic and microbially mediated gas hydrate capacitor." Earth and Planetary Science Letters **213**(3): 169-183.

Dickens, G. R., J. R. O'Neil, D. K. Rea and R. M. Owen (1995). "Dissociation of oceanic methane hydrate as a cause of the carbon isotope excursion at the end of the Paleocene." Paleoceanography **10**(6): 965-971.

Dobson, M. R. and R. J. Whittington (1987). "The geology of Cardigan Bay." Proceedings of the Geologists' Association **98**(4): 331-353.

Duarte, L. V., M. J. Comas-Rengifo, R. L. Silva, R. Paredes and A. Goy (2014). "Carbon isotope stratigraphy and ammonite biochronostratigraphy across the Sinemurian-Pliensbachian boundary in the western Iberian margin." Bulletin of Geosciences **89**(4): 719-736.

Duarte, L. V., R. L. Silva and J. G. Mendonça Filho (2011). The Lower Jurassic of west coast of Portugal: stratigraphy and organic matter in carbonate sedimentation. Field Trip Guide Book of 63rd Annual Meeting of the International Committee for Coal and Organic Petrology, Memórias.

Espitalie, J., M. Madec and B. Tissot (1980). "Role of mineral matrix in kerogen pyrolysis: influence on petroleum generation and migration." AAPG Bulletin **64**(1): 59-66.

Feng, X. and S. Epstein (1995). "Climatic temperature records in δD data from tree rings." Geochimica et Cosmochimica Acta **59**(14): 3029-3037.

Franceschi, M., J. Dal Corso, R. Posenato, G. Roghi, D. Masetti and H. C. Jenkyns (2014). "Early Pliensbachian (Early Jurassic) C-isotope perturbation and the diffusion of the Lithiotis Fauna: Insights from the western Tethys." Palaeogeography, Palaeoclimatology, Palaeoecology **410**(0): 255-263.

Franzese, J. R. and L. A. Spalletti (2001). "Late Triassic–early Jurassic continental extension in southwestern Gondwana: tectonic segmentation and pre-break-up rifting." Journal of South American Earth Sciences **14**(3): 257-270.

Franzese, J., L. Spalletti, I. G. Pérez and D. Macdonald (2003). "Tectonic and paleoenvironmental evolution of Mesozoic sedimentary basins along the Andean foothills of Argentina (32°–54°S)." Journal of South American Earth Sciences **16**(1): 81-90.

Franzese, J., G. Veiga, E. Schwarz and I. Gómez-Pérez (2006). "Tectonostratigraphic evolution of a Mesozoic graben border system: the Chachil depocentre, southern Neuquén Basin, Argentina." Journal of the Geological Society **163**(4): 707-721.

French, K. L., J. Sepulveda, J. Trabucho-Alexandre, D. Gröcke and R. E. Summons (2014). "Organic geochemistry of the early Toarcian oceanic anoxic event in Hawsker Bottoms, Yorkshire, England." Earth and Planetary Science Letters **390**: 116-127.

Friedrich, O., J. O. Herrle, P. A. Wilson, M. J. Cooper, J. Erbacher and C. Hemleben (2009). "Early Maastrichtian carbon cycle perturbation and cooling event: Implications from the South Atlantic Ocean." Paleoceanography **24**(2): PA2211.

Frieling, J., H. H. Svensen, S. Planke, M. J. Cramwinckel, H. Selnes and A. Sluijs (2016). "Thermogenic methane release as a cause for the long duration of the PETM." Proceedings of the National Academy of Sciences **113**(43): 12059.

Frimmel, A., W. Oschmann and L. Schwark (2004). "Chemostratigraphy of the Posidonia Black Shale, SW Germany: I. Influence of sea-level variation on organic facies evolution." Chemical Geology **206**(3): 199-230.

Gill, B. C., T. W. Lyons and H. C. Jenkyns (2011). "A global perturbation to the sulfur cycle during the Toarcian Oceanic Anoxic Event." Earth and Planetary Science Letters **312**(3): 484-496.

Giorgioni, M., H. Weissert, S. M. Bernasconi, P. A. Hochuli, R. Coccioni and C. E. Keller (2012). "Orbital control on carbon cycle and oceanography in the mid‐Cretaceous greenhouse." Paleoceanography **27**(1): PA1204.

Gómez, J. J., M. Comas-Rengifo and A. Goy (2016). "Palaeoclimatic oscillations in the Pliensbachian (Early Jurassic) of the Asturian Basin (Northern Spain)." Climate of the Past **12**: 1199-1214.

Gorbanenko, O. (2017). "A dry polishing technique for the petrographic examination of mudrocks." International Journal of Coal Geology **180**: 122-126.

Gorbanenko, O. and B. Ligouis (2015). "Variations of organo-mineral microfacies of Posidonia Shale from the Lower Saxony Basin and the West Netherlands Basin: Application to paleoenvironmental reconstruction." International Journal of Coal Geology **152**: 78-99.

Gradstein, F. M. (2012). Chapter 1 - Introduction. The Geologic Time Scale. F. M. Gradstein, J. G. O. D. Schmitz and G. M. Ogg. Boston, Elsevier**:** 1-29.

Gröcke, D., R. Hori, J. Trabucho-Alexandre, D. Kemp and L. Schwark (2011). "An open ocean record of the Toarcian oceanic anoxic event." Solid Earth **2**(2): 245.

Guex, J., A. Bartolini, J. Spangenberg, J.-C. Vicente and U. Schaltegger (2012). "Ammonoid multi-extinction crises during the Late Pliensbachian–Toarcian and carbon cycle instabilities." Solid Earth Discussions **4**(2): 1205-1228.

Guex, J., B. Schoene, A. Bartolini, J. Spangenberg, U. Schaltegger, L. O'Dogherty, D. Taylor, H. Bucher and V. Atudorei (2012). "Geochronological constraints on post-extinction recovery of the ammonoids and carbon cycle perturbations during the Early Jurassic." Palaeogeography, Palaeoclimatology, Palaeoecology **346–347**: 1-11.

Gulisano, C. and A. G. Pleimling (1995). Field Guide the Jurassic of the Neuquén Basin: B, Mendoza Province, Secretaría de Minería de la Nación. 103p.

Hames, W., P. Renne and C. Ruppel (2000). "New evidence for geologically instantaneous emplacement of earliest Jurassic Central Atlantic magmatic province basalts on the North American margin." Geology **28**(9): 859-862.

Handoh, I. C. and T. M. Lenton (2003). "Periodic mid-Cretaceous oceanic anoxic events linked by oscillations of the phosphorus and oxygen biogeochemical cycles." Global Biogeochemical Cycles **17**(4): 1092.

Haq, B., J. Hardenbol and P. Vail (1987). "The new chronostratigraphic basis of Cenozoic and Mesozoic sea level cycles." Timing and depositional history of eustatic sequences: constraints on seismic stratigraphy: Cushman Foundation for Forminiferal Research, Special Publications **24**: 7-13.

Haq, B. U. (2017). "Jurassic Sea-Level Variations: A Reappraisal." GSA Today **28**(1): 4-10.

Harazim, D., B. Van, B. van de Schootbrugge, K. Sorichter, J. Fiebig, A. Weug, G. Suanà and W. Oschmann (2013). Spatial variability of watermass conditions within the European Epicontinental Seaway during the Early Jurassic (Pliensbachian–Toarcian). Sedimentology **60**: 359-390.

Harries, P. J. and C. T. Little (1999). "The early Toarcian (Early Jurassic) and the Cenomanian–Turonian (Late Cretaceous) mass extinctions: similarities and contrasts." Palaeogeography, Palaeoclimatology, Palaeoecology **154**(1): 39-66.

Harrison, R. K. (1971). The Petrology of the Upper Triassic Rocks in the Llanbedr (Mochras Farm) Borehole. In: Woodland, A.W. (Ed.): The Llanbedr (Mochras Farm) Borehole. Institute of Geological Science **71**(18): 37-72.

Hermoso, M., L. Le Callonnec, F. Minoletti, M. Renard and S. P. Hesselbo (2009a). "Expression of the Early Toarcian negative carbon-isotope excursion in separated carbonate microfractions (Jurassic, Paris Basin)." Earth and Planetary Science Letters **277**(1–2): 194-203.

Hesselbo, S., D. Gröcke, H. Jenkyns, C. J. Bjerrum, P. Farrimond, H. S. Morgans Bell and O. Green (2000). "Massive dissociation of gas hydrate during a Jurassic oceanic anoxic event." Nature **406**: 392-395.

Hesselbo, S., S. Robinson, F. Surlyk and S. Piasecki (2002). "Terrestrial and marine extinction at the Triassic-Jurassic boundary synchronized with major carbon-cycle perturbation: A link to initiation of massive volcanism?" Geology **30**(3): 251-378.

Hesselbo, S. P., H. C. Jenkyns, L. V. Duarte and L. C. Oliveira (2007). "Carbon-isotope record of the Early Jurassic (Toarcian) Oceanic Anoxic Event from fossil wood and marine carbonate (Lusitanian Basin, Portugal)." Earth and Planetary Science Letters **253**(3): 455-470.

Hesselbo, S. P. (2008). "Sequence stratigraphy and inferred relative sea-level change from the onshore British Jurassic." Proceedings of the Geologists' Association **119**(1): 19-34.

Hesselbo, S. P. and G. Pieńkowski (2011). "Stepwise atmospheric carbon-isotope excursion during the Toarcian oceanic anoxic event (Early Jurassic, Polish Basin)." Earth and Planetary Science Letters **301**(1): 365-372.

Hesselbo, S., C. J. Bjerrum, L. Hinnov, C. MacNiocaill, K. Miller, J. Riding and B. Van de Schootbrugge (2013). "Mochras borehole revisited: a new global standard for Early Jurassic earth history." Scientific Drilling **16**: 81-91.

Hillebrandt, A. v., L. Krystyn and W. M. Kürschner (2007). "A candidate GSSP for the base of the Jurassic in the Northern Calcareous Alps (Kuhjoch section, Karwendel Mountains, Tyrol, Austria)." International Subcommission on Jurassic Stratigraphy Newsletter **34**: 2-20.

Hillebrandt, A. v., L. Krystyn, W. Kürschner, N. Bonis, M. Ruhl, S. Richoz, M. Schobben, M. Urlichs, P. Bown and K. Kment (2013). "The global stratotype sections and point (GSSP) for the base of the Jurassic System at Kuhjoch

(Karwendel Mountains, Northern Calcareous Alps, Tyrol, Austria)." Episodes **36**(3): 162-198.

Hinnov, L. A. and F. J. Hilgen (2012). Chapter 4 - Cyclostratigraphy and Astrochronology. In: The Geologic Time Scale. Boston, Elsevier**:** 63-83.

Holford, S. P., P. F. Green and J. P. Turner (2005). "Palaeothermal and compaction studies in the Mochras borehole (NW Wales) reveal early Cretaceous and Neogene exhumation and argue against regional Palaeogene uplift in the southern Irish Sea." Journal of the Geological Society **162**(5): 829-840.

Howell, J. A., E. Schwarz, L. A. Spalletti and G. D. Veiga (2005). "The Neuquén basin: an overview." Geological Society, London, Special Publications **252**(1): 1-14.

Huang, C. and S. P. Hesselbo (2014). "Pacing of the Toarcian Oceanic Anoxic Event (Early Jurassic) from astronomical correlation of marine sections." Gondwana Research **25**(4): 1348-1356.

Huggett, J., P. Dennis and A. Gale (2000). "Geochemistry of early siderite cements from the Eocene succession of Whitecliff Bay, Hampshire Basin, UK." Journal of Sedimentary Research **70**(5): 1107-1117.

Hüsing, S., A. Beniest, A. van der Boon, H. Abels, M. H. L. Deenen, M. Ruhl and W. Krijgsman (2014). "Astronomically-calibrated magnetostratigraphy of the Lower Jurassic marine successions at St. Audrie's Bay and East Quantoxhead (Hettangian–Sinemurian; Somerset, UK)." Palaeogeography Palaeoclimatology Palaeoecology **403**: 43–56.

Hutton, A. C. (1987). "Petrographic classification of oil shales." International Journal of Coal Geology **8**(3): 203-231.

Ikeda, M. and R. S. Hori (2014). "Effects of Karoo–Ferrar volcanism and astronomical cycles on the Toarcian Oceanic Anoxic Events (Early Jurassic)." Palaeogeography, Palaeoclimatology, Palaeoecology **410**(0): 134-142.

Ivimey-Cook, H. C. (1971). Stratigraphical paleontology of the Lower Jurassic of the Llanbedr (Mochras Farm) Borehole., Institute of Geological Sciences, pp. 87-92. Report No. 71/18.

Jarvis, I., A. Mabrouk, R. T. J. Moody and S. de Cabrera (2002). "Late Cretaceous (Campanian) carbon isotope events, sea-level change and correlation of the Tethyan and Boreal realms." Palaeogeography, Palaeoclimatology, Palaeoecology **188**(3): 215-248.

Jarvis, I. (2006). "The Santonian-Campanian phosphatic chalks of England and France." Proceedings of the Geologists' Association **117**(2): 219-237.

Jenkyns, H. C. (1988). "The early Toarcian (Jurassic) anoxic event; stratigraphic, sedimentary and geochemical evidence." American Journal of Science **288**(2): 101-151.

Jenkyns, H. C. (2003). "Evidence for rapid climate change in the Mesozoic–Palaeogene greenhouse world." Philosophical Transactions of the Royal Society

of London. Series A: Mathematical, Physical and Engineering Sciences **361**(1810): 1885-1916.

Jenkyns, H. C. (2010). "Geochemistry of oceanic anoxic events." Geochemistry, Geophysics, Geosystems **11**(3): Q03004.

Jenkyns, H. C. and C. J. Clayton (1986). "Black shales and carbon isotopes in pelagic sediments from the Tethyan Lower Jurassic." Sedimentology **33**(1): 87-106.

Jenkyns, H. C. and C. J. Clayton (1997). "Lower Jurassic epicontinental carbonates and mudstones from England and Wales: chemostratigraphic signals and the early Toarcian anoxic event." Sedimentology **44**(4): 687-706.

Jenkyns, H. C., C. E. Jones, D. R. Gröcke, S. P. Hesselbo and D. N. Parkinson (2002). "Chemostratigraphy of the Jurassic System: applications, limitations and implications for palaeoceanography." Journal of the Geological Society **159**(4): 351-378.

Jenkyns, H. C. and G. P. Weedon (2013). "Chemostratigraphy (CaCO3, TOC, $\delta^{13}C_{org}$) of Sinemurian (Lower Jurassic) black shales from the Wessex Basin, Dorset and palaeoenvironmental implications." Newsletters on Stratigraphy **46**(1): 1-21.

Jourdan, F., A. Marzoli, H. Bertrand, S. Cirilli, L. Tanner, D. Kontak, G. McHone, P. Renne and G. Bellieni (2009). "$^{40}Ar/^{39}Ar$ ages of CAMP in North America: Implications for the Triassic–Jurassic boundary and the 40 K decay constant bias." Lithos **110**(1): 167-180.

Jourdan, F. F., Gilbert; Bertrant Hervé; Kampunzu, Ali Bashira; Tshoso, Gomotsang; Watkeys Michael K.; Le Gall, Bernard (2005). "Karoo large igneous province: Brevity, origin, and relation to mass extinction questioned by new $^{40}Ar/^{39}Ar$ age data." Geology **33**(9): 745-748.

Katz, M. E., J. D. Wright, K. G. Miller, B. S. Cramer, K. Fennel and P. G. Falkowski (2005). "Biological overprint of the geological carbon cycle." Marine Geology **217**(3): 323-338.

Kemp, D. B., A. L. Coe, A. S. Cohen and L. Schwark (2005). "Astronomical pacing of methane release in the Early Jurassic period." Nature **437**(7057): 396-399.

Kemp, D. B., A. L. Coe, A. S. Cohen and G. P. Weedon (2011). "Astronomical forcing and chronology of the early Toarcian (Early Jurassic) oceanic anoxic event in Yorkshire, UK." Paleoceanography **26**(4): 1-17.

Kiel, S. (2009). "Global hydrocarbon seep‐carbonate precipitation correlates with deep‐water temperatures and eustatic sea‐level fluctuations since the Late Jurassic." Terra Nova **21**(4): 279-284.

Knight, K., S. Nomade, P. Renne, A. Marzoli, H. Bertrand and N. Youbi (2004). "The Central Atlantic Magmatic Province at the Triassic–Jurassic boundary: paleomagnetic and 40 Ar/39 Ar evidence from Morocco for brief, episodic volcanism." Earth and Planetary Science Letters **228**(1): 143-160.

Kohn, M. (2016). "Carbon isotope discrimination in C3 land plants is independent of natural variations in pCO_2." Geochemical Perspectives Letters **2**: 35-43.

Kohn, M. J. (2010). "Carbon isotope compositions of terrestrial C3 plants as indicators of (paleo) ecology and (paleo) climate." Proceedings of the National Academy of Sciences **107**(46): 19691-19695.

Kohn, M. J. (2010). "Carbon isotope compositions of terrestrial C3 plants as indicators of (paleo)ecology and (paleo)climate." Proceedings of the National Academy of Sciences **107**(46): 19691-19695.

Korte, C. and S. P. Hesselbo (2011). "Shallow marine carbon and oxygen isotope and elemental records indicate icehouse‐greenhouse cycles during the Early Jurassic." Paleoceanography **26**(4): PA4219.

Korte, C., S. P. Hesselbo, C. V. Ullmann, G. Dietl, M. Ruhl, G. Schweigert and N. Thibault (2015). "Jurassic climate mode governed by ocean gateway." Nature Communications **6**: 10015.

Kump, L. R. and M. A. Arthur (1999). "Interpreting carbon-isotope excursions: carbonates and organic matter." Chemical Geology **161**(1): 181-198.

Kuroda, J., N. O. Ogawa, M. Tanimizu, M. F. Coffin, H. Tokuyama, H. Kitazato and N. Ohkouchi (2007). "Contemporaneous massive subaerial volcanism and late cretaceous Oceanic Anoxic Event 2." Earth and Planetary Science Letters **256**(1): 211-223.

Kürschner, W. M., J. van der Burgh, H. Visscher and D. L. Dilcher (1996). "Oak leaves as biosensors of late Neogene and early Pleistocene paleoatmospheric CO2 concentrations." Marine Micropaleontology **27**(1-4): 299-312.

Lanes, S. (2005). "Late Triassic to Early Jurassic sedimentation in northern Neuquén Basin, Argentina: tectosedimentary evolution of the first transgression." Geologica Acta: an international earth science journal **3**(2): 81-106.

Lanes, S., M. Mancenido and S. Damborenea (2006). "Lapispira: a double helicoidal burrow from Jurassic marine nearshore environments." SPECIAL PUBLICATION-SEPM **88**: 59-77.

Laskar, J. (1993). "Frequency analysis for multi-dimensional systems. Global dynamics and diffusion." Physica D: Nonlinear Phenomena **67**(1): 257-281.

Laskar, J., A. Fienga, M. Gastineau and H. Manche (2011). "La2010: a new orbital solution for the long-term motion of the Earth." Astronomy & Astrophysics **532**: A89.

Laskar, J., P. Robutel, F. Joutel, M. Gastineau, A. Correia and B. A. Levrard (2004). "A Long-term Numerical Solution for the Insolation Quantities of the Earth." Astronomy and Astrophysics **428 (1)**: 261-285.

Laws, E. A., B. N. Popp, R. R. Bidigare, M. C. Kennicutt and S. A. Macko (1995). "Dependence of phytoplankton carbon isotopic composition on growth rate and [CO2) aq: Theoretical considerations and experimental results." Geochimica et cosmochimica acta **59**(6): 1131-1138.

Legarreta, L. and M. A. Uliana (1996). "The Jurassic succession in west-central Argentina: stratal patterns, sequences and paleogeographic evolution." Palaeogeography, Palaeoclimatology, Palaeoecology **120**(3-4): 303-330.

Léonide, P., M. Floquet and L. Villier (2007). "Interaction of tectonics, eustasy, climate and carbonate production on the sedimentary evolution of an early/middle Jurassic extensional basin (Southern Provence Sub‐basin, SE France)." Basin Research **19**: 125-152.

Linnert, C., S. A. Robinson, J. A. Lees, P. R. Bown, I. Pérez-Rodríguez, M. R. Petrizzo, F. Falzoni, K. Littler, J. A. Arz and E. E. Russell (2014). "Evidence for global cooling in the Late Cretaceous." Nature Communications **5**: 4194.

Linnert, C., S. A. Robinson, J. A. Lees, I. Pérez-Rodríguez, H. C. Jenkyns, M. R. Petrizzo, J. A. Arz, P. R. Bown and F. Falzoni (2017). "Did Late Cretaceous cooling trigger the Campanian–Maastrichtian Boundary Event?" Newsletters on Stratigraphy **51**(2): 145-166.

Lijmbach, W. (1975). On the Origin of Petroleum. 9th World Petroleum Congress, World Petroleum Congress. Tokyo, Japan.

Little, C. T. and M. J. Benton (1995). "Early Jurassic mass extinction: a global long-term event." Geology **23**(6): 495-498.

Littler, K. H., Stephen P.; Jenkyns, Hugh J. (2009). "A carbon-isotope perturbation at the Pliensbachian–Toarcian boundary: evidence from the Lias Group, NE England." Geological Magazine **147**(2): 181-192.

Lourens, L. J., A. Sluijs, D. Kroon, J. C. Zachos, E. Thomas, U. Röhl, J. Bowles and I. Raffi (2005). "Astronomical pacing of late Palaeocene to early Eocene global warming events." Nature **435**(7045): 1083-1087.

Ma, W., J. Tian, Q. Li and P. Wang (2011). "Simulation of long eccentricity (400-kyr) cycle in ocean carbon reservoir during Miocene Climate Optimum: Weathering and nutrient response to orbital change." Geophysical Research Letters **38**(10): L10701.

Mallarino, G., R. H. Goldstein and P. Di Stefano (2002). "New approach for quantifying water depth applied to the enigma of drowning of carbonate platforms." Geology **30**(9): 783-786.

Mann, M. E. and J. M. Lees (1996). "Robust estimation of background noise and signal detection in climatic time series." Climatic change **33**(3): 409-445.

Martinez, M. and G. Dera (2015). "Orbital pacing of carbon fluxes by a ~9-My eccentricity cycle during the Mesozoic." PNAS **112**(41): 12604-12609.

Marzoli, A., H. Bertrand, K. B. Knight, S. Cirilli, N. Buratti, C. Vérati, S. Nomade, P. R. Renne, N. Youbi and R. Martini (2004). "Synchrony of the Central Atlantic magmatic province and the Triassic-Jurassic boundary climatic and biotic crisis." Geology **32**(11): 973-976.

Marzoli, A., F. Jourdan, J. H. Puffer, T. Cuppone, L. H. Tanner, R. E. Weems, H. Bertrand, S. Cirilli, G. Bellieni and A. De Min (2011). "Timing and duration of the Central Atlantic magmatic province in the Newark and Culpeper basins, eastern USA." Lithos **122**(3): 175-188.

Marzoli, A., P. R. Renne, E. M. Piccirillo, M. Ernesto, G. Bellieni and A. De Min (1999). "Extensive 200-million-year-old continental flood basalts of the Central Atlantic Magmatic Province." Science **284**(5414): 616-618.

Masetti, D., B. Figus, H. C. Jenkyns, F. Barattolo, E. Mattioli and R. Posenato (2016). "Carbon-isotope anomalies and demise of carbonate platforms in the Sinemurian (Early Jurassic) of the Tethyan region: evidence from the Southern Alps (Northern Italy)." Geological Magazine **154**(3): 625-650.

Mattinson, J. M. (2005). "Zircon U–Pb chemical abrasion ("CA-TIMS") method: Combined annealing and multi-step partial dissolution analysis for improved precision and accuracy of zircon ages." Chemical Geology **220**(1–2): 47-66.

Mazzini, A., H. Svensen, H. A. Leanza, F. Corfu and S. Planke (2010). "Early Jurassic shale chemostratigraphy and U–Pb ages from the Neuquén Basin (Argentina): implications for the Toarcian Oceanic Anoxic event." Earth and Planetary Science Letters **297**(3): 633-645.

McElwain, J. C., J. Wade-Murphy and S. P. Hesselbo (2005). "Changes in carbon dioxide during an oceanic anoxic event linked to intrusion into Gondwana coals." Nature **435**(7041): 479-482.

Meyers, S. R. (2014). Astrochron: an R package for astrochronology (version 0.3.1). .

Milkov, A. V. (2004). "Global estimates of hydrate-bound gas in marine sediments: how much is really out there?" Earth-Science Reviews **66**(3): 183-197.

Newton, R. J., E. P. Reeves, N. Kafousia, P. B. Wignall, S. H. Bottrell and J.-G. Sha (2011). "Low marine sulfate concentrations and the isolation of the European epicontinental sea during the Early Jurassic." Geology **39**(1): 7-10.

Nomade, S., K. Knight, E. Beutel, P. Renne, C. Verati, G. Féraud, A. Marzoli, N. Youbi and H. Bertrand (2007). "Chronology of the Central Atlantic Magmatic Province: implications for the Central Atlantic rifting processes and the Triassic–Jurassic biotic crisis." Palaeogeography, Palaeoclimatology, Palaeoecology **244**(1): 326-344.

Oliveira, L. C. R., R.; Duarte, L. V.; Lemos, V. B. (2006). "Avaliação do potencial gerador de petróleo e interpretação paleoambiental com base em biomarcadores e isótopos estáveis do carbono da seção Pliensbaquiano-Toarciano inferior (Jurássico inferior) da região de Peniche (Bacia Lusitânica, Portugal)." Boletim de Geociências da Petrobras **14**(2): 207-234.

Page, K. N. (2004). "A sequence of biohorizons for the subboreal province Lower Toarcian in Northern Britain and their correlation with a submediterranean standard." Rivista Italiana di Paleontologia e Stratigrafia **110**(1): 109-14

Paillard, D. (2010). "Climate and the orbital parameters of the Earth." Comptes Rendus Geoscience **342**(4): 273-285.

Pálfy, J., R. R. Parrish and P. L. Smith (1997). "A U-Pb age from the Toarcian (Lower Jurassic) and its use for time scale calibration through error analysis of biochronologic dating." Earth and Planetary Science Letters **146**(3-4): 659-675.

Pálfy, J., J. K. Mortensen, P. L. Smith, R. M. Friedman, V. McNicoll and M. Villeneuve (2000a). New U-Pb zircon ages integrated with ammonite biochronology from the Jurassic of the Canadian Cordillera. Canadian Journal of Earth Sciences, NRC Research Press. **37:** 549-567.

Pálfy, J. and P. L. Smith (2000). "Synchrony between Early Jurassic extinction, oceanic anoxic event, and the Karoo-Ferrar flood basalt volcanism." Geology **28**(8): 747-750.

Pálfy, J., A. Demény, J. n. Haas, M. Hetényi, M. J. Orchard and I. Veto (2001). "Carbon isotope anomaly and other geochemical changes at the Triassic-Jurassic boundary from a marine section in Hungary." Geology **29**(11): 1047-1050.

Pálfy, J., Smith, P.L., Mortensen, J.K (2002). "Dating the end-Triassic and Early Jurassic mass extinctions, correlative large igneous provinces, and isotopic events." Special Paper of the Geological Society of America(356): 523-532.

Partington, M. A., P. Copestake, B. C. Mitchener and J. Underhill (1993). "Biostratigraphic Calibration od Genetic Stratigraphic Sequences in the Jurassic Lowermost Cretaceous (Hettangian to Ryazanian) of the North-Sea and Adjacent Areas. Geological Society, London, Petroleum Geology Conference series **1** (4) 4: 371-386.

Percival, L. M. E., A. S. Cohen, M. K. Davies, A. J. Dickson, S. P. Hesselbo, H. C. Jenkyns, M. J. Leng, T. A. Mather, M. S. Storm and W. Xu (2016). "Osmium isotope evidence for two pulses of increased continental weathering linked to Early Jurassic volcanism and climate change." Geology.

Percival, L. M. E., M. L. I. Witt, T. A. Mather, M. Hermoso, H. C. Jenkyns, S. P. Hesselbo, A. H. Al-Suwaidi, M. S. Storm, W. Xu and M. Ruhl (2015). "Globally enhanced mercury deposition during the end-Pliensbachian extinction and Toarcian OAE: A link to the Karoo–Ferrar Large Igneous Province." Earth and Planetary Science Letters **428**: 267-280.

Peti, L., N. Thibault, M.-E. Clémence, C. Korte, J.-L. Dommergues, C. Bougeault, P. Pellenard, M. E. Jelby and C. V. Ullmann (2017). "Sinemurian–Pliensbachian calcareous nannofossil biostratigraphy and organic carbon isotope stratigraphy in the Paris Basin: Calibration to the ammonite biozonation of NW Europe." Palaeogeography, Palaeoclimatology, Palaeoecology **468**: 142-161.

Popp, B. N., E. A. Laws, R. R. Bidigare, J. E. Dore, K. L. Hanson and S. G. Wakeham (1998). "Effect of phytoplankton cell geometry on carbon isotopic fractionation." Geochimica et cosmochimica acta **62**(1): 69-77.

Porter, S. J., D. Selby, K. Suzuki and D. Gröcke (2013). "Opening of a trans-Pangaean marine corridor during the Early Jurassic: Insights from osmium isotopes across the Sinemurian–Pliensbachian GSSP, Robin Hood's Bay, UK." Palaeogeography, Palaeoclimatology, Palaeoecology **375**: 50-58.

Porter, S. J., P. L. Smith, A. H. Caruthers, P. Hou, D. R. Gröcke and D. Selby (2014). "New high resolution geochemistry of Lower Jurassic marine sections in western North America: A global positive carbon isotope excursion in the Sinemurian?" Earth and Planetary Science Letters **397**: 19-31.

Price, G. D. (1999). "The evidence and implications of polar ice during the Mesozoic." Earth-Science Reviews **48**(3): 183-210.

Pyle, D. M. and T. A. Mather (2003). "The importance of volcanic emissions for the global atmospheric mercury cycle." Atmospheric Environment **37**(36): 5115-5124.

Quesada, S., S. Robles and I. Rosales (2005). "Depositional architecture and transgressive-regressive cycles within Liassic backstepping carbonate ramps in the Basque-Cantabrian basin, northern Spain." Journal of the Geological Society **162**: 531-548.

Ramos, V., H. Niemeyer, J. Skarmeta and J. Mun (1982). "Magmatic evolution of the austral Patagonian Andes." Earth-Science Reviews **18**(3): 411-443.

Rampino, M. R. and R. B. Stothers (1988). "Flood basalt volcanism during the past 250 million years." Science **241**(4866): 663-668.

Revelle, R. and H. E. Suess (1957). "Carbon dioxide exchange between atmosphere and ocean and the question of an increase of atmospheric CO2 during the past decades." Tellus **9**(1): 18-27.

Riccardi, A. (1983). "The Jurassic of Argentina and Chile." The Phanerozoic Geology of the World II. The Mesozoic, B: 201-263.

Riccardi, A. C. (2008a). "El Jurásico de la Argentina y sus amonites." Revista de la Asociación Geológica Argentina **63**(4): 625-643.

Riccardi, A. C. (2008b). "The marine Jurassic of Argentina: a biostratigraphic framework." Episodes **31**(3): 326-335.

Riccardi, A. C., S. E. Damborenea, M. O. Manceñido and H. A. Leanza (2011). Megainvertebrados del Jurásico y su importancia geobiológica. Geología y Recursos Naturales de la Provincia del Neuquén: Buenos Aires, Relatorio del 18 Congreso Geológico Argentino.

Riccardi, A. and S. Kamo (2014). Biostratigraphy and Geochronology of the Pliensbachian-Toarcian Boundary in Argentina. XIX Congreso Geológico Argentino. Córdoba. **1**.

Riding, J. B., M. J. Leng, S. Kender, S. P. Hesselbo and S. Feist-Burkhardt (2013). "Isotopic and palynological evidence for a new Early Jurassic environmental perturbation." Palaeogeography, Palaeoclimatology, Palaeoecology **374**(Supplement C): 16-27.

Röhl, H.-J., A. Schmid-Röhl, W. Oschmann, A. Frimmel and L. Schwark (2001). "The Posidonia Shale (Lower Toarcian) of SW-Germany: an oxygen-depleted ecosystem controlled by sea level and palaeoclimate." Palaeogeography, Palaeoclimatology, Palaeoecology **165**(1): 27-52.

Rosales, I., S. Quesada and S. Robles (2004). "Paleotemperature variations of Early Jurassic seawater recorded in geochemical trends of belemnites from the Basque–Cantabrian basin, northern Spain." Palaeogeography, Palaeoclimatology, Palaeoecology **203**(3): 253-275.

Rosales, I., S. Quesada and S. Robles (2006). "Geochemical arguments for identifying second‐order sea‐level changes in hemipelagic carbonate ramp deposits." Terra Nova **18**(4): 233-240.

Royer, D. L. (2006). "CO2-forced climate thresholds during the Phanerozoic." Geochimica et Cosmochimica Acta **70**(23): 5665-5675.

Ruhl, M., S. P. Hesselbo, L. Hinnov, H. C. Jenkyns, W. Xu, J. B. Riding, M. Storm, D. Minisini, C. V. Ullmann and M. J. Leng (2016). "Astronomical constraints on the duration of the Early Jurassic Pliensbachian Stage and global climatic fluctuations." Earth and Planetary Science Letters **455**: 149-165.

Ruhl, M., W. M. Kürschner and L. Krystyn (2009). "Triassic–Jurassic organic carbon isotope stratigraphy of key sections in the western Tethys realm (Austria)." Earth and Planetary Science Letters **281**(3): 169-187.

Ruhl, M., H. Veld and W. M. Kürschner (2010). "Sedimentary organic matter characterization of the Triassic–Jurassic boundary GSSP at Kuhjoch (Austria)." Earth and Planetary Science Letters **292**(1–2): 17-26.

Sælen, G., R. V. Tyson, N. Telnæs and M. R. Talbot (2000). "Contrasting watermass conditions during deposition of the Whitby Mudstone (Lower Jurassic) and Kimmeridge Clay (Upper Jurassic) formations, UK." Palaeogeography, Palaeoclimatology, Palaeoecology **163**(3): 163-196.

Schaltegger, U., J. Guex, A. Bartolini, B. Schoene and M. Ovtcharova (2008). "Precise U–Pb age constraints for end-Triassic mass extinction, its correlation to volcanism and Hettangian post-extinction recovery." Earth and Planetary Science Letters **267**(1): 266-275.

Schlanger, S. and H. Jenkyns (1976). "Cretaceous oceanic anoxic events: causes and consequences." Geologie en mijnbouw **55**(3-4): 179-184.

Schoene, B., J. Guex, A. Bartolini, U. Schaltegger and T. J. Blackburn (2010). "Correlating the end-Triassic mass extinction and flood basalt volcanism at the 100 ka level." Geology **38**(5): 387-390.

Schootbrugge, B., A. Bachan, G. Suan, S. Richoz and J. L. Payne (2013). "Microbes, mud and methane: cause and consequence of recurrent Early Jurassic anoxia following the end‐Triassic mass extinction." Palaeontology **56**(4): 685-709.

Schouten, S., H. M. van Kaam-Peters, W. I. C. Rijpstra, M. Schoell and J. S. S. Damste (2000). "Effects of an oceanic anoxic event on the stable carbon isotopic composition of early Toarcian carbon." American Journal of Science **300**(1): 1-22.

Schouten, S., M. Woltering, W. I. C. Rijpstra, A. Sluijs, H. Brinkhuis and J. S. S. Damsté (2007). "The Paleocene–Eocene carbon isotope excursion in higher plant organic matter: Differential fractionation of angiosperms and conifers in the Arctic." Earth and Planetary Science Letters **258**(3): 581-592.

Schubert, B. A. and A. H. Jahren (2012). "The effect of atmospheric CO 2 concentration on carbon isotope fractionation in C 3 land plants." Geochimica et Cosmochimica Acta **96**: 29-43.

Self, S., T. Thordarson and M. Widdowson (2005). "Gas Fluxes from Flood Basalt Eruptions." Elements **1**: 283-287.

Self, S., M. Widdowson, T. Thordarson and A. E. Jay (2006). "Volatile fluxes during flood basalt eruptions and potential effects on the global environment: A Deccan perspective." Earth and Planetary Science Letters **248**(1-2): 518-532.

Sell, B., M. Ovtcharova, J. Guex, A. Bartolini, F. Jourdan, J. E. Spangenberg, J.-C. Vicente and U. Schaltegger (2014). "Evaluating the temporal link between the Karoo LIP and climatic–biologic events of the Toarcian Stage with high-precision U–Pb geochronology." Earth and Planetary Science Letters **408**: 48-56.

Sellwood, B. (1971). "The genesis of some sideritic beds in the Yorkshire Lias (England)." Journal of Sedimentary Research **41**(3).

Silva, R. and L. Duarte (2015). "Organic matter production and preservation in the Lusitanian Basin (Portugal) and Pliensbachian climatic hot snaps." Global and Planetary Change **131**: 24-34.

Silva, R. L., L. V. Duarte, M. J. Comas-Rengifo, J. G. Mendonça Filho and A. C. Azerêdo (2011). "Update of the carbon and oxygen isotopic records of the Early–Late Pliensbachian (Early Jurassic,~ 187Ma): Insights from the organic-rich hemipelagic series of the Lusitanian Basin (Portugal)." Chemical Geology **283**(3): 177-184.

Simms, M. J. C., N.; Morton, N.; Page, K.N. (2004). "British Lower Jurassic Stratigraphy." Geological Conservation Review Series **30**, 458pp.

Sluijs, A. and G. R. Dickens (2012). "Assessing offsets between the δ13C of sedimentary components and the global exogenic carbon pool across early Paleogene carbon cycle perturbations." Global Biogeochemical Cycles **26**(4).

Sprovieri, M., R. Coccioni, F. Lirer, N. Pelosi and F. Lozar (2006). "Orbital tuning of a lower Cretaceous composite record (Maiolica Formation, central Italy)." Paleoceanography **21**(4).

Sprovieri, M., N. Sabatino, N. Pelosi, S. J. Batenburg, R. Coccioni, M. Iavarone and S. Mazzola (2013). "Late Cretaceous orbitally-paced carbon isotope stratigraphy from the Bottaccione Gorge (Italy)." Palaeogeography, Palaeoclimatology, Palaeoecology **379**: 81-94.

Suan, G., E. Mattioli, B. Pittet, C. Lécuyer, B. Suchéras-Marx, L. V. Duarte, M. Philippe, L. Reggiani and F. Martineau (2010). "Secular environmental precursors to Early Toarcian (Jurassic) extreme climate changes." Earth and Planetary Science Letters **290**(3–4): 448-458.

Suan, G., B. L. Nikitenko, M. A. Rogov, F. Baudin, J. E. Spangenberg, V. G. Knyazev, L. A. Glinskikh, A. A. Goryacheva, T. Adatte and J. B. Riding (2011). "Polar record of Early Jurassic massive carbon injection." Earth and Planetary Science Letters **312**(1): 102-113.

Suan, G., B. L. Nikitenko, M. A. Rogov, F. Baudin, J. E. Spangenberg, V. G. Knyazev, L. A. Glinskikh, A. A. Goryacheva, T. Adatte, J. B. Riding, K. B. Föllmi, B. Pittet, E. Mattioli and C. Lécuyer (2011). "Polar record of Early Jurassic massive carbon injection." Earth and Planetary Science Letters **312**(1–2): 102-113.

Suan, G., B. Schootbrugge, T. Adatte, J. Fiebig and W. Oschmann (2015). "Calibrating the magnitude of the Toarcian carbon cycle perturbation." Paleoceanography **30**(5): 495-509.

Svensen, H., F. Corfu, S. Polteau, Ø. Hammer and S. Planke (2012). "Rapid magma emplacement in the Karoo large igneous province." Earth and Planetary Science Letters **325**: 1-9.

Svensen, H., S. Planke, L. Chevallier, A. Malthe-Sørenssen, F. Corfu and B. Jamtveit (2007). "Hydrothermal venting of greenhouse gases triggering Early Jurassic global warming." Earth and Planetary Science Letters **256**(3–4): 554-566.

Tappin, D. R. (1994). The geology of Cardigan Bay and the Bristol Channel, HMSO, London, 107pp.

Taylor, G. H. (1998). Organic petrology : a new handbook incorporating some revised parts of Stach's Textbook of coal petrology. D. C. Glick. Berlin, Gebrüder Borntraeger**:** 704.

Teichert, B., A. Eisenhauer, G. Bohrmann, A. Haase-Schramm, B. Bock and P. Linke (2003). "U/Th systematics and ages of authigenic carbonates from Hydrate Ridge, Cascadia Margin: recorders of fluid flow variations." Geochimica et Cosmochimica Acta **67**(20): 3845-3857.

Teichert, B. and F. Luppold (2013). "Glendonites from an Early Jurassic methane seep—Climate or methane indicators?" Palaeogeography, Palaeoclimatology, Palaeoecology **390**: 81-93.

Teichmüller, M. (1989). "The genesis of coal from the viewpoint of coal petrology." International Journal of Coal Geology **12**(1-4): 1-87.

Them, T. R., B. C. Gill, A. H. Caruthers, D. R. Gröcke, E. T. Tulsky, R. C. Martindale, T. P. Poulton and P. L. Smith (2017a). "High-resolution carbon isotope records of the Toarcian Oceanic Anoxic Event (Early Jurassic) from North America and implications for the global drivers of the Toarcian carbon cycle." Earth and Planetary Science Letters. **459**: 118-126.

Them, T. R., B. C. Gill, D. Selby, D. R. Gröcke, R. M. Friedman and J. D. Owens (2017b). "Evidence for rapid weathering response to climatic warming during the Toarcian Oceanic Anoxic Event." Scientific Reports **7**(1): 5003.

Tissot, B. and D. Welte (1978). Petroleum occurrence and formation, Springer-Verlag: Heidelberg.

Traverse, A. (2007). Paleopalynology. Netherlands, Springer.

Tucker, R. M. and G. Arter (1987). "The tectonic evolution of the North Celtic Sea and Cardigan Bay basins with special reference to basin inversion." Tectonophysics **137**(1): 291-307.

Turgeon, S. C. and R. A. Creaser (2008). "Cretaceous oceanic anoxic event 2 triggered by a massive magmatic episode." Nature **454**(7202): 323-326.

Tyson, R. V. (1995). Sedimentary Organic Matter. London, Charman & Hall**:** 615.

Valencio, S. A., M. C. Cagnoni, A. M. Ramos, A. Riccardi and H. O. Panarello (2005). "Chemostratigraphy of the Pliensbachian, Puesto Araya Formation (Neuquén Basin, Argentina)." Geologica Acta **3**(2): 147-154.

van de Schootbrugge, B., T. R. Bailey, Y. Rosenthal, M. E. Katz, J. D. Wright, K. G. Miller, S. Feist-Burkhardt and P. G. Falkowski (2005). "Early Jurassic climate change and the radiation of organic-walled phytoplankton in the Tethys Ocean." Paleobiology **31**(1): 73-97.

van de Schootbrugge, B., D. Harazim, S. K, O. W, J. Fiebig, W. Püttmann, P. M, Z. F, B. M. A. Teichert, H. J, S. A and Y. Rosenthal (2010). "The enigmatic ichnofossil Tisoa siphonalis and widespread authigenic seep carbonate formation during the Late Pliensbachian in southern France." Biogeosciences **7**: 3123-3138.

Van der Zwan, C. (1990). "Palynostratigraphy and palynofacies reconstruction of the Upper Jurassic to lowermost Cretaceous of the Draugen Field, offshore Mid Norway." Review of palaeobotany and palynology **62**(1-2): 157-186.

Verati, C., C. Rapaille, G. Féraud, A. Marzoli, H. Bertrand and N. Youbi (2007). "40 Ar/39 Ar ages and duration of the Central Atlantic Magmatic Province volcanism in Morocco and Portugal and its relation to the Triassic–Jurassic boundary." Palaeogeography, Palaeoclimatology, Palaeoecology **244**(1): 308-325.

Vergani, G. D., A. J. Tankard, H. J. Belotti and H. J. Welsink (1995). Tectonic evolution and paleogeography of the Neuquén Basin, Argentina. Petroleum Basins of South America. A. J. Tankard, Suarez Soruco R, Belotti H.J., Welsink H J

Vicente, J. C. (2005). "Dynamic paleogeography of the Jurassic Andean Basin: pattern of transgression and localisation of main straits through the magmatic arc." Revista de la Asociación Geológica Argentina **60**(1): 221-250.

Voigt, S., A. Aurag, F. Leis and U. Kaplan (2007). "Late Cenomanian to Middle Turonian high-resolution carbon isotope stratigraphy: New data from the Münsterland Cretaceous Basin, Germany." Earth and Planetary Science Letters **253**(1): 196-210.

Voigt, S., A. S. Gale, C. Jung and H. C. Jenkyns (2012). "Global correlation of Upper Campanian–Maastrichtian successions using carbon-isotope stratigraphy: development of a new Maastrichtian timescale." Newsletters on Stratigraphy **45**(1): 25-53.

Weaver, C. E. (1931). Paleontology of the Jurassic and Cretaceous of west central Argentina, Washington, University of Washington Press (1): 1-496.

Weedon, G. and H. Jenkyns (1999). "Cyclostratigraphy and the Early Jurassic timescale: data from the Belemnite Marls, Dorset, southern England." Geological Society of America Bulletin **111**(12): 1823-1840.

Westerhold, T., U. Röhl and J. Laskar (2012). "Time scale controversy: Accurate orbital calibration of the early Paleogene." Geochemistry, Geophysics, Geosystems **13**(6).

Whitaker, M. (1984). The usage of palynostratigraphy and palynofacies in definition of Troll Field geology: 6th Offshore Northern Seas Conference and Exhibition, Stavanger.

Whiteside, J. H., P. E. Olsen, T. Eglinton, M. E. Brookfield and R. N. Sambrotto (2010). "Compound-specific carbon isotopes from Earth's largest flood basalt eruptions directly linked to the end-Triassic mass extinction." Proceedings of the National Academy of Sciences **107**(15): 6721-6725.

Wignall, P. (2001). "Large igneous provinces and mass extinctions." Earth-Science Reviews **53**(1): 1-33.

Wignall, P. B., D. P. Bond, K. Kuwahara, Y. Kakuwa, R. J. Newton and S. W. Poulton (2010). "An 80 million year oceanic redox history from Permian to Jurassic pelagic sediments of the Mino-Tamba terrane, SW Japan, and the origin of four mass extinctions." Global and Planetary Change **71**(1): 109-123.

Wilkin, R. and H. Barnes (1996). "Pyrite formation by reactions of iron monosulfides with dissolved inorganic and organic sulfur species." Geochimica et Cosmochimica Acta **60**(21): 4167-4179.

Wood, G. (1996). "Palynological techniques-processing and microscopy." Palynology: principles and applications **3**: 29.

Woodfine, R. G., H. C. Jenkyns, M. Sarti, F. Baroncini and C. Violante (2008). "The response of two Tethyan carbonate platforms to the early Toarcian (Jurassic) oceanic anoxic event: environmental change and differential subsidence." Sedimentology **55**(4): 1011-1028.

Woodland, A. W. (1971). The Llanbedr (Mochras Farm) Borehole., Institute of Geological Sciences, 115pp. Report No. 71/18.

Wotzlaw, J.-F., J. Guex, A. Bartolini, Y. Gallet, L. Krystyn, C. A. McRoberts, D. Taylor, B. Schoene and U. Schaltegger (2014). "Towards accurate numerical calibration of the Late Triassic: High-precision U-Pb geochronology constraints on the duration of the Rhaetian." Geology **42**(7): 571-574.

Xu, W., M. Ruhl, S. P. Hesselbo, J. B. Riding and H. C. Jenkyns (2017a). "Orbital pacing of the Early Jurassic carbon cycle, black-shale formation and seabed methane seepage." Sedimentology **64**(1): 127-149.

Xu, W., M. Ruhl, H. C. Jenkyns, S. P. Hesselbo, J. B. Riding, D. Selby, B. D. A. Naafs, J. W. Weijers, R. D. Pancost and E. W. Tegelaar (2017b). "Carbon sequestration in an expanded lake system during the Toarcian oceanic anoxic event." Nature Geoscience **10**(2): 129-134.

Xu, W., M. Ruhl, H. C. Jenkyns, M. J. Leng, J. M. Huggett, D. Minisini, C. V. Ullmann, J. B. Riding, J. W. H. Weijers, M. S. Storm, L. M. E. Percival, N. J. Tosca, E. F. Idiz, E. W. Tegelaar and S. P. Hesselbo (2018). "Evolution of the Toarcian (Early Jurassic) carbon-cycle and global climatic controls on local sedimentary processes (Cardigan Bay Basin, UK)." Earth and Planetary Science Letters **484**: 396–411.

Zachos, J. C., G. Dickens and R. E. Zeebe (2009). "Carbon dioxide forcing alone insufficient to explain Palaeocene–Eocene Thermal Maximum warming." Nature Geoscience **2**(8): 576-580.

Zachos, J. C., H. K. McCarren, B. Murphy, U. Röhl and T. Westerhold (2010). "Tempo and scale of late Paleocene and early Eocene carbon isotope cycles: Implications for the origin of hyperthermals." Earth and Planetary Science Letters **299**(1-2): 242-249.

Zachos, J. C., N. J. Shackleton, J. S. Revenaugh, H. Pälike and B. P. Flower (2001). "Climate response to orbital forcing across the Oligocene-Miocene boundary." Science **292**(5515): 274-278.

Ziegler (1982). "Geological Atlas of Western and Central Europe." Geological Magazine **121**(4): 371-372.

Ziegler (1990). Geological Atlas of Western and Central Europe, Shell Internationale Petroleum Maatschappij B.V.